ABSTRACT

THEORETICAL STUDIES OF STRUCTURAL AND ELECTRONIC PROPERTIES IN TRANSITION METAL OXIDES

by
Tsezár F. Seman

The following studies are presented: theory of K-edge resonant inelastic x-ray scattering and its application for $La_{0.5}Sr_{1.5}MnO_4$, effects of rare earth ion size on the stability of the coherent Jahn-Teller distortions in undoped perovskite manganites, and symmetry-mode-based classical and quantum mechanical formalism of lattice dynamics.

The formula based on tight-binding approach for the calculation of K-edge resonant inelastic x-ray scattering (RIXS) spectrum for transition metal oxides is presented first, by extending the previous existing result to include explicit momentum dependence and a basis with multiple core-hole sites. This formula is applied to layered charge, orbital and spin ordered manganites, $La_{0.5}Sr_{1.5}MnO_4$, and good agreement with experimental data was obtained, in particular, with regard to the large variation of the intensity with momentum. As a consequence, it is established that the electron screening in $La_{0.5}Sr_{1.5}MnO_4$ is highly localized around the core hole site and demonstrates the potential of K-edge RIXS, as a probe for the screening dynamics in materials.

Theoretical study is then introduced on the relation between the size of the rare earth ions, often known as chemical pressure, and the stability of the coherent Jahn-Teller distortions in undoped perovskite manganites. Using a Keating model expressed in terms of atomic scale symmetry modes, it is shown that there exists a coupling between the uniform shear distortion and the staggered buckling distortion within the Jahn-Teller energy term. It is found that this coupling provides a mechanism by which the coherent Jahn-Teller distortion is more stabilized by smaller rare

earth ions. Further analysis shows the appearance of the uniform shear distortion below the Jahn-Teller ordering temperature; the Jahn-Teller ordering temperature is estimated and its variation between $NdMnO_3$ and $LaMnO_3$, and the relations between distortions are obtained. A good agreement is found between theoretical results and the experimental data.

Finally, the classical and quantum mechanical descriptions of lattice dynamics are presented, from the atomic to the continuum scale, using atomic scale symmetry modes and their constraint equations. This approach is demonstrated for a one-dimensional chain and a two-dimensional square lattice on a monatomic basis. For the classical description, it is found that rigid modes, in addition to the distortional modes found before, are necessary to describe the kinetic energy. The long wavelength limit of the kinetic energy terms expressed in terms of atomic scale modes is shown to be consistent with the continuum theory, and leading order corrections are obtained. For the quantum mechanical description, conjugate momenta for the atomic scale symmetry modes are presented. In direct space, graphical rules for their commutation relations are obtained. Commutation relations in the reciprocal space are also calculated. As an example, phonon modes are analyzed in terms of symmetry modes. The approach presented here based on atomic scale symmetry modes could be useful for the study of complex emerging materials, in which competing structural phases and non-linearity of the lattice energy play an important role.

THEORETICAL STUDIES OF STRUCTURAL AND ELECTRONIC PROPERTIES IN TRANSITION METAL OXIDES

by
Tsezár F. Seman

A Dissertation
Submitted to the Faculty of
New Jersey Institute of Technology and
Rutgers, The State University of New Jersey – Newark
in Partial Fulfillment of the Requirements for the Degree of
Doctor of Philosophy in Applied Physics

Department of Physics

January 2013

APPROVAL PAGE

THEORETICAL STUDIES OF STRUCTURAL AND ELECTRONIC PROPERTIES IN TRANSITION METAL OXIDES

Tsezár F. Seman

Dr. Keun Hyuk Ahn, Dissertation Advisor — Date
Assistant Professor of Physics, NJIT

Dr. Trevor A. Tyson, Committee Member — Date
Distinguished Professor of Physics, NJIT

Dr. Andrei Sirenko, Committee Member — Date
Professor of Physics, NJIT

Dr. Nuggehalli M. Ravindra, Committee Member — Date
Professor of Physics, Department Chair, NJIT

Dr. Seongshik Oh, Committee Member — Date
Assistant Professor of Physics, Rutgers, New Brunswick

Dr. Tao Zhou, Committee Member — Date
Associate Professor of Physics, NJIT

BIOGRAPHICAL SKETCH

Author: Tsezár F. Seman

Degree: Doctor of Philosophy

Date: January 2013

Undergraduate and Graduate Education:

- Doctor of Philosophy in Physics,
  New Jersey Institute of Technology, Newark, New Jersey, 2012

- Masters in Applied Mathematics,
  New Jersey Institute of Technology, Newark, New Jersey, 2005

- Bachelor of Science in Applied Mathematics and
  Bachelor of Science in Computer Science,
  New Jersey Institute of Technology, Newark, New Jersey, 2002

Major: Physics

Publications:

T. F. Seman, K. H. Ahn, T. Lookman, A. Saxena, A. R. Bishop, and P. B. Littlewood: 2012, Effects of rare earth ion size on the stability of the coherent Jahn-Teller distortions in undoped perovskite manganites, *Physical Review B* **86**, (184106–184115).

T. F. Seman, J. Moon, and K. H. Ahn: 2012, Symmetry-mode-based classical and quantum mechanical formalism of lattice dynamics, *arXiv: 0707.1921* (In press).

X. Liu, T. F. Seman, K. H. Ahn, M. van Veenendaal, D. Casa, D. Prabhakaran, A. T. Boothroyd, H. Ding, and J. P. Hill: 2012, Strongly momentum-dependent screening dynamics in orbital ordered $La_{0.5}Sr_{1.5}MnO_4$, *arXiv: 1210.6634* (Submitted to Physical Review Letters).

T. F. Seman, K. H. Ahn, T. Lookman, and A. R. Bishop: 2012, Strain-induced metal-insulator phase coexistence and stability in perovskite manganites, *arXiv: 1208.4120* (Submitted).

T. F. Seman, *et al.*: 2012, Theory of K-edge resonant inelastic x-ray scattering and its application for $La_{0.5}Sr_{1.5}MnO_4$, (In preparation).

Presentations:

Computational Materials and Chemical Sciences Network (CMCSN) – Argonne National Laboratory, Argonne, IL. September 28-30, 2012 (Participant).

American Physical Society March Meeting – Boston Convention Center, MA. February 27-March 2, 2012 (Oral presentation).

In memory of my beloved parents, Nadya and Ferenc
For planting the seed of love

ACKNOWLEDGEMENT

For insightful collaboration in theoretical work on K-edge RIXS presented in Chapter 2, I would like to thank Michel van Veenendaal, Xuerong Liu, Diego Casa, John Hill, Andrew Boothroyd, Prabhakaran Dharmalingam, and Hong Ding. For collaborative work on rare earth in undoped perovskite manganites exhibited in Chapter 3, I would like to thank Turab Lookman, Avadh Saxena, Alan Bishop, and Peter Littlewood. In addition, I would like to thank Jichan Moon for formalism development for symmetry modes introduced in Chapter 4.

For earlier inspiration in my pursuit of research in physics, I would like to thank Louis Lanzerotti for those memorable times at Bell Labs. Furthermore, my gratitude extends to Lou Kondic for engaging me in challenging work in applied mathematics, as well as his valuable graduate advisement.

I would like to thank my doctoral committee represented by Seongshik Oh, Nuggehalli Ravindra, Andrei Sirenko, Trevor Tyson, and Tao Zhou, for their invaluable assessment of my achievements, and numerous helpful discussions throughout the past few years.

Throughout my graduate work in condensed matter physics, I have enjoyed a wonderful journey of learning new ideas through fulfilling work with Ken Ahn. I would like to thank Ken for his dedicated doctoral advisement that decisively prepared me for the path ahead.

My family has always remained central to me, and it is not without their support that I have reached this stage in my life. I am immensely thankful for my cousin, John Varga and his numerous efforts in helping me to achieve my goals. I am also grateful for bringing warmth into my life, to my aunts, Maria, Rosalie, and Valerie, and my uncles, Julius, János, and Joseph. And last, but not least, I want to thank my dear sister, Orsolya for simply being with me.

TABLE OF CONTENTS

Chapter **Page**

TABLE OF CONTENTS

(Continued)

Chapter **Page**

TABLE OF CONTENTS

(Continued)

Chapter **Page**

LIST OF TABLES

Table **Page**

LIST OF FIGURES

Figure **Page**

Figure **Page**

Figure **Page**

Figure **Page**

LIST OF FIGURES

(Continued)

Figure **Page**

LIST OF TERMS

AK	Alkali metal element
bk	Buckling term
br	"breathing" term
BZ	Brillouin Zone
Coul	Coulomb term
DOS	Density of States
FWHM	Full width at half maximum
HF	Hartree-Fock approximation
Hund	Hund's term
JT	Jahn-Teller term
KE	Kinetic Energy term
LDA	Local-Density Approximation from density functional theory
RE	Rare Earth element
RXS	Resonant X-ray Scattering
RIXS	Resonant Inelastic X-ray Scattering
r.l.u.	Reciprocal Lattice Unit
WFC	Wannier Function Center
1s	Term related to $1s$ electron configuration
3d	Term related to $3d$ electron configuration

CHAPTER 1

INTRODUCTION

In recent years, there have been a great interest in the K-edge resonant inelastic x-ray scattering (RIXS) (Ament et al. 2011), because of its unique advantages over other probes. K-edge RIXS provides information on momentum dependence of excitations, sensitive to the bulk properties, and can be directly compared with the electronic band structures because final states do not have the core hole. It is suggested that the K-edge RIXS intensity for transition metal oxides essentially represents the dynamics of electrons near the Fermi energy which screens the $1s$ core hole created by the x-ray (Ahn et al. 2009; Semba et al. 2008).

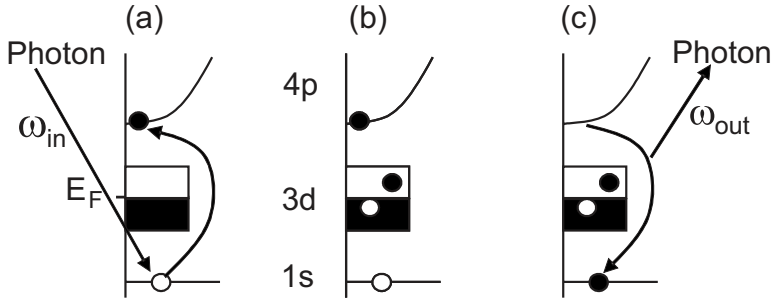

Figure 1.1 Indirect or K-edge RIXS process best described by three stages: (a) in the initial stage, from incoming photon an electron is excited from deep $1s$ core level into $4p$ valence band, (b) in the intermediate stage, excitations are created in the $3d$ band through Coulomb interaction between the core hole and the valence electron, and (c) in the final stage, electron decays leaving the excitation in the valence band and a photon is emitted. Courtesy of Ahn et al. (2009).

The result in Ahn et al. (2009) allows an approximation of replacing the sum over the intermediate states to a single lowest energy intermediate state. The study further showed that expanding RIXS intensity according to the number of final electron-hole pairs is a fast converging expansion with one-electron hole pair states dominant, particularly for insulators. From this consideration, the calculation showed that the electron excitation is from the whole unoccupied band, reflecting the

localized nature of screening of core hole by electron in direct space, whereas the hole excitation is mostly from occupied states close to the gap to minimize the kinetic energy, particularly when the gap energy is smaller than the band width. In Ahn et al. (2009), however, the focus was on energy dependence of the electron-hole excitations, and momentum dependence of RIXS spectrum was not considered explicitly. Further presented is a formula that includes the full momentum dependence, as well as multiple core hole sites within unit cell in the tight binding approach. In this approach, the formula is expressed in terms of the intermediate state basis with a completely localized 1s core hole, so that the RIXS spectrum in reciprocal space can be readily compared with the screening pattern in direct space.

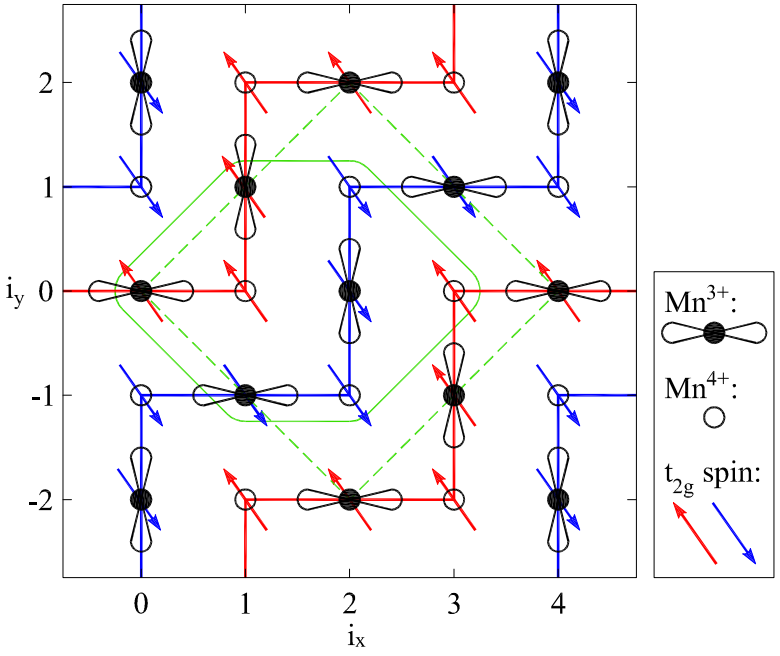

Figure 1.2 (Color) In-plane structural layout of Mn ions depicting t_{2g} spin arrangement along zig-zag chain.

To explain the K-edge RIXS spectrum, applied formula is recently obtained for $La_{0.5}Sr_{1.5}MnO_4$, which shows a drastic variation of the RIXS intensity in reciprocal space in spite of almost no change in the peak energy (Liu et al. 2012). $La_{0.5}Sr_{1.5}MnO_4$ has a layered two-dimensional perovskite structure and the hopping

of the Mn $3d$ e_g electrons between different MnO_2 layers is believed to be negligible. K-edge RIXS spectrum is measured on a single crystal of $La_{0.5}Sr_{1.5}MnO_4$ at 20 K (Liu et al. 2012), which has a magnetic, charge and orbital ordering known as CE-type ordering in the MnO_2 plane, schematically shown in Figure 1.2, where "Mn^{3+}" and "Mn^{4+}" are used to indicate the two sites not related by the symmetry. The strong Hund's coupling between the e_g electron spin and the t_{2g} electron spin channels the e_g electron hopping only along the zigzag chain, which influence the screening of the core hole in the RIXS intermediate state. This work is presented in depth in Chapter 2, as well as in Liu et al. (2012).

Since the discovery of the colossal magnetoresistance effect, a lot of attention has focused on a class of materials known as perovskite manganites (von Helmolt et al. 1993; Jin et al. 1994; Salamon and Jaime 2001). During the last two decades, substantial progress has been made in the theory for perovskite manganites. Importance of the electron-lattice coupling was identified shortly after the discovery of colossal magnetoresistance effect (Millis et al. 1995; Röder et al. 1996; Millis et al. 1996). First-order character of the metal-insulator phase transition has been found from Monte Carlo simulations (Vergés et al. 2002). Mechanism for inhomogeneity and its relation to metal-insulator transition have been studied (Moreo et al. 1999). Effects of disorder have been investigated for doped manganites (Kumar and Majumdar 2006; Pradhan et al. 2007). The competition between short range superexchange interaction and long range double exchange interaction has been analyzed for multiferroic undoped manganites (Salafranca and Brey 2006). Most recently, novel mechanisms for ferroelectricity, including electronic ferroelectricity, have been proposed for undoped manganites with E-type antiferromagnetic ordering (Sergienko et al. 2006; Yamauchi et al. 2008). These materials have the chemical formula in the form of $RE_{1-x}AK_xMnO_3$, where RE and AK represent the rare earth and alkali metal elements, and have a perovskite structure. One of the major research themes

for these materials is the relation between their physical properties and the average size of ions at the RE/AK site, often known as the chemical pressure effect. The size of the RE/AK ion is usually parameterized by a *tolerance factor* and one of the most important phase diagrams for these materials has been the one in the temperature versus tolerance factor plane for a fixed 30% ($x = 0.3$) doping ratio (Hwang et al. 1995). The RE/AK ions with size smaller than the space created by the surrounding MnO_6 octahedra induce buckling of the Mn-O-Mn bonds, observed through various structural refinement analyses.

To understand the effect of the chemical pressure, semi-classical theories (Millis et al. 1995; Röder et al. 1996; Millis et al. 1996; Moreo et al. 1999; Sergienko et al. 2006; Pradhan et al. 2007; Vergés et al. 2002; Salafranca and Brey 2006; Kumar and Majumdar 2006; Yamauchi et al. 2008) with quantum mechanical electrons coupled with the classical lattice through the Jahn-Teller (JT) interaction often present the phase diagram with one axis representing the ratio between the electron hopping energy and the JT energy gain. This ratio parameterizes the competition between the kinetic and potential energy in perovskite manganites. Theoretical phase diagrams from these approaches agree well with experimental phase diagrams, when this ratio is related to the Mn-O-Mn buckling distortion due to smaller RE/AK ions. However, whether this buckling distortion affects the electron hopping energy or the JT energy gain has been controversial. It is well known from experimental observations that there is a strong competition between the insulating phase with a coherent JT distortion and the metallic phase without such distortion (Salamon and Jaime 2001). So far, most of the attention has centered on the impact of the buckling on the metallic phase, in particular, the possible change in the effective Mn-O-Mn electron hopping parameter and the band width (Hwang et al. 1995). At the same time, there has been a debate whether the variation of the hopping parameter due to the Mn-O-Mn bond angle change of several degrees would be significant enough to

explain the observed metal-insulator transition (Dzero et al. 2000; Fernandez-Baca et al. 1998; Liu et al. 1999; Lynn et al. 1996; Radaelli et al. 1997). For instance, the spin wave stiffness, which depends sensitively on the electron hopping amplitude in double exchange model in ferromagnetic metallic phase, shows very little dependence on Mn-O-Mn bond angle (Lynn et al. 1996; Fernandez-Baca et al. 1998). A less studied effect of the Mn-O-Mn bond buckling, except for a few early efforts based on experimental data (Louca et al. 2001), is the possibility that the buckling distortion may significantly stabilize the insulating phase with a coherent JT distortion, by affecting the JT energy gain. The main goal of this topic is to examine such a possibility with a simplified model of the perovskite manganites. To be specific, the interplay between the JT ordering and chemical pressure is analyzed for undoped perovskite manganites. With one localized e_g electron per site, the electronic degrees of freedom can be integrated out in undoped manganites (except for electronically ferroelectric undoped manganites postulated at low temperatures for very small RE ions), which allows us to adopt a purely classical model with the energy expressed in terms of lattice distortions only. The study on undoped manganites is merited, because they are not only parent compounds of doped perovskite manganites (Millis 1996), but also because one of the first multiferroic materials discovered is an undoped manganite, $TbMnO_3$, with a relatively small RE element (Kimura, Goto, Shintani, Ishizaka, Arima and Tokura 2003). Recently, electronic ferroelectricity has been also proposed for undoped perovskite manganites (Sergienko et al. 2006; Yamauchi et al. 2008). Therefore, the chemical pressure effect in undoped manganites reported in this thesis would also be relevant for future studies on how the multiferroic and electronically ferroelectric properties would appear in $RE MnO_3$ with small RE ions, as well as how the chemical pressure affects the distorted insulating phase of doped manganites. This work is presented in Chapter 3, as well as in Seman, Ahn, Lookman, Saxena, Bishop and Littlewood (2012).

Further presented is classical and quantum mechanical multi-scale descriptions of lattice dynamics, from the atomic scale to the continuum scale, using symmetry modes and their constraint equations. This approach is demonstrated for a one-dimensional chain and a two-dimensional monatomic square lattice. For the classical description, it is found that rigid modes, in addition to the strain modes found before, are necessary to describe the kinetic energy, and obtain constraint equations among these modes. Lagrangian equations, modified with the Lagrange multiplier terms, are solved for phonon dispersion relations without using displacement variables explicitly. The long wavelength limit of the kinetic energy terms expressed in terms of atomic scale modes is shown to be consistent with the continuum theory, and the leading order corrections are obtained. The phonon in terms of symmetry modes is analyzed, and it is found how the contribution of different symmetry modes varies depending on the phonon branch and wavevector. For the quantum mechanical description, conjugate momenta derived for the atomic scale symmetry modes. In direct space, graphical rules for their commutation relations are obtained. Commutation relations in the reciprocal space are also calculated. It is emphasized that the approach based on atomic-scale symmetry-modes could be useful for description of multi-scale lattice dynamics, materials with electron-phonon coupling, and the dynamics of structural phase transition. Theoretical aspects of this topic are studied in Chapter 4, and also presented in Seman, Moon and Ahn (2012).

Summary and closing remarks are presented in Chapter 5. Several core algorithms used extensively in calculations can be found in Chapter 6.

CHAPTER 2

THEORY OF K-EDGE RESONANT INELASTIC X-RAY SCATTERING AND ITS APPLICATION FOR $La_{0.5}Sr_{1.5}MnO_4$

The work in this chapter was done in collaboration with Michel van Veenendaal from Advanced Photon Source at Argonne National Laboratory, John P. Hill, Xuerong Liu, and Diego Casa from Brookhaven National Laboratory, Andrew Boothroyd and Prabhakaran Dharmalingam from Department of Physics at University of Oxford, Hong Ding from Beijing National Laboratory for Condensed Matter Physics, as well as Keun H. Ahn from Department of Physics at New Jersey Institute of Technology.

2.1 Introduction

The dynamic screening of the Coulomb interaction plays a central role in determining the electronic properties of materials (Fetter and Walecka 2003). The response of valence electrons to a potential, in particular on time scales of the order of femtoseconds, is through excitation of electron-hole pairs which screen "bare" charges in the system. The screening is described theoretically by the density-density correlation function, or its Fourier transform, the dynamic structure factor (Pines and Nozières 1999). Spectroscopies that probe the valence band, such as photoemission, are sensitive to these screening dynamics. However, it is often not obvious how to separate the kinetics of a charged particle and the response of the rest of the system to its presence (Hüfner 2003). In contrast, core-level spectroscopies provide an alternative way of studying the screening dynamics. By removing a deep-lying core electron, a strong local potential is created that exists for a very short time, i.e., the core hole lifetime. Essentially, one creates a short-lived localized "test" particle, and measures the response of the electrons to this local transient potential. This type of

screening dynamics has intrigued scientists for decades (Nozières and de Dominicis 1969; van der Laan et al. 1981; van Veenendaal and Sawatzky 1993).

For transition metal compounds, K-edge resonant inelastic x-ray scattering (RIXS) (Ament et al. 2011) offers the intriguing possibility of projecting the excitations related to the core hole screening onto valence band excitations. Specifically, it has been shown that K-edge RIXS can be directly related to the dynamic structure factor in the limit of a strong or weak core hole potential, U_{core}, relative to the band width (van den Brink and van Veenendaal 2006). For the case where U_{core} is comparable to the bandwidth, more typical for $3d$ transition metal compounds, the screening is more complicated because there is an asymmetry between the electron and hole excitations and the intermediate states can not be integrated out (Ahn et al. 2009). In this case, the RIXS response is believed to be sensitive to the transient screening of the intermediate states to the core hole potential (Ahn et al. 2009).

Further presented are RIXS measurements of the momentum and energy dependence of the screening dynamics for a transient local potential in a CE-type charge, orbital, and spin ordered manganite, $La_{0.5}Sr_{1.5}MnO_4$. Strong momentum dependence of the intensity of the across-gap excitation is found, with a dramatic increase on moving away from the two-dimensional (2D) zone center. It is shown that this behavior reflects the size and shape of the real-space screening cloud and demonstrate that in $La_{0.5}Sr_{1.5}MnO_4$, the screening distance is very short, with a screening cloud of about 0.4-0.5 interatomic distances in size.

2.2 Experiments

A single crystal of $La_{0.5}Sr_{1.5}MnO_4$ was grown by the traveling solvent floating zone method. It has a tetragonal structure at room temperature with *I4/mmm* symmetry and undergoes a charge and orbital ordering transition around 230 K, accompanied by complex structural distortions (Herrero-Martín et al. 2011). For simplicity, the

I4/mmm notation is used here throughout. The wave vectors of the charge and orbital ordering are then of the form $(\frac{1}{2}, \frac{1}{2}, L)$ and $(\frac{1}{4}, \frac{1}{4}, L)$, respectively. In the low temperature ordered state, $La_{0.5}Sr_{1.5}MnO_4$ is an insulator with a large gap between the e_g states (Bała and Horsch 2005; Lee, Onoda, Arima, Tokunaga, He, Kaneko, Nagaosa and Tokura 2006). The behavior of the excitation between these predominantly Mn 3*d* states, labeled as a *d*-*d* transition, is the focus of this study. The Mn K-edge RIXS experiments were performed at Advanced Photon Source on beamlines 30-ID and 9-ID with an instrumental energy resolution of about 270 meV (FWHM). The polarization dependence of the RIXS process is controlled by placing the [001] and [110] directions of the crystal in the scattering plane. The incident beam polarization is perpendicular to the scattering plane, i.e., parallel to the $[1\bar{1}0]$ direction. Thus the incident polarization condition is fixed for all the $\mathbf{Q} = (H, H, L)$ points surveyed. All the data presented were collected at $T = 20$ K, well below the Néel temperature(110K) (Sternlieb et al. 1996). Data are normalized by incident beam intensity and corrected for footprint variations.

In Figure 2.1(a), RIXS spectra is taken at three $\mathbf{Q}$ points. In each case, there is a large elastic line centered at zero energy loss. The *d*-*d* transition appears as a peak on the tails of the elastic scattering at around 2 eV, consistent with optics (Lee et al. 2007) and EELS (Kraus et al. 2011) observations. This across-gap transition has also been observed by K-edge RIXS on other manganites (Inami et al. 2003; Grenier et al. 2005; Weber et al. 2010). Remarkably, the RIXS spectra show a strong momentum dependence of the intensity of this feature. At $\mathbf{Q_0} = (-0.03, -0.03, 7.20)$ with very small in-plane momentum transfer, the 2 eV peak is almost unobservable. This momentum dependence is confirmed with RIXS spectra collected at a large number of $\mathbf{Q}$ points, as shown in Figure 2.1(b) and 2.1(c). To control the systematics resulting from polarization factors, the data were taken either at fixed sample angle θ, or fixed detector angle 2θ. These conditions result in data taken along three lines

in reciprocal space. In all cases, the incident polarization is parallel to the $[1\bar{1}0]$ direction. With the detector position 2θ fixed, polarization effects associated with the outgoing x-ray are eliminated. Figure 2.1(c) shows RIXS spectra with the elastic line subtracted[1] for the $\mathbf{Q}$ points with $2\theta = 68°$. The integrated intensity, $I(\mathbf{Q})$, is taken over the 1-3 eV range as a measure of the strength of the 2 eV peak. The size of the symbols in Figure 2.1(b) is proportional to $I(\mathbf{Q})$. A clear systematic dependence on momentum transfer is observed.

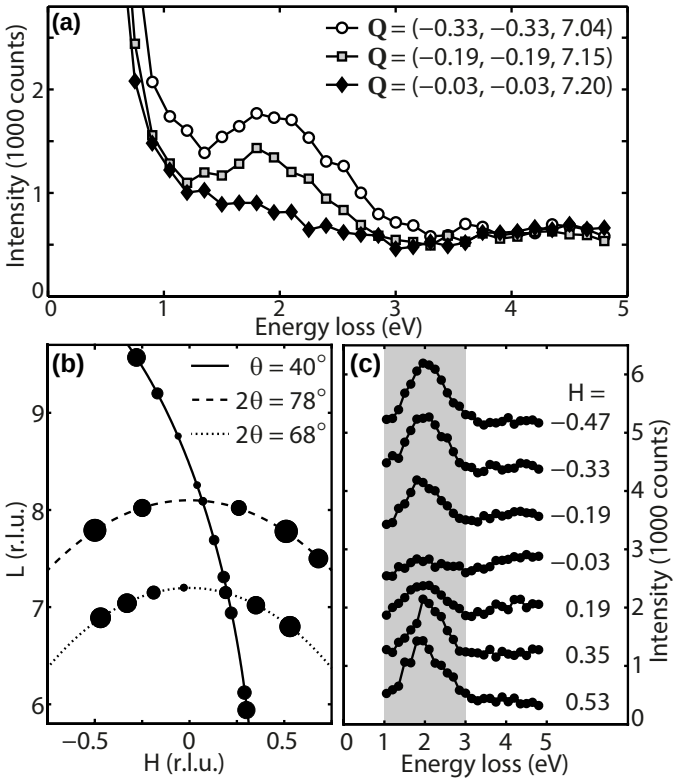

Figure 2.1 (a) RIXS spectra at three $\mathbf{Q}$ points. (b) The $\mathbf{Q}$ points surveyed in the (H, H, L) plane. The radius of the dot is proportional to the integrated intensity of the 2 eV peaks. θ and 2θ are the incident and detector angles. (c) RIXS spectra for the $\mathbf{Q}$ points along the $2\theta = 68°$ line, with the elastic intensity subtracted. The grey shaded region is the energy window used in calculating the integrated intensity of the feature.

[1]The elastic line was subtracted by using a model function. The latter was determined by measuring the elastic scattering at an off-resonant energy (7 eV below the edge), where there are negligible inelastic contributions.

The integrated intensities of the *d*-*d* excitation are plotted as a function of the in-plane momentum transfer in Figure 2.2(b). In order to quantitatively compare the experimental data with the theoretical calculations (discussed below), the integrated intensities are plotted relative to the intensity at $\mathbf{Q_0} = (-0.03, -0.03, 7.20)$ [2], i.e., $I(\mathbf{Q}) - I(\mathbf{Q_0})$. This removes the uncertainty in determining the common background for all $\mathbf{Q}$ points. The strength of the 2 eV *d*-*d* excitation exhibits a minimum at zero in-plane momentum transfer and a maximum at (0.5, 0.5, L). Interestingly, although there is a large variation in the L values for the various $\mathbf{Q}$ points [see Figure 2.1(b)], all the measurements collapse onto a single curve in Figure 2.2(b). This demonstrates that there is negligible L dependence to this behavior, a result consistent with the 2D nature of this single layered manganite. Further, it implies that the polarization factors are indeed constant for the experimental geometry. From here on, the momentum transfer will be denoted simply as $\mathbf{Q}_{2D} = (H, H)$ since the L component is irrelevant.

The experimental data in Figures 2.1 and 2.2 show the main experimental observations. The across-gap *d*-*d* excitation in $La_{0.5}Sr_{1.5}MnO_4$, as observed in the RIXS process, exhibits a strong momentum dependence. While the position of the peak shows no appreciable dispersion, the intensity increases rapidly as the in-plane momentum transfer increases away from the 2D zone center. Near the zone center, the spectral weight of the 2 eV feature almost disappears. This is a surprising result. The disappearance of this RIXS spectral weight at the 2D zone center cannot be the result of the dynamic structure factor going to zero, since this feature is still observed in the optical response (Lee et al. 2007), which probes the zero momentum transfer response function. This demonstrates that K-edge RIXS in $La_{0.5}Sr_{1.5}MnO_4$ is indeed in the intermediate core-hole potential regime, discussed in the introduction. In the following, momentum-dependence is described in detail and it is shown that it arises

[2] $\mathbf{Q}$ points such as (0, 0, L), which would have been preferable, are intentionally avoided due to specular reflection enhancement of the elastic line at such points.

from the intermediate state screening dynamics and in particular that it reflects the real-space extent of the screening cloud.

2.3 Results from Theory and Comparison With Experiments

To understand this strong in-plane momentum dependence, the RIXS response is calculated from $La_{0.5}Sr_{1.5}MnO_4$ for a two-dimensional 16×16 Mn cluster with periodic boundary conditions. The initial and final states of the unperturbed system, and the intermediate states in the presence of the $1s$ core hole on-site Coulomb potential, are solved numerically with a tight-binding approach. The Hamiltonian employed is similar to the one in Ahn and Millis (2000), which includes the nearest-neighbor electron hopping within the MnO_2 plane, the Jahn-Teller and isotropic electron-lattice coupling, the Hund's coupling to the CE-type ordered t_{2g} spins, and the Coulomb interaction between e_g electrons within the Hartree-Fock approximation, as later introduced in depth in Section 2.5. The sizes of the distortions of the oxygen octahedra are taken from Herrero-Martín et al. (2011). The RIXS spectra are then calculated from the Kramers-Heisenberg formula (Ament et al. 2011; Ahn et al. 2009):

$$I \propto \sum_f \left| \sum_n \frac{\langle f|\mathcal{D}'^{\dagger}|n\rangle\langle n|\mathcal{D}|g\rangle}{E_g + \hbar\omega_{\mathbf{k}} - E_n + i\Gamma_n} \right|^2 \delta(E_f - E_g - \hbar\Delta\omega), \tag{2.1}$$

where $|f\rangle$, $|n\rangle$, and $|g\rangle$ represent the final, intermediate and initial states, and E_f, E_n and E_g their energies. Γ_n is the inverse of the intermediate state lifetime, and $\mathcal{D}'^{\dagger}$ and $\mathcal{D}$ are the RIXS dipole transition operators. $\hbar\omega_{\mathbf{k}}$ and $\hbar\Delta\omega$ are the incident x-ray energy and the energy loss, respectively. The calculated RIXS intensity is averaged over configurations in which the zig-zag chains of orbital order are along either the [110] or the $[1\bar{1}0]$ directions, to take into account twining effects in real crystals. Details of the calculation will be published elsewhere.

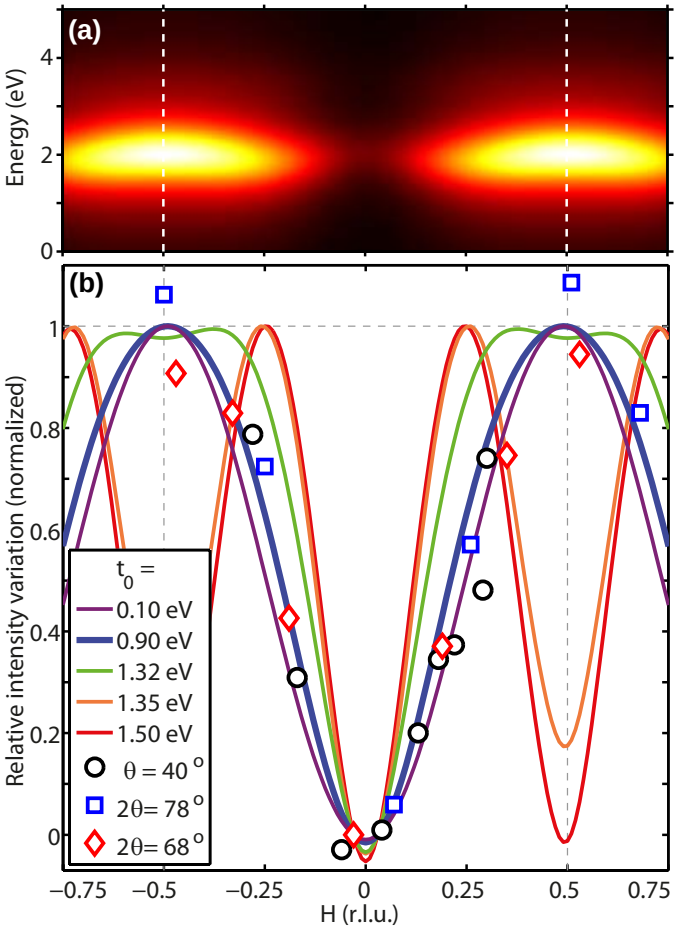

Figure 2.2 (Color) (a) Contour plot of RIXS intensity calculated for the electron hopping parameter $t_0 = 0.9$ eV, after averaging over twin domains. (b) The integrated RIXS intensity of the 2 eV peak relative to the (-0.03,-0.03) point, plotted with respect to the in-plane momentum transfer along the (H, H) direction. Symbols represent experimental data. Lines represent theoretical results for different values of t_0. Both experimental data and theoretical results are normalized for comparison.

The calculated RIXS spectra were found to be most sensitive to the e_g-e_g hybridization and the coupling of the e_g electrons to the distortions of oxygen octahedra. These two effects are parameterized as t_0 and λ in the Hamiltonian, where t_0 is the hopping between $3x^2$-r^2 orbitals along the x direction and λ is proportional to the strength of the electron-phonon coupling. With reasonable parameter values, as introduced in Section 2.5, and the combination of $t_0 = 0.9$ eV and $\lambda = 7.41$ eV/$\AA$, the calculated spectra shown in Figure 2.2(a) and the thick (blue) line in Figure 2.2(b)

closely resemble the experimental observations. The intensity of the calculated RIXS response peaks near 2 eV, and increases rapidly as $\mathbf{Q}_{2D}$ increases away from (0, 0), towards (0.5, 0.5), as seen in the experiments. The calculated spectra in Figure 2.2(a) suggest a slight dispersion of about 130 meV of the 2 eV peak, which is much smaller than that reported for $LaSr_2Mn_2O_7$ (Weber et al. 2010). Such a small dispersion, roughly equal to the experimental step size taken in Figure 2.1(c), is below the detection limit of the experiment.

The sensitivity of the RIXS response to intersite hopping and the electron-phonon coupling is shown in Figure 2.2(b) by varying t_0 and λ, see Section 2.5. For a given t_0, λ is constrained such that the *d*-*d* excitation in the RIXS response peaks near 2 eV. Henceforth, only t_0 is mentioned for simplicity. The details of the combinations of t_0 and λ can be found in Section 2.5. As was done for the experimental data, the calculated response is integrated over the same 1-3 eV window to generate the curves in Figure 2.2(b), and again the value at $\mathbf{Q}_{2D}$ =(-0.03, -0.03) is subtracted. The calculated results show the best agreement with the experimental observations when $t_0 = 0.9$ eV. For larger t_0 values, the calculated RIXS response differs significantly from the experimental data. Thus, this study sets the upper limit of t_0. Note that the inability to precisely determine the parameter values is largely due to the difficulty in determining the contributions from other inelastic scattering processes that give rise to a smooth "background" in the low energy loss region.

2.4 Discussion

To further understand the implications of the observed momentum dependence of the RIXS spectrum for the screening dynamics, the real-space screening configurations are calculated from the lowest energy intermediate eigenstates. These are shown in the top panels of Figure 2.3. Figures 2.3(a) and 2.3(b) compare the charge redistributions for $t_0 = 0.9$ and 1.5 eV, respectively, with the core hole at either a Mn^{3+}

or a Mn^{4+} site. The volumes of the red and blue spheres scale with the screening electron and hole densities on individual sites. Figures 2.3(c) and 2.3(d) show the calculated RIXS intensities for the two t_0 values over half of a Brillouin zone.

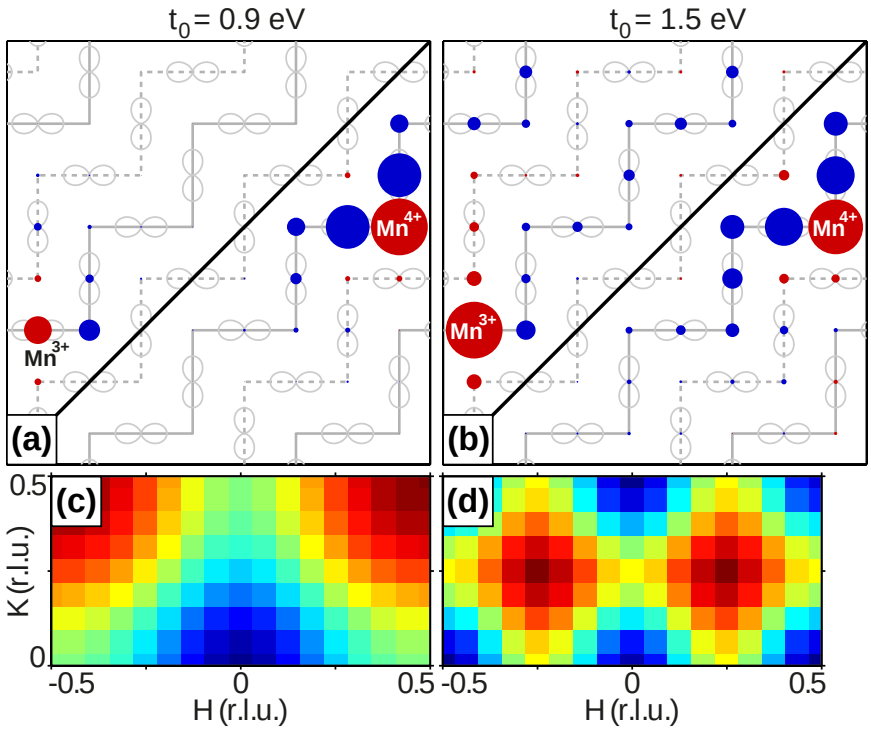

Figure 2.3 (Color) (a) and (b): Screening configuration in real space for $t_0 = 0.9$ and 1.5 eV, respectively. The top left half corresponds to the case with the core hole at a Mn^{3+} site, while the bottom right it is at a Mn^{4+} site. The volumes of the red and blue spheres are proportional to the electron and hole numbers. The big red spheres at Mn^{4+} core hole sites represent about 0.9 electrons. (c) and (d): Integrated RIXS intensity plotted in the (H, K, 0) plane of reciprocal space for $t_0 = 0.9$ eV and $t_0 = 1.5$ eV, respectively. Red and blue represent the maximum and minimum intensities, respectively.

As expected, the excited hole distributions are more localized near the core hole sites for the smaller value of t_0. For $t_0 = 0.9$ eV, the screening hole is tightly bound to the excited electron with more than 90 % of the excited charge located on the three nearest neighbor sites along the zig-zag chain. The predominant wave vector for these electron and hole distributions is (0.5, 0.5), coincident with the location of the RIXS peak intensity maximum in reciprocal space in Figure 2.3(c)

and in agreement with the experimental results. For the large hopping parameter, $t_0 = 1.5$ eV, the screening pattern in real space changes drastically. The majority of the hole distribution in Figure 2.3(b) is now beyond the nearest neighbor sites, and is spread throughout the zig-zag chains. This difference in screening dynamics is directly reflected in the RIXS response, with the maximum of the RIXS response then shifted to around (0.25, 0.25), as shown in Figures 2.2(b) and 2.3(d). This pattern is completely at odds with that seen in the experiment results.

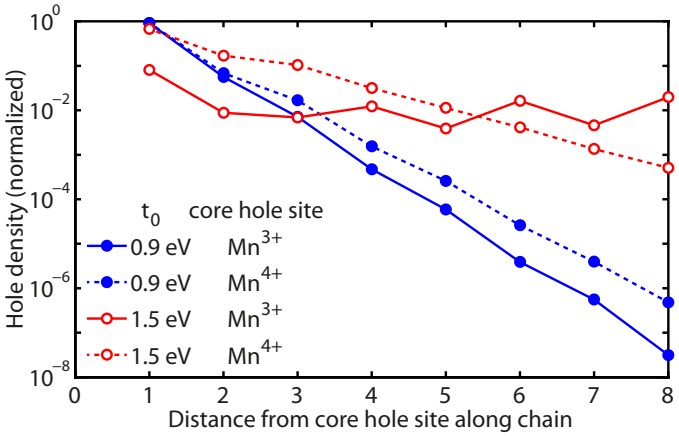

Figure 2.4 (Color) The excited hole number normalized by the excited electron number at the core hole site, plotted in semi-logarithmic scale with respect to the distance from the core hole site along the zig-zag chain.

The relationship between the hopping strength and the charge redistribution in the screening process apparent in the theoretical calculations is shown more clearly in Figure 2.4, where the relative hole number at a given site is plotted as a function of the distance from the core hole site, as measured along the zig-zag chain. The semi-logarithmic plot reveals an exponential decay of the hole density, confirming the presence of exciton-like screening clouds. The size of the screening cloud, which characterizes the screening dynamics and determines the RIXS response, depends strongly on the hopping strength t_0. Taking the $t_0 = 0.9$ eV case, which best describes the RIXS data, the excited hole distributions is fitted to an exponential function to

find that the size of the screening clouds are 0.4 and 0.5 atomic spacings for the Mn^{3+} and Mn^{4+} sites, respectively.

2.5 Details of Theory and Calculations

2.5.1 Tight Binding Hartree-Fock Hamiltonian and Core Hole Potential for $La_{0.5}Sr_{1.5}MnO_4$

In this section, the tight binding Hamiltonian is introduced that was used to calculate the RIXS spectrum for $La_{0.5}Sr_{1.5}MnO_4$. In the experimental results for this material (Liu et al. 2012), shown in Figure 2.1 after subtracting the elastic peak, the RIXS peak at around 2 eV shows prominent changes with momentum, which is the focus of the current study. This peak is believed to be from the transitions between Mn $3d$ e_g levels, and, therefore, Mn e_g levels are considered only in the tight binding Hamiltonian. As mentioned above, the MnO_2 planes in $La_{0.5}Sr_{1.5}MnO_4$ are separated from each other by the intervening, electronically inert, Sr, La, and O ions, which allows the use of the Hamiltonian for a single MnO_2 layer for the RIXS calculation.

Term $a^\dagger_{\sigma\vec{i}\xi}$ is defined as the creation operator of the e_g electron with the spin state $\sigma = \uparrow, \downarrow$ and orbital state $\xi = 1 \equiv \xi_1$ for $(3z^2 - r^2)/\sqrt{6}$ and $\xi = 2 \equiv \xi_2$ for $(x^2 - r^2)/\sqrt{2}$ e_g at a Mn site with an index vector $\vec{i} = (i_x, i_y)$, where i_x and i_y are integers. The electron hopping term, that is, kinetic energy term, is

$$\hat{H}_{\rm KE} = -\frac{1}{2} \sum_{\sigma,\vec{i},\vec{\delta},\xi,\xi'} t^{\xi\xi'}_{\vec{\delta}} \left(a^\dagger_{\sigma\vec{i}\xi} a_{\sigma,\vec{i}+\vec{\delta},\xi'} + a^\dagger_{\sigma,\vec{i}+\vec{\delta},\xi'} a_{\sigma\vec{i}\xi} \right). \tag{2.2}$$

The unit vector $\vec{\delta} = \pm\hat{x}, \pm\hat{y}$ represent the directions of the nearest neighbor sites of a Mn ion. The form of the hopping matrices within the MnO_2 plane are

$$t_x = t_{-x} = t_o \begin{pmatrix} 1/4 & -\sqrt{3}/4 \\ -\sqrt{3}/4 & 3/4 \end{pmatrix}, \tag{2.3}$$

$$t_y = t_{-y} = t_o \begin{pmatrix} 1/4 & \sqrt{3}/4 \\ \sqrt{3}/4 & 3/4 \end{pmatrix}, \tag{2.4}$$

reflecting the symmetry of the e_g orbitals. The parameter t_0 represents the effective hopping constant between two $(3x^2 - r^2)/\sqrt{6}$ orbitals along the x-direction.

Two kinds of electron-lattice couplings are included. The distortion of oxygen octahedron around a Mn ion at $\vec{i}$ is parameterized as follows. $u^{\zeta}_{\vec{i}}$ $(\zeta = x, y)$ represents the $\hat{\zeta}$ direction displacement of an oxygen ion located between Mn ions at $\vec{i}$ and $\vec{i}+\hat{\zeta}$ from the position for the ideal undistorted square MnO_2 lattice with the average in-plane Mn-O bond distance. The $u^{+z}_{\vec{i}}$ and $u^{-z}_{\vec{i}}$ represent the z direction displacements of oxygen ions, right above and right below the Mn ion at $\vec{i}$, from the location of the average in-plane Mn-O bond distance. The parameters, $Q_{1,\vec{i}}$, $Q_{2,\vec{i}}$, and $Q_{3,\vec{i}}$, represent the distortion modes of the oxygen octahedron around a Mn ion at site $\vec{i}$ and are defined in the following way.

$$Q_{1,\vec{i}} = (u^{x}_{\vec{i}} - u^{x}_{\vec{i}-\hat{x}} + u^{y}_{\vec{i}} - u^{y}_{\vec{i}-\hat{y}} + u^{+z}_{\vec{i}} - u^{-z}_{\vec{i}})/\sqrt{3} \tag{2.5}$$

$$Q_{2,\vec{i}} = (u^{x}_{\vec{i}} - u^{x}_{\vec{i}-\hat{x}} - u^{y}_{\vec{i}} + u^{y}_{\vec{i}-\hat{y}})/\sqrt{2} \tag{2.6}$$

$$Q_{3,\vec{i}} = (2u^{z}_{\vec{i}} - 2u^{-z}_{\vec{i}} - u^{x}_{\vec{i}} + u^{x}_{\vec{i}-\hat{x}} - u^{y}_{\vec{i}} + u^{y}_{\vec{i}-\hat{y}})/\sqrt{6} \tag{2.7}$$

The Mn-O bond distances estimated from the structural refinement of high-resolution synchrotron x-ray powder diffraction for $La_{0.5}Sr_{1.5}MnO_4$ in Herrero-Martín et al. (2011) indicate $Q_1 = 0.0531$ Å, $Q_2 = 0.1089$ Å, and $Q_3 = 0.0955$ Å around "Mn^{3+}" site and Q_1 = -0.0531 Å, $Q_2 = 0$, and $Q_3 = 0.1192$ Å around "Mn^{4+}" site.

The Q_2 and Q_3 distortions break the cubic symmetry of oxygen octahedron around Mn and interact with the e_g orbital state through the following Jahn-Teller Hamiltonian term,

$$\hat{H}_{\mathrm{JT}} = -\lambda_Q \sum_{\vec{i}\sigma} \begin{pmatrix} a^{\dagger}_{\sigma\vec{i}1} \\ a^{\dagger}_{\sigma\vec{i}2} \end{pmatrix}^{T} \begin{pmatrix} Q_{3,\vec{i}} & -Q_{2,\vec{i}} \\ -Q_{2,\vec{i}} & -Q_{3,\vec{i}} \end{pmatrix} \begin{pmatrix} a_{\sigma\vec{i}1} \\ a_{\sigma\vec{i}2} \end{pmatrix}, \tag{2.8}$$

where λ_Q represents the strength of this coupling. [3] The isotropic Q_1 distortion interacts with total e_g electron charge through the following "breathing" electron-

[3]Unlike the three-dimensional manganites, the degeneracy of the e_g levels are broken even without the Q_2 or Q_3 distortions because of the layered crystal structure. Therefore,

lattice Hamiltonian term,

$$\hat{H}_{\mathrm{br}} = -\beta\lambda_Q \sum_{\vec{i}\sigma} \begin{pmatrix} a^\dagger_{\sigma\vec{i}1} \\ a^\dagger_{\sigma\vec{i}2} \end{pmatrix}^T \begin{pmatrix} Q_{1,\vec{i}} & 0 \\ 0 & Q_{1,\vec{i}} \end{pmatrix} \begin{pmatrix} a_{\sigma\vec{i}1} \\ a_{\sigma\vec{i}2} \end{pmatrix}, \tag{2.9}$$

where β represents the ratio between the strengths of the breathing and the Jahn-Teller couplings, likely larger than 1.

In addition, the Hund's coupling of the e_g electron spin state to the CE-type magnetic ordering of the t_{2g} spins is included,

$$\hat{H}_{\mathrm{Hund}} = -\sum_{\sigma',\sigma'',\vec{i},\xi} J_{\mathrm{H}} \vec{S}_{t2g,\vec{i}} \cdot a^\dagger_{\sigma'\vec{i}\xi} \vec{\tau}_{\sigma'\sigma''} a_{\sigma''\vec{i}\xi}, \tag{2.10}$$

where $\vec{S}_{t2g,\vec{i}}$ represents the t_{2g} spin and $\vec{\tau}$ the Pauli matrix.

As in Ahn and Millis (2000), the $3d$-$3d$ same-site Coulomb interaction with parameter U is also included,

$$\hat{H}_{\mathrm{3d3d,Coul}} = \sum_{\vec{i}} \sum_{(\sigma,\eta=-,+)\neq(\sigma',\eta'=-,+)} U \hat{n}_{\sigma\vec{i}\eta} \hat{n}_{\sigma'\vec{i}\eta'}, \tag{2.11}$$

where $\hat{n}_{\sigma\vec{i}\eta} = a^\dagger_{\sigma\vec{i}\eta} a_{\sigma\vec{i}\eta}$ is the number operator. $\eta = -$ and $+$ represent the local orbital eigenstates of $\hat{H}_{\mathrm{JT}}$ with lower and higher energies, respectively, chosen for the following Hartree-Fock approximation,

$$\begin{aligned} \hat{H}^{\mathrm{HF}}_{\mathrm{3d3d,Coul}} = \sum_{\vec{i}} & U_{\uparrow\vec{i}+} a^\dagger_{\uparrow\vec{i}+} a_{\uparrow\vec{i}+} + U_{\uparrow\vec{i}-} a^\dagger_{\uparrow\vec{i}-} a_{\uparrow\vec{i}-} \\ & + U_{\downarrow\vec{i}+} a^\dagger_{\downarrow\vec{i}+} a_{\downarrow\vec{i}+} + U_{\downarrow\vec{i}-} a^\dagger_{\downarrow\vec{i}-} a_{\downarrow\vec{i}-}, \end{aligned} \tag{2.12}$$

where $U_{\uparrow\vec{i}+} = U < \hat{n}_{\uparrow\vec{i}-} > + U < \hat{n}_{\downarrow\vec{i}+} > + U < \hat{n}_{\downarrow\vec{i}-} >$, etc..

The total Hamiltonian for the calculations of RIXS initial state and final states is the sum of the terms described so far.

$$\hat{H}_{\mathrm{3d}} = \hat{H}_{\mathrm{KE}} + \hat{H}_{\mathrm{JT}} + \hat{H}_{\mathrm{br}} + \hat{H}_{\mathrm{Hund}} + \hat{H}^{\mathrm{HF}}_{\mathrm{3d3d,Coul}}. \tag{2.13}$$

E_{JT} should be considered as the effective Hamiltonian that includes not only the effect of the oxygen octahedron but also the crystal field of farther ions.

The CE type ordering of t_{2g} spins and lattice distortions gives rise to the unit cell shown in dotted lines in Figure 1.2. With the distance between Mn-Mn in undistorted lattice represented as a unit distance and the x and y axes chosen along Mn-O bond directions, the primitive reciprocal lattice vectors are $(\pi/2, \pi/2)$ and $(\pi/2, -\pi/2)$, and the first Brillouin zone is $\Omega_{\mathrm{1BZ}} = \{\vec{k}| -\pi/2 < k_x + k_y \leq \pi/2, -\pi/2 < k_x - k_y \leq \pi/2\}$.

The $1s$-$3d$ on-site Coulomb interaction is generally expressed as

$$\hat{H}_{\mathrm{1s3d,Coul}} = -U_c \sum_{\sigma,\xi,\vec{i},\sigma'} a^{\dagger}_{\sigma\vec{i}\xi} a_{\sigma\vec{i}\xi} \underline{s}^{\dagger}_{\sigma'\vec{i}} \underline{s}_{\sigma'\vec{i}}, \tag{2.14}$$

As shown in the next section, in the limit of completely localized $1s$ core hole, the RIXS intermediate energy eigenstates can be chosen as states with a single completely localized $1s$ core hole, which can be found from

$$\hat{H}_{\mathrm{total},\vec{i}_c} = \hat{H}_{\mathrm{3d}} + \hat{H}_{\mathrm{1s3d,Coul},\vec{i}_c}, \tag{2.15}$$

where

$$\hat{H}_{\mathrm{1s3d,Coul},\vec{i}_c} = -U_c \sum_{\sigma,\xi} a^{\dagger}_{\sigma,\vec{i}_c,\xi} a_{\sigma,\vec{i}_c,\xi}. \tag{2.16}$$

and $\vec{i}_c$ represents the $1s$ core hole site.

The parameter values chosen for the best fit of the measured RIXS spectrum are: $t_0 = 0.9$ eV, $\lambda_Q = 7.4$ eV/Å, $\beta = 1.5$, $J_H|\vec{S}_{t2g,\vec{i}}| = 2.2$ eV, $U = 3.5$ eV, and $U_c = 4.0$ eV. As a comparison, different values of t_0 and λ_Q are considered, including $t_0 = 1.5$ eV and $\lambda_Q = 3.5$ eV/Å, to study the implication of the momentum dependent RIXS intensity for the screening dynamics.

Further, $\hat{H}_{3d}$ and $\hat{H}_{\mathrm{total},\vec{i}_c}$ are transformed into the reciprocal space as follows,

$$\hat{H}_{\mathrm{3d}} = \sum_{\sigma} \sum_{\vec{k},\vec{k}'} \sum_{\vec{K},\vec{K}'} \sum_{\xi,\xi'} H^{\mathrm{3d}}_{\sigma,\vec{k}+\vec{K},\xi,\vec{k}'+\vec{K}',\xi'} a^{\dagger}_{\sigma,\vec{k}+\vec{K},\xi} a_{\sigma,\vec{k}'+\vec{K}',\xi'}, \tag{2.17}$$

and

$$\hat{H}_{\mathrm{total},\vec{i}_c} = \sum_{\sigma} \sum_{\vec{k},\vec{k}'} \sum_{\vec{K},\vec{K}'} \sum_{\xi,\xi'} H^{\mathrm{total},\vec{i}_c}_{\sigma,\vec{k}+\vec{K},\xi,\vec{k}'+\vec{K}',\xi'} a^{\dagger}_{\sigma,\vec{k}+\vec{K},\xi} a_{\sigma,\vec{k}'+\vec{K}',\xi'}, \tag{2.18}$$

where $\vec{k}, \vec{k'} \in \Omega_{1\mathrm{BZ}}$, $\vec{K}, \vec{K'} \in \{\vec{K}_1, \vec{K}_2, \vec{K}_3, \vec{K}_4, \vec{K}_5, \vec{K}_6, \vec{K}_7, \vec{K}_8\}$, and $\vec{K}_n$ represents (0,0), (π,0), (0,π), (π,π), (-π/2,-π/2), (π/2,-π/2) , (-π/2,π/2), and (π/2,π/2), for n = 1, 2, 3 …, 8, respectively. The details of these expressions are presented in the Appendix 2.A.

From the elements of the eigenvectors of the matrices $H^{\mathrm{3d}}_{\sigma,\vec{k}+\vec{K},\xi,\vec{k'}+\vec{K'},\xi'}$ and $H^{\mathrm{total},\vec{i}_c}_{\sigma,\vec{k}+\vec{K},\xi,\vec{k'}+\vec{K'},\xi'}$, the coefficients α's and γ's are defined in the following way:

$$b^{\dagger}_{\sigma l\vec{k}} = \sum_{\vec{K},\xi} a^{\dagger}_{\sigma,\vec{k}+\vec{K},\xi} \alpha_{\sigma,\vec{k}+\vec{K},\xi l\vec{k}}, \tag{2.19}$$

$$c^{\dagger}_{\sigma m} = \sum_{\vec{k},\vec{K},\xi} a^{\dagger}_{\sigma,\vec{k}+\vec{K},\xi} \gamma_{\sigma,\vec{k}+\vec{K},\xi m}, \tag{2.20}$$

where $b^{\dagger}_{\sigma l\vec{k}}$ and $c^{\dagger}_{\sigma m}$ are the creation operators of the eigenstates of $\hat{H}_{\mathrm{3d}}$ with the wavevector $\vec{k} \in \Omega_{1\mathrm{BZ}}$ within the l-th lowest energy band and the m-th lowest energy eigenstates of $\hat{H}_{\mathrm{total},\vec{i}_c}$, respectively. (Though it is suppressed in the notations for simplicity, $c^{\dagger}_{\sigma m}$ and $\gamma_{\sigma,\vec{k}+\vec{K},\xi m}$, defined above, and $\beta_{\sigma l\vec{k}m}$, defined below, depend on the core hole site $\vec{i}_c$.)

The relation between $a^{\dagger}$ and $b^{\dagger}$ is inverted in the Equation (2.19) to further obtain $\tilde{\alpha}$'s defined from

$$a^{\dagger}_{\sigma,\vec{k}+\vec{K},\xi} = \sum_{l} b^{\dagger}_{\sigma l\vec{k}} \tilde{\alpha}_{\sigma l\vec{k},\vec{k}+\vec{K},\xi}, \tag{2.21}$$

where the matrix of $\tilde{\alpha}$'s corresponds to the inverse of the matrix of α's. From $\tilde{\alpha}$'s and γ's, the coefficients β's can be found, which represent the eigenstates in the presence of the core hole in terms of the eigenstates in the absence of the core hole according to

$$c^{\dagger}_{\sigma m} = \sum_{l\vec{k}} b^{\dagger}_{\sigma l\vec{k}} \beta_{\sigma l\vec{k}m}, \tag{2.22}$$

where

$$\beta_{\sigma l\vec{k}m} = \sum_{\vec{k}+\vec{K},\xi} \tilde{\alpha}_{\sigma l\vec{k},\vec{k}+\vec{K},\xi} \gamma_{\sigma,\vec{k}+\vec{K},\xi m}. \tag{2.23}$$

2.5.2 K-edge RIXS Formula in the Limit of Completely Localized $1s$ Core Hole

The following Kramers-Heisenberg formula (Ament et al. 2011) is the starting point for the derivation of the RIXS formula:

$$I \propto \sum_f \left| \sum_n \frac{\langle f|\mathcal{D}'^{\dagger}|n\rangle\langle n|\mathcal{D}|g\rangle}{E_g + \hbar\omega_{\vec{k}} - E_n + i\Gamma_n} \right|^2 \delta(E_f + \hbar\omega_{\vec{k}'} - E_g - \hbar\omega_{\vec{k}}), \tag{2.24}$$

where $|f\rangle$, $|n\rangle$, and $|g\rangle$ represent the final, intermediate and initial state, E_f, E_n and E_g their energies, Γ_n inverse of the intermediate state life time, $\hbar\omega_{\vec{k}'}$ and $\hbar\omega_{\vec{k}}$ the energy of outgoing and incoming x-ray with wavevector $\vec{k}'$ and $\vec{k}$, and $\mathcal{D}'^{\dagger}$ and $\mathcal{D}$ the RIXS transition operators.

In general, the $1s$ core hole component within the intermediate eigenstates $|n\rangle$ can be chosen as a delocalized state with the momentum index (Semba et al. 2008). In the limit that the $1s$ electron hopping amplitude becomes zero, the intermediate state energy levels with different core hole momenta become degenerate, and the appropriate linear combinations can be made to form intermediate energy eigenstates with a $1s$ core hole completely localized at a site (Davis and Feldkamp 1979; Feldkamp and Davis 1980; Ahn et al. 2009). Therefore, the state $|n\rangle$ can be written as $|n^{\vec{R}+\vec{d}}\rangle$, which represents the intermediate energy eigenstate with the core hole at a site $\vec{R}+\vec{d}$ within the unit cell at a lattice point $\vec{R}$. Sum over intermediate state, $\sum_n$ is written as three kinds of sums, $\sum_{\vec{R}}\sum_{\vec{d}}\sum_{n^{\vec{R}+\vec{d}}}$.

Dipole approximation (Ament et al. 2011) is taken for the RIXS transition operator $\mathcal{D}'^{\dagger}$ and $\mathcal{D}$. By analyzing how the phases of intermediate and final eigenstates change with the translation by the lattice vector $\vec{R}$, it is found that the sum over $\vec{R}$ just contributes as a constant factor to the RIXS spectrum and the crystal momentum conservation. It should be noted that creation and annihilation of the intermediate $4p$ excited states do not introduce any phase factor. Polarization effect in the K-edge RIXS is a constant factor and the dipole operators can be replaced by

the core hole creation and annihilation operators, resulting in the following expression,

$$I \propto \sum_{\vec{K}} \sum_{f} \left| \sum_{\vec{d}} \sum_{n^{\vec{d}}} \frac{e^{-i(\vec{k}'-\vec{k})\cdot\vec{d}} \langle f | \underline{s}_{\vec{d}} | n^{\vec{d}} \rangle \langle n^{\vec{d}} | \underline{s}^{\dagger}_{\vec{d}} | g \rangle}{E_g + \hbar\omega_{\vec{k}} - E_{n^{\vec{d}}} + i\Gamma_{n^{\vec{d}}}} \right|^2$$
$$\delta(E_f + \hbar\omega_{\vec{k}'} - E_g - \hbar\omega_{\vec{k}}) \delta(\vec{k}_f + \vec{k}' - \vec{k} + \vec{K}). \tag{2.25}$$

Further detail of the derivation of the above formula is presented in Appendix 2.B.

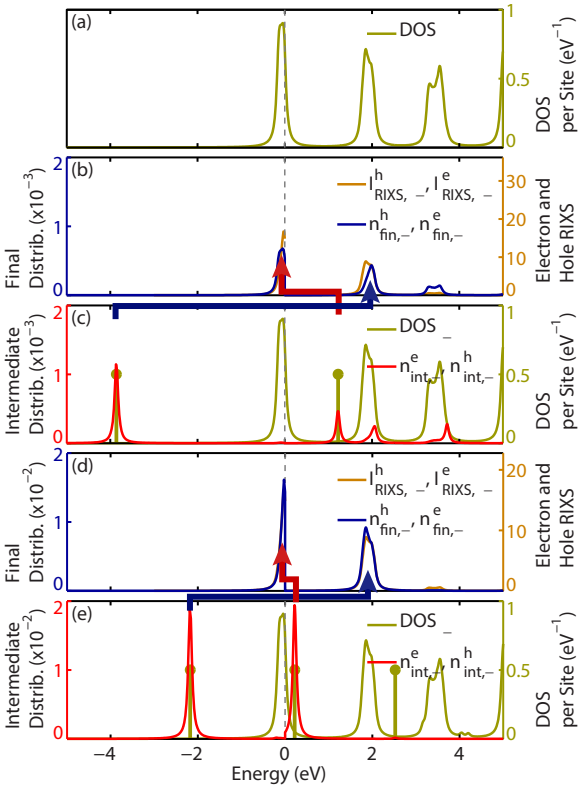

Figure 2.5 (Color) (a) Density of states per site. Core hole at Mn^{3+} with $t_0 = 0.9$ eV: (b) Final distribution compared to electron and hole RIXS intensity. (c) Intermediate distribution compared to density of states per site. Core hole at Mn^{4+} with $t_0 = 0.9$ eV: (d) Final distribution compared to electron and hole RIXS intensity. (e) Intermediate distribution compared to density of states per site.

As discussed in the introduction, further approximation is made to replace the sum $\sum_{n^{\vec{d}}}$ by a single term with $n^{\vec{d}} = n^{\vec{d}}_{\text{low}}$, that is, the lowest energy eigenstate with the core hole at site $\vec{d}$. Final states $\langle \sigma l_e \vec{k}_e l_h \vec{k}_h |$ are considered with only one pair of

an electron with momentum $\vec{k}_e$ and band index l_e and a hole with momentum $\vec{k}_h$ and band index l_h both with spin σ, while neglecting possible differences in resonance energy $E_{n^{\vec{d}}_{\text{low}}} - E_g$ and life time broadening $\Gamma_{n^{\vec{d}}_{\text{low}}}$ for different core hole site $\vec{d}$ within the unit cell. These approximations lead to the following formula for the numerical calculation of the RIXS spectrum.

$$I \propto \sum_{\vec{K}} \sum_{\sigma l_e \vec{k}_e l_h \vec{k}_h} \left| \sum_{\vec{d}} e^{-i(\vec{k}'-\vec{k})\cdot\vec{d}} \langle \sigma l_e \vec{k}_e l_h \vec{k}_h | \underline{s}_{\vec{d}} | n^{\vec{d}}_{\text{low}} \rangle \langle n^{\vec{d}}_{\text{low}} | \underline{s}^{\dagger}_{\vec{d}} | g \rangle \right|^2 \delta(\varepsilon_{l_e \vec{k}_e} - \varepsilon_{l_h \vec{k}_h} + \hbar\omega_{\vec{k}'} - \hbar\omega_{\vec{k}}) \delta(\vec{k}_e - \vec{k}_h + \vec{k}' - \vec{k} + \vec{K}). \tag{2.26}$$

Further, consider comments on the general features of the above expression. If the

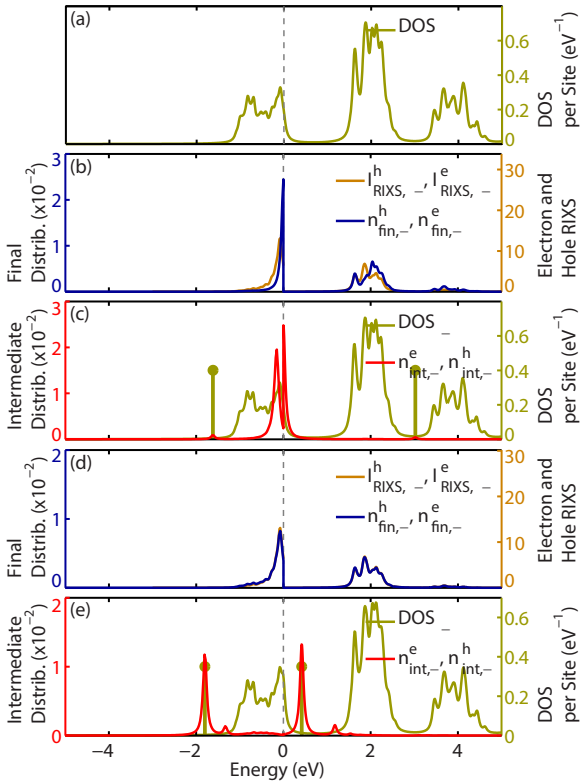

Figure 2.6 (Color) (a) Density of states per site. Core hole at Mn^{3+} with $t_0 = 1.5$ eV: (a) Final distribution compared to electron and hole RIXS intensity. (b) Intermediate distribution compared to density of states per site. Core hole at Mn^{4+} with $t_0 = 1.5$ eV: (a) Final distribution compared to electron and hole RIXS intensity. (b) Intermediate distribution compared to density of states per site.

solid has one core hole site per unit cell like high T_c cuprate, $\vec{d} = 0$ can be chosen to

simplify the above expression by omitting a constant factor as follows,

$$I \propto \sum_{\vec{K}} \sum_{\sigma l_e \vec{k}_e l_h \vec{k}_h} \left| \langle \sigma l_e \vec{k}_e l_h \vec{k}_h | \underline{s}_{\vec{d}=0} | n_{\text{low}}^{\vec{d}=0} \rangle \right|^2 \\ \delta(\varepsilon_{l_e \vec{k}_e} - \varepsilon_{l_h \vec{k}_h} + \hbar\omega_{\vec{k}'} - \hbar\omega_{\vec{k}}) \delta(\vec{k}_e - \vec{k}_h + \vec{k}' - \vec{k} + \vec{K}). \tag{2.27}$$

If the outgoing x-ray momentum is changed by reciprocal lattice vector $\vec{K}'$ to $\vec{k}'' = \vec{k}' + \vec{K}'$ while the outgoing x-ray energy is unchanged $\hbar\omega_{\vec{k}''} = \hbar\omega_{\vec{k}'}$, the RIXS intensity would be unchanged, consistent with the result in Kim et al. (2007) for cuprate. If the solid have multiple core hole sites per unit cell, such symmetry with respect to the shift by reciprocal lattice vectors does not exist in general. However, if the core hole sites within the unit cell can be approximated as a lattice, part of the symmetry can be approximately restored. For example, for $La_{0.5}Sr_{1.5}MnO_4$, the Mn ion core hole sites within MnO_2 plane approximately form a square lattice with the average Mn-Mn distance as a lattice constant. Since the reciprocal lattice vector for the approximate square core hole site, $\vec{K}_{\text{core}}$, is one of the reciprocal lattice vectors of the actual lattice, and since $e^{i\vec{K}_{\text{core}} \cdot \vec{d}} \approx 1$ in Equation (2.26), the RIXS spectrum has an approximate symmetry of $I(\vec{k}' + \vec{K}_{\text{core}} - \vec{k}) \approx I(\vec{k}' - \vec{k})$. Therefore, the approximate symmetry in reciprocal lattice is not with respect to the actual reciprocal lattice vectors, but with respect to the "core hole reciprocal lattice vectors" if the core hole sites approximately form a lattice.

Calculated $\langle n_{\text{low}}^{\vec{d}} | \underline{s}_{\vec{d}}^{\dagger} | g \rangle$ represents the transition probability from the initial to the lowest energy intermediate state, according to the following formula, where N_e represents the total electron number.

$$\langle n_{\text{low}}^{\vec{d}} | \underline{s}_{\vec{d}}^{\dagger} | g \rangle = \prod_{\sigma=\uparrow\downarrow} \begin{vmatrix} \beta_{\sigma 1 \vec{k}_1 1} & \beta_{\sigma 1 \vec{k}_1 2} & \cdots & \beta_{\sigma 1 \vec{k}_1 \frac{N_e}{2}} \\ \beta_{\sigma 1 \vec{k}_2 1} & \beta_{\sigma 1 \vec{k}_2 2} & \cdots & \beta_{\sigma 1 \vec{k}_2 \frac{N_e}{2}} \\ \vdots & \vdots & \ddots & \vdots \\ \beta_{\sigma 2 \vec{k}_{N_k} 1} & \beta_{\sigma 2 \vec{k}_{N_k} 2} & \cdots & \beta_{\sigma 2 \vec{k}_{N_k} \frac{N_e}{2}} \end{vmatrix}. \tag{2.28}$$

Further calculated is $\langle \sigma l_e \vec{k}_e l_h \vec{k}_h | \underline{s}_{\vec{d}} | n^{\vec{d}}_{\rm low} \rangle$, the transition probability from the intermediate to the final state, according to the following formula,

$$\langle \sigma l_e \vec{k}_e l_h \vec{k}_h | \underline{s}_{\vec{d}} | n^{\vec{d}}_{\rm low} \rangle = \begin{vmatrix} \beta_{\sigma 1 \vec{k}_1 1} & \beta_{\sigma 1 \vec{k}_1 2} & \cdots & \beta_{\sigma 1 \vec{k}_1 \frac{N_e}{2}} \\ \beta_{\sigma 1 \vec{k}_2 1} & \beta_{\sigma 1 \vec{k}_2 2} & \cdots & \beta_{\sigma 1 \vec{k}_2 \frac{N_e}{2}} \\ \vdots & \vdots & \ddots & \vdots \\ \beta_{\sigma l''_h \vec{k}''_h 1} & \beta_{\sigma l''_h \vec{k}''_h 2} & \cdots & \beta_{\sigma l''_h \vec{k}''_h \frac{N_e}{2}} \\ \beta_{\sigma l_e \vec{k}_e 1} & \beta_{\sigma l_e \vec{k}_e 2} & \cdots & \beta_{\sigma l_e \vec{k}_e \frac{N_e}{2}} \\ \beta_{\sigma l'''_h \vec{k}'''_h 1} & \beta_{\sigma l'''_h \vec{k}'''_h 2} & \cdots & \beta_{\sigma l'''_h \vec{k}'''_h \frac{N_e}{2}} \\ \vdots & \vdots & \ddots & \vdots \\ \beta_{\sigma 2 \vec{k}_{N_k} 1} & \beta_{\sigma 2 \vec{k}_{N_k} 2} & \cdots & \beta_{\sigma 2 \vec{k}_{N_k} \frac{N_e}{2}} \end{vmatrix} \times \begin{vmatrix} \beta_{-\sigma 1 \vec{k}_1 1} & \beta_{-\sigma 1 \vec{k}_1 2} & \cdots & \beta_{-\sigma 1 \vec{k}_1 \frac{N_e}{2}} \\ \beta_{-\sigma 1 \vec{k}_2 1} & \beta_{-\sigma 1 \vec{k}_2 2} & \cdots & \beta_{-\sigma 1 \vec{k}_2 \frac{N_e}{2}} \\ \vdots & \vdots & \ddots & \vdots \\ \beta_{-\sigma 2 \vec{k}_{N_k} 1} & \beta_{-\sigma 2 \vec{k}_{N_k} 2} & \cdots & \beta_{-\sigma 2 \vec{k}_{N_k} \frac{N_e}{2}} \end{vmatrix} \tag{2.29}$$

In the above determinant, the set of band and momentum indices, (l''_h, $\vec{k}''_h$) and (l'''_h, $\vec{k}'''_h$), represent the occupied states right before and right after the hole state represented by (l_h, $\vec{k}_h$) when the eigenstates of $\hat{H}_{\rm 3d}$ are ordered according to the band index and momentum index.[4]

2.5.3 Electronic Density of States in the Absence and in the Presence of the Core Hole

First, the results on energy eigenstates and eigenvalues of the Hamiltonians are presented, which are then used to calculate the RIXS spectrum. The electron density

[4]In other words, from the $N_e/2 \times N_e/2$ part of the matrix of β's with $m = 1, \cdots, N_e/2$ and $\varepsilon_{\sigma l \vec{k}} < \varepsilon_F$, the row corresponding to $\vec{k} = \vec{k}_h$ and $l = l_h$ is replaced by the spin σ part of the row corresponding to $\vec{k} = \vec{k}_e$ and $l = l_e$ in the matrix of β's.

of states (DOS) $D_{3d,\uparrow}(\varepsilon)$ for spin $\uparrow$ in the absence of the core hole is found from $\hat{H}_{3d}$ for 16×16 cluster is shown x in Figure 2.5(a) for $t_0 = 0.9$ eV and in Figure 2.6(a) for $t_0 = 1.5$ eV. The Lorentz broadening of $2\Gamma = 0.1$ eV is used to make the DOS curve smooth. Due to spin degeneracy in CE-type antiferromagnetic ordering, the electron DOS for spin $\downarrow$, $D_{3d,\downarrow}(\varepsilon)$, is identical to $D_{3d,\uparrow}(\varepsilon)$. In the absence of the electron hopping, the e_g levels with spin parallel to the local t_{2g} spin direction are shown schematically in Figure 1.2 for Mn^{3+} and Mn^{4+} sites in $La_{0.5}Sr_{1.5}MnO_4$. With one e_g electron per two Mn ions, the e_g electron would occupy the lower JT level at the Mn^{3+} site with spin parallel to the t_{2g} spin. With electron hopping between Mn sites, the lowest JT levels on Mn^{3+} and Mn^{4+} hybridize along the zigzag chain and form the occupied and unoccupied bands right around the gap, separated roughly by 2 eV, as shown in the electron DOS. The excitation across this gap is responsible for the 2 eV RIXS peak, which is the focus of the comparison with experiment data.

In the presence of the core hole at site $\vec{i}_c$, the Hamiltonian $\hat{H}_{\text{total},\vec{i}_c}$ is analyzed. The t_{2g} spin direction at $\vec{i}_c$ breaks the spin degeneracy in DOS. The green lines in Figures 2.5(b) and 2.5(b) show the density of states for spin $\uparrow$, $D_{\text{total},\vec{i}_c,\uparrow}(\varepsilon)$, in the presence of the core hole at Mn^{3+} site (0,0) and Mn^{4+} site (1,0), respectively, with $\uparrow$ spin t_{2g} electrons. The e_g energy levels with the spin states opposite to the t_{2g} spin direction at $\vec{i}_c$ play a minor role for the RIXS spectrum, typically less than 10 % of the total RIXS spectrum, because the e_g electrons with the same spin direction as the t_{2g} at $\vec{i}_c$ dominantly screen the core hole due to the large Hund's splitting.

For $t_0 = 0.9$ eV, as discussed in Figures 5(c) and 5(d) in Ahn et al. (2009), the core hole potential pulls bound states from band continuum, identified as vertical lines in DOS in Figures 2.5(b) and 2.5(b). One of the bound state for the core hole at Mn^{3+} is at around -4 eV, U_c below the occupied band with states primarily at Mn^{3+} site. Similarly, one of the bound states for the core hole at Mn^{4+} is located at around -2 eV, U_c below the unoccupied band with states primarily at Mn^{4+} site.

The DOS for the band continuum is almost unchanged, except that the number of states within each band continuum below and above the gap is one less to make up for the created bound states, since total number of states is unchanged, similar to the result in Ahn et al. (2009). Occupying from the lowest energy levels by the same number of electrons in the intermediate states, the lowest energy intermediate state is then obtained, that is $\underline{s}|n_{\text{low}}\rangle$. Therefore, the bound state below the lowest band is occupied and the bound state within the gap is empty in the intermediate state, and these two bound states play important roles in the formation of electron-hole pairs in the final state as well as the RIXS spectrum, as further analyzed in the following subsections.

For $t_0 = 1.5$ eV, the DOS in the presence of the core hole at Mn^{4+} is qualitatively similar to the one for $t_0 = 0.9$ eV case. The bound state within the gap is closer to the edge of the lower band continuum compared to $t_0 = 0.9$ eV case, so that the core distribution is more delocalized. Qualitatively different behavior occurs for the case with the core hole at Mn^{3+} sites. In this case, the state that would be in the gap for smaller t_0 resides in the occupied band and become a "resonant" rather than "bound" state. With this resonant state and the bound state below the lower band occupied, the top of the lower band is empty in the lowest energy intermediate state, responsible for the delocalized hole excitation, which will be analyzed further in the next subsection.

2.5.4 Contributions of the Intermediate and Initial/Final Eigenstates to Electron and Hole Excitations

As done in Ahn et al. (2009), further analysis is made on how the intermediate eigenstates contribute to the electron-hole excitations with $n^h_{\text{int},\sigma}(\varepsilon)$ and $n^e_{\text{int},\sigma}(\varepsilon)$, and how the final/initial eigenstates contribute to the electron-hole excitations with

$n^e_{\mathrm{fin},\sigma}(\varepsilon)$ and $n^h_{\mathrm{fin},\sigma}(\varepsilon)$, defined by

$$n^e_{\mathrm{int},\sigma}(\varepsilon) = \sum_{\varepsilon_{\sigma l\vec{k}}>\varepsilon_F} \sum_{m\le N_e/2} |\beta_{\sigma l\vec{k}m}|^2 \delta(\varepsilon - \varepsilon_{\sigma m}), \tag{2.30}$$

$$n^h_{\mathrm{int},\sigma}(\varepsilon) = \sum_{\varepsilon_{\sigma l\vec{k}}<\varepsilon_F} \sum_{m>N_e/2} |\beta_{\sigma l\vec{k}m}|^2 \delta(\varepsilon - \varepsilon_{\sigma m}), \tag{2.31}$$

$$n^h_{\mathrm{fin},\sigma}(\varepsilon) = \sum_{\varepsilon_{\sigma l\vec{k}}<\varepsilon_F} \sum_{m>N_e/2} |\beta_{\sigma l\vec{k}m}|^2 \delta(\varepsilon - \varepsilon_{\sigma l\vec{k}}), \tag{2.32}$$

$$n^e_{\mathrm{fin},\sigma}(\varepsilon) = \sum_{\varepsilon_{\sigma l\vec{k}}>\varepsilon_F} \sum_{m\le N_e/2} |\beta_{\sigma l\vec{k}m}|^2 \delta(\varepsilon - \varepsilon_{\sigma l\vec{k}}), \tag{2.33}$$

for each chosen core hole site, similar to n^e_m, n^h_m, $n^h_{k_<}$, and $n^e_{k_>}$ defined in Ahn et al. (2009). These are plotted in Figures 2.5 and 2.6 for $\sigma =\uparrow$ for the core hole at Mn^{3+} and Mn^{4+} site with spin $\uparrow$ t_{2g} electrons. For example, $n^h_{\mathrm{int},\sigma}(\varepsilon)$ represents the sum of the squared coefficients connecting the eigenstates occupied in the intermediate state and eigenstates empty in the initial state, with the intermediate energy δ-function multiplied, and, therefore, represents the contribution of intermediate state to the electron excitation. Electron and hole distributions for spin $\downarrow$ state are less than 10% of those for spin $\uparrow$ state. The plot of $n^h_{\mathrm{int},\uparrow}(\varepsilon)$ and $n^e_{\mathrm{int},\uparrow}(\varepsilon)$ show that the bound states in the intermediate state dominantly contribute to the electron-hole excitations, as identified in Figure 5(d) in Ahn et al. (2009), except the case with $t_0 = 1.5$ eV and core hole at Mn^{3+} site in Figure 2.6, for which the resonance within the lower band and the state at the top of the occupied band dominantly contribute $n^e_{\mathrm{int},\uparrow}(\varepsilon)$ and $n^h_{\mathrm{int},\uparrow}(\varepsilon)$.

The plot of $n^h_{\mathrm{fin},\uparrow}(\varepsilon)$ and $n^e_{\mathrm{fin},\uparrow}(\varepsilon)$ also confirms the conclusion in Figure 5(c) in Ahn et al. (2009) that the hole [electron] distribution projected into the final/initial eigenstates near the gap becomes sharper as the intermediate hole [electron] bound state becomes closer to the top [bottom] of the initial occupied [empty] band, which gives rise to asymmetric electron and hole distributions, namely, the hole distribution sharper than the electron distribution, representing different screening dynamics between electrons and holes. The above analysis in this subsection shows that the

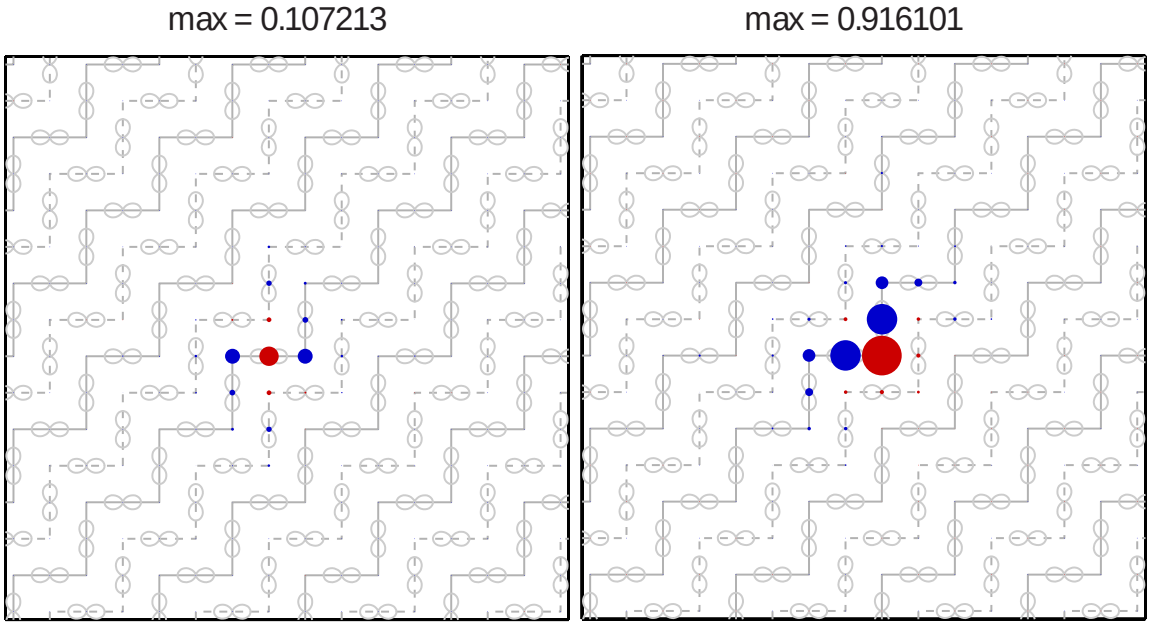

Figure 2.7 (Color) Screening configuration in real space for $t_0 = 0.9$ eV case for core hole at (left) Mn^{3+}, and (right) Mn^{4+}.

main conclusions of the study in Ahn et al. (2009), which mainly focuses on the energy-dependence of the screening dynamics associated with the RIXS process, holds for $La_{0.5}Sr_{1.5}MnO_4$, confirming the foundation of the current study. As pointed out above, the case with $t_0 = 1.5$ eV and core hole at Mn^{3+} site shows a different behavior. With the resonance state occupied in the intermediate state, the resonance state contribute to the electron excitation predominantly because the second bound state is pulled from the initially unoccupied bands, whereas the first bound state is mostly from the initially occupied band. The delocalized state at the top of the occupied band predominantly contributes to the hole excitation, because it is occupied in the initial state and empty in the intermediate state.

In Figures 2.5 and 2.6, also plotted are

$$I^{\mathrm{h}}_{\mathrm{RIXS},\sigma}(\varepsilon) = \sum_{l_e,\vec{k}_e}\sum_{l_h,\vec{k}_h}\sum_{\Delta\vec{K}} |F_\sigma(l_e,\vec{k}_e;l_h,\vec{k}_h;\Delta\vec{K})|^2\ \delta(\varepsilon_{l_h\vec{k}_h}-\varepsilon) \tag{2.34}$$

$$I^{\mathrm{e}}_{\mathrm{RIXS},\sigma}(\varepsilon) = \sum_{l_e,\vec{k}_e}\sum_{l_h,\vec{k}_h}\sum_{\Delta\vec{K}} |F_\sigma(l_e,\vec{k}_e;l_h,\vec{k}_h;\Delta\vec{K})|^2\ \delta(\varepsilon_{l_e\vec{k}_e}-\varepsilon). \tag{2.35}$$

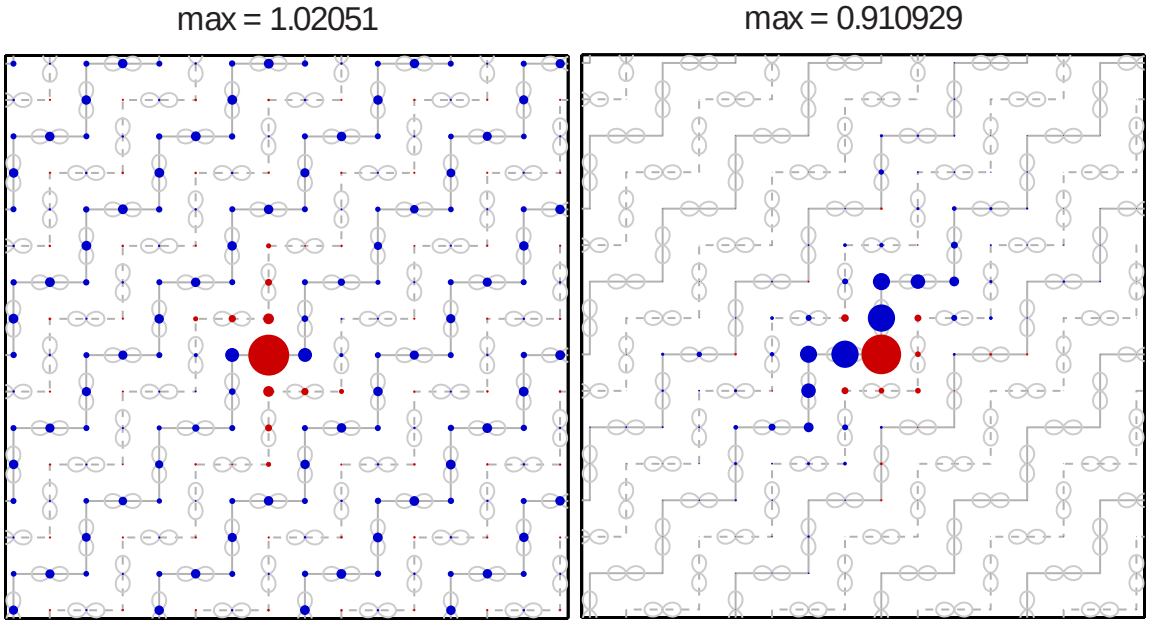

Figure 2.8 (Color) Screening configuration in real space for $t_0 = 1.5$ eV case for core hole at (left) Mn^{3+}, and (right) Mn^{4+}.

For comparison, the results for $I^h_{RIXS,\sigma}(\varepsilon)$ and $I^e_{RIXS,\sigma}(\varepsilon)$ in Figures 2.5(b,d) and 2.6(b,d) indeed show good agreement with $n^h_{fin,\sigma}(\varepsilon)$ and $n^e_{fin,\sigma}(\varepsilon)$, confirming close connection between electron-hole excitation and RIXS spectrum.

2.5.5 Electron and Hole Excitations by the Core Hole Represented in Direct Space

In this subsection, the pattern of electrons and holes excited by the core hole examined in direct space is related to the pattern of the RIXS spectrum in reciprocal space after being integrated with respect to the energy. In the absence of the core hole, the electron number $\langle \hat{n}_{\sigma\vec{i}\eta} \rangle$ is calculated for each spin state $\sigma = \uparrow, \downarrow$ and orbital state $\eta = +, -$ at each site $\vec{i}$ from the initial ground state $|g\rangle$ of the Hamiltonian $\hat{H}_{3d}$. The total e_g electron numbers calculated for the 16×16 cluster model in the absence of the core hole are 0.87 at the nominal Mn^{3+} site and 0.13 at the nominal Mn^{4+} site, indicating a difference of 0.74 in charge density. It must be noted that these numbers should not be directly compared with the LDA theory results or resonant

x-ray spectroscopy results, because the local basis states are not pure Mn orbital states but combinations of Mn and O orbitals, similar to the Zhang-Rice singlet for cuprates. Proper comparison is described in Appendix 2.A, which shows the electron numbers in the model are consistent with LDA or RXS results. It is found that most of these electrons occupy the lower Jahn-Teller level $\eta = -$ of spin parallel to t_{2g} spin at each site, approximately $x^2 - z^2/y^2 - z^2$ orbital at Mn^{3+} site and $3z^2 - r^2$ orbital at Mn^{4+} site, consistent with the orbital ordering proposed in Zeng et al. (2008). In the intermediate state, these electron numbers change to screen the core hole. The change in the electron number is shown in Figures 2.7 and 2.8 for the core hole at a Mn^{3+} site and a Mn^{4+} site (the site with the largest red dot in each panel), respectively. The gray solid and dashed lines in the background represent the zigzag chain with t_{2g} spin $\uparrow$ and $\downarrow$, respectively. The volume of the blue sphere is proportional to the decrease in the total electron number at each Mn site. Similarly, the volume of the red sphere represents the increase in the total electron number. Figures 2.7(a) and 2.7(b) show that the electron excitations are mostly confined right at the core hole site, consistent with the relatively flat electron distribution, $n^e_{\mathrm{fin}\uparrow}$, in Figure 2.5(a). Comparing the largest solid red circles in Figures 2.7(a) and 2.7(b) show that more screening electrons accumulate at the core hole site when the core hole is created at the Mn^{4+} site (0.92 electron) than at the Mn^{3+} (0.11 electron). This result can be understood from the orbital ordering pattern: Initially the Mn^{4+} site has less e_g electrons on the site itself but more electrons at nearest neighbor Mn sites along the zigzag chain with orbitals pointing towards the Mn^{4+} site, compared to the Mn^{3+} site. Hole distribution in Figures 2.7(a) and 2.7(b) show that these screening electrons are mostly from the nearest or next nearest neighbors along the zigzag chain. For the case of the core hole at the Mn^{3+} and Mn^{4+} site for $t_0 = 0.9$ eV, the holes at two nearest neighbor sites constitute 91.0% and 91.4%, respectively, of the total hole number. The results show that even though the hole excitation is not

as localized, as the electron excitation, residing over a few sites instead of just one site, consistent with different sharpness of $n^h_{\text{fin}\uparrow}$ and $n^e_{\text{fin}\uparrow}$ in Figure 2.5(b), the holes are still tightly bound to the core hole site with almost exciton-like electron and hole pair state. Such screening pattern in real space can be related to the variation of the RIXS intensity in reciprocal space, which is discussed in Section 2.4.

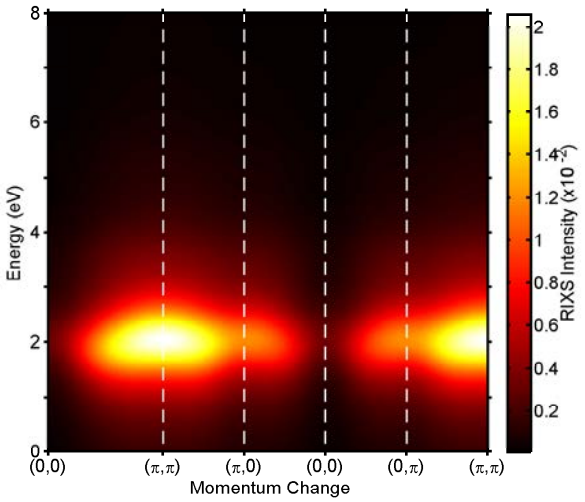

Figure 2.9 (Color) Contour plot of RIXS intensity calculated for $t_0 = 0.9$ eV case along the chosen path.

The situation changes for cases with a core hole at Mn^{3+} and with a large electron hopping, for example, $t_0 = 1.5$ eV. The hole distribution becomes delocalized, and only about 8.0% of the core is localized within the nearest neighbors, and the majority of the hole is delocalized along the zigzag chains with the same spin direction as the core hole site. The hole number does not decay with the distance from the core hole site, which indicates qualitatively different nature of the screening dynamics.

2.5.6 Calculated RIXS Spectrum and Comparison with Experimental Data

Once the Hamiltonians are solved in the absence and in the presence of the core hole, the RIXS intensity, $I_{\text{RIXS}}(\vec{q}, \omega)$ can be calculated according to the formula in Section 2.B. In this RIXS calculation, a small displacement is included of the Mn^{4+}

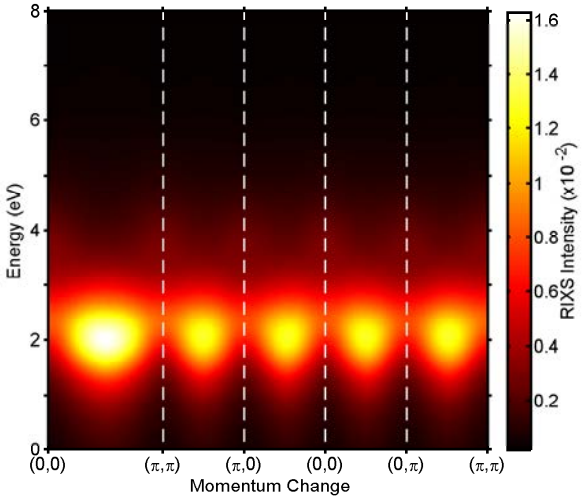

Figure 2.10 (Color) Contour plot of RIXS intensity calculated for $t_0 = 0.9$ eV case along the chosen path.

ions of 0.0265 Å along the diagonal direction from the ideal square lattice (Zeng et al. 2008). The results are shown in Figures 2.9 and 2.10 for $t_0 = 0.9$ eV and 1.5 eV, along a path in the extended zone Ω_{ExZ} in reciprocal space. As mentioned above, the electron-lattice coupling parameter λ was adjusted to $\lambda = 3.509$ eV/Å for $t_0 = 1.5$ eV from $\lambda = 7.407$ eV/Å for $t_0 = 0.9$ eV, so that the lowest energy RIXS peak stays near 2 eV.

Comparison between the experimental data and the calculated result for $t_0 = 0.9$ eV is made. In addition to the momentum dependent RIXS peak at around 2 eV, the experimental RIXS spectrum shows momentum independent spectral weight, in particular above 3 eV as shown in Figure 2.1(a). The RIXS spectrum at H = 0.03 is indicative that the RIXS spectral weight above 3 eV may have the same origin as the 4-5 eV O2*p*-Mn3*d* transition observed in optical experiments in related manganites. Based on such assumption, the experimental RIXS spectrum is fitted with a momentum-independent O2*p*–Mn3*d* transition peak centered at 4.5 eV and half-width at half-maximum 1.5 eV, similar to the optical peak, and the calculated momentum-dependent 3*d*-3*d* peaks. The results are shown in Figure 2.11 and show

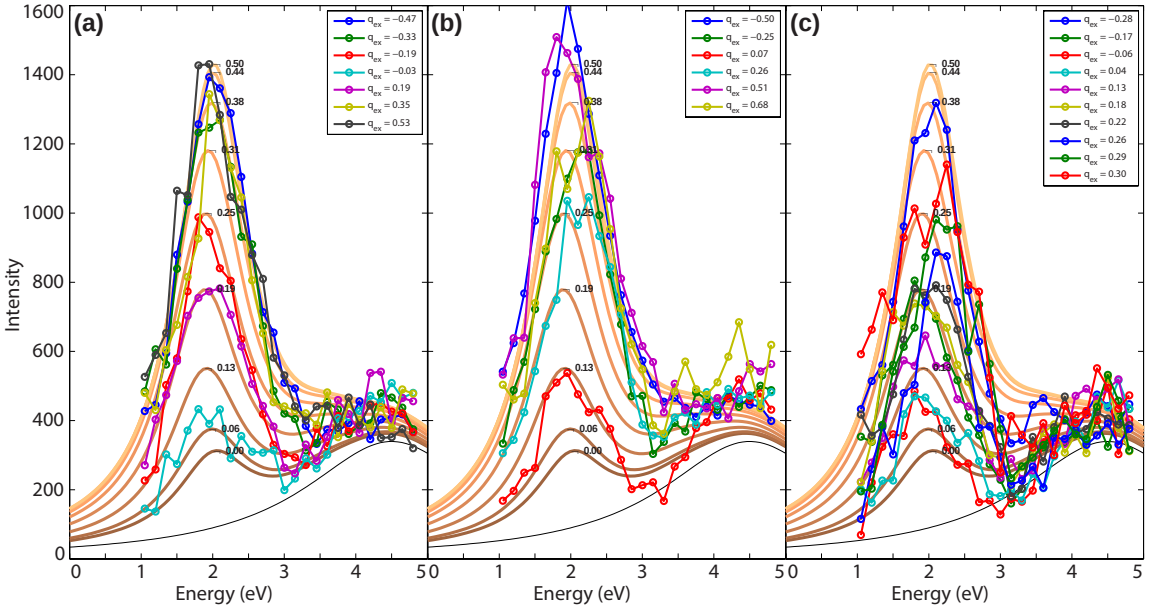

Figure 2.11 (Color) Theoretical RIXS intensity lines with Lorentzian broadening shown in brown color scheme, superimposed with experimental data represented in symbols connected with lines. Both, theoretical and experimental data have a distinctive peak at 2 eV. Experimental data measured along (a) $2\theta = 68°$, (b) $2\theta = 78°$, and (c) $\theta = 48°$, refer to Figure 2.1(b) for surveyed $\vec{Q}$-points in the (H, H, L) plane. Thin grey line at the bottom is added to the theoretical result, as a Lorentzian peak centered at 4.5 eV with $\gamma_{\rm bk} = 1.5$ eV.

a reasonable agreement between theory and experiment. The O2p-Mn3d transition has a substantial spectral weight tail even in the range of 1–3 eV. Such momentum-independent RIXS spectral weights with substantial tails even in the low energy range have been also observed in bilayer manganites (Weber et al. 2010). To make more quantitative comparison, the O2p-Mn3d peak is subtracted from experimental data, and the spectrum is integrated from 1 eV to 3 eV and compared with corresponding integrated intensity from theory results. The comparison is shown in Figure 2.12, in which both theoretical results and experimental data are normalized with respect to the integrated intensity at (π, π) point.

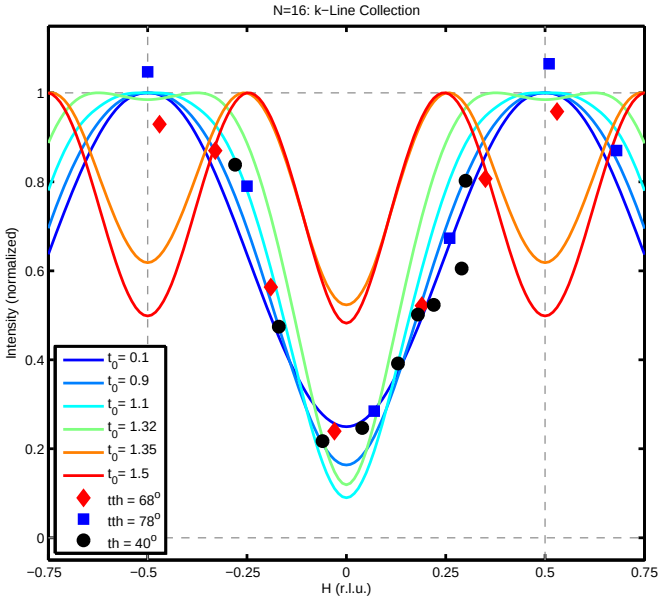

Figure 2.12 (Color) Integrated RIXS intensity variation for several t_0 cases normalized at $(|\pi|, |\pi|)$ for comparison. Symbols represent experimental data.

2.5.7 Periodicity of K-edge RIXS Spectrum in Reciprocal Space

In earlier studies of La_2CuO_4 by Kim et al. (2007), it was shown that the spectra did not depend on the choice of Brillouin zone being measured. This observation, depicted in Figure 2.13, led to the following conclusion: momentum dependence observed in K-edge RIXS obeys the periodicity of reduced wave vector $\vec{k}$, which defined as $\vec{q} = \vec{k} + \vec{G}$, where $\vec{q}$ is the total momentum change, and $\vec{G}$ is a reciprocal lattice vector (Ament et al. 2011, p.715). Hence, RIXS spectra depends purely on $\vec{k}$, and has a translational symmetry of the reciprocal lattice in reciprocal space.

The RIXS calculation and the experimental data for $La_{0.5}Sr_{1.5}MnO_4$ described in this chapter, clearly indicates that such periodicity is not present. Figure 2.14 shows integrated RIXS intensity in k-space, based on 16x16 Mn lattice. The diamond shape at the center enclosed by line running through the points $\vec{k} = (\pi/2, 0), (0, \pi/2), (-\pi/2, 0)$, and $(0, -\pi/2)$, is the first Brillouin zone, whereas the outer square domain $|k_x| \leq \pi$ and $|k_y| \leq \pi$, denotes the "extended Brillouin zone",

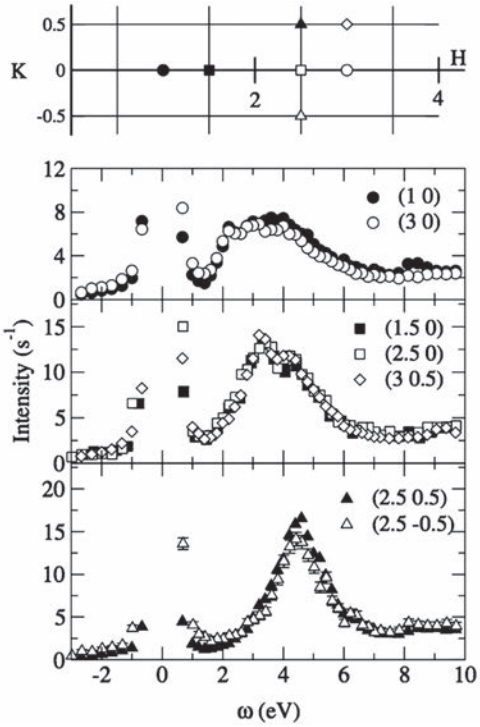

Figure 2.13 Kim et al. (2007) presents the experimentally observed comparison of RIXS spectra on La_2CuO_4 taken at different total q positions but with an equivalent reduced wave vector $\vec{k}$ for seven different qs corresponding to $\vec{k} = (0,0), (\pi,0)$, and (π,π), from top to bottom. The two-dimensional reciprocal space net is shown in the top panel.

or in some instances referred to as $|\mathrm{H}| \leq 0.5$ (r.l.u.). To bring more clarity to the term "extended", for example if a system does not have an orbital ordering, charge ordering, magnetic ordering, and Jahn-Teller distortion, then for a unit cell with one manganese atom, first Brillouin zone would be equivalent to the extended Brillouin zone. As it is further shown in Figure 2.14, the calculations were done over the neighboring extended Brillouin zones to cover wider domain within $|k_x| \leq 3\pi$ and $|k_y| \leq 3\pi$. It is evident that RIXS spectrum does not exhibit periodicity with respect to the first Brillouin zone, however the spectrum shows approximate periodicity with respect to the extended Brillouin zone.

Emphasis must be made, that even this periodicity is only approximate. In the extended Brillouin zone of Figure 2.14, global maximum of RIXS intensity occurs

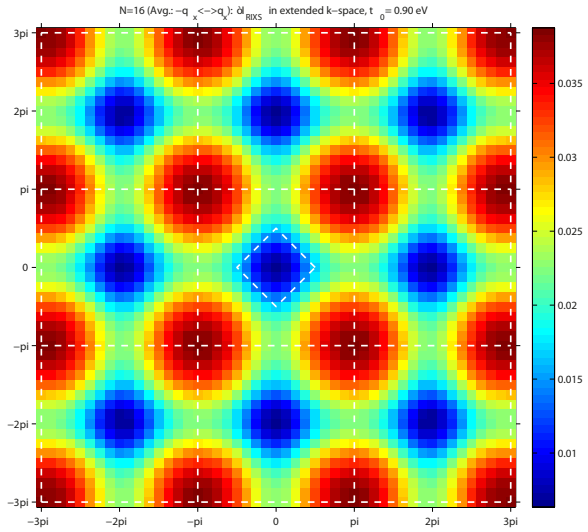

Figure 2.14 (Color) Integrated RIXS intensity in extended reciprocal space for $t_0 = 0.9$ eV case. First Brillouin zone is at the center bounded by diamond shape marked by points $(\pi/2, 0), (0, \pi/2), (-\pi/2, 0)$, and $(0, -\pi/2)$, whereas the square domain bounded by $|k_x| \leq \pi$ and $|k_y| \leq \pi$ denotes the extended Brillouin zone.

at four $(\pm\pi, \pm\pi)$ points, whereas global minimum occurs at $(0, 0)$. In Figure 2.14, the spectrum looks almost periodic with respect to the extended Brillouin zone, but after careful examination one may observe slight differences between corresponding points with maximums at $(\pm\pi, \pm\pi)$ and $(\pm 3\pi, \pm 3\pi)$, as well as minimums at $(0, 0)$ and $(\pm 2\pi, \pm 2\pi)$. This "slight" non-periodicity of the extended Brillouin zone can be further attributed to the experimental bond length data describing lattice geometry, particularly through inclusion of small diagonal displacements at Mn^{4+} ions (Zeng et al. 2008). Removing those displacements from calculation makes extended Brillouin zone periodic. Analytically, it can be shown through Equation (2.25). Similar results for $t_0 = 1.5$ eV is shown in Figure 2.15. In addition, this aperiodic behaviour can be seen more clearly in Figure 2.2(b), especially with the $t_0 = 1.32$ eV line.

2.6 Conclusions

In summary, highly momentum-dependent K-edge resonant inelastic x-ray scattering intensity is observed in the orbital ordered, layered manganite $La_{0.5}Sr_{1.5}MnO_4$.

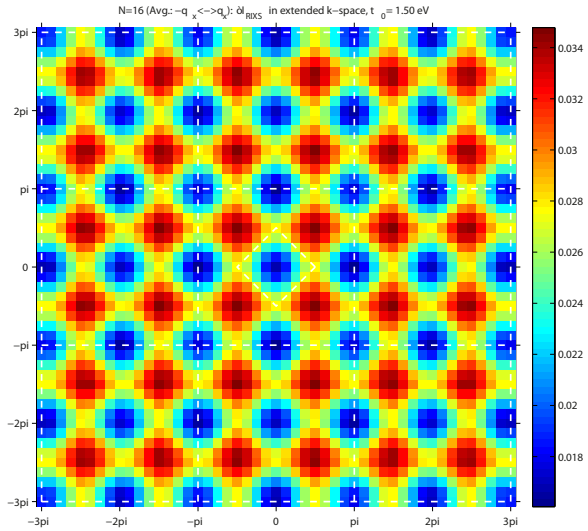

Figure 2.15 (Color) Integrated RIXS intensity in extended reciprocal space for $t_0 = 1.5$ eV case. First Brillouin zone is at the center bounded by diamond shape marked by points $(\pi/2, 0), (0, \pi/2), (-\pi/2, 0)$, and $(0, -\pi/2)$, whereas the square domain bounded by $|k_x| \leq \pi$ and $|k_y| \leq \pi$ denotes the extended Brillouin zone.

This is interpreted through a comparison with calculations based on a tight-binding approach, and also showed that these observations imply a highly localized, nearest neighbor screening of the local charge perturbation. It is further found that the momentum dependence of the RIXS spectrum reflects the pattern and range of the screening in real space, and thus the size and shape of the screening cloud can be measured. It is determined that the screening cloud is localized to a few Mn sites in the Mn-O plane, emphasizing the short range nature of the Coulomb interactions in the manganites. These results also show the potential of K-edge RIXS, as a probe of the screening dynamics in strongly correlated materials.

APPENDIX

2.A Hamiltonians in Reciprocal Space Without and With $1s$ Core Hole

In the absence of the core hole, the Hamiltonian has the following form in reciprocal space,

$$\hat{H}_{3d} = \sum_{\sigma,\vec{k}\in 1BZ} a^{\dagger}_{\sigma\vec{k}} H^{3d}_{\sigma\vec{k}} a_{\sigma\vec{k}}, \tag{2.36}$$

where $H^{3d}_{\sigma\vec{k}} = H^{3d,nonint}_{\sigma\vec{k}} + H^{\mathrm{3d3d,HF}}_{\sigma\vec{k}}$,

$$\begin{aligned} a^{\dagger}_{\sigma\vec{k}} &= (a^{\dagger}_{\sigma,\vec{k}+\vec{K}_1,1}, a^{\dagger}_{\sigma,\vec{k}+\vec{K}_1,2}, a^{\dagger}_{\sigma,\vec{k}+\vec{K}_2,1}, a^{\dagger}_{\sigma,\vec{k}+\vec{K}_2,2}, \\ &\quad a^{\dagger}_{\sigma,\vec{k}+\vec{K}_3,1}, a^{\dagger}_{\sigma,\vec{k}+\vec{K}_3,2}, a^{\dagger}_{\sigma,\vec{k}+\vec{K}_4,1}, a^{\dagger}_{\sigma,\vec{k}+\vec{K}_4,2}, \\ &\quad a^{\dagger}_{\sigma,\vec{k}+\vec{K}_5,1}, a^{\dagger}_{\sigma,\vec{k}+\vec{K}_5,2}, a^{\dagger}_{\sigma,\vec{k}+\vec{K}_6,1}, a^{\dagger}_{\sigma,\vec{k}+\vec{K}_6,2}, \\ &\quad a^{\dagger}_{\sigma,\vec{k}+\vec{K}_7,1}, a^{\dagger}_{\sigma,\vec{k}+\vec{K}_7,2}, a^{\dagger}_{\sigma,\vec{k}+\vec{K}_8,1}, a^{\dagger}_{\sigma,\vec{k}+\vec{K}_8,2}) \end{aligned} \tag{2.37}$$

with $\vec{K}_1$, $\vec{K}_2$, $\vec{K}_3$, $\vec{K}_4$, $\vec{K}_5$, $\vec{K}_6$, $\vec{K}_7$, and $\vec{K}_8$ representing (0,0), (π,0), (0,π), (π,π), (-π/2,-π/2), (π/2,-π/2) , (-π/2,π/2), and (π/2,π/2), respectively,

$$H^{\mathrm{3d,nonint}}_{\sigma\vec{k}} = \begin{pmatrix} H_1 & H_2 \\ H_2 & H_3 \end{pmatrix}, \tag{2.38}$$

with matrix blocks defined as follows

$$H_1 = \begin{pmatrix} M_1 + W_{3u} & -G_\sigma & G_\sigma & W_{1s} + W_{3s} \\ -G_\sigma & M_2 + W_{3u} & W_{1s} + W_{3s} & G_\sigma \\ G_\sigma & W_{1s} + W_{3s} & M_3 + W_{3u} & -G_\sigma \\ W_{1s} + W_{3s} & G_\sigma & -G_\sigma & M_4 + W_{3u} \end{pmatrix}, \tag{2.39}$$

$$H_2 = \begin{pmatrix} W_{2s} & G_\sigma & G_\sigma & W_{2s} \\ G_\sigma & W_{2s} & W_{2s} & G_\sigma \\ G_\sigma & W_{2s} & W_{2s} & G_\sigma \\ W_{2s} & G_\sigma & G_\sigma & W_{2s} \end{pmatrix}, \tag{2.40}$$

$$H_3 = \begin{pmatrix} M_5 + W_{3u} & -G_\sigma & G_\sigma & W_{1s} + W_{3s} \\ -G_\sigma & M_6 + W_{3u} & W_{1s} + W_{3s} & G_\sigma \\ G_\sigma & W_{1s} + W_{3s} & M_7 + W_{3u} & -G_\sigma \\ W_{1s} + W_{3s} & G_\sigma & -G_\sigma & M_8 + W_{3u} \end{pmatrix}, \quad (2.41)$$

where all the terms further defined as

$$M_j = \begin{pmatrix} -\frac{t_0}{2}[\cos(k_x + K_{j,x}) + \cos(k_y + K_{j,y})] & \frac{\sqrt{3}t_0}{2}[\cos(k_x + K_{j,x}) - \cos(k_y + K_{j,y})] \\ \frac{\sqrt{3}t_0}{2}[\cos(k_x + K_{j,x}) - \cos(k_y + K_{j,y})] & -\frac{3t_0}{2}[\cos(k_x + K_{j,x}) + \cos(k_y + K_{j,y})] \end{pmatrix}, \quad (2.42)$$

$$G_\uparrow = \begin{pmatrix} -\frac{J_H S_c}{2} & 0 \\ 0 & -\frac{J_H S_c}{2} \end{pmatrix}, \quad (2.43)$$

$$G_\downarrow = \begin{pmatrix} \frac{J_H S_c}{2} & 0 \\ 0 & \frac{J_H S_c}{2} \end{pmatrix}, \quad (2.44)$$

$$W_{1s} = \begin{pmatrix} -\beta\lambda_Q Q_{1s} & 0 \\ 0 & -\beta\lambda_Q Q_{1s} \end{pmatrix}, \quad (2.45)$$

$$W_{2s} = \begin{pmatrix} 0 & \lambda_Q Q_{2s} \\ \lambda_Q Q_{2s} & 0 \end{pmatrix}, \quad (2.46)$$

$$W_{3u} = \begin{pmatrix} -\lambda_Q Q_{3u} & 0 \\ 0 & \lambda_Q Q_{3u} \end{pmatrix}, \quad (2.47)$$

$$W_{3s} = \begin{pmatrix} -\lambda_Q Q_{3s} & 0 \\ 0 & \lambda_Q Q_{3s} \end{pmatrix}, \quad (2.48)$$

Q_{1s} = 0.053 Å, Q_{2s} = 0.054 Å, Q_{3u} = 0.107 Å, and Q_{3s} = -0.012 Å (Herrero-Martín et al. 2011). The element of 16 × 16 matrix $H^{\rm 3d3d,HF}_{\sigma\vec{k}}$ is independent of $\vec{k}$,

$$\left(H^{\rm 3d3d,HF}_{\sigma\vec{k}}\right)_{2(j-1)+\xi,2(j'-1)+\xi'} = \sum_{\vec{i}_u,\eta} \frac{U_{\sigma\vec{i}_u\eta}}{8} e^{-i(\vec{K}_j-\vec{K}_{j'})\cdot\vec{i}_u} \left(R_{\vec{i}_u\eta}\right)_{\xi\xi'} \tag{2.49}$$

where $\eta = +,-$, $j, j' = 1, 2, ..., 8, \xi, \xi' = 1, 2$, $\vec{i}_u$ represents the position index vector of the Mn ions within the unit cell, that is, (0,0), (1,0), (2,0), (3,0), (1,-1), (2,-1), (1,1), and (2,1),

$$R_{\vec{i}_u-} = \begin{pmatrix} \cos^2\theta_{\vec{i}_u} & \cos\theta_{\vec{i}_u}\sin\theta_{\vec{i}_u} \\ \cos\theta_{\vec{i}_u}\sin\theta_{\vec{i}_u} & \sin^2\theta_{\vec{i}_u} \end{pmatrix}, \tag{2.50}$$

$$R_{\vec{i}_u+} = \begin{pmatrix} \sin^2\theta_{\vec{i}_u} & -\cos\theta_{\vec{i}_u}\sin\theta_{\vec{i}_u} \\ -\cos\theta_{\vec{i}_u}\sin\theta_{\vec{i}_u} & \cos^2\theta_{\vec{i}_u} \end{pmatrix}, \tag{2.51}$$

$\theta_{\vec{i}}$ is defined from the local lower (−) and upper (+) Jahn-Teller eigenstate,

$$a^\dagger_{\sigma\vec{i}-} = a^\dagger_{\sigma\vec{i}1}\cos\theta_{\vec{i}} + a^\dagger_{\sigma\vec{i}2}\sin\theta_{\vec{i}}, \tag{2.52}$$

$$a^\dagger_{\sigma\vec{i}+} = -a^\dagger_{\sigma\vec{i}1}\sin\theta_{\vec{i}} + a^\dagger_{\sigma\vec{i}2}\cos\theta_{\vec{i}} \tag{2.53}$$

At Mn^{3+} sites in the x/y directional legs of the zigzag chain,

$$\tan\theta_{\vec{i}} = \pm\frac{Q_{3u}+Q_{3s}-\sqrt{(Q_{3u}+Q_{3s})^2+4Q_{2s}^2}}{2Q_{2s}} \tag{2.54}$$

At Mn^{4+} sites, $\theta_{\vec{i}}$=0. To evaluate $U_{\sigma\vec{i}\eta}$, the matrix for the number operator in reciprocal space is necessary, the element of which is given below.

$$\left(n^{\sigma\vec{i}_u\eta}_{\vec{k}}\right)_{2(j-1)+\xi,2(j'-1)+\xi'} = e^{-i(\vec{K}_j-\vec{K}_{j'})\cdot\vec{i}_u}\left(R_{\vec{i}_u\eta}\right)_{\xi\xi'} \tag{2.55}$$

The eigenstates and eigenenergies of 16 × 16 matrix $H^{3d}_{\sigma\vec{k}}$ are found through the Hartree-Fock iterative calculations at chosen set of k points, which gives the electronic DOS in Figure 2.5.

The Hamiltonian in the presence of the core hole at a site $\vec{i}_c$ for $N \times N$ clusters, with N multiple of 4, is presented below. The k points within the first Brillouin zone are $\vec{k}_1$, $\vec{k}_2$, ...,$\vec{k}_{N_k}$, where $N_k = N^2/8$.

$$\hat{H}_{\text{total}} = \sum_{\sigma} a_{\sigma}^{\dagger}(H_{\sigma}^{\text{3d,nonint}} + H_{\sigma}^{\text{3d3d,HF}} + H_{\sigma}^{\text{1s3d,}\vec{\text{i}}_{\text{c}}})a_{\sigma} \tag{2.56}$$

where

$$a_{\sigma}^{\dagger} = (a_{\sigma\vec{k}_1}^{\dagger}, a_{\sigma\vec{k}_2}^{\dagger}, \cdots, a_{\sigma\vec{k}_{N_k}}^{\dagger}) \tag{2.57}$$

$$H_{\sigma}^{\text{3d,nonint}} = \begin{pmatrix} H_{\sigma\vec{k}_1}^{\text{3d,nonint}} & 0 & \cdots & 0 \\ 0 & H_{\sigma\vec{k}_2}^{\text{3d,nonint}} & \cdots & 0 \\ \vdots & \vdots & \ddots & \vdots \\ 0 & 0 & \cdots & H_{\sigma\vec{k}_{N_k}}^{\text{3d,nonint}} \end{pmatrix} \tag{2.58}$$

$$H_{\sigma}^{\text{3d3d,HF}} = \begin{pmatrix} H_{\sigma\vec{k}_1\vec{k}_1}^{\text{3d3d,HF}} & H_{\sigma\vec{k}_1\vec{k}_2}^{\text{3d3d,HF}} & \cdots & H_{\sigma\vec{k}_1\vec{k}_{N_k}}^{\text{3d3d,HF}} \\ H_{\sigma\vec{k}_2\vec{k}_1}^{\text{3d3d,HF}} & H_{\sigma\vec{k}_2\vec{k}_2}^{\text{3d3d,HF}} & \cdots & H_{\sigma\vec{k}_2\vec{k}_{N_k}}^{\text{3d3d,HF}} \\ \vdots & \vdots & \ddots & \vdots \\ H_{\sigma\vec{k}_{N_k}\vec{k}_1}^{\text{3d3d,HF}} & H_{\sigma\vec{k}_{N_k}\vec{k}_2}^{\text{3d3d,HF}} & \cdots & H_{\sigma\vec{k}_{N_k}\vec{k}_{N_k}}^{\text{3d3d,HF}} \end{pmatrix} \tag{2.59}$$

where

$$\left(H_{\sigma\vec{k}_h\vec{k}_{h'}}^{\text{3d3d,HF}}\right)_{2(j-1)+\xi,2(j'-1)+\xi'} = \sum_{\vec{i},\eta} \frac{U_{\sigma\vec{i}\eta}}{N^2} e^{-i(\vec{k}_h-\vec{k}_{h'})\cdot\vec{i}} e^{-i(\vec{K}_j-\vec{K}_{j'})\cdot\vec{i}} \left(R_{\vec{i}\eta}\right)_{\xi\xi'} \tag{2.60}$$

where $\eta = +, -$, $j, j' = 1, 2, ..., 8, \xi, \xi' = 1, 2$, $\vec{i}$ represents the site index vector for $N \times N$ Mn cluster. Again, for the evaluation of $U_{\sigma\vec{i}\eta}$, the matrix for the number operator in reciprocal space is necessary, shown below.

$$n^{\sigma\vec{i}\eta} = \begin{pmatrix} n_{\vec{k}_1\vec{k}_1}^{\sigma\vec{i}\eta} & n_{\vec{k}_1\vec{k}_2}^{\sigma\vec{i}\eta} & \cdots & n_{\vec{k}_1\vec{k}_{N_k}}^{\sigma\vec{i}\eta} \\ n_{\vec{k}_2\vec{k}_1}^{\sigma\vec{i}\eta} & n_{\vec{k}_2\vec{k}_2}^{\sigma\vec{i}\eta} & \cdots & n_{\vec{k}_2\vec{k}_{N_k}}^{\sigma\vec{i}\eta} \\ \vdots & \vdots & \ddots & \vdots \\ n_{\vec{k}_{N_k}\vec{k}_1}^{\sigma\vec{i}\eta} & n_{\vec{k}_{N_k}\vec{k}_2}^{\sigma\vec{i}\eta} & \cdots & n_{\vec{k}_{N_k}\vec{k}_{N_k}}^{\sigma\vec{i}\eta} \end{pmatrix} \tag{2.61}$$

with

$$\left(n^{\sigma\vec{i}\eta}_{\vec{k}_h\vec{k}_{h'}}\right)_{2(j-1)+\xi,2(j'-1)+\xi'} = e^{-i(\vec{k}_h-\vec{k}_{h'})\cdot\vec{i}}e^{-i(\vec{K}_j-\vec{K}_{j'})\cdot\vec{i}}\left(R_{\vec{i}\eta}\right)_{\xi\xi'}. \tag{2.62}$$

Finally, the 1s-3d Coulomb interaction for the core hole present at $\vec{i}_c$ is represented by the following Hamiltonian matrix.

$$H^{1s3d,\vec{i}_c}_{\sigma} = \begin{pmatrix} H^{1s3d,\vec{i}_c}_{\sigma\vec{k}_1\vec{k}_1} & H^{1s3d,\vec{i}_c}_{\sigma\vec{k}_1\vec{k}_2} & \cdots & H^{1s3d,\vec{i}_c}_{\sigma\vec{k}_1\vec{k}_{N_k}} \\ H^{1s3d,\vec{i}_c}_{\sigma\vec{k}_2\vec{k}_1} & H^{1s3d,\vec{i}_c}_{\sigma\vec{k}_2\vec{k}_2} & \cdots & H^{1s3d,\vec{i}_c}_{\sigma\vec{k}_2\vec{k}_{N_k}} \\ \vdots & \vdots & \ddots & \vdots \\ H^{1s3d,\vec{i}_c}_{\sigma\vec{k}_{N_k}\vec{k}_1} & H^{1s3d,\vec{i}_c}_{\sigma\vec{k}_{N_k}\vec{k}_2} & \cdots & H^{1s3d,\vec{i}_c}_{\sigma\vec{k}_{N_k}\vec{k}_{N_k}} \end{pmatrix} \tag{2.63}$$

where

$$\left(H^{1s3d,\vec{i}_c}_{\sigma\vec{k}_h\vec{k}_{h'}}\right)_{2(j-1)+\xi,2(j'-1)+\xi'} = U_c e^{-i(\vec{k}_h-\vec{k}_{h'})\cdot\vec{i}_c}e^{-i(\vec{K}_j-\vec{K}_{j'})\cdot\vec{i}_c}\delta_{\xi\xi'}. \tag{2.64}$$

where $j, j' = 1, 2, ..., 8$ and $\xi, \xi' = 1, 2$.

Eigenvectors and eigenvalues are found for the $2N^2 \times 2N^2$ Hamiltonian matrix, $H^{tot}_{\sigma} = H^{3d,nonint}_{\sigma} + H^{\mathrm{3d3d,HF}}_{\sigma} + H^{1s3d,\vec{i}_c}_{\sigma}$ for each spin direction σ with the core hole potential, through Hartree-Fock iterative calculations. When necessary, Pullay mixing method is used to have a convergence. The eigenstates and energies in the absence of the core hole for the same cluster are found by setting $U_c = 0$ and repeating Hartree-Fock iterative calculations. The two sets of eigenstates and eigenvalues give $\varepsilon_{\sigma l\vec{k}}$, $\alpha_{\sigma,\vec{k}+\vec{K},\xi l\vec{k}}$, $\varepsilon_{\sigma m}$, and $\gamma_{\sigma,\vec{k}+\vec{K},\xi m}$, which are fed into the RIXS formula.

APPENDIX

2.B RIXS Formula Derivation

As explained in the text, the following formula is obtained from the Kramers-Heisenberg formula, Equation (2.24), in the limit of completely localized core hole,

$$I \propto \sum_f \left| \sum_{\vec{R}} \sum_{\vec{d}} \sum_{n^{\vec{R}+\vec{d}}} \frac{\langle f|\mathcal{D}'^{\dagger}|n^{\vec{R}+\vec{d}}\rangle\langle n^{\vec{R}+\vec{d}}|\mathcal{D}|g\rangle}{E_g + \hbar\omega_{\vec{k}} - E_{n^{\vec{d}}} + i\Gamma_{n^{\vec{d}}}} \right|^2 \delta(E_f + \hbar\omega_{\vec{k}'} - E_g - \hbar\omega_{\vec{k}}), \quad (2.65)$$

where $|n^{\vec{R}+\vec{d}}\rangle$ represents the intermediate energy eigenstate with the core hole at a site $\vec{R}+\vec{d}$ within the unit cell at a lattice point $\vec{R}$. Further applying dipole approximation to the RIXS transition operator, following expression is obtained,

$$\begin{aligned} \langle f|\mathcal{D}'^{\dagger}|n^{\vec{R}+\vec{d}}\rangle\langle n^{\vec{R}+\vec{d}}|\mathcal{D}|g\rangle = e^{-i(\vec{k}'-\vec{k})\cdot(\vec{R}+\vec{d})} \times \\ \vec{\epsilon}' \cdot \langle f|\vec{r} - (\vec{R}+\vec{d})|n^{\vec{R}+\vec{d}}\rangle\vec{\epsilon}\cdot\langle n^{\vec{R}+\vec{d}}|\vec{r} - (\vec{R}+\vec{d})|g\rangle \end{aligned} \quad (2.66)$$

Two many-body states $|\Psi^0\rangle$ and $|\Psi^{-\vec{R}}\rangle$ with total momentum $\hbar\vec{\kappa}$ with identical wave functions in two different coordinate systems, coordinate for $|\Psi^{-\vec{R}}\rangle$ is shifted with respect to the coordinate for $|\Psi^0\rangle$ by $-\vec{R}$, are related to each other by a phase factor, $|\Psi^{-\vec{R}}\rangle = e^{i\vec{\kappa}\cdot\vec{R}}|\Psi^0\rangle$. Assuming that $|g\rangle$ and $|f\rangle$ have net momenta of zero and $\hbar\vec{k}_f$, following relations are obtained,

$$\begin{aligned} \langle f|\vec{r} - (\vec{R}+\vec{d})|n^{\vec{R}+\vec{d}}\rangle &= e^{-i\vec{k}_f\cdot\vec{R}}\langle f|\vec{r} - \vec{d}|n^{\vec{d}}\rangle \\ \langle n^{\vec{R}+\vec{d}}|\vec{r} - (\vec{R}+\vec{d})|g\rangle &= \langle n^{\vec{d}}|\vec{r} - \vec{d}|g\rangle \end{aligned} \quad (2.67)$$

Therefore, the sum over lattice point $\vec{R}$ for $e^{-i(\vec{k}'-\vec{k}+\vec{k}_f)\cdot\vec{R}}$ leads to the conservation of the crystal momentum $\delta(\vec{k}' - \vec{k} + \vec{k}_f + \vec{K})$, where $\vec{K}$ represents the reciprocal lattice vectors, and the following expression for the RIXS intensity,

$$\begin{aligned} I \propto \sum_{\vec{K}} \sum_f \left| \sum_{\vec{d}} \sum_{n^{\vec{d}}} \frac{e^{-i(\vec{k}'-\vec{k})\cdot\vec{d}}\vec{\epsilon}'\cdot\langle f|\vec{r} - \vec{d}|n^{\vec{d}}\rangle\vec{\epsilon}\cdot\langle n^{\vec{d}}|\vec{r} - \vec{d}|g\rangle}{E_g + \hbar\omega_{\vec{k}} - E_{n^{\vec{d}}} + i\Gamma_{n^{\vec{d}}}} \right|^2 \\ \delta(E_f + \hbar\omega_{\vec{k}'} - E_g - \hbar\omega_{\vec{k}})\delta(\vec{k}_f + \vec{k}' - \vec{k} + \vec{K}). \end{aligned} \quad (2.68)$$

By further neglecting a constant factor associated with the polarization vectors $\vec{\epsilon}'$ and $\vec{\epsilon}$ as well as the dipole moment between $4p$ and $1s$ wave functions, Equation (2.25) is obtained.

CHAPTER 3

EFFECTS OF RARE EARTH ION SIZE ON THE STABILITY OF THE COHERENT JAHN-TELLER DISTORTIONS IN UNDOPED PEROVSKITE MANGANITES

The work in this chapter was done in collaboration with Turab Lookman, Avadh Saxena, and Alan R. Bishop from Theoretical Division at Los Alamos National Laboratory, and Peter B. Littlewood from Physical Sciences and Engineering Division at Argonne National Laboratory, as well as Keun H. Ahn from Department of Physics at New Jersey Institute of Technology.

3.1 Introduction

Since the discovery of the colossal magnetoresistance effect, a lot of attention has focused on a class of materials known as perovskite manganites (von Helmolt et al. 1993; Jin et al. 1994; Salamon and Jaime 2001). During the last two decades, substantial progress has been made in the theory for perovskite manganites. Importance of the electron-lattice coupling was identified shortly after the discovery of colossal magnetoresistance effect (Millis et al. 1995; Röder et al. 1996; Millis et al. 1996). First-order character of the metal-insulator phase transition has been found from Monte Carlo simulations (Vergés et al. 2002). Mechanism for inhomogeneity and its relation to metal-insulator transition have been studied (Moreo et al. 1999). Effects of disorder have been investigated for doped manganites (Kumar and Majumdar 2006; Pradhan et al. 2007). The competition between short range super-exchange interaction and long range double exchange interaction has been analyzed for multiferroic undoped manganites (Salafranca and Brey 2006). Most recently, novel mechanisms for ferroelectricity, including electronic ferroelectricity, have been proposed for undoped manganites with E-type antiferromagnetic ordering (Sergienko et al.

2006; Yamauchi et al. 2008). These materials have the chemical formula in the form of $RE_{1-x}AK_x\mathrm{MnO}_3$, where RE and AK represent the rare earth and alkali metal elements, and have a perovskite structure. One of the major research themes for these materials is the relation between their physical properties and the average size of ions at the RE/AK site, often known as the chemical pressure effect. The size of the RE/AK ion is usually parameterized by a *tolerance factor* and one of the most important phase diagrams for these materials has been the one in the temperature versus tolerance factor plane for a fixed 30% ($x = 0.3$) doping ratio (Hwang et al. 1995). The RE/AK ions with size smaller than the space created by the surrounding MnO_6 octahedra induce buckling of the Mn-O-Mn bonds, observed through various structural refinement analyses.

To understand the effect of the chemical pressure, semi-classical theories (Millis et al. 1995; Röder et al. 1996; Millis et al. 1996; Moreo et al. 1999; Sergienko et al. 2006; Pradhan et al. 2007; Vergés et al. 2002; Salafranca and Brey 2006; Kumar and Majumdar 2006; Yamauchi et al. 2008) with quantum mechanical electrons coupled with the classical lattice through the Jahn-Teller (JT) interaction often present the phase diagram with one axis representing the ratio between the electron hopping energy and the JT energy gain. This ratio parameterizes the competition between the kinetic and potential energy in perovskite manganites. Theoretical phase diagrams from these approaches agree well with experimental phase diagrams, when this ratio is related to the Mn-O-Mn buckling distortion due to smaller RE/AK ions. However, whether this buckling distortion affects the electron hopping energy or the JT energy gain has been controversial. It is well known from experimental observations that there is a strong competition between the insulating phase with a coherent JT distortion and the metallic phase without such distortion (Salamon and Jaime 2001). So far, most of the attention has centered on the impact of the buckling on the metallic phase, in particular, the possible change in the effective Mn-O-Mn

electron hopping parameter and the band width (Hwang et al. 1995). At the same time, there has been a debate whether the variation of the hopping parameter due to the Mn-O-Mn bond angle change of several degrees would be significant enough to explain the observed metal-insulator transition (Dzero et al. 2000; Fernandez-Baca et al. 1998; Liu et al. 1999; Lynn et al. 1996; Radaelli et al. 1997). For instance, the spin wave stiffness, which depends sensitively on the electron hopping amplitude in double exchange model in ferromagnetic metallic phase, shows very little dependence on Mn-O-Mn bond angle (Lynn et al. 1996; Fernandez-Baca et al. 1998). A less studied effect of the Mn-O-Mn bond buckling, except for a few early efforts based on experimental data (Louca et al. 2001), is the possibility that the buckling distortion may significantly stabilize the insulating phase with a coherent JT distortion, by affecting the JT energy gain. The main goal of this chapter is to examine such a possibility with a simplified model of the perovskite manganites. To be specific, the interplay between the JT ordering and chemical pressure is analyzed for undoped perovskite manganites. With one localized e_g electron per site, the electronic degrees of freedom can be integrated out in undoped manganites (except for electronically ferroelectric undoped manganites postulated at low temperatures for very small RE ions), which allows us to adopt a purely classical model with the energy expressed in terms of lattice distortions only. The study on undoped manganites is merited, because they are not only parent compounds of doped perovskite manganites (Millis 1996), but also because one of the first multiferroic materials discovered is an undoped manganite, $TbMnO_3$, with a relatively small RE element (Kimura, Goto, Shintani, Ishizaka, Arima and Tokura 2003). Recently, electronic ferroelectricity has been also proposed for undoped perovskite manganites (Sergienko et al. 2006; Yamauchi et al. 2008). Therefore, the chemical pressure effect in undoped manganites presented in this chapter would also be relevant for future studies on how the multiferroic and electronically ferroelectric properties would appear in $RE MnO_3$ with small RE ions,

as well as how the chemical pressure affects the distorted insulating phase of doped manganites.

3.2 Model System and Energy Expression

A study of a two-dimensional (2D) model for the perovskite structure is presented, which incorporates both buckling and the JT distortions. A 2D perovskite structure shown in Figure 3.1 is then defined, which includes the following aspects of the three-dimensional (3D) perovskite structure for undoped manganites: (1) symmetry breaking distortion of O ions around Mn ion, (2) chemical pressure effect, which is the attraction of surrounding O ions toward the small RE ions, and (3) the rotation of O ions with alternating directions around Mn ions, which is, in effect, the buckling of Mn-O-Mn bonds. Although the 2D model inevitably misses some aspects of 3D lattice distortions, it is proposed that the correct order of magnitude estimation of energies associated with the chemical pressure and the JT effect can still be achieved. For example, the size of the 3D tetragonal JT distortion mode, commonly known as Q_3 mode (Ahn and Millis 2001) with Mn-O bond lengths changed in all directions, is typically about a third of the size of the planar JT distortion mode, commonly known as Q_2 mode with Mn-O bond lengths changed only in the plane. The Q_2 mode is kept in the 2D model, but the Q_3 mode is not. The error from omitting the Q_3 mode in the 2D model can be estimated by comparing actual 3D and the approximate 2D Jahn-Teller energy gain, proportional to $\sqrt{Q_2^2 + Q_3^2}$ and $\sqrt{Q_2^2}$, respectively, which are different by only about 10%. The Q_2 mode is expected to couple dominantly with the in-plane Mn-O-Mn bond buckling and the in-plane contraction of O ions surrounding a small RE ion. Therefore, it is expected that the 2D model would be sufficient for an order of magnitude estimation of the energy associated with the stabilization of the phase with the JT distortion by small RE ions.

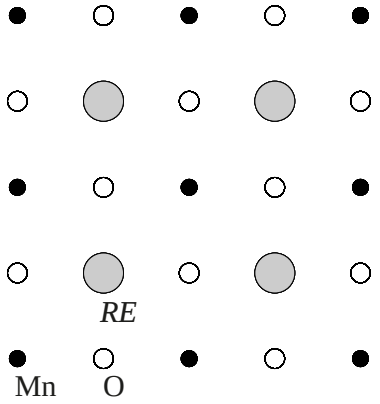

Figure 3.1 Two-dimensional model for the perovskite structure considered in the text.

For the 2D model of perovskite structure, the recently developed atomic scale description of lattice distortions (Ahn et al. 2003, 2004) is applied to describe the elastic energy of the system. In this approach, atomic scale modes of lattice distortions and their constraints are used instead of displacement variables. The structural motifs can be chosen in any convenient way as long as they have the symmetry of the crystal structure. Two "structural motifs" shown in Figure 3.2 are chosen: one consists of one Mn ion and four surrounding O ions and the other comprises one RE ion and four surrounding O ions. Further, ten symmetry modes for each motif are obtained, which are shown in Figure 3.3 for the MnO_4 motif.[1] Similar symmetry modes are defined for the REO_4 motif and are distinguished with primes on the symbols in this chapter. The modes defined for each plaquette on the lattice are constrained by each other because neighboring motifs share ions, which leads to constraint equations between the Fourier components of the modes. In terms of these twenty modes and constraint equations, any distortion of the 2D perovskite structure shown in Figure 3.1 can be described.

For the current study, since interest is in the ordered state, distortions with wavevectors $\vec{k} = (0, 0)$ and (π, π) are considered only. For these wavevectors, the

[1]The normalization factor is chosen in such a way that, for example, $e_3 = 2d_O$ if each O ion around Mn ion is displaced by d_O in the way shown in Figure 3.3.

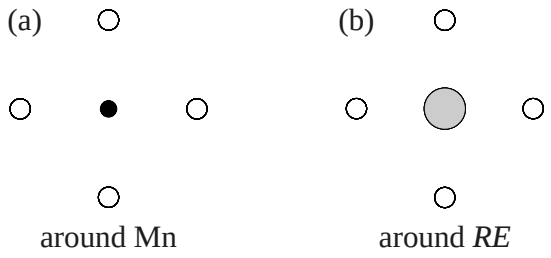

Figure 3.2 Two structural motifs chosen for the 2D structure shown in Figure 3.1.

constraint equations are as follows, where subscripts 0 and s are used to represent $\vec{k}$ = (0,0) and (π, π), respectively: $e_{10} = e'_{10}$, $e_{20} = e'_{20}$, $e_{30} = e'_{30}$, $s_{x0} = -s'_{x0}$, $s_{y0} = -s'_{y0}$, $e_{1s} = -e'_{2s}$, $e'_{1s} = -e_{2s}$, $s_{xs} = s_{ys} = s'_{xs} = s'_{ys} = 0$. Rest of the modes are unconstrained, particularly, e_{3s} and e'_{3s}. The search for the interplay between the staggered deviatoric distortion mode e_{3s} and the staggered rotation of O ions around Mn ion (or equivalently staggered Mn-O-Mn bond buckling mode) e'_{3s} is undertaken, where the latter is due to the compression $e'_{10} = e_{10}$ by small RE ions. Therefore, only the modes $e_{10} = e'_{10}$, $e_{20} = e'_{20}$, e_{3s}, and e'_{3s}, are shown in Figure 3.4. The uniform shear mode $e_{20} = e'_{20}$ is included because it is coupled to e'_{3s} through the JT term, as will be discussed later in this chapter.

Even though it is possible to analyze an energy expression including higher order symmetry-allowed anharmonic energy terms, such a method would generate many parameters and would make the model less predictive. Therefore, starting with a Keating model with a small number of parameters (Keating 1966; Littlewood 1986), the Keating model is mapped onto the approach based on the symmetry modes. In the Keating approach, the elastic energy is represented in terms of bond length and bond angle changes from equilibrium. For the 2D perovskite structure, the following set of Keating variables and harmonic moduli for each Mn ion are considered, as shown in Figure 3.5: δl_n (n = 1, 2, 3, 4) and modulus a_1 for Mn-O bond length change, $\delta\theta_n$ (n = 1, 2, 3, 4) and $b_1/4$ for 90° O-Mn-O bond angle change, δr_n (n = 1, 2, 3, 4) and a_2 for RE-O bond length change, and $\delta\varphi_n$ (n = 1, 2) and $b_2/4$ for 180°

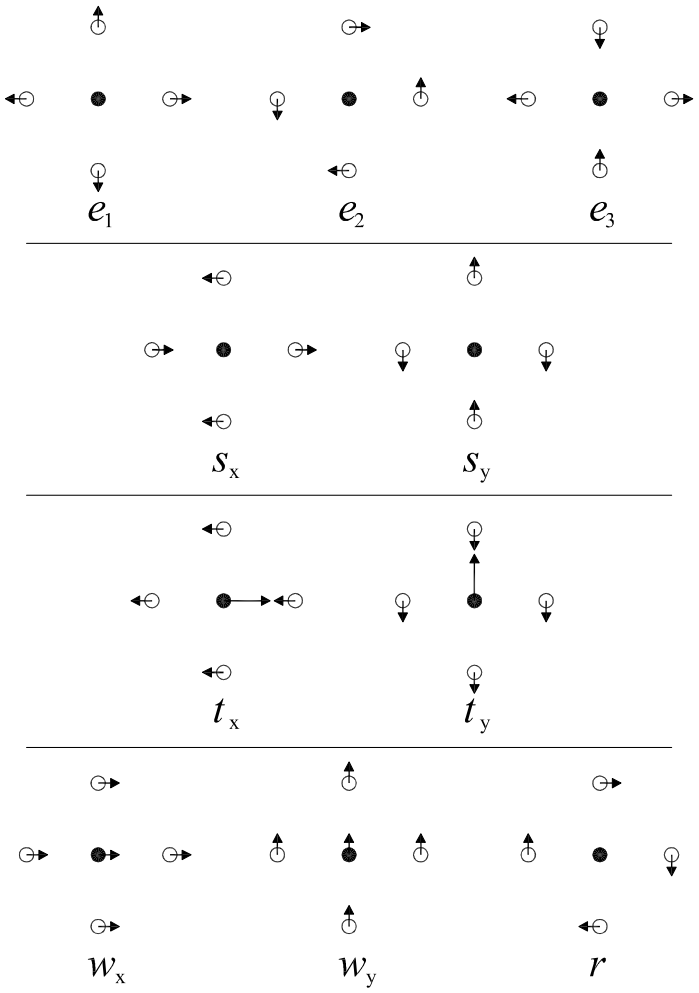

Figure 3.3 Distortion modes for the motif around the Mn ion in Figure 3.2. Similar distortion modes, e_1', e_2', e_3', s_x', s_y', t_x', t_y', w_x', w_y', and r' are defined for the motif around the RE ion.

Mn-O-Mn bond angle change. It should be noted that the MnO_4 motif is considered as relatively stiff compared to other components of the structure, so that $a_1 \gg a_2$ and $b_1 \gg b_2$.

Consider the following Keating elastic energy expression per Mn ion,

$$\begin{aligned} E_{\text{elastic}} &= \frac{1}{2}a_1 \sum_{n=1,2,3,4} (\delta l_n)^2 + \frac{1}{2}b_1 \sum_{n=1,2,3,4} (\delta\theta_n/2)^2 \\ &+ \frac{1}{2}a_2 \sum_{n=1,2,3,4} (\delta r_n)^2 + \frac{1}{2}b_2 \sum_{n=1,2} (\delta\varphi_n/2)^2. \end{aligned} \tag{3.1}$$

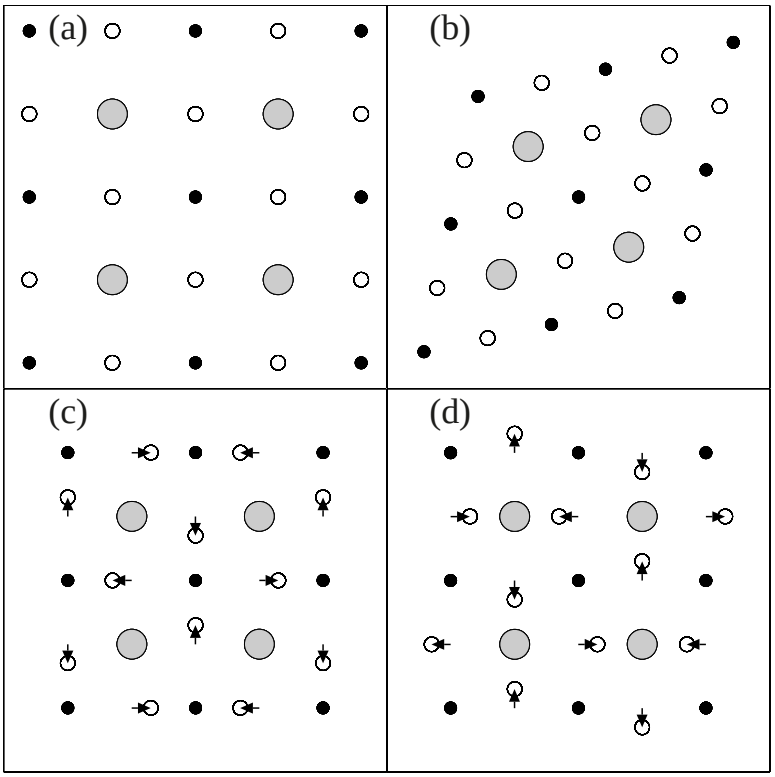

Figure 3.4 Four distortion modes considered in the current study: (a) uniform dilatation mode e_{10}, (b) uniform shear mode e_{20}, (c) staggered deviatoric mode e_{3s}, and (d) staggered buckling mode e'_{3s}. All figures are drawn for the positive values of the modes with the Mn site at the bottom left corner chosen as the origin.

The Keating variables are then expressed in terms of e_{10}, e_{20}, e_{3s} and e'_{3s}. For example, one obtains

$$\delta l_1 = \frac{\sqrt{(1+e_{10}+e_{3s})^2+(e_{20}+e'_{3s})^2}-1}{2}, \tag{3.2}$$

$$\delta\theta_1 = \tan^{-1}\left(\frac{e_{20}+e'_{3s}}{1+e_{10}+e_{3s}}\right)+\tan^{-1}\left(\frac{e_{20}-e'_{3s}}{1+e_{10}-e_{3s}}\right). \tag{3.3}$$

The Taylor expansion of E_{elastic} in terms of e_{10}, e_{20}, e_{3s} and e'_{3s} produces all the terms of any order. An approximation that b_2 is much smaller than other parameters is made, as mentioned above, and the terms with b_2 are dropped. All harmonic order terms are then kept and the cubic and quartic order terms that are responsible for the Mn-O-Mn bond buckling instability are selected, which are shown below as E_{har}, E_{cubic}, and E_{quartic}.

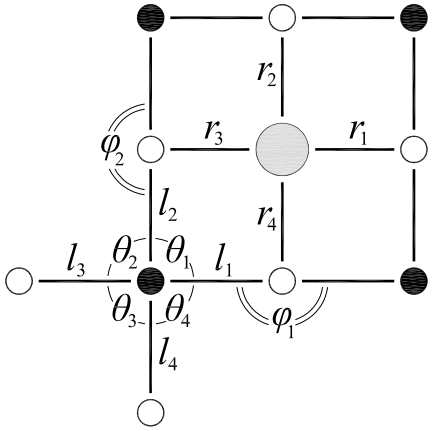

Figure 3.5 The Keating variables considered for each Mn ion. l_1, l_2, l_3, and l_4 represent the Mn-O bond lengths. θ_1, θ_2, θ_3, and θ_4 represent the O-Mn-O bond angles. r_1, r_2, r_3, and r_4 represent RE-O bond lengths. φ_1 and φ_2 indicate Mn-O-Mn bond angles.

Further, the JT energy per Mn ion $E_{\rm JT}$ is defined and the energy associated with the tolerance factor per Mn ion $E_{\rm tol}$ is as follows:

$$E_{\rm JT} = -\frac{\lambda}{2}|\delta l_1 + \delta l_3 - \delta l_2 - \delta l_4|, \tag{3.4}$$

$$E_{\rm tol} = \frac{\tilde{p}}{2}(\delta r_1 + \delta r_2 + \delta r_3 + \delta r_4), \tag{3.5}$$

where "chemical pressure" is defined as

$$\tilde{p} = C_1'(1 - t). \tag{3.6}$$

The parameter t is a two-dimensional analog of the tolerance factor for the 3D perovskite structure, and the coefficient C_1' represents the coupling between the average RE-O bond length and the tolerance factor t. The chemical pressure $\tilde{p}$ induces the shortening of the average RE-O bond length due to small RE ions. In addition, the JT distortion mode is defined as

$$e_{\rm JT} = (\delta l_1 + \delta l_3 - \delta l_2 - \delta l_4)/2, \tag{3.7}$$

which represents the anisotropic bond length change, similar to the JT distortion modes Q_2 and Q_3 for 3D perovskite manganites (Ahn and Millis 2001). As mentioned above, e_{JT} in the 2D model corresponds to Q_2 mode only and thus omitting the Q_3 mode. The expression $E_{\rm JT} = -\lambda|e_{\rm JT}|$ is based on the 3D JT energy $E_{\rm JT,3D} = -\lambda_Q\sqrt{Q_2^2+Q_3^2}$, which is obtained after minimizing JT electron-lattice coupling energy in manganites with respect to the e_g orbital state (Ahn and Millis 2001). In undoped manganites, Q_3/Q_2 is about 0.3 – 0.4 (Rodríguez-Carvajal et al. 1998; Balagurov et al. 2004), which allows an approximation $E_{\rm JT,3D} \approx -\lambda_Q|Q_2|[1+(Q_3/Q_2)^2/2]$. Further neglecting the small $(Q_3/Q_2)^2/2$ term of about 0.1, the 2D analog of the JT energy $E_{\rm JT}$ can be obtained with the 2D JT distortion $e_{\rm JT}$ corresponding to 3D JT distortion Q_2 except for a normalization factor difference.

Expressions $E_{\rm JT}$ and $E_{\rm tol}$ are expanded in the form of a Taylor series in e_{10}, e_{20}, e_{3s} and e'_{3s}. Only the leading order energy terms being kept, the total energy expression per Mn ion $E_{\rm tot}$ is given below.

$$E_{\rm tot} = E_{\rm har} + E_{\rm JT} + E_{\rm tol} + E_{\rm cubic} + E_{\rm quartic}, \tag{3.8}$$

$$E_{\rm har} = \frac{1}{2}(a_1+a_2)(e_{10})^2 + \frac{1}{2}(4b_1)(e_{20})^2 + \frac{1}{2}a_1e_{3s}^2 + \frac{1}{2}a_2(e'_{3s})^2, \tag{3.9}$$

$$E_{\rm JT} = -\lambda|e_{3s}+e_{20}e'_{3s}|, \tag{3.10}$$

$$E_{\rm tol} = \tilde{p}e_{10}, \tag{3.11}$$

$$E_{\rm cubic} = \frac{1}{2}a_1e_{10}(e'_{3s})^2, \tag{3.12}$$

$$E_{\rm quartic} = \frac{1}{4}\frac{a_1}{2}(e'_{3s})^4, \tag{3.13}$$

where the relation

$$e_{\rm JT} \approx e_{3s} + e_{20}e'_{3s} \tag{3.14}$$

is used for $E_{\rm JT}$. The physical origin of the coupling between e_{20} and e'_{3s} is important for the current study and is explained in more detail in Section 3.5.1.

3.3 Estimation of Parameters

In this section, the estimation of the parameters is described. The Mn-Mn distance before the distortion is chosen, which is around $u = 4$ Å, as 1. Therefore, e_{10}, e_{20}, e_{3s}, and e'_{3s} are unitless, and a_1, b_1, a_2, b_2, and λ have the unit of energy. The parameter a_1 can be estimated from the Mn-O bond stretching phonon mode energy, which is about 70 meV from optical measurements (Ahn and Millis 2001). From $\hbar\sqrt{2a_1/m_{\mathrm{O}}}$ = 70 meV with m_{O} the mass of the O ion, $a_1 \approx 150$ eV is obtained. From the elastic modulus b_1, c_{44} are estimated. From Darling et al. (1998), $c_{44} \approx 55$–60 GPa. The uniform shear mode e_{20} corresponds to the conventional $e_{xy}/2$ (Ashcroft and Mermin 1976). Using the identity 1 GPa Å^3 = 6.3 meV, it implies that $b_1 \approx 20$–25 eV. To estimate b_2, the results (Mirgorodsky and Smirnov 1993) for ReO_3 are used, which have no RE/AK ion and, therefore, $a_2 = 0$ and the buckling of Re-O-Re bond depends only on b_2. According to the analysis in Mirgorodsky and Smirnov (1993), the oxygen oscillation along Re-O-Re direction has the angular frequency $\omega_o^x = 905$ cm^{-1}, whereas the oscillation perpendicular to Re-O-Re direction has the angular frequency $\omega_o^y = 30$ cm^{-1}, from which $b_2/a_1 = (\omega_o^y/\omega_o^x)^2/2 \approx 0.5 \times 10^{-3}$ can be estimated. Similar order of magnitude for b_2 in manganites can be expected, order of $10^{-3}a_1$, for example 0.2 eV, which is negligible compared to other parameter values, while it justifies neglecting the terms with b_2 as mentioned above. Various probes, such as neutron or optical spectroscopy, indicate the buckling mode frequency in manganites of about 35–50 meV (Zhang et al. 2001). From the analysis of (π, π) phonon mode for this model, the frequency of buckling mode $\omega_{\mathrm{bk}} = \sqrt{(2a_2 + 4b_2)/m_{\mathrm{O}}}$ is then obtained. Therefore, one arrives to $a_2 \approx 30$–80 eV. For the estimation of λ, the JT energy gain for the 2D model is matched with that for the 3D model to ensure that the 2D model represents the energy scale of the 3D materials correctly. For the 2D model $\Delta E_{\mathrm{JT}} = -\lambda^2/(2a_1)$. For the 3D model in Ahn and Millis (2000, 2001), $\Delta E_{\mathrm{JT}} \approx -0.39$ eV, and therefore, $\lambda \approx 10.8$ eV is obtained.

3.4 Interplay Between Mn-O-Mn Bond Buckling and the Jahn-Teller Distortions

3.4.1 Buckling Instability Without the Jahn-Teller Term

The condition for the buckling instability is found to be without the effect of the JT energy term $E_{\rm JT}$. A perturbative approach is further applied, rather than an attempt to solve high order polynomial equations. By minimizing $E_{\rm har} + E_{\rm tol}$, one obtains

$$(e_{10})^{\rm min,*} = -\frac{\tilde{p}}{a_1 + a_2}, \tag{3.15}$$

where the superscript * indicates that the JT term is not yet taken into consideration. This isotropic compression of the MnO_4 motif renormalizes the coefficient of the $(e'_{3s})^2$ term through the $E_{\rm cubic}$ term. From this, the critical condition for the buckling instability is then obtained,

$$\tilde{p}^*_c = \frac{a_2}{a_1}(a_1 + a_2), \tag{3.16}$$

$$(e_{10})^{\rm min,*}_c = -\frac{a_2}{a_1}. \tag{3.17}$$

If $\tilde{p} > \tilde{p}^*_c$, Mn-O-Mn bond buckling occurs and the quartic order term, $E_{\rm quartic}$, should be considered for the equilibrium e'_{3s},

$$|(e'_{3s})^{\rm min,*}| = \sqrt{\frac{2}{a_1 + a_2}}\sqrt{\tilde{p} - \tilde{p}^*_c} \tag{3.18}$$

$$= \sqrt{2}\sqrt{(e_{10})^{\rm min,*}_c - (e_{10})^{\rm min,*}}. \tag{3.19}$$

The minimized $E_{\rm tot}$ without the $E_{\rm JT}$ term is given by

$$E^{\rm min,*}_{\rm tot} = -\frac{\tilde{p}^2}{2(a_1 + a_2)} - \frac{a_1}{2}\left(\frac{\tilde{p}}{a_1 + a_2} - \frac{a_2}{a_1}\right)^2. \tag{3.20}$$

3.4.2 Buckling Instability with the Jahn-Teller Term

It is now examined, on how the JT energy term $E_{\rm JT}$ alters the buckling instability. From $E_{\rm har} + E_{\rm tol} + E_{\rm JT}$, one obtains

$$(e_{10})^{\rm min} = -\frac{\tilde{p}}{a_1 + a_2}, \tag{3.21}$$

$$(e_{3s})^{\min} = \frac{\lambda}{a_1}, \tag{3.22}$$

where the $(e_{3s})^{\min} > 0$ case is considered only. The buckling instability is found from the second order terms in e_{20} and e'_{3s} in $E_{\rm tot}$:

$$\frac{1}{2}(4b_1)(e_{20})^2 + \frac{1}{2}[a_2 + a_1(e_{10})^{\min}](e'_{3s})^2 - \lambda e_{20} e'_{3s}, \tag{3.23}$$

where it is assumed $(e_{3s})^{\min} + e_{20}e'_{3s} > 0$. From the condition $4b_1[a_2 + a_1(e_{10})^{\min}] < \lambda^2$, one obtains the critical condition

$$\tilde{p}_c = \frac{a_2}{a_1}(a_1 + a_2) - \frac{\lambda^2}{4b_1 a_1}(a_1 + a_2) \tag{3.24}$$

and the buckling distortion occurs for $\tilde{p} > \tilde{p}_c$. Comparing with $\tilde{p}^*_c$ in Equation (3.16), it is easy to find that the JT energy makes buckling more likely. After this buckling instability, the $E_{\rm quartic}$ term should be included to find the equilibrium result. For this, $E_{\rm tot}$ is first minimized with respect to the shear distortion e_{20} to obtain

$$(e_{20})^{\min} = \frac{\lambda}{4b_1} e'_{3s}. \tag{3.25}$$

Inserting this back, an energy expression for $E_{\rm tot}$ is then obtained in terms of e'_{3s} only, which gives the equilibrium buckling distortion and the minimum energy,

$$(e'_{3s})^{\min} = \sqrt{\frac{2}{a_1 + a_2}}\sqrt{\tilde{p} - \tilde{p}_c}, \tag{3.26}$$

$$\begin{aligned} E_{\rm tot}^{\min} &= -\frac{\tilde{p}^2}{2(a_1 + a_2)} - \frac{\lambda^2}{2a_1} \\ &\quad -\frac{a_1}{2}\left(\frac{\tilde{p}}{a_1 + a_2} - \frac{a_2}{a_1} + \frac{\lambda^2}{4b_1 a_1}\right)^2. \end{aligned} \tag{3.27}$$

Therefore, the energy gain due to the JT energy term is given by

$$\Delta E_{\rm JT} = -\frac{\lambda^2}{2a_1} - \frac{(\tilde{p} - \tilde{p}^*_c)\lambda^2}{4(a_1 + a_2)b_1} \tag{3.28}$$

up to order λ^2. The second term corresponds to the part of $\Delta E_{\rm JT}$ which depends on the size of RE ion, or $\tilde{p}$. This result shows that the small rare earth ion, or large chemical pressure, stabilizes the JT distortion.

3.5 Comparison with Experiments

Comparisons between the model and experimental results are further presented. In Section 3.5.1, the simultaneous appearance of the uniform shear distortion and the long range JT distortion observed in undoped manganites (Rodríguez-Carvajal et al. 1998) are explained. In Section 3.5.2, the changes in the JT ordering temperature $T_{\rm JT}$ are estimated among $LaMnO_3$, $PrMnO_3$, and $NdMnO_3$, and then compared with the experiments. In Section 3.5.3, the ratios between different distortion modes are calculated and compared with the experimental data for $LaMnO_3$, $PrMnO_3$, $NdMnO_3$, and other undoped manganites with even smaller RE ions.

3.5.1 Appearance of Uniform Shear Distortion Below the Jahn-Teller Ordering Temperature

Experimental data in Rodríguez-Carvajal et al. (1998), Balagurov et al. (2004), and Sánchez et al. (2002) show that the difference between the lattice constants a and b along the diagonal directions in the plane appears simultaneously with the long range JT distortion below $T_{\rm JT}$ for $LaMnO_3$, $PrMnO_3$, and $NdMnO_3$. This distortion corresponds to the uniform shear distortion in the model, related by $e_{20} = (b-a)/(2\sqrt{2}u)$ with $u = 4$ Å. The coupling between the JT distortion and the uniform shear distortion is then analyzed, which is important for the stabilization of JT ordered state by the chemical pressure. In this model, such coupling originates from the term $e_{20}e'_{3s}$ in $e_{\rm JT}$ in Equation (3.14) or in $E_{\rm JT}$ in Equation (3.10), which can be understood as follows. Applying a positive e_{20} shear distortion to the lattice is initially considered, as shown in Figure 3.6 by the axis of elongation and compression along 45° and 135°, respectively. Such uniform shear distortion makes the Mn-O bond lengths either longer or shorter depending on whether the direction of the bond is closer to the orientation of elongation (45°) or compression (135°), except for the bonds with directions right between the two directions. If the system *does not* have (π, π) buckling, as shown by the *thin* solid lines in Figure 3.6, all Mn-O bonds

make equal angles from the axis of elongation/compression, and therefore e_{20} shear distortion keeps all Mn-O bond lengths equal. This implies that e_{20} distortion alone does not contribute to the JT distortion or JT energy gain. In contrast, if the system has a buckling distortion e'_{3s} with a wave vector $\vec{k} = (\pi, \pi)$, as shown by the *thick* solid lines in Figure 3.6, the e_{20} shear distortion elongates Mn-O bonds marked with l and shortens Mn-O bonds marked with s, depending on whether the bond direction is closer to the axis of elongation or the axis of compression, which results in the JT distortion $e_{\rm JT}$ with a wave vector $\vec{k} = (\pi, \pi)$. If this extra JT distortion is in the same [opposite] phase as [to] the deviatoric e_{3s} distortion, in other words, if $e_{20}e'_{3s}$ and e_{3s} have the same [opposite] sign, this extra JT distortion increases [decreases] the net JT distortion, which explains the expression for $E_{\rm JT}$ in Equation (3.10) or $e_{\rm JT}$ in Equation (3.14). It is emphasized here that the extra JT energy gain occurs only when the e_2, e_3 and e'_3 distortions are in the right phase with respect to each other. Experiments (Rodríguez-Carvajal et al. 1998) show that the (π, π) Mn-O-Mn bond buckling persists even above $T_{\rm JT}$ without much change in size. However, above $T_{\rm JT}$, the coherent e_3 distortion does not exist, and therefore the extra JT distortion due to the uniform e_{20} distortion in the presence of staggered buckling distortion would increase the JT energy gain in some regions and decrease the JT energy gain in other regions, and does not change the net JT energy. In other words, the energy gain due to the cooperative effect between e_3, e'_3, and e_2 does not exist at $T > T_{\rm JT}$. Therefore it is expected that the e_{20} mode does not exist above $T_{\rm JT}$ and appears simultaneously with the long range JT ordering, consistent with the experimental results.

3.5.2 Jahn-Teller Ordering Temperature and Its Variation Among $LaMnO_3$, $PrMnO_3$, and $NdMnO_3$

It is reported (Kimura, Ishihara, Shintani, Arima, Takahashi, Ishizaka and Tokura 2003; Sánchez et al. 2002) that $T_{\rm JT}$ changes from 750 K for $LaMnO_3$ to 1050 K

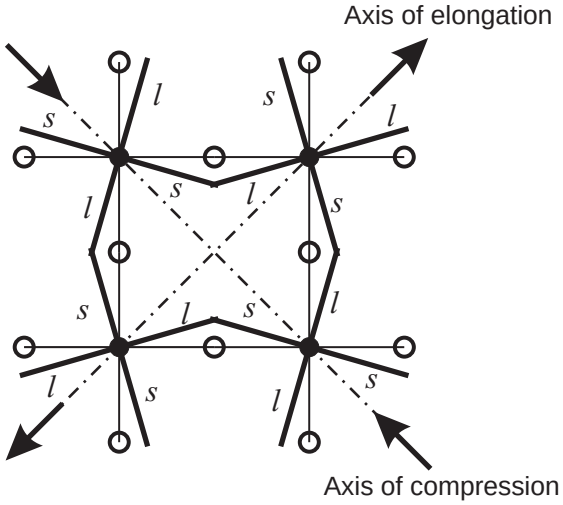

Figure 3.6 Superposition of (π,π) buckling e'_{3s} and uniform shear distortion e_{20} effectively generates the extra (π,π) JT distortion of Mn-O bond lengths, as indicated by the s and l for the shortened and elongated bonds, which is responsible for the $e_{20}e'_{3s}$ coupling within $e_{\rm JT}$ and the JT coupling $E_{\rm JT}$. In the (π,π) JT ordered state, this adds up to the e_{3s} deviatoric mode if e_{3s} and $e_{20}e'_{3s}$ have the same sign. This mechanism is responsible for the appearance of the uniform shear distortion below the JT ordering temperature, as explained in Section3.5.1. The extra JT energy gain for the buckled lattice is responsible for the increase in $T_{\rm JT}$ in REMnO$_3$ with small RE ions, as explained in Section 3.5.2.

for PrMnO$_3$, and further to 1100 K for NdMnO$_3$, that is, by about $\Delta T_{\rm JT}({\rm Pr}) =$ 300 K and $\Delta T_{\rm JT}({\rm Nd}) = 350$ K relative to LaMnO$_3$ respectively, where $\Delta T_{\rm JT}(RE) = T_{\rm JT}(RE{\rm MnO_3}) - T_{\rm JT}({\rm LaMnO_3})$. The term $\Delta T_{\rm JT}(RE)$ is further estimated from the model to understand how such a drastic change of the JT ordering temperature can occur by the increase in chemical pressure.

The term $E_{\rm tot}^{\rm min}$ in Equation (3.27) is rewritten for $\tilde{p} > \tilde{p}_c$ as follows.

$$E_{\rm tot}^{\rm min} = -\frac{\tilde{p}^2}{2(a_1+a_2)} - \frac{\lambda^2}{2a_1} - \frac{a_1(\tilde{p}-\tilde{p}_c)^2}{2(a_1+a_2)^2}, \tag{3.29}$$

where

$$\tilde{p}_c = \tilde{p}_c^* - \delta\tilde{p}_c, \tag{3.30}$$

$$\delta\tilde{p}_c = \frac{\lambda^2}{4b_1a_1}(a_1+a_2), \tag{3.31}$$

and $\tilde{p}_c^*$ represents the critical chemical pressure without the JT energy term. Since $\delta\tilde{p}_c$, the change in the critical chemical pressure due to the $E_{\rm JT}$ term, is small relative to $\tilde{p}-\tilde{p}_c^*$, with $\delta\tilde{p}_c/(\tilde{p}-\tilde{p}_c^*) \approx 0.3$ for parameter values in Section 3.3, the terms linear in $\delta\tilde{p}_c$ are kept only and then rewritten according to the origin of each term as follows.

$$
\begin{aligned}
E_{\rm tot}^{\rm min} &\approx E_{\rm comp}^{\rm min} + E_{\rm JT}^{\rm min} + E_{\rm bk}^{\rm min} + E_{\rm bk,JT,sh}^{\rm min}, && (3.32)\\
E_{\rm comp}^{\rm min} &= -\frac{1}{2}\frac{\tilde{p}^2}{a_1+a_2}, && (3.33)\\
E_{\rm JT}^{\rm min} &= -\frac{1}{2}\frac{\lambda^2}{a_1}, && (3.34)\\
E_{\rm bk}^{\rm min} &= -\frac{1}{2}\frac{a_1}{(a_1+a_2)^2}\left(\tilde{p}-\tilde{p}_c^*\right)^2, && (3.35)\\
E_{\rm bk,JT,sh}^{\rm min} &= -\frac{a_1}{(a_1+a_2)^2}\left(\tilde{p}-\tilde{p}_c^*\right)\delta\tilde{p}_c,\\
&= -\frac{\lambda^2}{4b_1(a_1+a_2)}(\tilde{p}-\tilde{p}_c^*). && (3.36)
\end{aligned}
$$

The first three terms, $E_{\rm comp}^{\rm min}$, $E_{\rm JT}^{\rm min}$, and $E_{\rm bk}^{\rm min}$, represent the energy terms purely due to compression, JT distortion, and buckling, respectively. The fourth term is the energy due to the coherent buckling, JT and shear distortions, indicated by its dependence on $\tilde{p}-\tilde{p}_c^*$, λ and b_1, which gives extra stability to the JT ordering due to the chemical pressure.

To estimate $T_{\rm JT}$, a high temperature state with random JT distortions must be considered, for which the energy can be written in a similar way as Equation (3.32) except for the absence of the fourth term due to the lack of coherence among distortions as explained in Section 3.5.1,

$$E_{\rm tot}^{\rm ran} = E_{\rm comp}^{\rm ran} + E_{\rm JT}^{\rm ran} + E_{\rm bk}^{\rm ran}. \qquad (3.37)$$

It is expected that $E_{\rm comp}^{\rm ran} \approx E_{\rm comp}^{\rm min}$ and $E_{\rm bk}^{\rm ran} \approx E_{\rm bk}^{\rm min}$, since the unit cell volume and buckling angle do not change very much as the temperature crosses $T_{\rm JT}$ (Rodríguez-Carvajal et al. 1998). Therefore, the energy difference between JT ordered and JT disordered state is

$$E_{\rm tot}^{\rm ran} - E_{\rm tot}^{\rm min} \approx E_{\rm JT}^{\rm ran} - E_{\rm JT}^{\rm min} - E_{\rm bk,JT,sh}^{\rm min}. \qquad (3.38)$$

It is important to verify that this model gives the correct order of magnitude of $T_{\rm JT}$ itself. An order of magnitude estimate for $T_{\rm JT}$ can be made from the energy difference between two different JT ordered states, one the most favored state and the other relatively unfavored state. The most favored state is that with the JT distortion of $\vec{k} = (\pi, \pi)$ considered so far in this chapter and has the JT energy of $E_{\rm JT}^{\rm min} = -\lambda^2/(2a_1)$. A state with the same size of JT distortion e_3 is chosen but with a wave vector $\vec{k} = (0, 0)$, as a relatively unfavored state, with energy $E_{\rm JT}^{\rm unif} = -\lambda^2/[2(a_1 + a_2)]$. Using the estimated parameter values, $a_1 = 150$ eV, $a_2 =$ 30–80 eV, $\lambda = 10.8$ eV, $E_{\rm JT}^{\rm unif} - E_{\rm JT}^{\rm min} \approx$ 600–1300 K are then obtained, which have the same order of magnitude, as the experimentally observed $T_{\rm JT}$ in the range of 750–1100 K.

For the change in $T_{\rm JT}$ between $LaMnO_3$ and REMnO$_3$ (RE=Pr, Nd), the only term in Equation (3.38) which changes with the RE ion size is $-E_{\rm bk,JT,shear}^{\rm min}$. Therefore, the JT ordering temperature variation between $LaMnO_3$ and REMnO$_3$ can be related to $-E_{\rm bk,JT,sh}^{\rm min}(RE{\rm MnO_3}) + E_{\rm bk,JT,sh}^{\rm min}({\rm LaMnO_3})$ within a factor of the order of one. Further, $E_{\rm bk,JT,sh}^{\rm min}$ is expressed in terms of $(e'_{3s})^{\rm min}$,

$$E_{\rm bk,JT,sh}^{\rm min} = -\frac{1}{2}\frac{\lambda^2}{4b_1}[(e'_{3s})^{\rm min}]^2. \tag{3.39}$$

According to the experimental data (Kimura, Ishihara, Shintani, Arima, Takahashi, Ishizaka and Tokura 2003; Rodríguez-Carvajal et al. 1998; Sánchez et al. 2002; Balagurov et al. 2004), the Mn-O-Mn bond angle is 155.1° for $LaMnO_3$, 150.5° for $PrMnO_3$, and 149.8° for $NdMnO_3$, which corresponds to $(e'_{3s})^{\rm min}$ of 0.217, 0.257, and 0.264, respectively. These distortions, along with parameter values $\lambda = 10.8$ eV and $b_1 =$ 20–25 eV, result in $-E_{\rm bk,JT,sh}^{\rm min}(RE{\rm MnO_3}) + E_{\rm bk,JT,sh}^{\rm min}({\rm LaMnO_3})$ of 11–14 meV $\approx$ 130–160 K for RE=Pr and 12–16 meV $\approx$ 140–190 K for RE=Nd. From a classical Monte Carlo simulation for the double-well potential model in Ahn et al. (2003), it has been found that the structural ordering temperature is

about twice the energy difference between the distorted ground state and undistorted high energy state.[2] Although such a relation would depend on the details of the model, if a similar situation in the current model is assumed, the JT ordering temperature variation can be estimated as twice the energy difference, therefore, $T_{\rm JT}(\mathrm{NdMnO_3}) - T_{\rm JT}(\mathrm{LaMnO_3}) \approx 2 \times [-E^{\rm min}_{\rm bk,JT,sh}(\mathrm{NdMnO_3}) + E^{\rm min}_{\rm bk,JT,sh}(\mathrm{LaMnO_3})] =$ 300–375 K, which agrees well with the experimental change in $T_{\rm JT}$, 350 K. Similar analysis for $\mathrm{PrMnO_3}$ leads to $T_{\rm JT}(\mathrm{PrMnO_3}) - T_{\rm JT}(\mathrm{LaMnO_3}) \approx$ 255–320 K, which agrees well with the experimental value of 300 K.

This agreement shows that indeed the JT ordered state is more stabilized when the buckling increases for smaller RE ions for undoped compounds. The relatively large increase in the JT ordering temperature, both in theory and experimental data, shows that the interplay between the RE ion size and the JT distortion is significant, and should be taken into account to explain the well-known temperature-tolerance factor phase diagram of both undoped and doped perovskite manganites.

3.5.3 Relation Between Shear, Buckling, and Deviatoric Distortion and Comparison for Other Undoped Manganites

Equations (3.22) and (3.25) imply that the following quantities remain constant regardless of the variation in chemical pressure:

$$(e_{3s})^{\rm min} = \frac{\lambda}{a_1}, \tag{3.40}$$

$$\frac{(e_{20})^{\rm min}}{(e'_{3s})^{\rm min}} = \frac{\lambda}{4b_1}, \tag{3.41}$$

$$\frac{(e_{20})^{\rm min}}{(e_{3s})^{\rm min}(e'_{3s})^{\rm min}} = \frac{a_1}{4b_1}. \tag{3.42}$$

These quantities are calculated from the experimental data for $\mathrm{LaMnO_3}$, $\mathrm{PrMnO_3}$, and $\mathrm{NdMnO_3}$, and in turn present the results shown in Table 3.1, in which the

[2]Classical Monte Carlo simulations is carried out with the same energy expression and parameter values used for the results in Figure 3 in Ahn et al. (2003). Further, the structural phase transition temperature is about 0.15, which is about twice the depth of the potential well 0.08.

relation between the distortion variables in the model and experimental parameters is also shown, while the estimate of $T_{\rm JT}$ and $\Delta T_{\rm JT}$ is obtained in Section 3.5.2. The results show that $(e_{3s})^{\rm min}$, $(e_{20})^{\rm min}/(e'_{3s})^{\rm min}$, and $(e_{20})^{\rm min}/[(e_{3s})^{\rm min}(e'_{3s})^{\rm min}]$ agree well with theoretical estimates obtained from the parameters in Section 3.3, and vary 7%, 29%, and 32%, respectively, smaller than up to 41% changes in $(e_{20})^{\rm min}$ and $(e'_{3s})^{\rm min}$. The results underscore the strong coupling between these distortions, in particular, the important role played by the uniform shear distortion in connecting the JT and buckling distortions, an aspect neglected in the literature so far.

The analysis to undoped perovskite manganites is further extended with even smaller RE ions. The results are summarized in Figure 3.7, along with values from available experimental data. Figure 3.7(a) shows the JT ordering temperature variation with respect to $LaMnO_3$ from the theory along with measured $T_{\rm JT}$ for $LaMnO_3$, $PrMnO_3$, and $NdMnO_3$, which indicates rapid increase of the JT energy gain as the RE size becomes smaller. Figure 3.7(b) shows that the ratio e_{20}/e'_{3s} from experimental data remains relatively close to the range of theoretical constant ratios of $\lambda/(4b_1)$. Explanation for the deviation from theoretically estimated constant for the whole range of RE ions may require higher order expansions of the energy expression. Figure 3.7(c) shows $e_{\rm JT}$ from experimental data and theory. For the experimental data, $e_{\rm JT}$ is calculated from $(l-s)/u$, where l and s are in-plane long and short Mn-O bond lengths, as in Table I. Theoretical range of $e_{\rm JT}$ versus e'_{3s} is from $e_{\rm JT} \approx e_{3s} + e_{20}e'_{3s}$ with $e_{3s} \approx \lambda/a_1$ and $e_{20} \approx e'_{3s}\lambda/(4b_1)$. Both theory and experiment consistently show an overall increase of $e_{\rm JT}$ as Mn-O-Mn bond buckling increases.

3.6 Discussion on How to Extend the Model to Doped Manganites and Electronically Ferroelectric Undoped Manganites

Although primary focus in this chapter is the high temperature JT structural phase transition in undoped perovskite manganites, it is briefly commented on in this sec-

Table 3.1 Parameters from Experimental Data and Comparison with Theoretical Estimates

Parameters	Experimental data			Theoretical estimates
	$LaMnO_3$	$PrMnO_3$	$NdMnO_3$	
Lattice constant, a	5.54 Å	5.45 Å	5.41 Å	
Lattice constant, b	5.75 Å	5.81 Å	5.73 Å	
Long Mn-O bond length within ab plane, l	2.18 Å	2.21 Å	2.20 Å	
Short Mn-O bond length within ab plane, s	1.91 Å	1.91 Å	1.90 Å	
Mn-O-Mn bond angle within ab plane, φ	155.1°	150.5°	149.8°	
Mn-Mn distance with e_{10} only, $(a+b)/(2\sqrt{2})$	3.99 Å	3.98 Å	3.94 Å	Compressed from $u \approx 4$ Å
$e_{20} = (b-a)/(2\sqrt{2}u)$	0.0186	0.0322	0.0280	
$e'_{3s} = (\pi - \varphi)/2$	0.217	0.257	0.264	
e_{20}/e'_{3s}	0.086	0.125	0.106	$\lambda/(4b_1) = 0.108$–0.135
$e_{\rm JT} = (l-s)/u$	0.0678	0.0753	0.0750	
$e_{3s} \approx e_{\rm JT} - e_{20}e'_{3s}$	0.0637	0.0670	0.0676	$\lambda/a_1 = 0.072$
$e_{20}/(e_{3s}e'_{3s})$	1.35	1.86	1.57	$a_1/(4b_1) = 1.5$–1.9
$T_{\rm JT}$	750 K	1050 K	1100 K	$E_{\rm JT}^{\rm unif} - E_{\rm JT}^{\rm min} = 600$–$1300$ K
$\Delta T_{\rm JT}$(Pr)=$T_{\rm JT}(PrMnO_3) - T_{\rm JT}(LaMnO_3)$		300 K		$-2\Delta E_{\rm bk,JT,sh}^{\rm min} = 255$–$320$ K
$\Delta T_{\rm JT}$(Nd)=$T_{\rm JT}(NdMnO_3) - T_{\rm JT}(LaMnO_3)$			350 K	$-2\Delta E_{\rm bk,JT,sh}^{\rm min} = 300$–$375$ K

Experimental data for the lattice constants, bond lengths, and bond angles for $LaMnO_3$, $PrMnO_3$ and $NdMnO_3$ are from Rodríguez-Carvajal et al. (1998), Balagurov et al. (2004), Sánchez et al. (2002), and Liu et al. (1996), measured at room temperature.

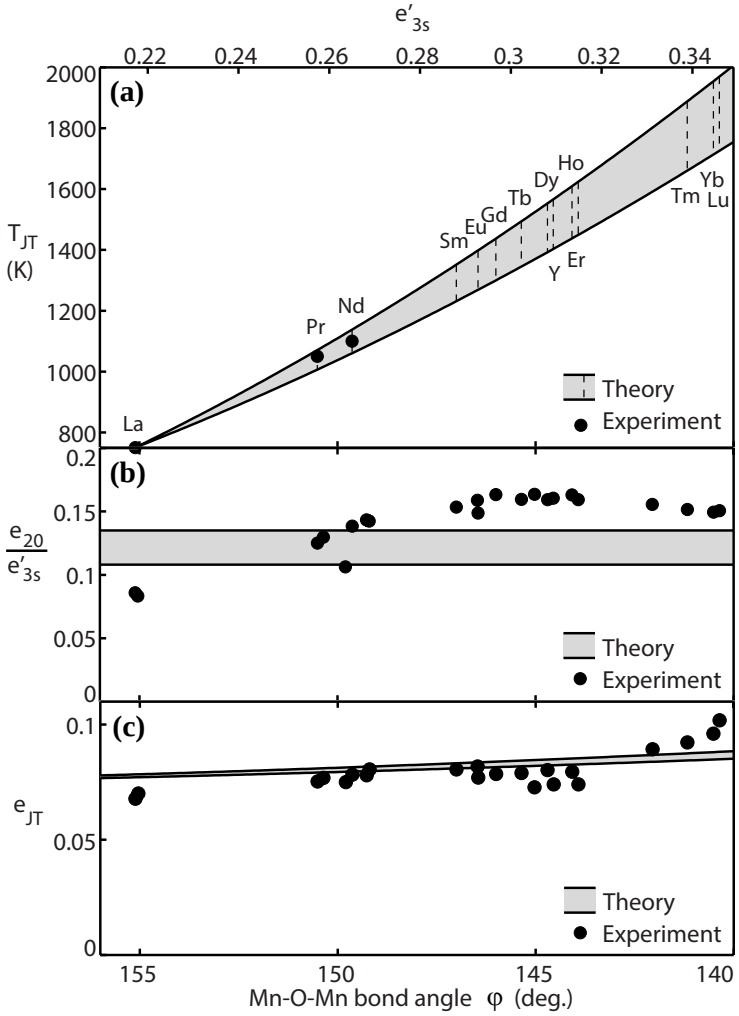

Figure 3.7 Available experimental data and bounds estimated from theory, plotted against Mn-O-Mn bond angle and e'_{3s}, for (a) JT ordering temperature, (b) e_{20}/e'_{3s} ratio, and (c) e_{JT}. Experimental data are from Sánchez et al. (2002), Liu et al. (1996), Alonso et al. (2000), Mochizuki and Furukawa (2009), and references therein.

tion on how to extend the model to doped manganites and electronically ferroelectric undoped manganites. In the case of doped manganites, each Mn site has a fractional number of $3d$ e_g electrons, which would require quantum mechanical description of e_g electrons, similar to the ones in Moreo et al. (1999); Pradhan et al. (2007); Vergés et al. (2002); Salafranca and Brey (2006); Kumar and Majumdar (2006). Furthermore, RE and AK ions with different sizes distribute randomly, effectively generating site-dependent chemical pressure. Experimentally, it is observed that the increased

variance of RE and AK ion sizes has a similar effect as the decreased average RE and AK ion size in doped manganites. If focus is set on the effects of chemical pressure, the first necessary modification to the existing models in Moreo et al. (1999); Pradhan et al. (2007); Vergés et al. (2002); Salafranca and Brey (2006); Kumar and Majumdar (2006) would be a classical coupling between local chemical pressure and local dilatation mode of surrounding O ions, similar to e_1'. The second necessary modification would be anharmonic lattice energy terms obtained from the Keating model, similar to the ones presented in this chapter. Because chemical pressure $\tilde{p}_{\vec{i}}$ is dependent on site, one should consider all modes shown in Figure 3.3 at each site and the constraints between Fourier transforms of these variables, instead of just the four modes in Figure 3.4. With many variables involved, numerical approaches, such as Monte Carlo methods, would be essential.

This model can be extended and serve as a phenomenological model for the magnetism and electronic ferroelectricity in undoped manganites (Kimura, Ishihara, Shintani, Arima, Takahashi, Ishizaka and Tokura 2003; Mochizuki and Furukawa 2009; Sergienko et al. 2006), complementing existing theories, such as the ones based on local density approximation (Yamauchi et al. 2008). In undoped manganites, the magnetic interaction also shows a prominent dependence on the size of RE ions, changing the ground state from A-type to E-type antiferromagnetic phase through incommensurate phases as RE ion becomes smaller. This behavior has been proposed to originate from the reduced nearest neighbor ferromagnetism and the increased next nearest neighbor antiferromagnetism (Kimura, Ishihara, Shintani, Arima, Takahashi, Ishizaka and Tokura 2003), or alternatively, the reduced antiferromagnetism between t_{2g} spins and long range ferromagnetic double exchange interaction (Salafranca and Brey 2006). It has been further proposed that electronically ferroelectric phase may emerge in E-type antiferromagnetic phase, associated with the displacement of Wannier function center (WFC) from the ionic location due to the magnetic inversion

symmetry breaking for E-type spin ordering (Yamauchi et al. 2008). Within this phenomenological approach, the dependence of the first nearest and the second nearest neighbor magnetic interaction J_1 and J_2 on the Mn-O-Mn bond buckling can be expressed as $J_1 = J_{10}(1 + \alpha_1 e'_{3s})$ and $J_2 = J_{20}(1 + \alpha_2 e'_{3s})$ for a small range of e'_{3s}, in which the linear coefficients α_1 and α_2 can be decided from more fundamental theories. The $t_{2g} - t_{2g}$ super-exchange interaction can be expressed in a similar way.

As for the electronic ferroelectricity, although the explicit form of the Wannier function would require quantum mechanical analysis, the WFC itself can be treated as a classical variable and the lattice of the WFC can be considered in addition to the lattice of Mn ions. Therefore, symmetry-based analysis can be applied to both the WFC lattice and the ionic lattice. To demonstrate the idea, an example of three connected Mn-O motifs at sites (-1,0), (0,0), and (1,0) must be considered that is shown in Figure 3.8. The x directional displacement of Mn ion at site $\vec{i}$, the x directional displacement of WFC associated with Mn $3d_{3x^2-r^2}$ state with spin parallel to the t_{2g} core spin at site $\vec{i}$, and the t_{2g} spin at site $\vec{i}$ with magnitude of $|S_{t_{2g}}|$ are represented by $d_{\vec{i}}$, $D_{\vec{i}}$, and $\vec{S}_{\vec{i}}$. In addition, the buckling distortion e'_{3s} is considered. If a situation without any other distortions persists, the energy associated with these limited degrees of freedom can be written in the following form based on the symmetry:

$$\begin{aligned} E_{\text{eFE}} &= \frac{K_d}{2}\left(d^2_{(-1,0)} + d^2_{(0,0)} + d^2_{(1,0)}\right) \\ &+ \frac{K_D}{2}\left[\left(D_{(-1,0)} - d_{(-1,0)}\right)^2 + \left(D_{(0,0)} - d_{(0,0)}\right)^2 + \left(D_{(1,0)} - d_{(1,0)}\right)^2\right] \\ &+ J_{10}\vec{S}_{(-1,0)} \cdot \vec{S}_{(0,0)}\left[1 + \alpha_1 e'_{3s} + \beta\left(D_{(0,0)} - D_{(-1,0)}\right)\right] \\ &+ J_{10}\vec{S}_{(0,0)} \cdot \vec{S}_{(1,0)}\left[1 + \alpha_1 e'_{3s} + \beta\left(D_{(1,0)} - D_{(0,0)}\right)\right], \end{aligned} \tag{3.43}$$

where the terms with β represent how the magnetic interaction depends on the distance between the nearest neighbor WFC's. In the case of $d_{(0,0)} = d_{(-1,0)} = d_{(1,0)} = 0$ due to other elastic energy terms that are not considered above and $\vec{S}_{(-1,0)} =$

$\vec{S}_{(0,0)} = -\vec{S}_{(1,0)}$ due to the E-type magnetic ordering, the minimization with respect to $D_{(0,0)}$ leads to $D_{(0,0)} = -2J_{10}|S_{t_{2g}}|^2\beta/K_D$, shown schematically in Figure 3.8 with a thin arrow and an open square representing WFC, which demonstrates how this model can be expanded for modeling of ferroelectric moment of electronic origin. The symmetry-mode-based approach can be also used to model conventional ionic ferroelectricity in perovskite transition metal oxides by including energy terms with inversion symmetry breaking modes, such as t_x, t_y, t'_x, and t'_y in Figure 3.3.

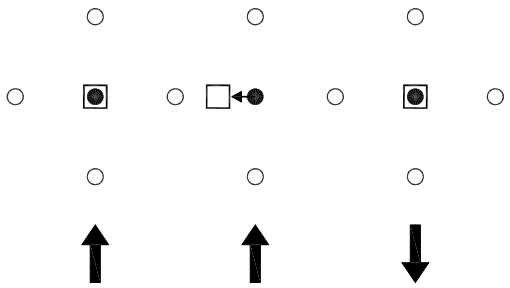

Figure 3.8 Schematic drawing that demonstrates how this model can be extended to include electronic ferroelectricity in undoped manganites. Three connected MnO_4 motifs are shown. Open and solid circles represent O and Mn ions. Open squares represent WFC's associated with the Mn $3d_{3x^2-r^2}$ state with spin parallel to the t_{2g} core spin, which would coincide with Mn ions in the non-ferroelectric phase. Thick arrows at the bottom represent the t_{2g} spin directions for E-type antiferromagnetic phase of undoped manganites. Thin horizontal arrow represents the displacement of WFC from Mn ion location, resulting in the ferroelectric moment of electronic origin.

3.7 Conclusions

From the analysis of a Keating energy expression expanded in terms of the atomic-scale symmetry-modes, it is found that the effect of small *RE* ion size, known as chemical pressure effect, is significant in stabilizing the long range JT distortion in undoped perovskite manganites. A good agreement with the experimental data on the JT ordering temperature and the substantial increase of the JT ordering temperature from $LaMnO_3$ to $PrMnO_3$ and $NdMnO_3$ have been obtained. It is proposed that similar effects need to be considered to understand the phase diagram for the

doped perovskite manganites. Further, the explanation is presented on the appearance of the uniform shear distortion below the JT ordering temperature in terms of the coupling between coherent shear, buckling, and deviatoric distortions within the JT energy. Moreover, the ratio between these distortions at low temperature is estimated, and a good agreement with experimental data for $LaMnO_3$, $PrMnO_3$, and $NdMnO_3$ is found, which confirms the coupling proposed in this model.

CHAPTER 4

SYMMETRY-BASED ATOMIC-SCALE DESCRIPTIONS OF LATTICE DYNAMICS

The work in this chapter was done in collaboration with Jichan Moon from Department of Physics, Konkuk University of Seoul, South Korea, as well as Keun H. Ahn from Department of Physics at New Jersey Institute of Technology.

4.1 Introduction

These days a lot of attention has been focused on physical properties in nanometer length scale. In particular, materials with competing ground states, such as high temperature superconducting cuprates (Lee, Nagaosa and Wen 2006) and colossal magnetoresistive manganites (Jin et al. 1994; Millis 1998; Salamon and Jaime 2001), often show nanometer scale features, either static or dynamic. Examples are stripes in cuprates (Tranquada et al. 1995; Kivelson et al. 2003) and anisotropic correlations in manganites (Kiryukhin 2004; Ahn et al. 2004). It is believed that understanding these nano-scale features is essential to explain macroscopic properties of these materials.

For the description of mesoscopic scale domain structures and phase transitions, phenomenological Ginzburg-Landau formalism has been very successful (Shenoy et al. 1999; Lookman et al. 2003). One of the keys for such success is the use of symmetry in the definition of variables, which makes the selection of free energy terms self-evident. Motivated by the success of symmetry-based continuum approach, symmetry-based atomic-scale description of lattice distortions has been recently proposed, and demonstrated for a two-dimensional square lattice (Ahn et al. 2003). In this approach, atomic-scale symmetry-modes are defined on a plaquette of atoms, and are used to express potential energy terms associated with lattice distortions. This method has been used to understand atomic scale structures of twin boundaries (Ahn

et al. 2003) and antiphase boundaries and associated electronic textures (Ahn et al. 2005), strain-induced metal insulator phase-coexistence in manganites (Ahn et al. 2004), superconducting order parameter textures around structural defects (Zhu et al. 2003), and the coupling between electronic nematic order parameter and structural domains in metamagnets near a quantum critical point (Doh et al. 2007). So far, this approach has been used for frozen lattices or the relaxation of lattice distortions through the Euler method (Shenoy et al. 1999), which does not require kinetic energy terms. In the current chapter (Moon 2006), the study on how the approach based on atomic scale symmetry modes can be extended to include kinetic energy terms and describe lattice dynamics within the formalism of both classical and quantum mechanics is presented. The study within the formalism of classical mechanics is first presented in Section 4.2, where the comparison with the continuum results (Lookman et al. 2003) are presented, and the phonon spectrum in terms of symmetry modes is also analyzed. Quantum mechanical formalism is formulated in terms of atomic scale symmetry modes in Section 4.3, whereas the conclusions are given in Section 4.4. In addition, intermediate steps of the calculations and 2D phonon spectrum examples are presented in Appendix 4.A.

4.2 Classical Formalism

4.2.1 One Dimensional Lattice with a Monatomic Basis

The underlying idea of mode-based lattice dynamics for one-dimensional lattice is first demonstrated, with a monatomic basis shown in Figure 4.1. The displacements

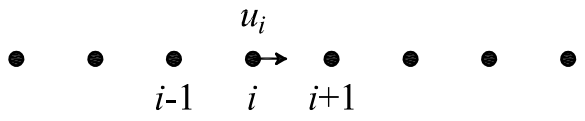

Figure 4.1 The one-dimensional lattice.

of atoms are confined along the direction of the chain, and are represented by $u(i)$,

where i is the index for sites. M is the mass of the atom. To be specific, it is assumed that the interaction between nearest neighbor atoms are described by a spring with a spring constant k and other potential energy terms are negligible, which gives rise to the following Lagrangian.

$$L_{chain} = \sum_i \frac{1}{2} M \dot{u}(i)^2 - \frac{1}{2} k[u(i+1) - u(i)]^2. \tag{4.1}$$

A two-atom unit is taken as a motif for this lattice (Ahn et al. 2003), and the symmetry modes are defined, $e(i)$ and $t(i)$, as follows, where a normalization factor is introduced according to the number of displacement variables in the definition.

$$e(i) \equiv \frac{1}{\sqrt{2}}[u(i+1) - u(i)], \tag{4.2}$$

$$t(i) \equiv \frac{1}{\sqrt{2}}[u(i+1) + u(i)]. \tag{4.3}$$

Figure 4.2 The lattice modes for the one-dimensional chain in Figure 4.1.

The two variables, e and t, correspond to the distortion and rigid translation of the motif, respectively. Similarly to the findings in Ahn et al. (2003), since the two modes are defined at each site i from one physically independent displacement variable, these modes are related through one constraint equation, shown below in the reciprocal space and direct space, respectively.

$$f_k \equiv (e^{ik} + 1)e(k) - (e^{ik} - 1)t(k) = 0, \tag{4.4}$$

$$e(i+1) + e(i) - t(i+1) + t(i) = 0 \tag{4.5}$$

In terms of these modes, the Lagrangian in Equation (4.1) can be expressed in the following way.

$$L_{chain} = \sum_i \frac{1}{2}(\frac{M}{2})\dot{e}(i)^2 + \frac{1}{2}(\frac{M}{2})\dot{t}(i)^2 - \frac{1}{2}(2k)e(i)^2, \tag{4.6}$$

The result shows that the introduction of atomic scale rigid modes, such as t, which are not considered in Ahn et al. (2003), allows the kinetic energy term expressed in a quadratic form in terms of modes. To obtain the equations of motion for constrained variables, the Lagrangian with Lagrange multiplier, λ_k, and constraint equations, f_{-k} are modified, as shown below.

$$\begin{aligned}\tilde{L} &= \sum_k \frac{1}{2}\left(\frac{M}{2}\right)\left(\dot{e}_k\dot{e}_{-k}+\dot{t}_k\dot{t}_{-k}\right)-\frac{1}{2}(2k)e_ke_{-k} \\ &\quad +\lambda_k\{(e^{-ik}+1)e_{-k}-(e^{-ik}-1)t_{-k}\}. \end{aligned} \tag{4.7}$$

Lagrangian formalism of dynamics leads to the two equations of motion,

$$\frac{M}{2}\ddot{e}_k+2ke_k-\lambda_k(e^{-ik}+1) = 0, \tag{4.8}$$

$$\frac{M}{2}\ddot{t}_k+\lambda_k(e^{-ik}-1) = 0, \tag{4.9}$$

and a well-known dispersion relation for one-dimensional chain (Kittel 2005),

$$\omega=\sqrt{\frac{k}{M}(1-\cos k)}. \tag{4.10}$$

This result shows that the lattice dynamics can be studied within the framework of atomic scale symmetry modes and their constraint equations, without using the displacement variables explicitly. The advantage of this approach lies in the convenience in expressing high order anharmonic potential energy terms in more concise ways, compared to the approach based on displacement variables. Such advantage will be more relevant for lattices in 2D or 3D, where anharmonic energy landscape with multiple local energy minima and consequent domain structures could occur naturally (Ahn et al. 2003). In the next subsection, it is demonstrated how this approach can be applied for lattices in higher dimensions, for example, a two-dimensional square lattice with a monatomic basis.

4.2.2 Two-Dimensional Square Lattice With a Monatomic Basis

Symmetry-based atomic scale modes for a two-dimensional square lattice with a monatomic basis, shown in Figure 4.3, have been studied in Ahn et al. (2003, 2004),

where strain modes, e_1, e_2, and e_3, and short wavelength modes, s_x and s_y, are defined, as shown in Figure 4.4. Specifically, in terms of displacement variables,

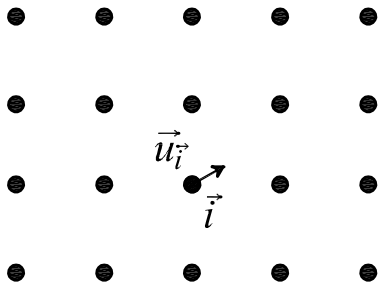

Figure 4.3 The two-dimensional square lattice with a mono-atomic basis.

$u_x(\vec{i})$ and $u_y(\vec{i})$, shown in Figure 4.3, where i_x and i_y represent site indices, these modes are expressed as follows along with proper normalization factors.

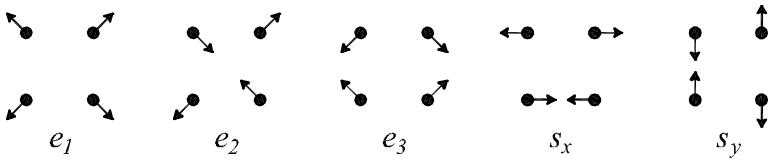

Figure 4.4 Normal distortion modes for a square object of four atoms in 2D.

$$
\begin{aligned}
e_1(\vec{i}) &= \frac{1}{2\sqrt{2}}[-u_i^x - u_i^y + u_{i+10}^x - u_{i+10}^y \\
&\quad -u_{i+01}^x + u_{i+01}^y + u_{i+11}^x + u_{i+11}^y], && (4.11)\\
e_2(\vec{i}) &= \frac{1}{2\sqrt{2}}[-u_i^x - u_i^y - u_{i+10}^x + u_{i+10}^y \\
&\quad +u_{i+01}^x - u_{i+01}^y + u_{i+11}^x + u_{i+11}^y], && (4.12)\\
e_3(\vec{i}) &= \frac{1}{2\sqrt{2}}[-u_i^x + u_i^y + u_{i+10}^x + u_{i+10}^y \\
&\quad -u_{i+01}^x - u_{i+01}^y + u_{i+11}^x - u_{i+11}^y], && (4.13)\\
s_x(\vec{i}) &= \frac{1}{2}[u_i^x - u_{i+10}^x - u_{i+01}^x + u_{i+11}^x], && (4.14)\\
s_y(\vec{i}) &= \frac{1}{2}[u_i^y - u_{i+10}^y - u_{i+01}^y + u_{i+11}^y]. && (4.15)
\end{aligned}
$$

Instead of s_x and s_y modes, the following s_+ and s_- modes can be used.

$$
s_+(\vec{i}) = \frac{1}{\sqrt{2}}[s_x(\vec{i}) + s_y(\vec{i})] \qquad (4.16)
$$

$$s_-(\vec{i}) = \frac{1}{\sqrt{2}}[s_x(\vec{i}) - s_y(\vec{i})] \tag{4.17}$$

These five modes have been used to describe various forms of potential energy terms for lattice distortions, in which harmonic and anharmonic interactions among atoms within the same plaquette have been considered (Ahn et al. 2003, 2004). However, these five modes are not sufficient to represent the kinetic energy term adequately. For example, to obtain the phonon spectrum shown in Figure 2 in Ahn et al. (2003), the expression has been converted back to the displacement variables.

In current work, it is shown that additional modes, associated with the rigid motion of the motif, similar to the mode t in the previous subsection, allow a formalism entirely based on symmetry modes without resorting to displacement variables. The three rigid modes for the two-dimensional square lattice are shown in Figure 4.5 and are defined as follows.

$$t_x(\vec{i}) = \frac{1}{2}[u^x_i + u^x_{i+10} + u^x_{i+01} + u^x_{i+11}], \tag{4.18}$$

$$t_y(\vec{i}) = \frac{1}{2}[u^y_i + u^y_{i+10} + u^y_{i+01} + u^y_{i+11}], \tag{4.19}$$

$$\begin{aligned} r(\vec{i}) = \frac{1}{2\sqrt{2}}[&u^x_i - u^y_i + u^x_{i+10} + u^y_{i+10} \\ &-u^x_{i+01} - u^y_{i+01} - u^x_{i+11} + u^y_{i+11}], \end{aligned} \tag{4.20}$$

Instead of t_x and t_y, the following t_+ and t_- modes can be also used.

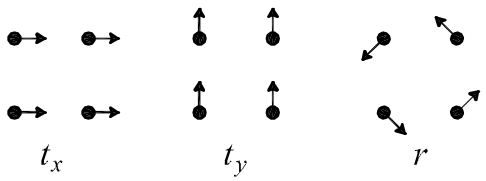

Figure 4.5 Three rigid mode in the two-dimensional square lattice.

$$t_+(\vec{i}) = \frac{1}{\sqrt{2}}[t_x(\vec{i}) + t_y(\vec{i})] \tag{4.21}$$

$$t_-(\vec{i}) = \frac{1}{\sqrt{2}}[t_x(\vec{i}) - t_y(\vec{i})] \tag{4.22}$$

The first two modes, t_x and t_y correspond to the rigid translation of the motif along x and y direction, and r represents a rigid rotation of the motif. Straight-forward expansion shows that the kinetic energy of the lattice can be expressed in terms of eight symmetry modes in the following quadratic form, where M is the mass of the atom.

$$T_{sq.lat} = \sum_{\vec{i}} \frac{1}{2} M[\dot{u}_x(\vec{i})^2 + \dot{u}_y(\vec{i})^2] \tag{4.23}$$

$$= \sum_{\vec{i}} \frac{1}{2}(\frac{M}{4})[\dot{e}_1(\vec{i})^2 + \dot{e}_2(\vec{i})^2 + \dot{e}_3(\vec{i})^2 + \dot{s}_x(\vec{i})^2 + \dot{s}_y(\vec{i})^2 + \dot{t}_x(\vec{i})^2 + \dot{t}_y(\vec{i})^2 + \dot{r}(\vec{i})^2]. \tag{4.24}$$

As discussed in Ahn et al. (2003), constraint equations can be found by representing the relations between symmetry modes and displacement variables in the reciprocal space. For example, by inverting the relations between $[s_x(\vec{k}),s_y(\vec{k})]$ and $[u_x(\vec{k}),u_y(\vec{k})]$, one can represent $[u_x(\vec{k}),u_y(\vec{k})]$ in terms of $[s_x(\vec{k}),s_y(\vec{k})]$, which leads to the following six constraint equations.[1]

$$\sin\tfrac{k_x}{2}\cos\tfrac{k_y}{2}s_x(\vec{k}) + \cos\tfrac{k_x}{2}\sin\tfrac{k_y}{2}s_y(\vec{k}) - \\ -\sqrt{2}i\sin\tfrac{k_x}{2}\sin\tfrac{k_y}{2}e_1(\vec{k}) = 0, \tag{4.25}$$

$$\cos\tfrac{k_x}{2}\sin\tfrac{k_y}{2}s_x(\vec{k}) + \sin\tfrac{k_x}{2}\cos\tfrac{k_y}{2}s_y(\vec{k}) - \\ -\sqrt{2}i\sin\tfrac{k_x}{2}\sin\tfrac{k_y}{2}e_2(\vec{k}) = 0, \tag{4.26}$$

$$\sin\tfrac{k_x}{2}\cos\tfrac{k_y}{2}s_x(\vec{k}) - \cos\tfrac{k_x}{2}\sin\tfrac{k_y}{2}s_y(\vec{k}) - \\ -\sqrt{2}i\sin\tfrac{k_x}{2}\sin\tfrac{k_y}{2}e_3(\vec{k}) = 0, \tag{4.27}$$

$$\cos\tfrac{k_x}{2}\sin\tfrac{k_y}{2}s_x(\vec{k}) - \sin\tfrac{k_x}{2}\cos\tfrac{k_y}{2}s_y(\vec{k}) + \\ +\sqrt{2}i\sin\tfrac{k_x}{2}\sin\tfrac{k_y}{2}r(\vec{k}) = 0, \tag{4.28}$$

[1]It should be noted that inverting the relation between $s_x(\vec{k})$ and $s_y(\vec{k})$ versus $u_x(\vec{k})$ and $u_y(\vec{k})$ is not possible for certain wave vectors, for example, wave vectors with k_x=0 or k_y=0. In those cases, new constraint equations should be found from the definition of the modes.

$$\cos\tfrac{k_x}{2}\cos\tfrac{k_y}{2}s_x(\vec{k}) + \sin\tfrac{k_x}{2}\sin\tfrac{k_y}{2}t_x(\vec{k}) = 0, \tag{4.29}$$

$$\cos\tfrac{k_x}{2}\cos\tfrac{k_y}{2}s_y(\vec{k}) + \sin\tfrac{k_x}{2}\sin\tfrac{k_y}{2}t_y(\vec{k}) = 0. \tag{4.30}$$

For a potential energy V represented in terms of symmetry modes, the Lagrangian is

$$\tilde{L} = T - V + \sum_{n=1}^{6}\sum_{k}\lambda_{n,k}f_{n,-k}, \tag{4.31}$$

where $\lambda_{n,k}$ are Lagrange multipliers and $f_{n,k} = 0$'s are the six compatibility equations, Equations (4.25)-(4.30). By solving the Lagrangian equations, the dynamic properties of the lattice can be analyzed.

In the next two subsections, the two applications of description of lattice dynamics using atomic-scale symmetry-modes developed in this subsection are presented.

4.2.3 Comparison With Continuum Description of Lattice Dynamics

In Lookman et al. (2003), continuum description of lattice dynamics has been presented in the context of ferroelastic dynamics, with the lattice kinetic energy, Equation (3.12a) in Lookman et al. (2003), represented in terms of strain modes, e_1 and e_3 (e_2 in the notation of Lookman et al. (2003)). The atomic-scale theory developed in the previous subsection is compared with the existing continuum theory. Either by using Equations (4.11) and (4.13) or by using the constraint equations, the kinetic energy in terms of e_1 and e_3 can be obtained,

$$T = \sum_{\vec{k}}\sum_{s=1,3}\sum_{s'=1,3}\frac{1}{2}M\gamma_{ss'}(\vec{k})\dot{e}_s(\vec{k})\dot{e}_{s'}(-\vec{k}), \tag{4.32}$$

where

$$\gamma_{11}(\vec{k}) = \gamma_{33}(\vec{k}) = \frac{1-\cos k_x\cos k_y}{\sin^2 k_x\sin^2 k_y} \tag{4.33}$$

$$\gamma_{13}(\vec{k}) = \gamma_{31}(\vec{k}) = \frac{\cos k_x - \cos k_y}{\sin^2 k_x\sin^2 k_y}. \tag{4.34}$$

By taking the long wavelength limit, one obtains the following leading order term for $\gamma_{ss'}$,

$$\gamma^{(0)}_{ss'}(\vec{k}) = \begin{bmatrix} \dfrac{k_x^2+k_y^2}{2k_x^2k_y^2} & \dfrac{k_y^2-k_x^2}{2k_x^2k_y^2} \\ \dfrac{k_y^2-k_x^2}{2k_x^2k_y^2} & \dfrac{k_x^2+k_y^2}{2k_x^2k_y^2} \end{bmatrix}, \tag{4.35}$$

which is identical[2] to the result in Lookman et al. (2003). It shows that the approach is a natural extension of continuum theory, and is suitable for multiscale description of lattice dynamics within a single theoretical framework. The next order correction to the above continuum results is as follows.

$$\gamma^{(1)}_{ss'}(\vec{k}) = \begin{bmatrix} \dfrac{1}{12}+\dfrac{k_x^4+k_y^4}{8k_x^2k_y^2} & \dfrac{k_y^4-k_x^4}{8k_x^2k_y^2} \\ \dfrac{k_y^4-k_x^4}{8k_x^2k_y^2} & \dfrac{1}{12}+\dfrac{k_x^4+k_y^4}{8k_x^2k_y^2} \end{bmatrix}. \tag{4.36}$$

Specifically, in the long wavelength limit, the definition of symmetry modes are as follows.

$$\begin{aligned}
e_1(\vec{j}) &= \frac{1}{\sqrt{2}}[\nabla_x u_x(\vec{j}) + \nabla_y u_y(\vec{j})], && (4.37)\\
e_2(\vec{j}) &= \frac{1}{\sqrt{2}}[\nabla_x u_y(\vec{j}) + \nabla_y u_x(\vec{j})], && (4.38)\\
e_3(\vec{j}) &= \frac{1}{\sqrt{2}}[\nabla_x u_x(\vec{j}) - \nabla_y u_y(\vec{j})], && (4.39)\\
r(\vec{j}) &= \frac{1}{\sqrt{2}}[\nabla_x u_y(\vec{j}) - \nabla_y u_x(\vec{j})], && (4.40)\\
s_x(\vec{j}) &= \frac{1}{2}\nabla_x\nabla_y u_x(\vec{j}), && (4.41)\\
s_y(\vec{j}) &= \frac{1}{2}\nabla_x\nabla_y u_y(\vec{j}), && (4.42)\\
t_x(\vec{j}) &= 2u_x, && (4.43)\\
t_y(\vec{j}) &= 2u_y, && (4.44)
\end{aligned}$$

which shows that in $k \to 0$ limit,

$$t_x, t_y \sim u,$$

[2]The difference in the pre-factor with Equation (3.12a) in Lookman et al. (2003) is due to the typographical error in Lookman et al. (2003).

$$\begin{aligned} e_1, e_2, e_3, r &\sim ku, \\ s_x, s_y &\sim k^2 u. \end{aligned} \tag{4.45}$$

It is noteworthy that even if rotation is a rigid mode, it is related to displacement in the order of k, unlike translation modes, t_x and t_y.

4.2.4 Phonon Mode Analysis in Terms of Symmetry Modes

In this subsection, the analysis of phonon modes in terms of atomic scale symmetry modes is presented. Specifically, a harmonic potential energy with a square lattice ground state (Ahn et al. 2003) is considered, as shown below.

$$\begin{aligned} V_{sq.lat} = \sum_{\vec{i}} \quad & \frac{1}{2}A_1 e_1(\vec{i})^2 + \frac{1}{2}A_2 e_2(\vec{i})^2 + \frac{1}{2}A_3 e_3(\vec{i})^2 \\ & + \frac{1}{2}B[s_x(\vec{i})^2 + s_y(\vec{i})^2]. \end{aligned} \tag{4.46}$$

By solving the Lagrangian equations, Equation (4.31), the dispersion relations are found,

$$\begin{aligned} M\omega^2 &= B(1-\cos k_x)(1-\cos k_y) \\ &\quad + \frac{1}{2}(1-\cos k_x \cos k_y)(A_1 + A_2 + A_3) \\ &\quad \pm \left[\frac{1}{4}(\cos k_x - \cos k_y)^2 (A_1 - A_2 + A_3)^2 \right. \\ &\quad \left. + \frac{1}{4}\sin^2 k_x \sin^2 k_y (A_1 + A_2 - A_3)^2 \right]^{1/2}. \end{aligned} \tag{4.47}$$

Furthermore, the square of normalized amplitude of each symmetry mode within phonon modes can be found. Their general expressions are shown in the second column in Table 4.1, where $\beta_1 = 1 - \cos k_x \cos k_y$, $\beta_2 = -\sin k_x \sin k_y$, $\beta_3 = \cos k_x - \cos k_y$, $\beta_4 = (1-\cos k_x)(1-\cos k_y)$, $\beta_5 = (1+\cos k_x)(1+\cos k_y)$, and $a = (A_1 - A_2 + A_3)/(A_1 + A_2 - A_3)$. First, the mode amplitude does not depend on the short wavelength mode modulus B, but depends only on the long wavelength mode moduli, A_1, A_2, and A_3, through the parameter a. Comparison of general expressions for the

mode amplitudes between upper and lower branches shows that the amplitudes of the e_1 mode in the upper[lower] branch are identical to that of r mode in the lower[upper] branch. Similar relations exist between e_2 and e_3, between s_x and s_y, between t_x and t_y, between s_+ and s_-, and between t_+ and t_-. Furthermore, mode amplitudes for the short wavelength modes, s_x, s_y, s_+ and s_-, at $\vec{k}$ are identical to those for the translational modes, t_x, t_y, t_+, and t_- at $(\pi, \pi) - \vec{k}$.

For special cases of $a = 0$ (i.e., $A_1 + A_3 = A_2$), $a = 1$ (i.e., $A_2 = A_3$), and $a = \infty$ (i.e., $A_1 + A_2 = A_3$), the general expressions can be simplified, which is also shown in the Table 4.1. It is noteworthy that, if $a = 1$, or $A_2 = A_3$, the upper phonon branch includes no rotational mode, r, and the lower branch no area-changing mode, e_1, which can be explained in the following way. If the two shape changing modes, e_2 and e_3, have identical moduli, the lattice sustains isotropic phonon dispersion in the long wavelength limit, in which the lattice behaves like an isotropic continuum medium. Such medium would support longitudinal phonon mode in the upper branch and transverse phonon modes in the lower branch: the former rotationless and the latter locally area-preserving. For finite wavelengths, the phonon dispersion is not exactly isotropic, and the phonon modes are not exactly longitudinal nor transverse. However, the upper and lower branch phonon modes remain locally rotationless and area-preserving, even for finite wavelength, if the two shape changing modes have an identical modulus.

Squared mode amplitudes for the upper branches within the first Brillouin zone are plotted in Figures 4.6-4.10 for $a = 0$, 0.1, 1, 10, and ∞, which reveals that different regions in k-space are dominated by different modes. For all values of a, the phonons around the Brillouin zone center, $\vec{k} = 0$, have mostly the translational modes, t_x, t_y, or t_+, t_-, [Figures 4.6-4.10 (e),(f),(i), and (j)] consistent with Equation (4.45). In contrast, the short wavelength modes, s_x, s_y, s_+, and s_- contribute dominantly near the corners of the first Brillouin zone [Figures 4.6-4.10 (g),(h),(k), and (l)]. The

upper and lower branch phonon modes at $\vec{k} = (\pi, 0)$ are longitudinal and transverse, as shown in Figures 4.11(a) and 4.11(b) respectively. Therefore, the phonon at $\vec{k} = (\pi, 0)$ in the upper branch consists of e_1 and e_3 modes, and that in the lower branch of e_2 and r modes, which explains the large contribution of these modes near $\vec{k} = (\pi, 0)$ and, equivalently, near $\vec{k} = (0, \pi)$ [Figures 4.6-4.10 (a) and (c)]. The contribution of e_2 mode in the upper branch and, equivalently, e_3 mode in the lower branch, for $a = 0.1, 1, 10, \infty$ [Figures 4.7-4.10 (b)] is relatively weak, except near $\vec{k} = (\pm\pi/2, \pm\pi/2)$. Rotational mode r in the upper branch and, equivalently, e_1 mode in the lower branch are very small except for $a = 0$ [Figures 4.7-4.10 (d)], and, in particular, vanish for $a = 1$ as discussed above [Figure 4.8 (d)]. For $a = 0$, or $A_1 + A_3 = A_2$, the two phonon modes at $\vec{k} = (\pi, 0)$ and $(0, \pi)$ shown in Figure 4.11 have the same moduli and, therefore, are degenerate, which give rise to the equal contribution of the four modes, e_1, e_2, e_3 and r at these k points, as shown in Figure 4.6 (a), (b), (c), and (d). Understanding how different modes contribute different parts in the k-space could be useful, for example, to gain insight into materials with electron-phonon coupling, such as, manganites, phonon-mediated superconductors, and materials near structural phase transition.

4.3 Quantum Mechanical Formalism

4.3.1 One Dimensional Lattice With a Monatomic Basis

The symmetry-based atomic-scale description of lattice dynamics is further extended to the quantum mechanical formalism for the one-dimensional chain. In particular, quantum mechanical commutation relations can be found among modes and conjugate momenta. Conjugate momenta for the two modes, $P_e(i)$ and $P_t(i)$, are

$$P_e(i) = \frac{\partial L}{\partial \dot{e}(i)} = \frac{M}{2}\dot{e}(i) = \frac{1}{2\sqrt{2}}(p_{i+1} - p_i), \tag{4.48}$$

$$P_t(i) = \frac{\partial L}{\partial \dot{t}(i)} = \frac{M}{2}\dot{t}(i) = \frac{1}{2\sqrt{2}}(p_{i+1} + p_i), \tag{4.49}$$

Table 4.1 Mode Amplitudes

Mode	General expression	$a=0$	$a=1$		$a=\infty$
			upper	lower	
$\lvert e_1\rvert^2$	$\frac{1}{8}\left(\beta_1 \pm \frac{\beta_2^2+a\beta_3^2}{\sqrt{\beta_2^2+a^2\beta_3^2}}\right)$	$\frac{1}{8}\left(\beta_1 \pm \lvert\beta_2\rvert\right)$	$\frac{\beta_1}{4}$	0	$\frac{1}{8}\left(\beta_1 \pm \lvert\beta_3\rvert\right)$
$\lvert e_2\rvert^2$	$\frac{1}{8}\left(\beta_1 \pm \frac{\beta_2^2-a\beta_3^2}{\sqrt{\beta_2^2+a^2\beta_3^2}}\right)$	$\frac{1}{8}\left(\beta_1 \pm \lvert\beta_2\rvert\right)$	$\frac{\beta_2^2}{4\beta_1}$	$\frac{\beta_3^2}{4\beta_1}$	$\frac{1}{8}\left(\beta_1 \mp \lvert\beta_3\rvert\right)$
$\lvert e_3\rvert^2$	$\frac{1}{8}\left(\beta_1 \pm \frac{-\beta_2^2+a\beta_3^2}{\sqrt{\beta_2^2+a^2\beta_3^2}}\right)$	$\frac{1}{8}\left(\beta_1 \mp \lvert\beta_2\rvert\right)$	$\frac{\beta_3^2}{4\beta_1}$	$\frac{\beta_2^2}{4\beta_1}$	$\frac{1}{8}\left(\beta_1 \pm \lvert\beta_3\rvert\right)$
$\lvert r\rvert^2$	$\frac{1}{8}\left(\beta_1 \pm \frac{-\beta_2^2-a\beta_3^2}{\sqrt{\beta_2^2+a^2\beta_3^2}}\right)$	$\frac{1}{8}\left(\beta_1 \mp \lvert\beta_2\rvert\right)$	0	$\frac{\beta_1}{4}$	$\frac{1}{8}\left(\beta_1 \mp \lvert\beta_3\rvert\right)$
$\lvert s_x\rvert^2$	$\frac{\beta_4}{8}\left(1 \pm \frac{-a\beta_3}{\sqrt{\beta_2^2+a^2\beta_3^2}}\right)$	$\frac{\beta_4}{8}$	$\frac{\beta_4}{8\beta_1}\left(\beta_1-\beta_3\right)$	$\frac{\beta_4}{8\beta_1}\left(\beta_1+\beta_3\right)$	$\frac{\beta_4}{8}\left[1 \mp \mathrm{sign}(\beta_3)\right]$
$\lvert s_y\rvert^2$	$\frac{\beta_4}{8}\left(1 \pm \frac{a\beta_3}{\sqrt{\beta_2^2+a^2\beta_3^2}}\right)$	$\frac{\beta_4}{8}$	$\frac{\beta_4}{8\beta_1}\left(\beta_1+\beta_3\right)$	$\frac{\beta_4}{8\beta_1}\left(\beta_1-\beta_3\right)$	$\frac{\beta_4}{8}\left[1 \pm \mathrm{sign}(\beta_3)\right]$
$\lvert t_x\rvert^2$	$\frac{\beta_5}{8}\left(1 \pm \frac{-a\beta_3}{\sqrt{\beta_2^2+a^2\beta_3^2}}\right)$	$\frac{\beta_5}{8}$	$\frac{\beta_5}{8\beta_1}\left(\beta_1-\beta_3\right)$	$\frac{\beta_5}{8\beta_1}\left(\beta_1+\beta_3\right)$	$\frac{\beta_5}{8}\left[1 \mp \mathrm{sign}(\beta_3)\right]$
$\lvert t_y\rvert^2$	$\frac{\beta_5}{8}\left(1 \pm \frac{a\beta_3}{\sqrt{\beta_2^2+a^2\beta_3^2}}\right)$	$\frac{\beta_5}{8}$	$\frac{\beta_5}{8\beta_1}\left(\beta_1+\beta_3\right)$	$\frac{\beta_5}{8\beta_1}\left(\beta_1-\beta_3\right)$	$\frac{\beta_5}{8}\left[1 \pm \mathrm{sign}(\beta_3)\right]$
$\lvert s_+\rvert^2$	$\frac{\beta_4}{8}\left(1 \pm \frac{-\beta_2}{\sqrt{\beta_2^2+a^2\beta_3^2}}\right)$	$\frac{\beta_4}{8}\left[1 \mp \mathrm{sign}(\beta_2)\right]$	$\frac{\beta_4}{8\beta_1}\left(\beta_1-\beta_2\right)$	$\frac{\beta_4}{8\beta_1}\left(\beta_1+\beta_2\right)$	$\frac{\beta_4}{8}$
$\lvert s_-\rvert^2$	$\frac{\beta_4}{8}\left(1 \pm \frac{\beta_2}{\sqrt{\beta_2^2+a^2\beta_3^2}}\right)$	$\frac{\beta_4}{8}\left[1 \pm \mathrm{sign}(\beta_2)\right]$	$\frac{\beta_4}{8\beta_1}\left(\beta_1+\beta_2\right)$	$\frac{\beta_4}{8\beta_1}\left(\beta_1-\beta_2\right)$	$\frac{\beta_4}{8}$
$\lvert t_+\rvert^2$	$\frac{\beta_5}{8}\left(1 \pm \frac{-\beta_2}{\sqrt{\beta_2^2+a^2\beta_3^2}}\right)$	$\frac{\beta_5}{8}\left[1 \mp \mathrm{sign}(\beta_2)\right]$	$\frac{\beta_5}{8\beta_1}\left(\beta_1-\beta_2\right)$	$\frac{\beta_5}{8\beta_1}\left(\beta_1+\beta_2\right)$	$\frac{\beta_5}{8}$
$\lvert t_-\rvert^2$	$\frac{\beta_5}{8}\left(1 \pm \frac{\beta_2}{\sqrt{\beta_2^2+a^2\beta_3^2}}\right)$	$\frac{\beta_5}{8}\left[1 \pm \mathrm{sign}(\beta_2)\right]$	$\frac{\beta_5}{8\beta_1}\left(\beta_1+\beta_2\right)$	$\frac{\beta_5}{8\beta_1}\left(\beta_1-\beta_2\right)$	$\frac{\beta_5}{8}$

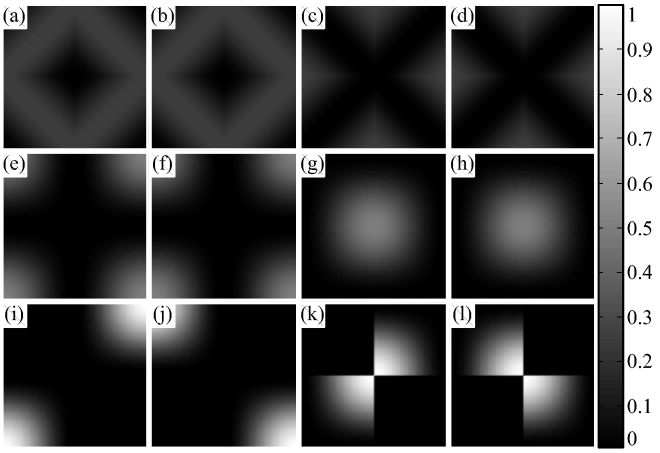

Figure 4.6 Squared phonon mode amplitudes for the upper branch for $a = 0$: (a)$|e_1|^2$, (b)$|e_2|^2$, (c)$|e_3|^2$, (d)$|r|^2$, (e)$|t_x|^2$, (f)$|t_y|^2$, (g)$|s_x|^2$, (h)$|s_y|^2$, (i)$|t_+|^2$, (j)$|t_-|^2$, (k)$|s_+|^2$, (l)$|s_-|^2$. [For the lower branch, they correspond to (a)$|r|^2$, (b)$|e_3|^2$, (c)$|e_2|^2$, (d)$|e_1|^2$, (e)$|t_y|^2$, (f)$|t_x|^2$, (g)$|s_y|^2$, (h)$|s_x|^2$, (i)$|t_-|^2$, (j)$|t_+|^2$, (k)$|s_-|^2$, (l)$|s_+|^2$.]

where p_i represent the momentum of the atom at the site i. From the usual commutation relations between momentum and displacement operators, $\hat{p}_i$ and $\hat{u}_j$, the following commutation relations between the mode and the conjugate momentum are found with the same site index i.

$$\begin{aligned} [P_e(i), e(i)] = [P_t(i), t(i)] &= \frac{1}{2}\frac{\hbar}{i}, \\ [P_e(i), t(i)] = [P_t(i), e(i)] &= 0. \end{aligned}$$

Since the nearest neighbor modes share an atom, the commutation relation between them can be non-zero, as shown below.

$$\begin{aligned} [P_e(i), t(i+1)] = [P_t(i), t(i+1)] &= \frac{\hbar}{4i}, \\ [P_e(i), e(i+1)] = [P_t(i), e(i+1)] &= -\frac{\hbar}{4i}, \\ [P_e(i), e(i-1)] = [P_e(i), t(i-1)] &= -\frac{\hbar}{4i}, \\ [P_t(i), e(i-1)] = [P_t(i), t(i-1)] &= \frac{\hbar}{4i}. \end{aligned}$$

The commutation relations between the momentum and the mode defined at the plaquettes farther than the nearest neighbors vanish.

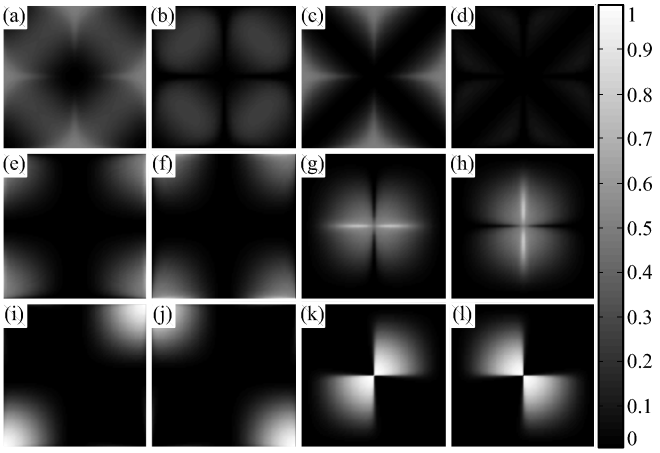

Figure 4.7 Squared phonon mode amplitudes for the upper branch for $a = 0.1$. Mode for each panel is identical to Figure 4.6.

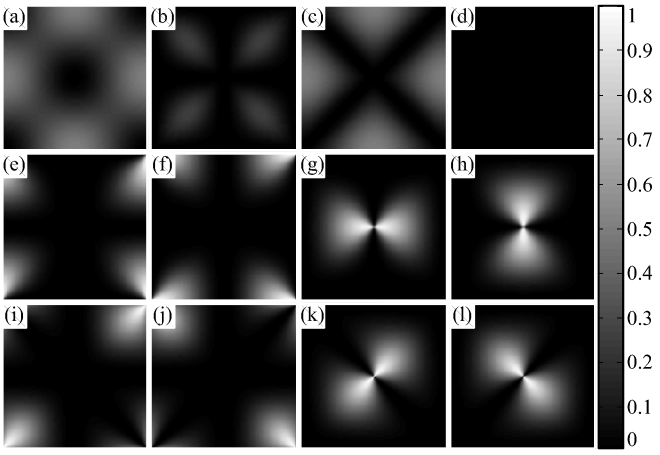

Figure 4.8 Squared phonon mode amplitudes for the upper branch for $a = 1$. Mode for each panel is identical to Figure 4.6.

The above relations can also be established graphically. For example, $[P_e(i), t(i+1)]$ can be found from the drawing in Figure 4.12, where $P_e(i)$ and $t(i+1)$ are represented with arrows. The arrows are then treated as unit vectors, and it can be found that the sum of scalar products of unit vectors defined for the same atom, which multiplied by $(\hbar/i)(1/2)^2$, leads to the commutation relation. From the graphical rule, the following relation can be understood, where a and b represent e or t.

$$[P_a(i), b(i+1)] = [P_b(i), a(i-1)] \tag{4.50}$$

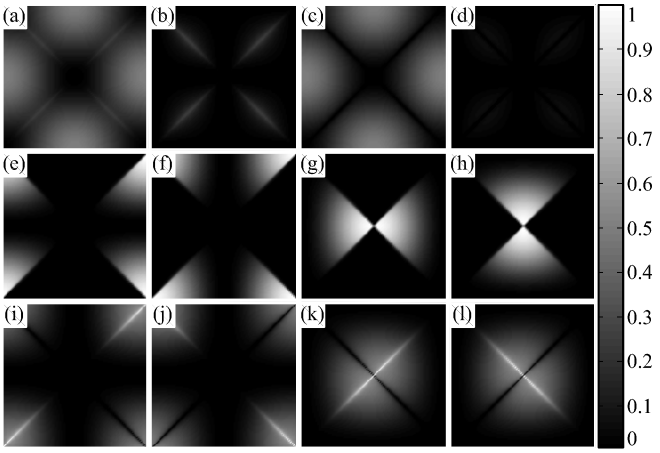

Figure 4.9 Squared phonon mode amplitudes for the upper branch for $a = 10$. Mode for each panel is identical to Figure 4.6.

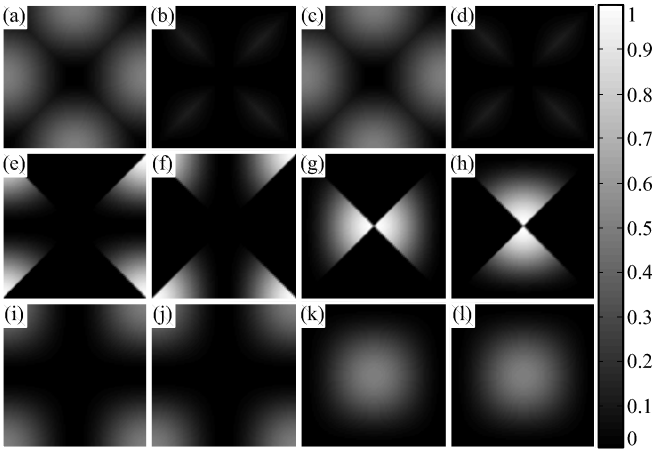

Figure 4.10 Squared phonon mode amplitudes for the upper branch for $a = \infty$. Mode for each panel is identical to Figure 4.6.

Similarly, using the fact that e and t have even and odd point reflection symmetry respectively and the scalar product in the graphic rule is invariant under the point reflection symmetry operation, the following relation is obtained.

$$[P_e(i), t(j)] = -[P_t(i), e(j)] \tag{4.51}$$

Using the commutation relation in the reciprocal space for the displacement variables and their momenta, the commutation relations in the reciprocal space for modes and their conjugate momenta are obtained, $[P_a(k), b(k')]$, which vanish for $k' \neq -k$. The commutation $[\frac{i}{\hbar}P_a(k), b(-k)]$ is shown in Table 4.2. The k

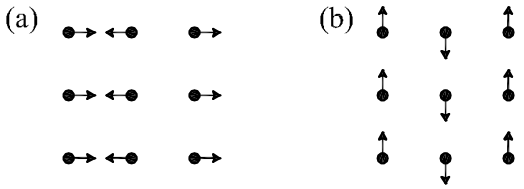

Figure 4.11 Phonon modes at $\vec{k} = (\pi, 0)$.

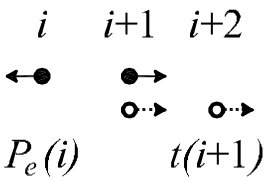

Figure 4.12 Commutation relation of $P_e(i)$ and $t(i+1)$.

dependent prefactors of the commutation relations reflect the fact that the modes and conjugate momenta at neighboring plaquettes are defined in terms of shared atoms.

4.3.2 Two-Dimensional Square Lattice With a Monatomic Basis

The quantum mechanical commutation relations for the two-dimensional square lattice can be found as follows. Conjugate momenta of atomic scale modes are obtained by the same method as in the one-dimensional case, and are written as

$$\begin{aligned} P_{e_1}(i) &= \frac{1}{8\sqrt{2}}[-p_i^x - p_i^y + p_{i+10}^x - p_{i+10}^y \\ &\quad -p_{i+01}^x + p_{i+01}^y + p_{i+11}^x + p_{i+11}^y], \\ P_{e_2}(i) &= \frac{1}{8\sqrt{2}}[-p_i^x - p_i^y - p_{i+10}^x + p_{i+10}^y \\ &\quad +p_{i+01}^x - p_{i+01}^y + p_{i+11}^x + p_{i+11}^y], \end{aligned}$$

Table 4.2 Commutation Relation in the 1D Reciprocal Space, $[P_a(k), b(k')]$

	$\frac{i}{\hbar}P_e(k)$	$\frac{i}{\hbar}P_t(k)$
$e(-k)$	$\frac{1}{2}(1-\cos k)$	$-\frac{i}{2}\sin k$
$t(-k)$	$\frac{i}{2}\sin k$	$\frac{1}{2}(1+\cos k)$

$$
\begin{aligned}
P_{e_3}(i) &= \frac{1}{8\sqrt{2}}[-p_i^x + p_i^y + p_{i+10}^x + p_{i+10}^y \\
&\quad -p_{i+01}^x - p_{i+01}^y + p_{i+11}^x - p_{i+11}^y], \\
P_r(i) &= \frac{1}{8\sqrt{2}}[p_i^x - p_i^y + p_{i+10}^x + p_{i+10}^y \\
&\quad -p_{i+01}^x - p_{i+01}^y - p_{i+11}^x + p_{i+11}^y], \\
P_{s_x}(i) &= \frac{1}{8}[p_i^x - p_{i+10}^x - p_{i+01}^x + p_{i+11}^x], \\
P_{s_y}(i) &= \frac{1}{8}[p_i^y - p_{i+10}^y - p_{i+01}^y + p_{i+11}^y], \\
P_{t_x}(i) &= \frac{1}{8}[p_i^x + p_{i+10}^x + p_{i+01}^x + p_{i+11}^x], \\
P_{t_y}(i) &= \frac{1}{8}[p_i^y + p_{i+10}^y + p_{i+01}^y + p_{i+11}^y].
\end{aligned}
$$

From the fundamental commutation relations for displacement operators and usual momentum operators,

$$
\begin{aligned}
[p_i^x, u_j^x] = [p_i^y, u_j^y] &= \frac{\hbar}{i}\delta_{ij} \\
[p_i^x, u_j^y] = [p_i^y, u_j^x] &= 0
\end{aligned}
$$

the commutation relations between modes and their conjugate momenta are calculated in a straight forward way. Alternatively, one can use graphical method, explained for one-dimensional chain in the previous subsection.

The above fundamental commutation relations for $i = j$ have the form of

$$
\begin{aligned}
\hat{x} \cdot \hat{x} = \hat{y} \cdot \hat{y} &= 1 \\
\hat{x} \cdot \hat{y} = \hat{y} \cdot \hat{x} &= 0
\end{aligned}
$$

except for the factor $\hbar/i$, where $\hat{x}$ and $\hat{y}$ represent unit vectors, not operators. Therefore, the commutation relation $[P_a(\vec{i}), b(\vec{j})]$, where a and b represent eight atomic-scale modes, can be found from the drawings of a and b modes on the square lattice. The sum of the scalar products of the unit vectors at the sites shared by the two modes, multiplied by $(\hbar/i)(1/4)^2$, gives the commutation of the two operators. The multiplication factor after $\hbar/i$ is associated with the number of atoms in the motif,

that is, 4 for the monatomic 2D square lattice and 2 for the monatomic 1D chain. For example, from Figure 4.13, $[P_{e1}(\vec{i}), e_2(\vec{i}+11)]$ can be found as follows.

$$[P_{e1}(\vec{i}), e_2(\vec{i}+11)] = \frac{\hbar}{i} \cdot \left(\frac{1}{4}\right)^2 \cdot (-1) \tag{4.52}$$

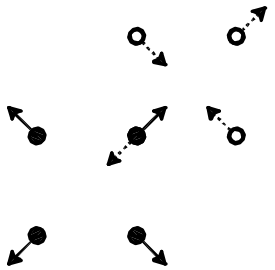

Figure 4.13 Commutation relation of $P_{e_1}(i)$ and $e_2(i+11)$.

Graphical method is also useful to find symmetry related properties of the commutation relations. From the orthogonality of modes, the commutation relation between a conjugate momentum and a mode at the same motif vanishes except for the case that the two modes are identical, as follows.

$$[P_a(i), b(i)] = \frac{1}{4}\frac{\hbar}{i}\delta_{ab}. \tag{4.53}$$

Also, from the symmetry under point inversion, the following equations are obtained, where *even* and *odd* represent the even modes, namely, e_1, e_2, e_3, r, and the odd modes, namely, s_x, s_y, t_x, t_y, respectively.

$$[P_{even}(i), even'(j)] = [P_{even'}(i), even(j)], \tag{4.54}$$

$$[P_{even}(i), odd(j)] = -[P_{odd}(i), even(j)], \tag{4.55}$$

$$[P_{odd}(i), odd'(j)] = [P_{odd'}(i), odd(j)]. \tag{4.56}$$

The commutation relations in the reciprocal space are calculated from the usual reciprocal space commutation relations for displacement variables. The commutation relations in modes in the reciprocal space are given in Table 4.3.

Table 4.3 Commutation Relation in the 2D Reciprocal Space, $[\frac{i}{\hbar}P_a(k), b(-k)]$

	$\frac{i}{\hbar}P_{e1}(k)$	$\frac{i}{\hbar}P_{e2}(k)$	$\frac{i}{\hbar}P_{e3}(k)$	$\frac{i}{\hbar}P_{r}(k)$	$\frac{i}{\hbar}P_{sx}(k)$	$\frac{i}{\hbar}P_{sy}(k)$	$\frac{i}{\hbar}P_{tx}(k)$	$\frac{i}{\hbar}P_{ty}(k)$
$e_1(-k)$	$\frac{1-C_{kx}C_{ky}}{4}$	$\frac{S_{kx}S_{ky}}{4}$	$\frac{-C_{kx}+C_{ky}}{4}$	0	$\frac{i(1-C_{kx})S_{ky}}{4\sqrt{2}}$	$\frac{i(1-C_{ky})S_{kx}}{4\sqrt{2}}$	$\frac{i(1+C_{ky})S_{kx}}{-4\sqrt{2}}$	$\frac{i(1+C_{kx})S_{ky}}{-4\sqrt{2}}$
$e_2(-k)$	$\frac{S_{kx}S_{ky}}{4}$	$\frac{1-C_{kx}C_{ky}}{4}$	0	$\frac{-C_{kx}+C_{ky}}{4}$	$\frac{i(1-C_{ky})S_{kx}}{4\sqrt{2}}$	$\frac{i(1-C_{kx})S_{ky}}{4\sqrt{2}}$	$\frac{i(1+C_{kx})S_{ky}}{-4\sqrt{2}}$	$\frac{i(1+C_{ky})S_{kx}}{-4\sqrt{2}}$
$e_3(-k)$	$\frac{-C_{kx}+C_{ky}}{4}$	0	$\frac{1-C_{kx}C_{ky}}{4}$	$\frac{-S_{kx}S_{ky}}{4}$	$\frac{i(1-C_{kx})S_{ky}}{4\sqrt{2}}$	$\frac{i(1-C_{ky})S_{kx}}{-4\sqrt{2}}$	$\frac{i(1+C_{ky})S_{kx}}{-4\sqrt{2}}$	$\frac{i(1+C_{kx})S_{ky}}{4\sqrt{2}}$
$r(-k)$	0	$\frac{-C_{kx}+C_{ky}}{4}$	$\frac{-S_{kx}S_{ky}}{4}$	$\frac{1-C_{kx}C_{ky}}{4}$	$\frac{i(1-C_{ky})S_{kx}}{-4\sqrt{2}}$	$\frac{i(1-C_{kx})S_{ky}}{4\sqrt{2}}$	$\frac{i(1+C_{kx})S_{ky}}{4\sqrt{2}}$	$\frac{i(1+C_{ky})S_{kx}}{-4\sqrt{2}}$
$s_x(-k)$	$\frac{i(1-C_{kx})S_{ky}}{-4\sqrt{2}}$	$\frac{i(1-C_{ky})S_{kx}}{-4\sqrt{2}}$	$\frac{i(1-C_{kx})S_{ky}}{-4\sqrt{2}}$	$\frac{i(1-C_{ky})S_{kx}}{4\sqrt{2}}$	$\frac{(1-C_{kx})(1-C_{ky})}{4}$	0	$\frac{-S_{kx}S_{ky}}{4}$	0
$s_y(-k)$	$\frac{i(1-C_{ky})S_{kx}}{-4\sqrt{2}}$	$\frac{i(1-C_{kx})S_{ky}}{-4\sqrt{2}}$	$\frac{i(1-C_{ky})S_{kx}}{4\sqrt{2}}$	$\frac{i(1-C_{kx})S_{ky}}{-4\sqrt{2}}$	0	$\frac{(1-C_{kx})(1-C_{ky})}{4}$	0	$\frac{-S_{kx}S_{ky}}{4}$
$t_x(-k)$	$\frac{i(1+C_{ky})S_{kx}}{4\sqrt{2}}$	$\frac{i(1+C_{kx})S_{ky}}{4\sqrt{2}}$	$\frac{i(1+C_{ky})S_{kx}}{4\sqrt{2}}$	$\frac{i(1+C_{kx})S_{ky}}{-4\sqrt{2}}$	$\frac{-S_{kx}S_{ky}}{4}$	0	$\frac{(1+C_{kx})(1+C_{ky})}{4}$	0
$t_y(-k)$	$\frac{i(1+C_{kx})S_{ky}}{4\sqrt{2}}$	$\frac{i(1+C_{ky})S_{kx}}{4\sqrt{2}}$	$\frac{i(1+C_{kx})S_{ky}}{-4\sqrt{2}}$	$\frac{i(1+C_{ky})S_{kx}}{4\sqrt{2}}$	0	$\frac{-S_{kx}S_{ky}}{4}$	0	$\frac{(1+C_{kx})(1+C_{ky})}{4}$

C_{kx}, C_{ky}, S_{kx}, and S_{ky} represent $\cos k_x$, $\cos k_y$, $\sin k_x$, and $\sin k_y$, respectively.

4.4 Conclusions

In this chapter, the mode-based atomic-scale description of the lattice dynamics is presented in detail. It is found that not only the potential energy but also the kinetic energy can be described in terms of the atomic-scale modes, for which the inclusion of the rigid modes is essential. Further, the atomic-scale mode-based approach is demonstrated for the dynamics of the one-dimensional chain and two-dimensional square lattice with a mono-atomic basis. By using the constraint equations, the modified Lagrangian equations are obtained in terms of atomic-scale modes only, without explicit use of the displacement variables. This approach to quantum mechanics is then extended, and the conjugate momenta and the commutation relations in real and reciprocal space are obtained. This approach becomes useful in describing systems with strong anharmonicity.

APPENDIX

4.A 2D Phonon Spectrum of the Uniform Phase

4.A.1 Potential Energy in 2D Lattice

Consider six symmetry modes, namely $e_1(\vec{j}), e_2(\vec{j}),\ e_3(\vec{j}),\ s_+(\vec{j}),\ s_-(\vec{j})$ and $r(\vec{j})$. Every mode defined by four atoms, which in turn defined by two coordinate components $u_x(\vec{j})$ and $u_y(\vec{j})$. Remaining two symmetry modes of translation have no direct relevance in this work. For example, mode $e_1(\vec{j})$ is defined as

$$\begin{aligned} e_1(\vec{j}) &= \frac{1}{2\sqrt{2}}\Big[- u_x(\vec{j}) + u_x(\vec{j}+10) - u_x(\vec{j}+01) + u_x(\vec{j}+11) \\ &\quad + u_y(\vec{j}) - u_y(\vec{j}+10) + u_y(\vec{j}+01) + u_y(\vec{j}+11)\Big], \end{aligned}$$

where $\vec{j}$ is the position of every atom in the desired domain. For simplicity of notation, the reference to $\vec{j}$ is dropped with every symmetry mode.

The goal is to derive a general mathematical expression of two-dimensional phonon spectrum for a lattice with rectangular unit base. To accomplish this, start with the shape of a square unit cell. With idealized two-dimensional square lattice, consider potential expression of the following form

$$\begin{aligned} V_{sq} &= \sum_{\vec{j}} \Big[\frac{A_1}{2}e_1^2 + \frac{A_2}{2}e_2^2 + \frac{A_3}{2}e_3^2 + \frac{F_3}{4}e_3^4 + \frac{A_s}{2}(s_+^2 + s_-^2) \\ &\quad + C_{12}e_1e_2^2 + C_{13}e_1e_3^2 + C_{1s}e_1(s_+^2 + s_-^2) + C_{2s}e_2(s_+^2 - s_-^2) \\ &\quad + C_{3s}e_3s_+s_- + C_{23r}e_2e_3r + \frac{F_{3r}}{2}e_3^2r^2\Big], \end{aligned} \tag{4.57}$$

with selection of constants as

$$A_1, A_2, F_3, F_{3r} > 0 \quad \text{and} \quad A_3, C_{12}, C_{13}, C_{1s}, C_{2s}, C_{3s} < 0.$$

Various denominator constants selected to simplify further form of algebraic expressions. The choice of mixed modes comprising in third order with C-type pre-factors is due to invariance of symmetry operations over six modes used. There are eight possible symmetry group operations for a square unit cell, which are reflection with

respect to horizontal, vertical and both diagonal bisectors passing through center of the cell, and rotations around $0, \pi/2, \pi$, and $3\pi/2$ with cell center being the pivot point. Note that the most obvious and allowed third order term e_1^3 is omitted from Equation (4.57) to simplify the point of expansion that is further introduced. There are two forth order terms, from which $\frac{F_3}{4}e_3^4$ is essential to introduce two non-zero minimums in the expansion for e_3 mode, and $\frac{F_{3r}}{2}e_3^2r^2$ to reduce degeneracy of eigenvalues obtained later on.

To arrive to a rectangular type lattice, point of expansion must be chosen with consideration of modes e_1 and e_3, whereas other resulting geometries can be considered in analogous fashion.

Consider point of expansion $p(e_1, e_2, e_3, s_+, s_-, r) = (\tilde{e}_1, 0, \tilde{e}_3, 0, 0, 0) = p_0$. To establish values for $\tilde{e}_1$ and $\tilde{e}_3$, set $\nabla V_{sq} = 0$.

$$\frac{\partial V}{\partial e_1} = A_1 e_1 + C_{12}e_2^2 + C_{13}e_3^2 + C_{1s}(s_+^2 + s_-^2) \tag{4.58}$$

$$\frac{\partial V}{\partial e_2} = A_2 e_2 + 2C_{12}e_1e_2 + C_{2s}(s_+^2 - s_-^2) + C_{23r}e_3 r \tag{4.59}$$

$$\frac{\partial V}{\partial e_3} = A_3 e_3 + F_3 e_3^3 + 2C_{13}e_1e_3 + C_{3s}s_+s_- + C_{23r}e_2 r + F_{3r}e_3 r^2 \tag{4.60}$$

$$\frac{\partial V}{\partial s_+} = A_s s_+ + 2C_{1s}e_1s_+ + 2C_{2s}e_2s_+ + C_{3s}e_3s_- \tag{4.61}$$

$$\frac{\partial V}{\partial s_-} = A_s s_- + 2C_{1s}e_1s_- - 2C_{2s}e_2s_- + C_{3s}e_3s_+ \tag{4.62}$$

$$\frac{\partial V}{\partial r} = C_{23r}e_2e_3 + F_{3r}e_3^2 r \tag{4.63}$$

From Equations (4.58) and (4.60) it can be found that

$$A_1\tilde{e}_1 = -C_{13}\tilde{e}_3^2 \quad \text{and} \quad A_3 + F_3\tilde{e}_3^2 = -2C_{13}\tilde{e}_1$$

and therefore

$$\tilde{e}_1 = \frac{A_3C_{13}}{A_1F_3 - 2C_{13}^2} \tag{4.64}$$

$$\tilde{e}_3 = \pm\sqrt{\frac{-A_1A_3}{A_1F_3 - 2C_{13}^2}} = \pm\sqrt{\frac{-A_3}{F_3 - \frac{2C_{13}^2}{A_1}}} \tag{4.65}$$

Since $A_3 < 0$, a numerical constraint on C_{13} is then obtained, eg.

$$|C_{13}| < \sqrt{\frac{A_1 F_3}{2}}. \tag{4.66}$$

Now consider non-zero second order derivative terms

$$\begin{aligned}
\frac{\partial^2 V}{\partial e_1^2}\Big|_{p_0} &= A_1, & (4.67)\\
\frac{\partial^2 V}{\partial e_2^2}\Big|_{p_0} &= A_2 + 2C_{12}\tilde{e}_1, & (4.68)\\
\frac{\partial^2 V}{\partial e_3^2}\Big|_{p_0} &= A_3 + 3F_3\tilde{e}_3^2 + 2C_{13}\tilde{e}_1, & (4.69)\\
\frac{\partial^2 V}{\partial s_+^2}\Big|_{p_0} &= \frac{\partial^2 V}{\partial s_-^2}\Big|_{p_0} = A_s + 2C_{1s}\tilde{e}_1, & (4.70)\\
\frac{\partial^2 V}{\partial r^2}\Big|_{p_0} &= F_{3r}\tilde{e}_3^2, & (4.71)\\
\frac{\partial^2 V}{\partial e_1 \partial e_3}\Big|_{p_0} &= 2C_{13}\tilde{e}_3, & (4.72)\\
\frac{\partial^2 V}{\partial s_+ \partial s_-}\Big|_{p_0} &= C_{3s}\tilde{e}_3, & (4.73)\\
\frac{\partial^2 V}{\partial e_2 \partial r}\Big|_{p_0} &= C_{23r}\tilde{e}_3. & (4.74)
\end{aligned}$$

This allows us to form the second order expansion

$$\begin{aligned}
V_{sq} \approx \sum_{\vec{j}} \Big[V_0 + \frac{1}{2}\Big[& A_1(e_1 - \tilde{e}_1)^2 + (A_2 + 2C_{12}\tilde{e}_1)e_2^2 \\
& + (A_3 + 3F_3\tilde{e}_3^2 + 2C_{13}\tilde{e}_1)(e_3 - \tilde{e}_3)^2 + (A_s + 2C_{1s}\tilde{e}_1)(s_+^2 + s_-^2) \\
& + (F_{3r}\tilde{e}_3^2)r^2 + 2(2C_{13}\tilde{e}_3)(e_1 - \tilde{e}_1)(e_3 - \tilde{e}_3) + 2(C_{3s}\tilde{e}_3)s_+ s_- \\
& + 2(C_{23r}\tilde{e}_3)e_2 r \Big]\Big]
\end{aligned} \tag{4.75}$$

To further simplify the notation, one must re-normalize the constant terms

$$\begin{aligned}
\tilde{A}_1 &= A_1, \quad \tilde{A}_2 = A_2 + 2C_{12}\tilde{e}_1, & (4.76)\\
\tilde{A}_3 &= A_3 + 3F_3\tilde{e}_3^2 + 2C_{13}\tilde{e}_1, & (4.77)\\
\tilde{A}_s &= A_s + 2C_{1s}\tilde{e}_1, & (4.78)\\
\tilde{A}_r &= F_{3r}\tilde{e}_3^2, & (4.79)
\end{aligned}$$

$$\tilde{C}_{13} = 2C_{13}\tilde{e}_3, \tag{4.80}$$

$$\tilde{C}_s = C_{3s}\tilde{e}_3, \tag{4.81}$$

$$\tilde{C}_{2r} = C_{23r}\tilde{e}_3, \tag{4.82}$$

which brings us to expression

$$\begin{aligned} V_{rec} = \sum_{\vec{j}} \Big[& \frac{\tilde{A}_1}{2}(e_1-\tilde{e}_1)^2 + \frac{\tilde{A}_2}{2}e_2^2 + \frac{\tilde{A}_3}{2}(e_3-\tilde{e}_3)^2 + \frac{\tilde{A}_s}{2}(s_+^2+s_-^2) + \frac{\tilde{A}_r}{2}r^2 \\ & + \tilde{C}_{13}(e_1-\tilde{e}_1)(e_3-\tilde{e}_3) + \tilde{C}_s s_+ s_- + \tilde{C}_{2r}e_2 r \Big]. \end{aligned} \tag{4.83}$$

that is suitable to describe vibrational dynamics of rectangular base lattice.

4.A.2 Formalizing Extraction of Pure Vibrational Modes

In order to construct suitable expressions for evaluation of the Lagrange equation, one must extract non-vibrational equilibrium part of the expansion, namely $\tilde{e}_1$ and $\tilde{e}_3$. Also, analytically it is desirable since this equilibrium contribution is non Fourier transformable. The outline of bases is introduced in (Ahn)[3]. Directional displacements can be written as follows

$$u_x(\vec{i}) = u_{x,eq}(\vec{i}) + \delta u_x(\vec{i}), \quad \text{and} \quad u_y(\vec{i}) = u_{y,eq}(\vec{i}) + \delta u_y(\vec{i})$$

where δ terms represent the vibrational term. Hence, the procedure follows

$$\frac{\varepsilon_0^{xx}+\varepsilon_0^{yy}}{\sqrt{2}} = \tilde{e}_1, \quad \frac{\varepsilon_0^{xy}}{\sqrt{2}} = 0, \quad \frac{\varepsilon_0^{xx}-\varepsilon_0^{yy}}{\sqrt{2}} = \tilde{e}_3,$$

which implies

$$\varepsilon_0^{xx} = \frac{1}{\sqrt{2}}(\tilde{e}_1+\tilde{e}_3), \quad \varepsilon_0^{yy} = \frac{1}{\sqrt{2}}(\tilde{e}_1-\tilde{e}_3), \quad \varepsilon_0^{xy} = 0.$$

Since

$$u_{x,eq}(\vec{i}) = \varepsilon_0^{xx}i_x + \varepsilon_0^{xy}i_y = \frac{1}{\sqrt{2}}(\tilde{e}_1+\tilde{e}_3)i_x$$
$$u_{y,eq}(\vec{i}) = \varepsilon_0^{xy}i_x + \varepsilon_0^{yy}i_y = \frac{1}{\sqrt{2}}(\tilde{e}_1-\tilde{e}_3)i_y$$

[3]K. H. Ahn, T. Lookman and A. R. Bishop. *Model for strain-induced metal-insulator phase coexistence in perovskite manganites*

it can be readily show that

$$e_1(\vec{i}) = \tilde{e}_1 + \delta e_1, \quad \text{and} \quad e_3(\vec{i}) = \tilde{e}_3 + \delta e_3$$

and therefore (4.83) is re-written as

$$\begin{aligned} V_{rec} &= \sum_{\vec{j}} V_{rec}(\vec{j}) && (4.84) \\ &= \sum_{\vec{j}} \Big[\frac{\tilde{A}_1}{2}\delta e_1^2 + \frac{\tilde{A}_2}{2} e_2^2 + \frac{\tilde{A}_3}{2}\delta e_3^2 + \frac{\tilde{A}_s}{2}(s_+^2 + s_-^2) + \frac{\tilde{A}_r}{2} r^2 \\ &\quad + \tilde{C}_{13}\delta e_1 \delta e_3 + \tilde{C}_s s_+ s_- + \tilde{C}_{2r} e_2 r \Big]. && (4.85) \end{aligned}$$

which is a somewhat an obvious result. From this point on, the δ prefix will be dropped for simplicity of notation, otherwise all symmetry modes should be prefixed with δ for rigor.

4.A.3 Lagrange Equation

With kinetic energy term defined as

$$T = \sum_{\vec{j}} \frac{M}{2} \Big[\dot{u}_x(\vec{j})^2 + \dot{u}_y(\vec{j})^2 \Big]$$

where M being a unit of mass and (4.85) being included in $L = T - V_{rec}$, one can write Lagrange equation of motion

$$\frac{d}{dt}\frac{\partial L}{\partial \dot{u}_{x,y}(\vec{i})} - \frac{\partial L}{\partial u_{x,y}(\vec{i})} = 0, \tag{4.86}$$

with indication that derivatives in u_x and u_y are taken independently from each other. With

$$\frac{\partial}{\partial \dot{u}_x(\vec{i})}\Big(\sum_{\vec{j}} \frac{M}{2} \dot{u}_x(\vec{j})^2 \Big) = \sum_{\vec{j}} M \dot{u}_x(\vec{j}) \delta_{\vec{i},\vec{j}} = M \dot{u}_x(\vec{i})$$

where $\delta_{\vec{i},\vec{j}}$ is Kronecker delta, while (4.86) can be re-written as

$$-M\ddot{u}_{x,y}(\vec{i}) = \frac{\partial V_{rec}(\vec{j})}{\partial u_{x,y}(\vec{i})} \tag{4.87}$$

where $\vec{j}$ remains a reference to every atom inside of summation, and $\vec{i}$ being a reference to every atom regardless of summation. This leads to us to relation between $\vec{i}$ and $\vec{j}$, e.g.

$$\vec{j} \in \vec{i} + \{\bar{1}\bar{1}, 0\bar{1}, 1\bar{1}, \bar{1}0, 00, 10, \bar{1}1, 01, 11\}$$

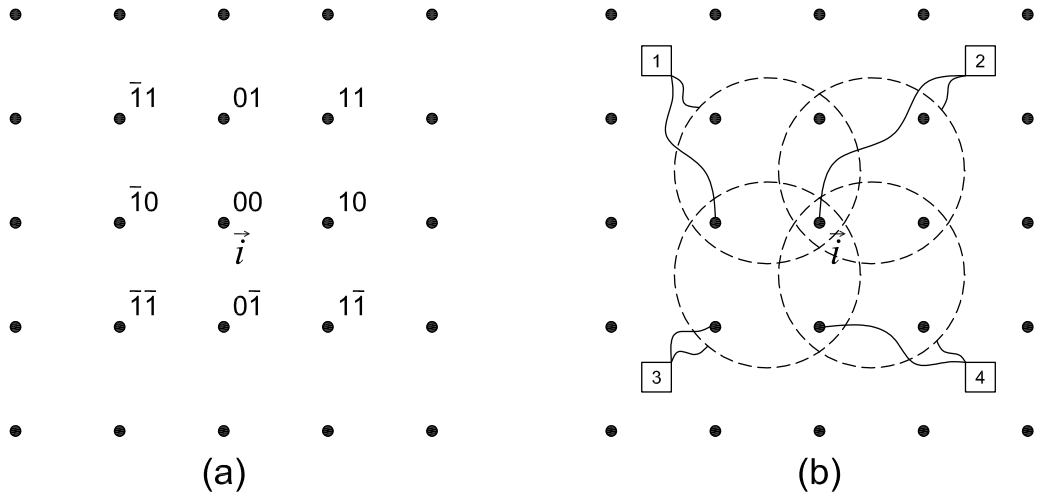

Figure 4.14 Figure (a) shows labeling of atoms with respect to $\vec{i}$, whereas (b) shows references to a symmetry group containing atom $\vec{i}$ and its identifying (lower left) atom, both pointed to by curvy line.

The goal is to evaluate the derivative (4.87) of V_{rec} on the right side. Define an arbitrary symmetry mode $a(\vec{i})$ as

$$\begin{aligned} a(\vec{i}) &= \xi_a \Big[s^x_{1a} u^x_{00} + s^x_{2a} u^x_{10} + s^x_{3a} u^x_{01} + s^x_{4a} u^x_{11} \\ &\quad + s^y_{1a} u^y_{00} + s^y_{2a} u^y_{10} + s^y_{3a} u^y_{01} + s^y_{4a} u^y_{11} \Big] \end{aligned} \tag{4.88}$$

with $s^{x,y}_{ka} \in \{-1, +1\}$. For example, for symmetry mode $e_1(\vec{i})$, $\xi_{e_1} = \frac{1}{2\sqrt{2}}$ and $\mathbf{s}_{e_1} = (-1, +1 - 1, +1, -1, -1, +1, +1)$. Now consider most general second order potential term with an arbitrary constant A

$$V_{ab} = \sum_{\vec{j}} A a(\vec{j}) b(\vec{j}) \tag{4.89}$$

so that with the help of Figure 4.14 (a) and (b)

$$\frac{\partial V_{ab}}{\partial u_{x,y}(\vec{i})} = \frac{\partial}{\partial u_{x,y}(\vec{i})} \sum_{\vec{j}} Aa(\vec{j})b(\vec{j}) \tag{4.90}$$

$$= A\Big[a(\vec{j})\frac{\partial b(\vec{j})}{\partial u_{x,y}(\vec{i})} + b(\vec{j})\frac{\partial a(\vec{j})}{\partial u_{x,y}(\vec{i})}\Big]_{\vec{j}\in\vec{i}+\{\bar{1}0,00,\bar{1}\bar{1},0\bar{1}\}} \tag{4.91}$$

$$\begin{aligned} = A\Big[&a(\vec{i}+\bar{1}0)\xi_b s^{x,y}_{2b} + b(\vec{i}+\bar{1}0)\xi_a s^{x,y}_{2a} \\ &+a(\vec{i})\xi_b s^{x,y}_{1b} + b(\vec{i})\xi_a s^{x,y}_{1a} \\ &+a(\vec{i}+\bar{1}\bar{1})\xi_b s^{x,y}_{4b} + b(\vec{i}+\bar{1}\bar{1})\xi_a s^{x,y}_{4a} \\ &+a(\vec{i}+0\bar{1})\xi_b s^{x,y}_{3b} + b(\vec{i}+0\bar{1})\xi_a s^{x,y}_{3a}\Big] \end{aligned} \tag{4.92}$$

$$\begin{aligned} = &A\xi_b\Big[s^{x,y}_{2b}a(\vec{i}+\bar{1}0) + s^{x,y}_{1b}a(\vec{i}) + s^{x,y}_{4b}a(\vec{i}+\bar{1}\bar{1}) + s^{x,y}_{3b}a(\vec{i}+0\bar{1})\Big] + \\ &A\xi_a\Big[s^{x,y}_{2a}b(\vec{i}+\bar{1}0) + s^{x,y}_{1a}b(\vec{i}) + s^{x,y}_{4a}b(\vec{i}+\bar{1}\bar{1}) + s^{x,y}_{3a}b(\vec{i}+0\bar{1})\Big] \end{aligned} \tag{4.93}$$

Since (4.93) consist of two parts mutually symmetrical with respect to a and b, consider taking a closer look at one part. From this point on, the direct use of actual mode is no longer required, since underlying $u_{x,y}$ notation is used, which in turn has a group of nine neighboring atoms as shown in Figure 4.14(a). Now first part of (4.93) can be re-written as

$$\sum_{\vec{j}\in\vec{i}+\{\bar{1}0,00,\bar{1}\bar{1},0\bar{1}\}} A\frac{a(\vec{j})\partial b(\vec{j})}{\partial u_{x,y}(\vec{i})} =$$

$$= A\xi_b\Big[s^{x,y}_{2b}a(\vec{i}+\bar{1}0) + s^{x,y}_{1b}a(\vec{i}) + s^{x,y}_{4b}a(\vec{i}+\bar{1}\bar{1}) + s^{x,y}_{3b}a(\vec{i}+0\bar{1})\Big]$$

$$\begin{aligned} = A\xi_a\xi_b\Big[&s^{x,y}_{2b}(s^x_{1a}u^x_{\bar{1}0} + s^x_{2a}u^x_{00} + s^x_{3a}u^x_{\bar{1}1} + s^x_{4a}u^x_{01} + s^y_{1a}u^y_{\bar{1}0} + s^y_{2a}u^y_{00} + s^y_{3a}u^y_{\bar{1}1} + s^y_{4a}u^y_{01}) \\ &+s^{x,y}_{1b}(s^x_{1a}u^x_{00} + s^x_{2a}u^x_{10} + s^x_{3a}u^x_{01} + s^x_{4a}u^x_{11} + s^y_{1a}u^y_{00} + s^y_{2a}u^y_{10} + s^y_{3a}u^y_{01} + s^y_{4a}u^y_{11}) \\ &+s^{x,y}_{4b}(s^x_{1a}u^x_{\bar{1}\bar{1}} + s^x_{2a}u^x_{0\bar{1}} + s^x_{3a}u^x_{\bar{1}0} + s^x_{4a}u^x_{00} + s^y_{1a}u^y_{\bar{1}\bar{1}} + s^y_{2a}u^y_{0\bar{1}} + s^y_{3a}u^y_{\bar{1}0} + s^y_{4a}u^y_{00}) \\ &+s^{x,y}_{3b}(s^x_{1a}u^x_{0\bar{1}} + s^x_{2a}u^x_{1\bar{1}} + s^x_{3a}u^x_{00} + s^x_{4a}u^x_{10} + s^y_{1a}u^y_{0\bar{1}} + s^y_{2a}u^y_{1\bar{1}} + s^y_{3a}u^y_{00} + s^y_{4a}u^y_{10})\Big] \end{aligned}$$

$$\begin{aligned} = A\xi_a\xi_b\Big[&(s^{x,y}_{4b}s^x_{1a})u^x_{\bar{1}\bar{1}} + (s^{x,y}_{4b}s^y_{1a})u^y_{\bar{1}\bar{1}} + (s^{x,y}_{4b}s^x_{2a} + s^{x,y}_{3b}s^x_{1a})u^x_{0\bar{1}} + (s^{x,y}_{4b}s^y_{2a} + s^{x,y}_{3b}s^y_{1a})u^y_{0\bar{1}} \\ &+(s^{x,y}_{3b}s^x_{2a})u^x_{1\bar{1}} + (s^{x,y}_{3b}s^y_{2a})u^y_{1\bar{1}} + (s^{x,y}_{2b}s^x_{1a} + s^{x,y}_{4b}s^x_{3a})u^x_{\bar{1}0} + (s^{x,y}_{2b}s^y_{1a} + s^{x,y}_{4b}s^y_{3a})u^y_{\bar{1}0} \end{aligned}$$

$$
\begin{aligned}
&+(s^{x,y}_{2b}s^{x}_{2a}+s^{x,y}_{1b}s^{x}_{1a}+s^{x,y}_{4b}s^{x}_{4a}+s^{x,y}_{3b}s^{x}_{3a})u^{x}_{00}\\
&+(s^{x,y}_{2b}s^{y}_{2a}+s^{x,y}_{1b}s^{y}_{1a}+s^{x,y}_{4b}s^{y}_{4a}+s^{x,y}_{3b}s^{y}_{3a})u^{y}_{00}\\
&+(s^{x,y}_{1b}s^{x}_{2a}+s^{x,y}_{3b}s^{x}_{4a})u^{x}_{10}+(s^{x,y}_{1b}s^{y}_{2a}+s^{x,y}_{3b}s^{y}_{4a})u^{y}_{10}\\
&+(s^{x,y}_{2b}s^{x}_{3a})u^{x}_{\bar{1}1}+(s^{x,y}_{2b}s^{y}_{3a})u^{y}_{\bar{1}1}\\
&+(s^{x,y}_{2b}s^{x}_{4a}+s^{x,y}_{1b}s^{x}_{3a})u^{x}_{01}+(s^{x,y}_{2b}s^{y}_{4a}+s^{x,y}_{1b}s^{y}_{3a})u^{y}_{01}\\
&+(s^{x,y}_{1b}s^{x}_{4a})u^{x}_{11}+(s^{x,y}_{1b}s^{y}_{4a})u^{y}_{11}\Big]
\end{aligned}
$$

where $u^{x}_{\bar{1}0}=u^{x}(\vec{i}+\bar{1}0)$, for example. Lets denote

$$\mathbf{u}_x(\vec{i})=(u^{x}_{\bar{1}\bar{1}},u^{x}_{0\bar{1}},u^{x}_{1\bar{1}},u^{x}_{\bar{1}0},u^{x}_{00},u^{x}_{10},u^{x}_{\bar{1}1},u^{x}_{01},u^{x}_{11})_{\vec{i}} \tag{4.94}$$

$$\mathbf{u}_y(\vec{i})=(u^{y}_{\bar{1}\bar{1}},u^{y}_{0\bar{1}},u^{y}_{1\bar{1}},u^{y}_{\bar{1}0},u^{y}_{00},u^{y}_{10},u^{y}_{\bar{1}1},u^{y}_{01},u^{y}_{11})_{\vec{i}} \tag{4.95}$$

so that using inner product, one can compactly write

$$\sum_{\vec{j}}Aa(\vec{j})\frac{\partial b(\vec{j})}{\partial u_x(\vec{i})}=A\xi_a\xi_b(\mathbf{s}_{1,ab},\mathbf{s}_{2,ab})\begin{pmatrix}\mathbf{u}_x\\ \mathbf{u}_y\end{pmatrix} \tag{4.96}$$

$$\sum_{\vec{j}}Aa(\vec{j})\frac{\partial b(\vec{j})}{\partial u_y(\vec{i})}=A\xi_a\xi_b(\mathbf{s}_{3,ab},\mathbf{s}_{4,ab})\begin{pmatrix}\mathbf{u}_x\\ \mathbf{u}_y\end{pmatrix} \tag{4.97}$$

where

$$
\begin{aligned}
\mathbf{s}_{1,ab} &= (s^{x}_{4b}s^{x}_{1a},s^{x}_{4b}s^{x}_{2a}+s^{x}_{3b}s^{x}_{1a},s^{x}_{3b}s^{x}_{2a},\\
&\quad s^{x}_{2b}s^{x}_{1a}+s^{x}_{4b}s^{x}_{3a},s^{x}_{2b}s^{x}_{2a}+s^{x}_{1b}s^{x}_{1a}+s^{x}_{4b}s^{x}_{4a}+s^{x}_{3b}s^{x}_{3a},s^{x}_{1b}s^{x}_{2a}+s^{x}_{3b}s^{x}_{4a},\\
&\quad s^{x}_{2b}s^{x}_{3a},s^{x}_{2b}s^{x}_{4a}+s^{x}_{1b}s^{x}_{3a},s^{x}_{1b}s^{x}_{4a})\\
\mathbf{s}_{2,ab} &= (s^{x}_{4b}s^{y}_{1a},s^{x}_{4b}s^{y}_{2a}+s^{x}_{3b}s^{y}_{1a},s^{x}_{3b}s^{y}_{2a},\\
&\quad s^{x}_{2b}s^{y}_{1a}+s^{x}_{4b}s^{y}_{3a},s^{x}_{2b}s^{y}_{2a}+s^{x}_{1b}s^{y}_{1a}+s^{x}_{4b}s^{y}_{4a}+s^{x}_{3b}s^{y}_{3a},s^{x}_{1b}s^{y}_{2a}+s^{x}_{3b}s^{y}_{4a},\\
&\quad s^{x}_{2b}s^{y}_{3a},s^{x}_{2b}s^{y}_{4a}+s^{x}_{1b}s^{y}_{3a},s^{x}_{1b}s^{y}_{4a})\\
\mathbf{s}_{3,ab} &= (s^{y}_{4b}s^{x}_{1a},s^{y}_{4b}s^{x}_{2a}+s^{y}_{3b}s^{x}_{1a},s^{y}_{3b}s^{x}_{2a},\\
&\quad s^{y}_{2b}s^{x}_{1a}+s^{y}_{4b}s^{x}_{3a},s^{y}_{2b}s^{x}_{2a}+s^{y}_{1b}s^{x}_{1a}+s^{y}_{4b}s^{x}_{4a}+s^{y}_{3b}s^{x}_{3a},s^{y}_{1b}s^{x}_{2a}+s^{y}_{3b}s^{x}_{4a},\\
&\quad s^{y}_{2b}s^{x}_{3a},s^{y}_{2b}s^{x}_{4a}+s^{y}_{1b}s^{x}_{3a},s^{y}_{1b}s^{x}_{4a})
\end{aligned}
$$

$$\begin{aligned}\mathbf{s}_{4,ab} &= (s^y_{4b}s^y_{1a}, s^y_{4b}s^y_{2a} + s^y_{3b}s^y_{1a}, s^y_{3b}s^y_{2a},\\ &\quad s^y_{2b}s^y_{1a} + s^y_{4b}s^y_{3a}, s^y_{2b}s^y_{2a} + s^y_{1b}s^y_{1a} + s^y_{4b}s^y_{4a} + s^y_{3b}s^y_{3a}, s^y_{1b}s^y_{2a} + s^y_{3b}s^y_{4a},\\ &\quad s^y_{2b}s^y_{3a}, s^y_{2b}s^y_{4a} + s^y_{1b}s^y_{3a}, s^y_{1b}s^y_{4a})\end{aligned}$$

Note, that for $b = a$, which implies a square term in the expression for potential, the middle elements of $\mathbf{s}_1$ and $\mathbf{s}_4$ automatically equal to largest possible integer 4 that corresponds to the center atom at $\vec{i}$. This can be observed in the table below.

To summarize this chapter, lets rewrite

$$\begin{aligned}\begin{pmatrix} \partial/\partial u_x(\vec{i}) \\ \partial/\partial u_y(\vec{i}) \end{pmatrix} \sum_{\vec{j}} Aa(\vec{j})b(\vec{j}) &= A\xi_a\xi_b\Bigg[\begin{pmatrix} \mathbf{s}_{1,ab} & \mathbf{s}_{2,ab} \\ \mathbf{s}_{3,ab} & \mathbf{s}_{4,ab} \end{pmatrix} \begin{pmatrix} \mathbf{u}_x \\ \mathbf{u}_y \end{pmatrix}\\ &\quad + \begin{pmatrix} \mathbf{s}_{1,ba} & \mathbf{s}_{2,ba} \\ \mathbf{s}_{3,ba} & \mathbf{s}_{4,ba} \end{pmatrix} \begin{pmatrix} \mathbf{u}_x \\ \mathbf{u}_y \end{pmatrix} \Bigg] \end{aligned} \tag{4.98}$$

where $\mathbf{s}_{n,ab} \neq \mathbf{s}_{n,ba}$, or less generally for $b(\vec{i}) = a(\vec{i})$

$$\begin{pmatrix} \partial/\partial u_x(\vec{i}) \\ \partial/\partial u_y(\vec{i}) \end{pmatrix} \sum_{\vec{j}} Aa(\vec{j})^2 = 2A\xi_a^2 \begin{pmatrix} \mathbf{s}_{1,aa} & \mathbf{s}_{2,aa} \\ \mathbf{s}_{3,aa} & \mathbf{s}_{4,aa} \end{pmatrix} \begin{pmatrix} \mathbf{u}_x \\ \mathbf{u}_y \end{pmatrix} \tag{4.99}$$

where upper matrix row corresponds to derivative in u_x, while lower corresponds to derivative in u_y.

Also, for all the symmetry modes of interest

$$\xi_{e_1} = \xi_{e_2} = \xi_{e_3} = \xi_{s_+} = \xi_{s_-} = \xi_r = \frac{1}{2\sqrt{2}}.$$

4.A.4 Matrix Elements

From previously derived results summarized in (4.98) and (4.99), quantities for all $\mathbf{s}$ values relevant to Equation (4.87) can be calculated. These quantities appear in the following table

case	$\bar{1}\bar{1}, 0\bar{1}, 1\bar{1}, \bar{1}0, 00, 10, \bar{1}1, 01, 11$	$\bar{1}\bar{1}, 0\bar{1}, 1\bar{1}, \bar{1}0, 00, 10, \bar{1}1, 01, 11$
$\mathbf{s}_{1,e_1e_1} : \mathbf{s}_{2,e_1e_1}$	-1 2 -1 -2 4 -2 -1 2 -1	-1 0 1 0 0 0 1 0 -1
$\mathbf{s}_{3,e_1e_1} : \mathbf{s}_{4,e_1e_1}$	-1 0 1 0 0 0 1 0 -1	-1 -2 -1 2 4 2 -1 -2 -1
$\mathbf{s}_{1,e_2e_2} : \mathbf{s}_{2,e_2e_2}$	-1 -2 -1 2 4 2 -1 -2 -1	-1 0 1 0 0 0 1 0 -1
$\mathbf{s}_{3,e_2e_2} : \mathbf{s}_{4,e_2e_2}$	-1 0 1 0 0 0 1 0 -1	-1 2 -1 -2 4 -2 -1 2 -1
$\mathbf{s}_{1,e_3e_3} : \mathbf{s}_{2,e_3e_3}$	-1 2 -1 -2 4 -2 -1 2 -1	1 0 -1 0 0 0 -1 0 1
$\mathbf{s}_{3,e_3e_3} : \mathbf{s}_{4,e_3e_3}$	1 0 -1 0 0 0 -1 0 1	-1 -2 -1 2 4 2 -1 -2 -1
$\mathbf{s}_{1,s_+s_+} : \mathbf{s}_{2,s_+s_+}$	1 -2 1 -2 4 -2 1 -2 1	1 -2 1 -2 4 -2 1 -2 1
$\mathbf{s}_{3,s_+s_+} : \mathbf{s}_{4,s_+s_+}$	1 -2 1 -2 4 -2 1 -2 1	1 -2 1 -2 4 -2 1 -2 1
$\mathbf{s}_{1,s_-s_-} : \mathbf{s}_{2,s_-s_-}$	1 -2 1 -2 4 -2 1 -2 1	-1 2 -1 2 -4 2 -1 2 -1
$\mathbf{s}_{3,s_-s_-} : \mathbf{s}_{4,s_-s_-}$	-1 2 -1 2 -4 2 -1 2 -1	1 -2 1 -2 4 -2 1 -2 1
$\mathbf{s}_{1,rr} : \mathbf{s}_{2,rr}$	-1 -2 -1 2 4 2 -1 -2 -1	1 0 -1 0 0 0 -1 0 1
$\mathbf{s}_{3,rr} : \mathbf{s}_{4,rr}$	1 0 -1 0 0 0 -1 0 1	-1 2 -1 -2 4 -2 -1 2 -1
$\mathbf{s}_{1,e_1e_3} : \mathbf{s}_{2,e_1e_3}$	-1 2 -1 -2 4 -2 -1 2 -1	-1 0 1 0 0 0 1 0 -1
$\mathbf{s}_{3,e_1e_3} : \mathbf{s}_{4,e_1e_3}$	1 0 -1 0 0 0 -1 0 1	1 2 1 -2 -4 -2 1 2 1
$\mathbf{s}_{1,e_3e_1} : \mathbf{s}_{2,e_3e_1}$	-1 2 -1 -2 4 -2 -1 2 -1	1 0 -1 0 0 0 -1 0 1
$\mathbf{s}_{3,e_3e_1} : \mathbf{s}_{4,e_3e_1}$	-1 0 1 0 0 0 1 0 -1	1 2 1 -2 -4 -2 1 2 1
$\mathbf{s}_{1,s_+s_-} : \mathbf{s}_{2,s_+s_-}$	1 -2 1 -2 4 -2 1 -2 1	1 -2 1 -2 4 -2 1 -2 1
$\mathbf{s}_{3,s_+s_-} : \mathbf{s}_{4,s_+s_-}$	-1 2 -1 2 -4 2 -1 2 -1	-1 2 -1 2 -4 2 -1 2 -1
$\mathbf{s}_{1,s_-s_+} : \mathbf{s}_{2,s_-s_+}$	1 -2 1 -2 4 -2 1 -2 1	-1 2 -1 2 -4 2 -1 2 -1
$\mathbf{s}_{3,s_-s_+} : \mathbf{s}_{4,s_-s_+}$	1 -2 1 -2 4 -2 1 -2 1	-1 2 -1 2 -4 2 -1 2 -1
$\mathbf{s}_{1,re_2} : \mathbf{s}_{2,re_2}$	1 2 1 -2 -4 -2 1 2 1	-1 0 1 0 0 0 1 0 -1
$\mathbf{s}_{3,re_2} : \mathbf{s}_{4,re_2}$	1 0 -1 0 0 0 -1 0 1	-1 2 -1 -2 4 -2 -1 2 -1
$\mathbf{s}_{1,e_2r} : \mathbf{s}_{2,e_2r}$	1 2 1 -2 -4 -2 1 2 1	1 0 -1 0 0 0 -1 0 1
$\mathbf{s}_{3,e_2r} : \mathbf{s}_{4,e_2r}$	-1 0 1 0 0 0 1 0 -1	-1 2 -1 -2 4 -2 -1 2 -1

To interpret this table of coefficients, recall

$$\begin{aligned}
\mathbf{u}_x(\vec{i}) &= (u^x_{\bar{1}\bar{1}}, u^x_{0\bar{1}}, u^x_{1\bar{1}}, u^x_{\bar{1}0}, u^x_{00}, u^x_{10}, u^x_{\bar{1}1}, u^x_{01}, u^x_{11}) \\
&= e^{i\omega t} e^{-i(\vec{i}\cdot\vec{k})} \mathbf{U}_{0x} \cdot \mathbf{v}(\vec{k}) \\
\mathbf{u}_y &= (u^y_{\bar{1}\bar{1}}, u^y_{0\bar{1}}, u^y_{1\bar{1}}, u^y_{\bar{1}0}, u^y_{00}, u^y_{10}, u^y_{\bar{1}1}, u^y_{01}, u^y_{11}) \\
&= e^{i\omega t} e^{-i(\vec{i}\cdot\vec{k})} \mathbf{U}_{0y} \cdot \mathbf{v}(\vec{k})
\end{aligned}$$

where $\mathbf{U}_{0x}$ and $\mathbf{U}_{0y}$ are diagonal matrices with corresponding initial displacements along the diagonal, and

$$\mathbf{v}(\vec{k}) = \left(e^{i(k_x+k_y)}, e^{ik_y}, e^{i(-k_x+k_y)}, e^{ik_x}, 1, e^{-ik_x}, e^{-i(k_x+k_y)}, e^{-ik_y}, e^{-i(k_x+k_y)}\right)$$

As an example consider a case:

$$\mathbf{s}_{1,e_1e_1} = (\texttt{-1 2 -1 -2 4 -2 -1 2 -1}) \;\Rightarrow\; \mathbf{s}_{1,e_1e_1} \cdot \mathbf{v}$$

$$\begin{aligned}
\mathbf{s}_{1,e_1e_1} \cdot \mathbf{v} &= -e^{i(k_x+k_y)} + 2e^{ik_y} - e^{i(-k_x+k_y)} - 2e^{ik_x} + 4 - 2e^{-ik_x} \\
&\quad -e^{-i(k_x+k_y)} + 2e^{-ik_y} - e^{-i(k_x+k_y)} \\
&= -(e^{ik_x} - 2 + e^{-ik_x})(e^{ik_y} + 2 + e^{-ik_y}) \\
&= 4(1-\cos k_x)(1+\cos k_y).
\end{aligned}$$

Total of four unique pattern-cases (using intermediate roman numeral notation) can be identified, down to $\pm$:

$$\boxed{\text{I}}: \quad \texttt{-1 2 -1 -2 4 -2 -1 2 -1} \;\Rightarrow\; 4(1-\cos k_x)(1+\cos k_y) \tag{4.100}$$

$$\boxed{\text{II}}: \quad \texttt{-1 0 1 0 0 0 1 0 -1} \;\Rightarrow\; 4\sin k_x \sin k_y \tag{4.101}$$

$$\boxed{\text{III}}: \quad \texttt{-1 -2 -1 2 4 2 -1 -2 -1} \;\Rightarrow\; 4(1+\cos k_x)(1-\cos k_y) \tag{4.102}$$

$$\boxed{\text{IV}}: \quad \texttt{1 -2 1 -2 4 -2 1 -2 1} \;\Rightarrow\; 4(1-\cos k_x)(1-\cos k_y) \tag{4.103}$$

$$\frac{\partial e_1^2}{\partial u_{x,y}} = \frac{2}{(2\sqrt{2})^2}\left(\begin{array}{c|c} \text{I} & \text{II} \\ \hline \text{II} & \text{III} \end{array}\right) = \frac{1}{4}\left(\begin{array}{c|c} \text{I} & \text{II} \\ \hline \text{II} & \text{III} \end{array}\right) \tag{4.104}$$

$$\frac{\partial e_2^2}{\partial u_{x,y}} = \frac{2}{(2\sqrt{2})^2}\left(\begin{array}{c|c} \text{III} & \text{II} \\ \hline \text{II} & \text{I} \end{array}\right) = \frac{1}{4}\left(\begin{array}{c|c} \text{III} & \text{II} \\ \hline \text{II} & \text{I} \end{array}\right) \tag{4.105}$$

$$\frac{\partial e_3^2}{\partial u_{x,y}} = \frac{2}{(2\sqrt{2})^2}\left(\begin{array}{c|c} \text{I} & -\text{II} \\ \hline -\text{II} & \text{III} \end{array}\right) = \frac{1}{4}\left(\begin{array}{c|c} \text{I} & -\text{II} \\ \hline -\text{II} & \text{III} \end{array}\right) \tag{4.106}$$

$$\frac{\partial(s_+^2 + s_-^2)}{\partial u_{x,y}} = \frac{2}{(2\sqrt{2})^2}\left(\begin{array}{c|c} \text{IV} & \text{IV} \\ \hline \text{IV} & \text{IV} \end{array}\right) + \frac{2}{(2\sqrt{2})^2}\left(\begin{array}{c|c} \text{IV} & -\text{IV} \\ \hline -\text{IV} & \text{IV} \end{array}\right)$$

$$= \frac{1}{2}\left(\begin{array}{c|c} \mathrm{IV} & 0 \\ \hline 0 & \mathrm{IV} \end{array}\right) \tag{4.107}$$

$$\frac{\partial r^2}{\partial u_{x,y}} = \frac{2}{(2\sqrt{2})^2}\left(\begin{array}{c|c} \mathrm{III} & -\mathrm{II} \\ \hline -\mathrm{II} & \mathrm{I} \end{array}\right) = \frac{1}{4}\left(\begin{array}{c|c} \mathrm{III} & -\mathrm{II} \\ \hline -\mathrm{II} & \mathrm{I} \end{array}\right) \tag{4.108}$$

$$\begin{aligned} \frac{\partial(e_1e_3)}{\partial u_{x,y}} &= \frac{1}{(2\sqrt{2})^2}\left(\begin{array}{c|c} \mathrm{I} & \mathrm{II} \\ \hline -\mathrm{II} & -\mathrm{III} \end{array}\right) + \frac{1}{(2\sqrt{2})^2}\left(\begin{array}{c|c} \mathrm{I} & -\mathrm{II} \\ \hline \mathrm{II} & -\mathrm{III} \end{array}\right) \\ &= \frac{1}{4}\left(\begin{array}{c|c} \mathrm{I} & 0 \\ \hline 0 & -\mathrm{III} \end{array}\right) \end{aligned} \tag{4.109}$$

$$\begin{aligned} \frac{\partial(s_+s_-)}{\partial u_{x,y}} &= \frac{1}{(2\sqrt{2})^2}\left(\begin{array}{c|c} \mathrm{IV} & \mathrm{IV} \\ \hline -\mathrm{IV} & -\mathrm{IV} \end{array}\right) + \frac{1}{(2\sqrt{2})^2}\left(\begin{array}{c|c} \mathrm{IV} & -\mathrm{IV} \\ \hline \mathrm{IV} & -\mathrm{IV} \end{array}\right) \\ &= \frac{1}{4}\left(\begin{array}{c|c} \mathrm{IV} & 0 \\ \hline 0 & -\mathrm{IV} \end{array}\right) \end{aligned} \tag{4.110}$$

$$\begin{aligned} \frac{\partial(re_2)}{\partial u_{x,y}} &= \frac{1}{(2\sqrt{2})^2}\left(\begin{array}{c|c} -\mathrm{III} & \mathrm{II} \\ \hline -\mathrm{II} & \mathrm{I} \end{array}\right) + \frac{1}{(2\sqrt{2})^2}\left(\begin{array}{c|c} -\mathrm{III} & -\mathrm{II} \\ \hline \mathrm{II} & \mathrm{I} \end{array}\right) \\ &= \frac{1}{4}\left(\begin{array}{c|c} -\mathrm{III} & 0 \\ \hline 0 & \mathrm{I} \end{array}\right) \end{aligned} \tag{4.111}$$

Now with corresponding normalized coefficients, the full expression for potential term of Lagrange Equation can be written as

$$\begin{aligned} \frac{\partial V_{rec}}{\partial u_{x,y}} &= \frac{\tilde{A}_1}{8}\left(\begin{array}{c|c} \mathrm{I} & \mathrm{II} \\ \hline \mathrm{II} & \mathrm{III} \end{array}\right) + \frac{\tilde{A}_2}{8}\left(\begin{array}{c|c} \mathrm{III} & \mathrm{II} \\ \hline \mathrm{II} & \mathrm{I} \end{array}\right) + \frac{\tilde{A}_3}{8}\left(\begin{array}{c|c} \mathrm{I} & -\mathrm{II} \\ \hline -\mathrm{II} & \mathrm{III} \end{array}\right) \\ &\quad + \frac{\tilde{A}_s}{4}\left(\begin{array}{c|c} \mathrm{IV} & 0 \\ \hline 0 & \mathrm{IV} \end{array}\right) + \frac{\tilde{A}_r}{8}\left(\begin{array}{c|c} \mathrm{III} & -\mathrm{II} \\ \hline -\mathrm{II} & \mathrm{I} \end{array}\right) + \frac{\tilde{C}_{13}}{4}\left(\begin{array}{c|c} \mathrm{I} & 0 \\ \hline 0 & -\mathrm{III} \end{array}\right) \\ &\quad + \frac{\tilde{C}_s}{4}\left(\begin{array}{c|c} \mathrm{IV} & 0 \\ \hline 0 & -\mathrm{IV} \end{array}\right) + \frac{\tilde{C}_{2r}}{4}\left(\begin{array}{c|c} -\mathrm{III} & 0 \\ \hline 0 & \mathrm{I} \end{array}\right) \end{aligned} \tag{4.112}$$

$$= \begin{pmatrix} D_{xx}(\vec{k}) & D_{xy}(\vec{k}) \\ D_{yx}(\vec{k}) & D_{yy}(\vec{k}) \end{pmatrix}. \tag{4.113}$$

with individual matrix elements written as

$$\begin{aligned} D_{xx}(\vec{k}) &= \frac{1}{8}\Big[(\tilde{A}_1 + \tilde{A}_3 + 2\tilde{C}_{13})\boxed{\mathrm{I}} + (\tilde{A}_2 + \tilde{A}_r - 2\tilde{C}_{2r})\boxed{\mathrm{III}} \\ &\quad + (2\tilde{A}_s + 2\tilde{C}_s)\boxed{\mathrm{IV}}\Big] \end{aligned} \tag{4.114}$$

$$D_{xy}(\vec{k}) = \frac{1}{8}\Big[(\tilde{A}_1 + \tilde{A}_2 - \tilde{A}_3 - \tilde{A}_r)\boxed{\mathrm{II}}\Big] \tag{4.115}$$

$$D_{yx}(\vec{k}) = \frac{1}{8}\Big[(\tilde{A}_1+\tilde{A}_2-\tilde{A}_3-\tilde{A}_r)\boxed{\text{II}}\Big] \tag{4.116}$$

$$\begin{aligned} D_{yy}(\vec{k}) &= \frac{1}{8}\Big[(\tilde{A}_2+\tilde{A}_r+2\tilde{C}_{2r})\boxed{\text{I}}+(\tilde{A}_1+\tilde{A}_3-2\tilde{C}_{13})\boxed{\text{III}} \\ &\quad +(2\tilde{A}_s-2\tilde{C}_s)\boxed{\text{IV}}\Big] \end{aligned} \tag{4.117}$$

In case of the kinetic term of Lagrange Equation (4.87), one can write

$$\sum_{\vec{j}} -M\ddot{u}_{x,y}(\vec{j}) = \begin{pmatrix} -M\ddot{\mathbf{u}}_x(\vec{i}) \\ -M\ddot{\mathbf{u}}_y(\vec{i}) \end{pmatrix} = M\omega^2 \begin{pmatrix} \mathbf{u}_x(\vec{k}) \\ \mathbf{u}_y(\vec{k}) \end{pmatrix}$$

and therefore

$$M\omega^2 \begin{pmatrix} \mathbf{u}_x(\vec{k}) \\ \mathbf{u}_y(\vec{k}) \end{pmatrix} = \begin{pmatrix} D_{xx}(\vec{k}) & D_{xy}(\vec{k}) \\ D_{yx}(\vec{k}) & D_{yy}(\vec{k}) \end{pmatrix} \begin{pmatrix} \mathbf{u}_x(\vec{k}) \\ \mathbf{u}_y(\vec{k}) \end{pmatrix} \tag{4.118}$$

4.A.5 Phonon Spectrum

It can be easily shown that for any 2x2 matrix the eigenvalues can be calculated as

$$\text{eigenvalues}\left(\begin{array}{c|c} a & b \\ \hline c & d \end{array}\right) = \frac{1}{2}\left[(a+d)\pm\sqrt{(a-d)^2+4bc}\right] \tag{4.119}$$

which can be applied to the right side of (4.118).

$$\begin{aligned} D_{xx}+D_{yy} &= \frac{1}{8}(\tilde{A}_1+\tilde{A}_2+\tilde{A}_3+\tilde{A}_r+2\tilde{C}_{13}+2\tilde{C}_{2r})\boxed{\text{I}} \\ &\quad +\frac{1}{8}(\tilde{A}_1+\tilde{A}_2+\tilde{A}_3+\tilde{A}_r-2\tilde{C}_{13}-2\tilde{C}_{2r})\boxed{\text{III}}+\frac{1}{2}\tilde{A}_s\boxed{\text{IV}} \\ &= (\tilde{A}_1+\tilde{A}_2+\tilde{A}_3+\tilde{A}_r)(1-\cos k_x\cos k_y) \\ &\quad +(2\tilde{C}_{13}+2\tilde{C}_{2r})(\cos k_y-\cos k_x) \\ &\quad +2\tilde{A}_s(1-\cos k_x)(1-\cos k_y) \end{aligned}$$

$$\begin{aligned} \Big[D_{xx}-D_{yy}\Big]^2 &= \Big[\frac{1}{8}(\tilde{A}_1-\tilde{A}_2+\tilde{A}_3-\tilde{A}_r+2\tilde{C}_{13}-2\tilde{C}_{2r})\boxed{\text{I}} \\ &\quad +\frac{1}{8}(-\tilde{A}_1+\tilde{A}_2-\tilde{A}_3+\tilde{A}_r+2\tilde{C}_{13}-2\tilde{C}_{2r})\boxed{\text{III}} \\ &\quad +\frac{1}{4}2\tilde{C}_s\boxed{\text{IV}}\Big]^2 \\ &= \Big[(\tilde{A}_1-\tilde{A}_2+\tilde{A}_3-\tilde{A}_r)(\cos k_y-\cos k_x) \end{aligned}$$

$$
\begin{aligned}
& +(2\tilde{C}_{13} - 2\tilde{C}_{2r})(1 - \cos k_x \cos k_y) \\
& +2\tilde{C}_s(1 - \cos k_x)(1 - \cos k_y)\Big]^2 \\
4D_{xy}D_{yx} &= \frac{1}{16}(\tilde{A}_1 + \tilde{A}_2 - \tilde{A}_3 - \tilde{A}_r)^2 \boxed{\text{II}}^{\,2} \\
&= (\tilde{A}_1 + \tilde{A}_2 - \tilde{A}_3 - \tilde{A}_r)^2 \sin^2 k_x \sin^2 k_y
\end{aligned}
$$

The two-dimensional phonon spectrum or dispersion relation based on (4.85) can be finalized as

$$\omega(\vec{k})^2 = \frac{1}{2M}\Big[E_1(\vec{k}) \pm \sqrt{E_2(\vec{k})^2 + E_3(\vec{k})^2}\Big] \tag{4.120}$$

where

$$
\begin{aligned}
E_1(\vec{k}) &= (\tilde{A}_1 + \tilde{A}_2 + \tilde{A}_3 + \tilde{A}_r)(1 - \cos k_x \cos k_y) + \\
&\quad +(2\tilde{C}_{13} + 2\tilde{C}_{2r})(\cos k_y - \cos k_x) + \\
&\quad +2\tilde{A}_s(1 - \cos k_x)(1 - \cos k_y), \qquad (4.121) \\
E_2(\vec{k}) &= (\tilde{A}_1 - \tilde{A}_2 + \tilde{A}_3 - \tilde{A}_r)(\cos k_y - \cos k_x) + \\
&\quad +(2\tilde{C}_{13} - 2\tilde{C}_{2r})(1 - \cos k_x \cos k_y) + \\
&\quad +2\tilde{C}_s(1 - \cos k_x)(1 - \cos k_y), \qquad (4.122) \\
E_3(\vec{k}) &= (\tilde{A}_1 + \tilde{A}_2 - \tilde{A}_3 - \tilde{A}_r)\sin k_x \sin k_y. \qquad (4.123)
\end{aligned}
$$

4.A.6 Verifying and Plotting Results

Consider a set of initial values

```
==================================================
INPUT PARAMETERS:
  A1 = 5, A2 = 4, A3 = -4, As = 5
  C12 = -3, C13 = -5, C1s = -7, C3s = 2, C23r = 0.5
  F3 = 50, F3r = 0.5
EXPANSION POINT:
  e0_1 = 0.1, e0_3 = 0.316228
NORMALIZED PARAMETERS:
  A1 = 5, A2 = 3.4, A3 = 10, As = 3.6, Ar = 0.05
  C13 = -3.16228, Cs = 0.632456, C2r = 0.158114
==================================================
```

Note that $\tilde{e}_3$ (computer: `e0_3`) chosen as a positive value.

Plot of both branches can be seen in Figure 4.17. The plotted continuous spectrum is superimposed with eigenvalues of discrete system of 4x4 atoms. Calculations for discrete system are done independently to make a verification case for obtained analytical dispersion relation (4.120). Points in k-space are placed on 4x4 grid with

$$k_x, k_y \in \{-\frac{\pi}{2}, 0, \frac{\pi}{2}, \pi\}.$$

Increasing set of eigenvalues for discrete system produced following eigenvalues

```
=======================================
      0     8.6754    11.5987    17.1404
      0     8.6754    11.5987    17.1404
 3.1338     9.7013    11.8702    17.3509
 3.1338     9.7013    15.6367    21.3246
 3.7662    10.0133    15.6367    21.3246
 3.7662    10.0133    15.6367    27.2596
 6.2675    10.0133    15.6367    27.2596
 7.5325    10.0133    16.9298    42.6491
=======================================
```

shown in increasing order. On the other hand, continuous spectrum (4.120) generated following results

```
=======================================
Upper Branch:
27.2596    42.6491    27.2596    16.9298
15.6367    21.3246    15.6367    17.1404
 8.6754          0     8.6754    17.3509
15.6367    21.3246    15.6367    17.1404
Lower Branch:
11.5987     6.2675    11.5987    11.8702
10.0133     3.1338    10.0133     9.7013
3.7662           0     3.7662     7.5325
10.0133     3.1338    10.0133     9.7013
=======================================
```

at the corresponding k-points, as seen on the plots of Figure 4.17. Accuracy of 4 significant digits is sufficient to observe one-to-one comparison of both sets. Closer observation indicates a perfect match.

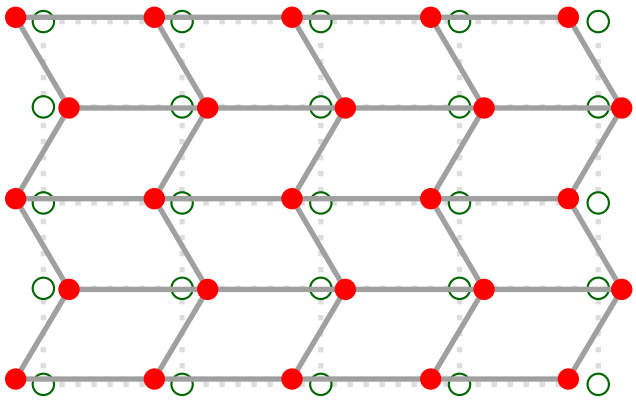

Figure 4.15 (Color) Sample eigenmode corresponding to eigenvalue of 6.2675 on 4x4 system, with the point located at $k_x = 0, k_y = \pi$ on the phonon spectrum.

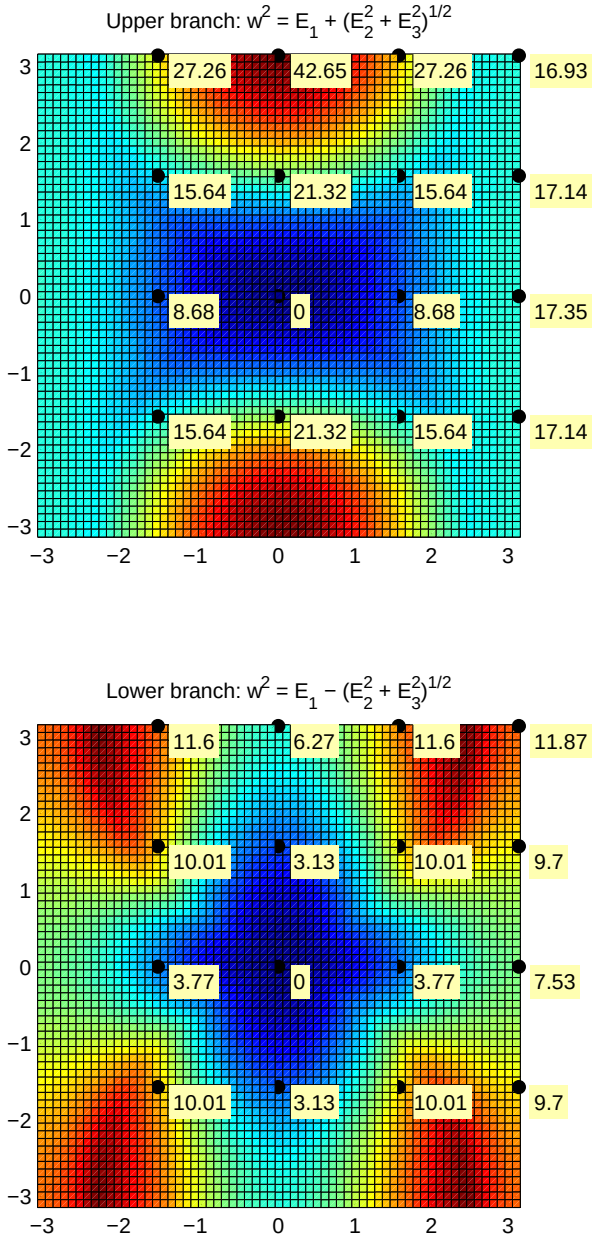

Figure 4.16 (Color) Figure (a) shows upper branch of phonon spectrum squared, whereas (b) shows lower branch. Labeled points are discrete values of 4x4 system of atoms with corresponding values superimposed.

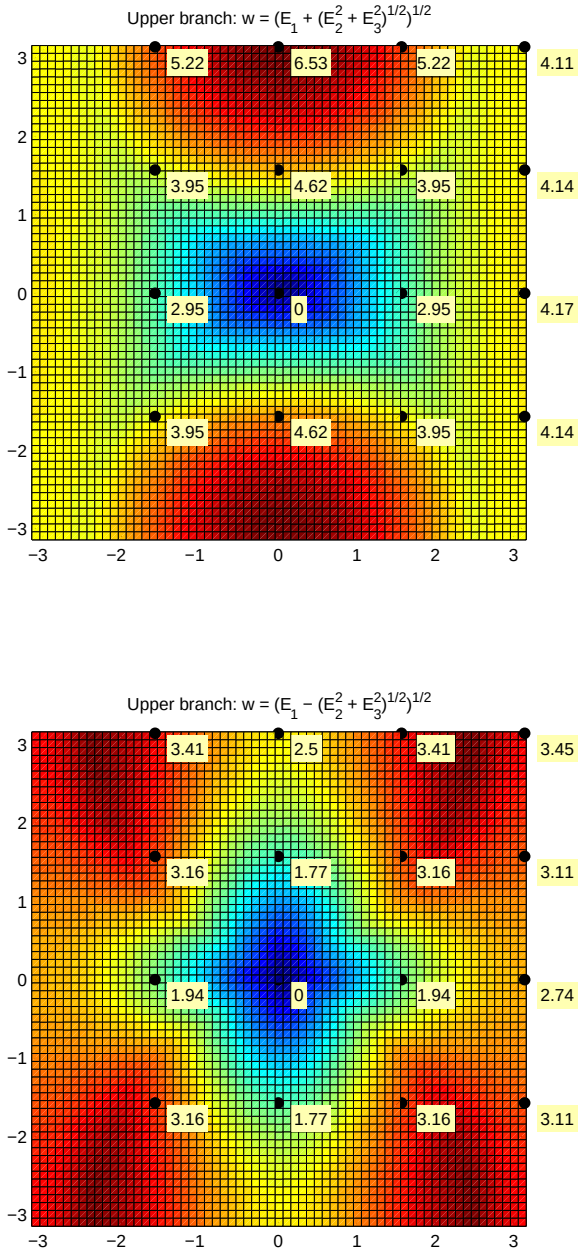

Figure 4.17 (Color) Figure (a) shows upper branch of phonon spectrum, whereas (b) shows lower branch. Labeled points are discrete values of 4x4 system of atoms with corresponding values superimposed.

CHAPTER 5

SUMMARY AND CLOSING REMARKS

Strongly momentum-dependent local charge screening dynamics is presented in CE-type charge, orbital, and spin ordered $La_{0.5}Sr_{1.5}MnO_4$, based on Mn K-edge resonant inelastic x-ray scattering data. Through a comparison with theoretical calculations, it is shown that the observed momentum dependence reflects highly localized, nearest neighbor screening of the transient local charge perturbation in this compound with an exciton-like screening cloud, rather than delocalized screening. The size of the screening cloud is estimated to be about 0.4–0.5 interatomic distances.

From the analysis of a Keating energy expression expanded in terms of the atomic-scale symmetry-modes, it is found that the effect of small *RE* ion size, known as chemical pressure effect, is significant in stabilizing the long range Jahn-Teller distortion in undoped perovskite manganites. Good agreement with the experimental data is obtained on the Jahn-Teller ordering temperature and the substantial increase of the Jahn-Teller ordering temperature from $LaMnO_3$ to $PrMnO_3$ and $NdMnO_3$. It is proposed that similar effects need to be considered to understand the phase diagram for doped perovskite manganites. The appearance of the uniform shear distortion below the Jahn-Teller ordering temperature is also explained in terms of the coupling between coherent shear, buckling, and deviatoric distortions within the Jahn-Teller energy. Moreover, the ratio between these distortions at low temperature is estimated, and good agreement with experimental data for $LaMnO_3$, $PrMnO_3$, and $NdMnO_3$ is found, which confirms the coupling proposed between them in the model.

The mode-based atomic-scale description of the lattice dynamics is also presented. It is established that not only the potential energy but also the kinetic energy can be described in terms of the atomic-scale modes, for which the inclusion of the rigid modes is essential. The atomic-scale mode-based approach for the dynamics of

the one-dimensional chain and two-dimensional square lattice with a mono-atomic basis is demonstrated. By using the constraint equations, the modified Lagrangian equations are obtained in terms of atomic-scale modes only, without explicit use of the displacement variables. This approach is extended to quantum mechanics, to obtain the conjugate momenta and commutation relations in real and reciprocal space. It is expected that this approach would be useful in describing systems with strong anharmonicity.

CHAPTER 6

CODES DEVELOPED FOR RIXS CALCULATION

Many computer programs have been created during the course of theoretical formalism development for K-edge RIXS, applied to $La_{0.5}Sr_{1.5}MnO_4$ crystal structure. In this chapter, it is noteworthy to present small fraction with two programs detailed in Sections 6.1 and 6.3, as they describe the central algorithms behind calculations, whereas Section 6.2 describes inclusion of physical parameters.

6.1 Code for Setting Up Hamiltonian Matrices with Hartree-Fock Approximation

Following computer code is related to the discussion in Chapter 2 and was developed for Matlab.[1] Program sets up all the necessary Hamiltonian matrices and evaluates total Hamiltonian described in Equation (2.18), with inclusion of Hartree-Fock approximation. All the related figure plotting routines are omitted for compactness and clarity.

```
001    % Entry point (Hit F5 to run)
002    %{
003    ================================================================================
004    DESIGNED BY:    Tsezar F. Seman
005    AFFILIATION:    NJIT University, Physics Department
006    MODIFIED ON:    06/16/2012
007    COPYRIGHT:      (c) Tsezar F. Seman. All rights reserved.
008    PURPOSE:        Program calculates various Hamiltonians for LaSrMnO4 using
009                    tight binding model.
010    ================================================================================
011    %}
012    function run1_HF(N,CH, bReloadLastState)
013        clc; addpath('_functions_','../__common__');
014        %-------------------------------------------------------
015        % STARTING PARAMS:
016        if nargin < 1
017            clear all;
018            N = 4;
019            CH = 0;
020        end
```

[1] MATLAB® (matrix laboratory) is a numerical computing environment and fourth-generation programming language, developed by MathWorks®. At the time of code development Matlab version R2012a (7.14.0.739) on 64-bit multi-core platform was used.

```
021         if nargin < 3
022             % 0:start from scratch, 1:reload from last state, 2:plot quickly
023             bReloadLastState = 0;
024         end
025         maxSteps = 300;
026         %-------------------------------------------------------
027         % INITIALIZATION:
028         if bReloadLastState
029             % STARTING FROM SAVED DATA:
030             CmdTitle('RE-LOADING SAVED DATA FOR LaSrMnO4');
031             LoadLastState(N,CH);
032             fprintf('%sSYSTEM: N=%i, CH=%i\n\n', StageId(), N,CH);
033         else
034             % STARTING FROM SCRATCH:
035             CmdTitle('LaSrMnO4 HAMILTONIAN CALCULATION');
036             Initialize(N,CH);
037             fprintf('%sSYSTEM: N=%i, CH=%i\n', StageId(), N,CH);
038             fprintf('\n%sCONSTRUCTING OPERATORS:... \n\n', StageId());
039             Set_nOper_All();    % set all n operators for entire i-Space
040             Set_H_nonint();
041             Set_H_corehole();
042         end
043 
044         if bReloadLastState < 2
045             %-------------------------------------------------------
046             % CORE ALGORITHM:
047             % converging toward stable <n> values
048             ConvergeData(maxSteps, bReloadLastState);
049 
050             %-------------------------------------------------------
051             % SAVE MISC DATA
052             SaveLastState();    % save all the final data
053 
054             fprintf('\n%sSAVING TABLES: ...\n', StageId());
055             Table_nXpt();
056             Table_SysParams();
057 
058             %-------------------------------------------------------
059             % EXPORT DATA:
060             %{-
061             fprintf('\n%sEXPORING DATA FOR RIXS AND nDIFF: ...\n', StageId());
062             Save_nDiff();    % For nDiff analysis
063             Save_RIXS();        % For RIXS analysis
064 
065             Save_Hcoloumb_Bands();
066             %}
067         end
068 
069         % use ONLY for Uch estimation:
070         %ExtractDataForUch();
071 
072         GetEocc();
073 
074         %-------------------------------------------------------
075         % PLOTS:
076         %{
077         fprintf('\n%sPLOTTING VARIOUS DATA: ...\n', StageId());
078     %    Plot_Energies();
079         Plot_Tracking();
080 
081     %    Plot_NetSpin();
082     %    Plot_NetCharge();
083         %}
084     end
085 
086     %=========================================================
087     % KEY ALGORITHMIC COMPONNETS:
```

```
088
089     % Construct all <n> operators
090     function Set_nOper_All()
091         % ACCESS:
092         global GL
093
094         % Gather all n_Operaors and save them for later use
095         nPt = size(GL.iPoints,1);
096         for iPt = 1:nPt
097             szFile = sprintf(GL.file_nOper, iPt);
098             if exist(szFile, 'file') ~= 2
099                 c_nOper = cell(1,2);
100                 % Eg:
101                 nOper_eg = Oper_n_eg( GL.iPoints(iPt,:) );
102                 for i=1:2
103                     c_nOper{i} = sparse(nOper_eg(:,:,i));
104                 end
105                 % saving file:
106                 save(szFile,'c_nOper');
107             end
108         end
109     end
110     % Construct H_nonint matrices with block-diagonal values
111     function Set_H_nonint()
112         % ACCESS:
113         global GL
114
115         nk = size(GL.kPoints,1);
116         GL.H_nonint_eg = zeros(16*nk,16*nk,2);
117         for i=1:nk
118             ii = (i-1)*16+1;
119             GL.H_nonint_eg(ii:ii+15,ii:ii+15,:) = Oper_Hnonint_eg( GL.kPoints(i,:) );
120         end
121     end
122     % Construct H_1s3d matrices with core hole
123     function Set_H_corehole()
124         % ACCESS:
125         global GL  Eg
126
127         % Core-Hole site:
128         switch GL.CH
129             case 0
130                 return;
131             case 1
132                 site = [0 0];
133             case 2
134                 site = [1 0];
135             case 3
136                 site = [1 1];
137             case 4
138                 if GL.N == 4
139                     site = [-1 0];    % this is due to iPoints choice
140                 else
141                     site = [3 0];
142                 end
143             case 5
144                 site = [1 -1];
145             case 6
146                 site = [2 -1];
147             case 7
148                 site = [2 0];
149             case 8
150                 site = [2 1];
151             otherwise
152                 error('ERR: Erroneous CH value! CH can only be {0,1,..,8}');
153         end
154         GL.Track_iPoint = find(GL.iPoints(:,1)==site(1) & GL.iPoints(:,2)==site(2));
```

```
155         if isempty(GL.Track_iPoint); error('ERR: Suggested tracking (CH) site is not
     within the domain of iPoints.');end;
156         site = GL.iPoints(GL.Track_iPoint,:);
157
158         % Eg CASE:
159         GL.H_corehole_eg = Eg.C.Uch * sum( Oper_n_eg(site), 3 );
160         GL.H_corehole_eg(:,:,2) = GL.H_corehole_eg(:,:,1);
161     end
162
163
164     % Update nXpt table
165     function Update_nXpt()
166         % ACCESS:
167         global GL
168
169         % extract eigen vectors
170         [vEg_up, eEg_up] = eig(GL.H_tot_eg(:,:,1));        eEg_up = diag(eEg_up);
171         [vEg_dn, eEg_dn] = eig(GL.H_tot_eg(:,:,2));        eEg_dn = diag(eEg_dn);
172         nnEg = size(vEg_up,1) / 8;
173
174         % count number of spins/orbitals for all occupied electrons
175         ii = [1 1];
176         while sum(ii)-2 < 2*nnEg
177             [~,ind] = min([ eEg_up(ii(1),1), eEg_dn(ii(2),1) ]);
178             ii(ind) = ii(ind) + 1;
179         end
180         nEg_up = ii(1) - 1;
181         nEg_dn = ii(2) - 1;
182
183     %{-
184     % Make spins even
185     nEg_up = nnEg;
186     nEg_dn = nnEg;
187     %}
188
189         % just to keep an eye on the count
190         if nEg_up ~= nnEg || nEg_dn ~= nnEg
191             fprintf('!!! Split for %i electrons: [UP:eg|DN:eg]=[%i|%i]\n',...
192                 2*nnEg, nEg_up, nEg_dn);
193         end
194
195         LL1_up = vEg_up(:,1:nEg_up);
196         LL1_dn = vEg_dn(:,1:nEg_dn);
197
198         nPt = size(GL.iPoints,1);
199         nXpt_list_new = zeros(nPt,4);
200         c_nOper = cell(1,2);
201         for iPt = 1:nPt
202             load(sprintf(GL.file_nOper, iPt));    % load nOper into: c_nOper
203             %{-
204             n_xpt = [ ...
205                 sum( sum( (LL1_up' * c_nOper{1}).' .* LL1_up, 1)), ...
206                 sum( sum( (LL1_up' * c_nOper{2}).' .* LL1_up, 1)), ...
207                 sum( sum( (LL1_dn' * c_nOper{1}).' .* LL1_dn, 1)), ...
208                 sum( sum( (LL1_dn' * c_nOper{2}).' .* LL1_dn, 1)) ];
209             %}
210             %{
211             n_xpt = zeros(1,4);
212             % Eg spin UP case:
213             for iv = 1:nEg_up
214                 L = vEg_up(:,iv);
215                 n_xpt(1:2) = n_xpt(1:2) + [L' * c_nOper{1} * L, L' * c_nOper{2} * L];
216             end
217             % Eg spin DOWN case:
218             for iv = 1:nEg_dn
219                 L = vEg_dn(:,iv);
220                 n_xpt(3:4) = n_xpt(3:4) + [L' * c_nOper{1} * L, L' * c_nOper{2} * L];
```

```
221             end
222             %}
223             nXpt_list_new(iPt,:) = real(n_xpt);
224         end
225
226         % Pullay Mixing segment:
227         if GL.isPullay == 1
228             if GL.Track.Size(1) >= 2
229                 alpha = GL.alphaPullay;
230                 nXpt_list_new = alpha        .* nXpt_list_new + ...
231                                 (1-alpha)    .* GL.nXpt_list_old;
232                 GL.nXpt_list_old = GL.nXpt_list;
233             else
234                 GL.nXpt_list_old = GL.nXpt_list;
235             end
236         elseif GL.isPullay == 2
237             nXpt_list_new = GL.alphaPullay    .* nXpt_list_new + ...
238                             GL.betaPullay    .* GL.nXpt_list_old + ...
239                             (1-GL.alphaPullay-GL.betaPullay)    .* GL.nXpt_list_old2;
240             GL.nXpt_list_old2 = GL.nXpt_list_old;
241             GL.nXpt_list_old = GL.nXpt_list;
242         end
243         GL.nXpt_list = nXpt_list_new;
244
245         % this is for data tracking and stopping criteria
246         Eocc = sum(eEg_up(1:nEg_up)) + sum(eEg_dn(1:nEg_dn));
247         GL.Track.Add([Eocc, nXpt_list_new(GL.Track_iPoint,:)], 1:5);
248     end
249     % Calculate total Hamiltonian
250     function Update_Htot()
251         % ACCESS:
252         global GL  Eg
253
254         % Create U-based list for Hartree-Fock
255         U_list = zeros(size(GL.nXpt_list));
256         nXpt_sum = Eg.C.U * sum(GL.nXpt_list(:,1:4),2);
257         for ic = 1:4
258             U_list(:,ic) = nXpt_sum - Eg.C.U * GL.nXpt_list(:,ic);
259         end
260
261         % Create H_coulomb due to Hartree-Fock
262         nPt = size(GL.iPoints,1);
263         H_coulomb_eg = zeros(2*nPt,2*nPt, 2);
264         c_nOper = cell(1,2);
265         for iPt = 1:nPt
266             load(sprintf(GL.file_nOper, iPt));    % load nOper into: c_nOper
267             U = U_list(iPt,:);
268             H_coulomb_eg(:,:,1) = H_coulomb_eg(:,:,1) + U(1)*c_nOper{1} + U(2)*c_nOper{2};
269             H_coulomb_eg(:,:,2) = H_coulomb_eg(:,:,2) + U(3)*c_nOper{1} + U(4)*c_nOper{2};
270         end
271
272         GL.H_tot_eg = GL.H_nonint_eg + H_coulomb_eg;
273         if GL.CH ~= 0
274             GL.H_tot_eg = GL.H_tot_eg + GL.H_corehole_eg;
275         end
276     end
277     function bval = isStopping()
278         global GL
279
280         choice = 1;    % {1,2}
281
282         bval = false;
283         switch choice
284             case 1
285                 del_Eocc = abs(GL.Track.GetLast(1) - GL.Track.GetLast(1,-1));
286                 if del_Eocc < 1e-4
287                     bval = true;
```

```
288                 end
289             case 2
290                 del_n = max( abs(GL.Track.GetLast(2:5) - GL.Track.GetLast(2:5,-1)) );
291                 if del_n < 1e-3
292                     bval = true;
293                 end
294         end
295     end
296     % Converging Loop
297     function ConvergeData(maxSteps, bReloadLastState)
298         global GL
299 
300         % set initial Hamiltonians
301         if bReloadLastState == 0
302             GL.H_tot_eg = GL.H_nonint_eg;
303         end
304         fprintf('%sCALCULATING nXpt and H_tot^(eg): ...\n', StageId());
305         tic;
306         for step = 1:maxSteps
307             fprintf('    * Step %03i/%03i\n', step,maxSteps);
308             Update_nXpt();
309             Update_Htot();
310             % stopping criteria
311             if isStopping(); break; end;
312             % incremental saving for large calculations
313             if GL.N >= 16; SaveLastState(); end;
314         end
315         toc;
316     end
317     %=========================================================
318     % PRINTING / SAVING:
319     function SaveLastState()
320         % ACCESS to save
321         global GL  Eg  stage_id
322 
323         % correct for ellapsed time
324         GL.timediff = GL.timediff + cputime - GL.timecpu;
325         GL.timecpu = cputime;
326 
327         save(sprintf('%s__LastState.mat',GL.file_main), ...
328             'GL','Eg', 'stage_id');
329     end
330     function LoadLastState(N,CH)
331         % ACCESS to overwrite
332         global GL  Eg  stage_id
333 
334         szFile = sprintf('_N%02d_data_/_main_/N%02i_CH%i__LastState.mat',N,N,CH);
335         if exist(szFile, 'file') == 2
336             GL = {};
337             Eg = {};
338             Etot = {};
339             ZnXpt = {};
340             stage_id = {};
341             load(szFile);
342         else
343             error('ERR: File [%s] does not exist. Set bReloadLastState=0
        to generate the file.',szFile);
344         end
345 
346         % correct for ellapsed time
347         GL.timecpu = cputime;
348     end
349 
350     function szId = StageId()
351         global stage_id   % local static storage
352         if isempty(stage_id); stage_id = 0; end;
353         stage_id = stage_id + 1;
```

```
354         szId = sprintf('## % 3i ## - ',stage_id);
355     end
356     function Table_nXpt()
357         global GL
358 
359         cType = {'Mn3x','Mn4 ','Mn3y'};
360         net_spin = GL.nXpt_list * [1 1 -1 -1]';
361 
362         data = [GL.iPoints(:,1:3), GL.nXpt_list(:,1:4), net_spin, sum(GL.nXpt_list(:,1:4), 2)];
363 
364         file = sprintf('%s__nXptTable.txt',GL.file_tables);
365         fid = fopen(file, 'w');
366         fprintf(fid, '+-------------------------------------------------------------+\r\n');
367         fprintf(fid, '| N = %2i: ELECTRON NUMBER TABLE (CH = %i)                    |\r\n',
        GL.N,GL.CH);
368         fprintf(fid, '+------+------+-----------------------------+--------+------+\r\n');
369         fprintf(fid, ' i-pos | orb. |     eg case: < n_{..} >     |  net   | sum(n)\r\n');
370         fprintf(fid, ' ix iy | type | -,up   +,up   -,dn   +,dn   |  spin  |       \r\n');
371         fprintf(fid, '-------+------+-----------------------------+--------+-------\r\n');
372         for i = 1:size(data,1)
373             fprintf(fid, ' % i % i | %s | %6.4f %6.4f %6.4f %6.4f | %+5.3f | %6.4f\r\n', ...
374                 data(i,1:2), cType{data(i,3)}, data(i,4:9)  );
375         end
376         fprintf(fid, '+------+------+-----------------------------+--------+------+\r\n');
377         fprintf(fid, '| CHECK: Sum(n)/N^2 = %5.3f                                  |\r\n',
        sum(sum(GL.nXpt_list))/size(GL.iPoints,1));
378         fprintf(fid, '+-------------------------------------------------------------+\r\n');
379         fclose(fid);
380 
381         fprintf('    * File [%s] have been generated.\n',file);
382     end
383     function Table_SysParams()
384         global GL  Eg
385 
386         nxpt = [GL.nXpt_list(GL.iPoints(:,1)==0 & GL.iPoints(:,2)==0,:); ...
387             GL.nXpt_list(GL.iPoints(:,1)==1 & GL.iPoints(:,2)==0,:); ...
388             GL.nXpt_list(GL.iPoints(:,1)==1 & GL.iPoints(:,2)==1,:); ...
389             GL.nXpt_list(GL.iPoints(:,1)==-1 & GL.iPoints(:,2)==0,:) ...
390             ];
391         cTF = {'false','true '};
392         cCH = {'n/a     ',...
393                'Mn3x+ up','Mn4+  up','Mn3y+ up','Mn4+  up',...
394                'Mn3x+ dn','Mn4+  dn','Mn3y+ dn','Mn4+  dn',};
395 
396         file = sprintf('%s__SysParams.txt',GL.file_tables);
397         fid = fopen(file, 'w');
398         fprintf(fid, '+-----------------------------------------------+\r\n');
399         fprintf(fid, '|        SIMULATION SYSTEM PARAMETERS           |\r\n');
400         fprintf(fid, '+------------+----------------------------------+\r\n');
401         fprintf(fid, '| System:    | N = %2i, Ni = %03i, Nk = %03i      |\r\n',
        GL.N, (GL.N^2), (GL.N^2/8));
402         fprintf(fid, '+------------+---------+---------+-------------+\r\n');
403         fprintf(fid, '| Parameters | Eg      | T2g     | Units       |\r\n');
404         fprintf(fid, '+------------+---------+---------+-------------+\r\n');
405         fprintf(fid, '| Q_1s       | % 6.4f |    -    | angstrom    |\r\n', Eg.C.Q_1s);
406         fprintf(fid, '| Q_2s       | % 6.4f |    -    | angstrom    |\r\n', Eg.C.Q_2s);
407         fprintf(fid, '| Q_3u       | % 6.4f |    -    | angstrom    |\r\n', Eg.C.Q_3u);
408         fprintf(fid, '| Q_3s       | % 6.4f |    -    | angstrom    |\r\n', Eg.C.Q_3s);
409         fprintf(fid, '+------------+---------+---------+-------------+\r\n');
410         fprintf(fid, '| t0         | % 6.4f |    -    | eV          |\r\n', Eg.C.t0);
411         fprintf(fid, '| beta       | % 6.4f |    -    |             |\r\n', Eg.C.beta);
412         fprintf(fid, '| lambda     | % 6.4f |    -    | eV/angstrom |\r\n', Eg.C.lambda);
413         fprintf(fid, '| JhSc       | % 6.4f |    -    | eV          |\r\n', Eg.C.JhSc);
414         fprintf(fid, '| U          | % 6.4f |    -    | eV          |\r\n', Eg.C.U);
415         fprintf(fid, '| Uch        | % 6.4f |    -    | eV          |\r\n', Eg.C.Uch);
416         fprintf(fid, '| shift      | % 6.4f |    -    | eV          |\r\n', Eg.C.shift);
417         fprintf(fid, '+------------+---------+---------+-------------+\r\n');
```

```
418         Q_33 = (Eg.C.Q_3u + Eg.C.Q_3s);
419         Q_34 = (Eg.C.Q_3u - Eg.C.Q_3s);
420         Gap_br = 2 * Eg.C.lambda * Eg.C.beta * Eg.C.Q_1s;
421         Gap_jt = Eg.C.lambda * (sqrt(4 * Eg.C.Q_2s^2 + Q_33^2) - abs(Q_34));
422         Gap_tot = Gap_br + Gap_jt;
423         Gap_jt_Mn3 = 2 * Eg.C.lambda * (sqrt(4 * Eg.C.Q_2s^2 + Q_33^2));
424         fprintf(fid, '| Gap: br    | % 6.4f |    -    | eV          |\r\n', Gap_br);
425         fprintf(fid, '| Gap: JT    | % 6.4f |    -    | eV          |\r\n', Gap_jt);
426         fprintf(fid, '| Gap: Tot   | % 6.4f |    -    | eV          |\r\n', Gap_tot);
427         fprintf(fid, '| Gap: JT Mn3| % 6.4f |    -    | eV          |\r\n', Gap_jt_Mn3);
428         fprintf(fid, '+------------+---------+---------+-------------+\r\n');
429         fprintf(fid, '| Select Eg n_xpt Values:                       |\r\n');
430         fprintf(fid, '| ix iy :   -,up    +,up    -,dn    +,dn       |\r\n');
431         fprintf(fid, '|  0  0 : %6.4f  %6.4f  %6.4f  %6.4f       |\r\n', nxpt(1,1:4));
432         fprintf(fid, '|  1  0 : %6.4f  %6.4f  %6.4f  %6.4f       |\r\n', nxpt(2,1:4));
433         fprintf(fid, '|  1  1 : %6.4f  %6.4f  %6.4f  %6.4f       |\r\n', nxpt(3,1:4));
434         fprintf(fid, '| -1  0 : %6.4f  %6.4f  %6.4f  %6.4f       |\r\n', nxpt(4,1:4));
435         fprintf(fid, '+------------+-------------------------------+\r\n');
436         fprintf(fid, '| C-H Type   | %s                         |\r\n', cCH{GL.CH+1});
437         if GL.CH == 0
438             szCH = 'n/a    ';
439         else
440             szCH = sprintf('(% i,% i)',GL.iPoints(GL.Track_iPoint,1:2));
441         end
442         fprintf(fid, '| C-H Site   | %s                          |\r\n', szCH);
443         fprintf(fid, '| isPullay   | %s                            |\r\n',
      cTF{logical(GL.isPullay)+1} );
444         if GL.isPullay > 0
445             fprintf(fid, '| alpha Pull.| %3.2f                             |\r\n',
      GL.alphaPullay);
446         end
447         fprintf(fid, '| Calc. Time | %s|\r\n', strjust(sprintf('%27.3f sec.',
      GL.timediff), 'left') );
448         fprintf(fid, '| Cycles     | %s|\r\n', strjust(sprintf('%32i',
      GL.Track.Size()), 'left') );
449         fprintf(fid, '| Time Stamp | %s            |\r\n', datestr(now));
450         fprintf(fid, '+------------+-------------------------------+\r\n');
451         fclose(fid);
452
453         fprintf('    * File [%s] have been generated.\n',file);
454     end
455     %============================================================
456     % FIGURE PLOTTING:
457     % private function
458     function Plot_Energies()
459         % ACCESS:
460         global GL  Eg
461
462         E1 = sortrows([eig(GL.H_nonint_eg(:,:,1)); eig(GL.H_nonint_eg(:,:,2))]);
463         E2 = sortrows([eig(GL.H_tot_eg(:,:,1)); eig(GL.H_tot_eg(:,:,2))]);
464         ind = 1:size(E1,1);
465
466         szCH = '';
467         if GL.CH ~= 0
468             szCH = sprintf(', U_{CH}=%4.1f_{eg} (eV)', Eg.C.Uch);
469         end
470         szTitle = sprintf('N=%i, CH=%i: Energy Profile for H_{eg}%s',GL.N,GL.CH,szCH);
471         GL.figId = FigId(GL.figId, szTitle);
472         hold on;
473         plot(ind,E1, '.','MarkerSize',5, 'Color',[.2 .8 1]);
474         plot(ind,E2, '.','MarkerSize',5, 'Color',[0 0 1]);
475
476         minNN = min( E1 );
477         maxNN = max( E2 );
478         title(szTitle);
479         ylabel('Energy - E_F (eV)');
480         legend('E_{nonint}^{eg}' ,'E_{tot}^{eg}', 'Location','SouthEast');
```

```
481
482
483         NN = size(E1,1);
484         plot([1 NN], [0 0], ':k');
485         fermi = size(E1,1) / 8 + 0.5;
486         plot([fermi fermi], [minNN maxNN], ':k');
487         text(fermi,maxNN-.1,'occupied', ...
488             'Rotation',90, 'HorizontalAlignment','right', 'VerticalAlignment','bottom' );
489         text(fermi,maxNN-.1,'unoccupied', ...
490             'Rotation',90, 'HorizontalAlignment','right', 'VerticalAlignment','top' );
491         hold off;
492     end
493     function Plot_Tracking()
494         global GL  Eg
495
496         data = GL.Track.GetData();
497         n = size(data,1);
498
499         Eocc = data(:,1);
500         Sp_up = data(:,[2 3]);
501         Sp_dn = data(:,[4 5]);
502         clrE = [0 .6 0];
503         clrEg = [0 0 1];
504
505         GL.figId = FigId(GL.figId, 'Evolution of various parametes.');
506
507         subplot(3,1,1);
508         plot(Eocc,'.-', 'Color',clrE);
509         szCH = '';
510         if GL.CH == 1
511             szCH = sprintf(', U_{CH}=%4.1f_{eg} (eV)', Eg.C.Uch);
512         end
513         title(sprintf('N=%i, CH=%i: E_{tot}^{OCC} Tracking, E = %.2f (eV)%s',
     GL.N,GL.CH, Eocc(n), szCH ) );
514         xlabel('Steps');
515         ylabel('Energy of Occupied Sites (eV)');
516         xlim([1,n]);
517         ylim([min(Eocc)-5, max(Eocc)+5]);
518
519         szSite = sprintf('(%i,%i)', GL.iPoints(GL.Track_iPoint,1:2));
520
521         subplot(3,1,2); hold on;
522         plot(Sp_up(:,1),'.-', 'Color',clrEg);
523         plot(Sp_up(:,2),'.--', 'Color',clrEg);
524         hold off;
525         title(sprintf('Spin \\uparrow n-Values at site %s',szSite));
526         xlabel('Steps');
527         xlim([1,n]);
528         ylim([-0.1, 1.1]);
529         legend(sprintf('n^{eg}_{-,\\uparrow} = %5.3f',Sp_up(n,1)),...
530             sprintf('n^{eg}_{+,\\uparrow} = %5.3f',Sp_up(n,2)),...
531             'Location','NorthWest');
532
533         subplot(3,1,3); hold on;
534         plot(Sp_dn(:,1),'.-', 'Color',clrEg);
535         plot(Sp_dn(:,2),'.--', 'Color',clrEg);
536         hold off;
537         title(sprintf('Spin \\downarrow n-Values at site %s',szSite));
538         xlabel('Steps');
539         xlim([1,n]);
540         ylim([-0.1, 1.1]);
541         legend(sprintf('n^{eg}_{-,\\downarrow} = %5.3f',Sp_dn(n,1)),...
542             sprintf('n^{eg}_{+,\\downarrow} = %5.3f',Sp_dn(n,2)),...
543             'Location','NorthWest');
544     end
545
546     function Plot_ColoredAtoms(data_C, minmax_C, szTitle)
```

```
547         global GL
548
549         MS = 40;    % marker size limits
550         nPt = size(GL.iPoints,1);
551
552         % define orbital loops
553         orb_size = 0.5;
554         th = 0:0.1:2*pi+0.1;
555         r_hor = orb_size * cos(th).^2;
556         r_ver = orb_size * sin(th).^2;
557         xy_hor = [r_hor.*cos(th); r_hor.*sin(th)];
558         xy_ver = [r_ver.*cos(th); r_ver.*sin(th)];
559         clrCH =  [1 .9 .9];
560         clrOrb = [1 1 1]*.8;
561         clrZig = [1 1 1]*.95;
562
563         GL.figId = FigId(GL.figId, szTitle);
564
565         hold on;
566         % draw CH site
567         if GL.CH ~= 0
568             CH_site = GL.iPoints(GL.Track_iPoint,:);
569             plot(CH_site(1),CH_site(2),'.', 'Color',clrCH, 'MarkerSize',MS*4);
570         end
571         % draw zig-zag and orbitals
572         for iPt = 1:nPt
573             x = GL.iPoints(iPt,1);
574             y = GL.iPoints(iPt,2);
575             switch GL.iPoints(iPt,3)
576                 case 1
577                     plot(x+[-1 1],y+[0 0],'-', 'Color',clrZig,'LineWidth',3);
578                     plot(x+xy_hor(1,:),y+xy_hor(2,:),'-', 'Color',clrOrb);
579                 case 3
580                     plot(x+[0 0],y+[-1 1],'-', 'Color',clrZig,'LineWidth',3);
581                     plot(GL.iPoints(iPt,1)+xy_ver(1,:),GL.iPoints(iPt,2)+xy_ver(2,:),'-',
      'Color',clrOrb);
582             end
583         end
584         % draw color dots
585         nC = 64;
586         cmap = colormap( jet(nC) );
587         for iPt = 1:nPt
588             q = (data_C(iPt) - minmax_C(1)) ./ (minmax_C(2) - minmax_C(1));
589             iColor = max( 1, min(nC, round((nC-1)*q+1) ) );
590             plot(GL.iPoints(iPt,1),GL.iPoints(iPt,2),'.', 'MarkerSize',MS,
      'Color',cmap(iColor,:));
591         end
592
593         hold off;
594         colorbar;
595         caxis(minmax_C);
596         minmax_xy = [min(GL.iPoints(:,1)), max(GL.iPoints(:,1))];
597         xlim(minmax_xy + [-.6, .6]);
598         ylim(minmax_xy + [-.6, .6]);
599         title(szTitle);
600         xlabel('i_x');
601         ylabel('i_y');
602         set(gca,'XTick',(minmax_xy(1):minmax_xy(2)), 'YTick',(minmax_xy(1):minmax_xy(2)), ...
603             'DataAspectRatio',[1 1 1]);
604     end
605     function Plot_NetSpin()
606         global GL
607
608         net_spin = GL.nXpt_list * [1 1 -1 -1]';
609         msp = max(abs(net_spin));
610         minmax_C = [-msp,+msp];
611         Plot_ColoredAtoms(net_spin, minmax_C, ...
```

```
612             sprintf('N=%i, CH=%i: Atomic Net Spin',GL.N,GL.CH));
613     end
614     function Plot_NetCharge()
615         global GL
616
617         net_charge = sum(GL.nXpt_list(:,1:4), 2);
618         minmax_C = [0,max(net_charge)];
619         Plot_ColoredAtoms(net_charge, minmax_C, ...
620             sprintf('N=%i, CH=%i: Atomic Net Charge',GL.N,GL.CH));
621     end
622     %============================================================
623     % EXPORT DATA FOR FURTHER ANALYSIS:
624     function Save_nDiff()
625         global GL  Eg
626
627         data.nXpt_list = GL.nXpt_list;
628     data.U_eg = Eg.C.U;
629     data.Uch_eg = Eg.C.Uch;
630         data.C = Eg.C;
631         if GL.CH == 0
632             % data file without Core Hole, used as a basis
633             data.N = GL.N;
634             data.figId = 20;
635             data.iPoints = GL.iPoints;
636         else
637             data.CH_site = GL.iPoints(GL.Track_iPoint,:);
638         end
639         eval( sprintf('CH%d = data;',GL.CH) );
640         save(GL.file_ndiff, sprintf('CH%d',GL.CH));
641     end
642     function Save_RIXS()
643         global GL  Eg
644
645          data.H_eg = GL.H_tot_eg;
646         data.N = GL.N;
647         data.CH = GL.CH;
648         data.C = Eg.C;
649         if GL.CH == 0
650             % data without Core Hole, used as a basis
651             data.kPoints = GL.kPoints;
652             CH0 = data;    %#ok
653             save(GL.file_rixs, 'CH0');
654         else
655             % data with Core Hole
656             data.CH_site = GL.iPoints(GL.Track_iPoint, 1:2);
657             CH1 = data;    %#ok
658             save(GL.file_rixs, 'CH1');
659         end
660     end
661
662     function Save_Hcoloumb_Bands()
663         global GL
664
665         % n-values are only valid for CH=0, for band's H_coulomb
666         if GL.CH ~= 0; return; end;
667         file = sprintf('%s__nXpt_list.mat', GL.file_main);
668
669         iPoints = GL.iPoints;
670         nXpt_list = GL.nXpt_list;
671         save(file, 'iPoints','nXpt_list');
672     end
673     %============================================================
674
675     function ExtractDataForUch()
676         global GL  Eg
677
678         fid = fopen(sprintf('DataForUch_N%02d_t%.2f.txt', GL.N, Eg.C.t0), 'a');
```

```
679
680         ch = [0,0; 1,0; 1,1; -1,0];
681         if GL.CH == 0
682             for i=1:2%4
683                 indCH = find(GL.iPoints(:,1)==ch(i,1) & GL.iPoints(:,2)==ch(i,2));
684                 S = sum(GL.nXpt_list(indCH,:));
685                 fprintf(fid, '%d  % d  % d  %.4f  %.4f\r\n', ...
686                     GL.CH, ch(i,1),ch(i,2), Eg.C.Uch, S);
687             end
688         else
689                 i = GL.CH;
690                 indCH = find(GL.iPoints(:,1)==ch(i,1) & GL.iPoints(:,2)==ch(i,2));
691                 S = sum(GL.nXpt_list(indCH,:));
692                 fprintf(fid, '%d  % d  % d  %.4f  %.4f\r\n', ...
693                     GL.CH, ch(i,1),ch(i,2), Eg.C.Uch, S);
694         end
695         fclose(fid);
696     end
697
698     function GetEocc()
699         global GL
700
701         Eup = eig(GL.H_tot_eg(:,:,1));
702         Edn = eig(GL.H_tot_eg(:,:,2));
703
704         nF = size(Eup,1) / 8;
705         Eocc = [Eup(1:nF), Edn(1:nF)];
706         Eocc = sum(sum(Eocc));
707         Eocc
708     end
709     %=========================================================
```

6.2 Code for Initialization of Variables

Following computer code written for Matlab, provides initialization for the system described in previous Section 6.1 and specifically related to the physical parameters of a crystal $La_{0.5}Sr_{1.5}MnO_4$, which is related to the discussion in Chapter 2. Additional purpose for this code is to provide initialization for band structure calculation, not included in this chapter.

```
001     %{
002     ================================================================================
003     DESIGNED BY:    Tsezar F. Seman
004     AFFILIATION:    NJIT University, Physics Department
005     MODIFIED ON:    06/16/2012
006     COPYRIGHT:      (c) Tsezar F. Seman. All rights reserved.
007     PURPOSE:        Function initializes all static components, allocates all global
008                     variables. This function must be called ONCE at the beginning.
009     INPUT:          N - system base => N^2 atoms
010                     CH - flag for Core-Hole presence
011     ================================================================================
012     %}
```

```
013    function Initialize(N,CH)
014        if nargin < 0; error('ERR: Initialize(..) must have input parameters.'); end;
015        if nargin == 1; isCluster = false; else isCluster = true; end;
016        %-----------------------------------------------------
017        % DEFINE COMMON GLOBAL STRUCTURE
018        %-----------------------------------------------------
019        global GL
020        GL.path = MakeDir(sprintf('_N%02i_data_',N));
021        % do not define GL for band plots
022        if isCluster
023            if mod(N,4) ~= 0 || N<4; error('ERR: System prameter N must be a positive
       integer divisible by 4.'); end;
024            if mod(round(CH),9) ~= CH; error('ERR: Core-Hole parameter CH must be one
       of: {0,1,..,8}.'); end;
025            GL.N = N;
026            GL.CH = CH;
027            GL.kPoints = GetAll_kPoints(GL.N);    % create all k-points in reduced
       Bruloin zone (N^2/8)
028            GL.iPoints = GetAll_iPoints(GL.N);    % create all i-space points (N^2)
029            GL.nXpt_list = zeros(GL.N^2, 4);      % allocate table for <n..>: 1:4->eg
030
031            % constant matrices
032            GL.H_nonint_eg = [];
033            GL.H_corehole_eg = [];
034            GL.H_tot_eg = [];
035            GL.R_eg = [];                    % used in Oper_n_eg() (see init below..)
036            GL.kDiff_eg = Get_kDiff_eg();    % used in Oper_n_eg()
037
038            % create/verify directory/file prefix for: {n-Operators, main data, tables}
039            GL.file_nOper = sprintf('%s/nOper_%%04i.mat',
       MakeDir(sprintf('_nOper_N%02i_',GL.N)) );
040            GL.file_main = sprintf('%s/N%02i_CH%i',
       MakeDir([GL.path,'/_main_']), GL.N, GL.CH);
041            GL.file_tables = sprintf('%s/N%02i_CH%i',
       MakeDir([GL.path,'/_tables_']), GL.N, GL.CH);
042            GL.file_ndiff = sprintf('%s/N%02i_CH%i',
       MakeDir([GL.path,'/_nDiff_']), GL.N, GL.CH);
043            GL.file_rixs = sprintf('%s/N%02i_CH%i',
       MakeDir([GL.path,'/_RIXS_']), GL.N, GL.CH);
044
045            % miscellaneous
046            GL.figId = 1;            % starting figId
047            GL.timecpu = cputime;    % cpu time to calculate GL.timediff
048            GL.timediff = 0;        % time that already ellapsed in sec
049            GL.Track = clDataTrack(5);    % tracking data: [E_occ, nXpt(0,0,0)]
050            GL.Track_iPoint = find(GL.iPoints(:,1)==0 & GL.iPoints(:,2)==0);
051            if isempty(GL.Track_iPoint); error('ERR: Suggested tracking (CH) site
       is not within the domain of iPoints.');end;
052
053            GL.isPullay = 0;    % {0,1,2}
054            %{-
055            if mod(CH,2) == 1
056                GL.isPullay = 2;
057            else
058                GL.isPullay = 0;
059            end
060            %}
061            if GL.isPullay == 1
062                GL.alphaPullay = 0.1;
063                if GL.alphaPullay > 1.0; error('ERR: alpha > 1, must be < 1.'); end;
064                GL.nXpt_list(:,1) = 0.25;
065                GL.nXpt_list(:,3) = 0.25;
066                GL.nXpt_list_old = GL.nXpt_list;    % allocate table for <n..>
       USED for Pullay Mixing only!
067            elseif GL.isPullay == 2
068                GL.alphaPullay = 0.3;
069                GL.betaPullay = 0.3;
```

```
070             if (GL.alphaPullay+GL.betaPullay) > 1.0; error('ERR: alpha+beta > 1,
      must be < 1.'); end;
071             GL.nXpt_list(:,1) = 0.25;
072             GL.nXpt_list(:,3) = 0.25;
073             GL.nXpt_list_old = GL.nXpt_list;
074             GL.nXpt_list_old2 = GL.nXpt_list;
075         end
076     end
077
078     %-----------------------------------------------------
079     % DEFINE Eg GLOBAL STRUCTURE
080     %-----------------------------------------------------
081     global Eg
082     % Physical Constants:
083     %Eg.C.lambda = sqrt(3/2)*1.38*0.4/0.228;    % (eV/angstrom), J-T param, (= 2.9652)
084 %    Eg.C.lambda = 1.69;                        % (eV/angstrom), J-T param
085 %    Eg.C.JhSc = 2.47 / 2;                      % (eV), Hund's param, (= 1.235)
086 %    Eg.C.U = 1.6;                              % (eV), Coulomb potential
087 %    Eg.C.Uch = -2.6;                           % (eV), core-hole potential
088
089     % Experimentally determined:
090     Eg.C.Q_1s =  0.05311622;                   % (A) distortion parameter
091     Eg.C.Q_2s =  0.05444722;                   % (A) distortion parameter
092     Eg.C.Q_3u =  0.10736930;                   % (A) distortion parameter
093     Eg.C.Q_3s = -0.01183920;                   % (A) distortion parameter
094
095     % Resonance parameters (used in RIXS model only):
096     %Eg.C.omega_in =    0.0;  % (eV), calculated later
097     Eg.C.Gamma1 =    0.75;    % (eV), set here for Mn3 C-H
098     Eg.C.Gamma2 =    0.75;    % (eV), set here for Mn4 C-H
099
100
101     % CHOSEN PARAMETERS:
102     Eg.C.beta = 2.0;                           % (unitless) breathing parameter
103     Eg.C.t0 = 1.2;
104     Eg.C.lambda =  4.566; % 5.953;
105     Eg.C.U = 0.95 * 1.6;  %(= 1.52)
106     Eg.C.JhSc = 1.8 * 2.47 / 2;  % (=2.2230)
107     Eg.C.Uch = -2.0;
108
109     Eg.C.shift = 4.17279306;    % value for N16 t0 = 0.9
110
111
112     %    beta    t0      lambda  U       Uch
113     %----------------------------------------
114     Params = [...
115         1.5,    0.1,    10.79,    3.5,    -4.0,    4.64902595; ...
116         1.5,    0.6,    9.606,    3.5,    -4.0,    4.50117621; ...
117         1.5,    0.9,    7.407,    3.5,    -4.0,    4.17279306; ...
118         1.5,    1.1,    4.810,    3.5,    -4.0,    3.73921945; ...
119         1.5,    1.3,    3.800,    3.5,    -4.0,    3.61694785; ...
120         1.5,    1.32,   3.760,    3.5,    -4.0,    3.61736508; ...
121         1.5,    1.33,   3.748,    3.5,    -4.0,    3.61938530; ...
122         1.5,    1.35,   3.725,    3.5,    -4.0,    3.62362752; ...
123         1.5,    1.40,   3.650,    3.5,    -4.0,    3.62999964; ...
124         1.5,    1.5,    3.509,    3.5,    -4.0,    3.64416614; ...
125         ];
126         %1.5,    1.45,    3.575,    3.5,    -4.0,    0;
127 pCase = 3;
128
129     Eg.C.beta    = Params(pCase,1);
130     Eg.C.t0        = Params(pCase,2);
131     Eg.C.lambda = Params(pCase,3);
132     Eg.C.U         = Params(pCase,4);
133     Eg.C.Uch    = Params(pCase,5);
134     Eg.C.shift    = Params(pCase,6);
135
```

```
136
137
138         % Enable ONLY for running: run_Uch() and Uch_Estimation()
139         %Eg.C.Uch = -1 * load('_temp_.txt');
140
141         %------------------------------------------------------
142         % Hamiltonians 16x16:
143         Eg.H_hund = SetHund_eg(Eg.C.JhSc);
144         Eg.H_jt = SetJahnTeller_eg(Eg.C.lambda, Eg.C.Q_3u, Eg.C.Q_3s, Eg.C.Q_2s);
145         Eg.H_brtng = SetBreathing_eg(Eg.C.lambda,Eg.C.beta, Eg.C.Q_1s);
146         Eg.H_shift = Eg.C.shift .* eye(16);
147
148         if isCluster
149             GL.R_eg = Set_R_eg(Eg.C.Q_3u, Eg.C.Q_3s, Eg.C.Q_2s);
150         end
151
152         %------------------------------------------------------
153         % FOR BANDS ONLY
154         %------------------------------------------------------
155         if not(isCluster)
156             Eg.H_coloumb = SetCoulomb_Bands_eg(N);
157         end
158     end
159     %============================================================
160     function kPoints = GetAll_kPoints(N)
161         kPoints = zeros(N*N/8, 2);
162         dk = 2*pi/N;
163         kx = dk*(-N/4+1:N/4);
164         nkx = length(kx);
165         i = 1;
166         kPoints(i:i+nkx-1,1) = kx';
167         i = i+nkx;
168         ky = dk;
169         while nkx > 2
170             kx = kx(2:nkx-1);
171             nkx = length(kx);
172             kPoints(i:i+nkx-1,1) = kx';
173             kPoints(i:i+nkx-1,2) = ky;
174             i = i+nkx;
175             kPoints(i:i+nkx-1,1) = kx';
176             kPoints(i:i+nkx-1,2) = -ky;
177             i = i+nkx;
178             ky = ky+dk;
179         end
180         kPoints = sortrows(kPoints,[2 1]);
181     end
182     %{
183     Function creates an array of N^2 equally spaced (in 3D) i-points symmetrical w.r.t (0,0).
184     All dimensions run from -N/2+1 to N/2 with increments of 1.
185     NOTE: 3-rd dimension (3-rd column) are orbital id labels: {1,2,3},  not z-coordinate
186     %}
187     function iPoints = GetAll_iPoints(N)
188         iPoints = zeros(N^2, 3);
189         nx = -N/2+1:N/2;
190         ny = nx;
191         nn = length(nx);
192         for iy = 1:nn
193             i = (iy-1)*nn+1;
194             iPoints(i:i+nn-1,1) = nx';
195             iPoints(i:i+nn-1,2) = ny(iy);
196         end
197         % create orbital id labels: 1: Mn^{3+}_-,  2: Mn^{4+}, 3: Mn^{3+}_+
198         for i = 1:size(iPoints,1)
199             switch mod(-iPoints(i,2) - iPoints(i,1), 4)
200                 case 0    % Mn^{3+}_-
201                     iPoints(i,3) = 1;
202                 case 1    % Mn^{4+}
```

```
203                 iPoints(i,3) = 2;
204             case 2    % Mn^{3+}_+
205                 iPoints(i,3) = 3;
206             case 3    % Mn^{4+}
207                 iPoints(i,3) = 2;
208         end
209     end
210 end
211 %=============================================================
212 function m16 = SetHund_eg(JhSc)
213     Z = zeros(2);
214     G = (JhSc / 2) * eye(2);
215     m16 = [ ...
216          Z, G,-G, Z,   Z,-G,-G, Z; ...
217          G, Z, Z,-G,  -G, Z, Z,-G; ...
218         -G, Z, Z, G,  -G, Z, Z,-G; ...
219          Z,-G, G, Z,   Z,-G,-G, Z; ...
220          Z,-G,-G, Z,   Z, G,-G, Z; ...
221         -G, Z, Z,-G,   G, Z, Z,-G; ...
222         -G, Z, Z,-G,  -G, Z, Z, G; ...
223          Z,-G,-G, Z,   Z,-G, G, Z ];
224     m16(:,:,2) = -m16(:,:,1);
225 end
226
227 function m16 = SetJahnTeller_eg(lambda, Q_3u, Q_3s, Q_2s)
228     Z = zeros(2);
229     A = -lambda * Q_3u * [ 1,  0;  0, -1];
230     B = -lambda * Q_3s * [ 1,  0;  0, -1];
231     C = -lambda * Q_2s * [ 0, -1; -1,  0];
232     m16 = [ ...
233         A, Z, Z, B,   C, Z, Z, C; ...
234         Z, A, B, Z,   Z, C, C, Z; ...
235         Z, B, A, Z,   Z, C, C, Z; ...
236         B, Z, Z, A,   C, Z, Z, C; ...
237         C, Z, Z, C,   A, Z, Z, B; ...
238         Z, C, C, Z,   Z, A, B, Z; ...
239         Z, C, C, Z,   Z, B, A, Z; ...
240         C, Z, Z, C,   B, Z, Z, A ];
241 end
242
243 function m16 = SetBreathing_eg(lambda, beta, Q_1s)
244     Z = zeros(2);
245     A = -lambda * beta * Q_1s * [1, 0; 0, 1];
246     m16 = [ ...
247         Z, Z, Z, A,   Z, Z, Z, Z; ...
248         Z, Z, A, Z,   Z, Z, Z, Z; ...
249         Z, A, Z, Z,   Z, Z, Z, Z; ...
250         A, Z, Z, Z,   Z, Z, Z, Z; ...
251         Z, Z, Z, Z,   Z, Z, Z, A; ...
252         Z, Z, Z, Z,   Z, Z, A, Z; ...
253         Z, Z, Z, Z,   Z, A, Z, Z; ...
254         Z, Z, Z, Z,   A, Z, Z, Z ];
255 end
256 %=============================================================
257 %{
258 Creates a pair of 16x16 matrices used in Oper_n()
259 First 16x16 matrix is for kx component, second is for ky
260 %}
261 function m16z2 = Get_kDiff_eg()
262     m16z2 = zeros(16,16,2);
263     m2 = ones(2);
264     del_kx = [0, pi,  0, pi,   -pi/2,  pi/2, -pi/2, pi/2];
265     del_ky = [0,  0, pi, pi,   -pi/2, -pi/2,  pi/2, pi/2];
266     for ir = 1:8
267         iir = (ir-1)*2+1;
268         for ic = 1:8
269             iic = (ic-1)*2+1;
```

```
270                 m16z2(iir:iir+1, iic:iic+1, 1) = (del_kx(ic) - del_kx(ir)) .* m2;
271                 m16z2(iir:iir+1, iic:iic+1, 2) = (del_ky(ic) - del_ky(ir)) .* m2;
272             end
273         end
274     end
275
276     %{
277     Creates 3 pairs of 16x16 matrices used  in Oper_n()
278     There are 3 atom types {1,2,3}, and two orbital types each {-,+}
279     %}
280     function m16_R = Set_R_eg(Q_3u, Q_3s, Q_2s)
281         if abs(Q_2s) > eps
282             Q_33 = Q_3u + Q_3s;
283             th0 = atan( (-Q_33 + sqrt(Q_33^2 + 4*Q_2s^2)) / (2*Q_2s) );
284             theta = [-th0, 0, th0];
285         else
286             theta = [0, 0, 0];
287         end
288
289         % 1-2 dim is 16x16
290         % 3-rd dim is atom type based on theta {1,2,3}    => {Mn3_x, Mn4, Mn3_y}
291         % 4-th dim is orbital {1,2} => {-,+}
292         m16_R = zeros(16,16,3,2);
293
294         c2 = cos(theta).^2;
295         s2 = sin(theta).^2;
296         cs = cos(theta).*sin(theta);
297
298         ind = 1:2:16;
299         for i = 1:3
300             m16_R(ind,ind,        i,1) =  c2(i);
301             m16_R(ind,ind+1,    i,1) =  cs(i);
302             m16_R(ind+1,ind,    i,1) =  cs(i);
303             m16_R(ind+1,ind+1,    i,1) =  s2(i);
304
305             m16_R(ind,ind,        i,2) =  s2(i);
306             m16_R(ind,ind+1,    i,2) = -cs(i);
307             m16_R(ind+1,ind,    i,2) = -cs(i);
308             m16_R(ind+1,ind+1,    i,2) =  c2(i);
309         end
310     end
311     %=========================================================
312     % FOR BANDS ONLY:
313     function H_coulomb = SetCoulomb_Bands_eg(N_base)
314         global GL  Eg
315
316         NN = N_base^2;
317         iPoints = []; nXpt_list = [];
318         load(sprintf('%s/_main_/N%02d_CHO__nXpt_list',GL.path,N_base));
319         nP = size(iPoints,1);
320
321         % Create U-based list for Hartree-Fock
322         U_list = zeros(size(nXpt_list));
323         nXpt_sum = Eg.C.U * sum(nXpt_list(:,1:4),2);
324         for ic = 1:4
325             U_list(:,ic) = nXpt_sum - Eg.C.U * nXpt_list(:,ic);
326         end
327
328         m16_R = Set_R_eg(Eg.C.Q_3u, Eg.C.Q_3s, Eg.C.Q_2s);
329         kDiff_eg = Get_kDiff_eg();
330
331         spUp = 1; spDn = 2;
332         oMn = 1; oPl = 2;
333         H_coulomb = zeros(16,16,2);
334         for i = 1:nP
335             U = U_list(i,:);
336             vi = iPoints(i,1:2);
```

```
337             iType = iPoints(i,3);
338             m16_Exp = (1/NN) .* exp(1i.*( vi(1) .* kDiff_eg(:,:,1) + vi(2) .* kDiff_eg(:,:,2) ));
339
340             H_coulomb(:,:,spUp) = H_coulomb(:,:,spUp) + ...
341                 m16_Exp .* ( U(1) .* m16_R(:,:,iType,oMn) + U(2) .* m16_R(:,:,iType,oPl) );
342
343             H_coulomb(:,:,spDn) = H_coulomb(:,:,spDn) + ...
344                 m16_Exp .* ( U(3) .* m16_R(:,:,iType,oMn) + U(4) .* m16_R(:,:,iType,oPl) );
345         end
346     end
347     %=========================================================
```

6.3 Code for RIXS Spectrum Calculation with Kramers-Heisenberg Formula

Further, presented is Matlab code segment for calculation of RIXS intensity based upon exact diagonalization approach, applied to calculated Hamiltonian operators. This code is related to the discussion in Chapter 2. RIXS spectrum is calculated using Equation (2.26), that have been derived from Kramers-Heisenberg formula. All the related figure plotting routines are omitted for compactness and clarity.

```
001     % Entry point (Hit F5 to run)
002     %{
003     ================================================================================
004     DESIGNED BY:    Tsezar F. Seman
005     AFFILIATION:    NJIT University, Physics Department
006     MODIFIED ON:    06/06/2012
007     COPYRIGHT:      (c) Tsezar F. Seman. All rights reserved.
008     PURPOSE:        Calculating RIXS data for eg case.
009     ================================================================================
010     %}
011     function run2_rixs_calc(N,minmax_E)
012         clc; addpath('_functions_','../__common__');
013         if nargin < 1
014             clear all;
015             N = 8;        % must be divisible by 4
016         end;
017         if nargin < 2
018             % energy bounds for RIXS table
019             minmax_E = [-1, 20];    % units: eV
020         end
021
022         %-----------------------------------------
023         % GENERATE RIXS DATASET:
024         CmdTitle(sprintf('LaSrMnO4 RIXS: N = %i', N));
025         fprintf('## SETTING GLOBAL PARAMS... \n');
026         tic; SetGlobals(N); toc;
027         fprintf('\n## CALCULATING RIXS... \n');
028         tic; SetRIXS(minmax_E); toc;
029         fprintf('\n## SAVING CALCULATED RIXS: ... \n');
030         SaveCalcRixs();
031
032         %-----------------------------------------
033         % SAVE RESULTS AS TABLES:
```

```
034         fprintf('\n## SAVING DATA TABLES: ... \n');
035         TableEnergy();
036         TableIntensity();
037         TableSumIntensity();
038 
039         Table_Matrix_kMap();
040         %-----------------------------------------
041         fprintf('\nFINISHED... \n');
042     end
043     %=========================================================
044     % PREPARE DATA FROM CH CORE-HOLE SITES:
045     % Collect all the extended points for the reduced Bruilloin zone and
046     % their indexes mapped to the kPoints
047     function [kPoints_ext, ind_ext] = GetExtended_kPoints(kPoints)
048         sq = 1/sqrt(2);
049         ROT = [sq sq; -sq sq];    % +45 rotation
050         kR = kPoints * ROT;
051 
052         del = 1e-10;
053         v1 = pi / 2 / sqrt(2);
054         v2 = pi / sqrt(2);
055 
056         % stage 1: x
057         ind1 = find(abs(kR(:,1)-v1) < del);
058         kR_ext1 = kR(ind1,:);
059         kR_ext1(:,1) = kR_ext1(:,1) - v2;
060         % stage 2: y
061         ind2 = find(abs(kR(:,2)-v1) < del);
062         kR_ext2 = kR(ind2,:);
063         kR_ext2(:,2) = kR_ext2(:,2) - v2;
064         % stage 3: x & y
065         ind3 = find(abs(kR(:,1)-v1) < del & abs(kR(:,2)-v1) < del);
066         kR_ext3 = kR(ind3,:);
067         kR_ext3(:,1:2) = kR_ext3(:,1:2) - v2;
068 
069         % finilize
070         kR_ext = [kR_ext1, ind1; kR_ext2, ind2; kR_ext3, ind3];
071         kPoints_ext = kR_ext(:,1:2) * ROT';
072         ind_ext = kR_ext(:,3);
073     end
074     function [kPoints, kPointsExt, kIndexExt] = GetFull_kPoints(N)
075         dk = 2*pi/N;
076         kPoints = zeros(N^2, 2);
077         kx = dk*(-N/2+1:N/2);
078         ky = kx;
079         nn = length(kx);
080         for iy = 1:nn
081             i = (iy-1)*nn+1;
082             kPoints(i:i+nn-1,1) = kx';
083             kPoints(i:i+nn-1,2) = ky(iy);
084         end
085 
086         % extended k-points
087         kPointsExt = [-pi, -pi];
088         kIndexExt = N^2;
089 
090         kSet = [kx', 0.*kx']; kSet(:,2) = -pi;
091         kPointsExt = [kPointsExt; kSet];
092         kIndexExt = [kIndexExt; (N^2-N+1:N^2)'];
093 
094         kSet = [0.*kx', kx']; kSet(:,1) = -pi;
095         kPointsExt = [kPointsExt; kSet];
096         kIndexExt = [kIndexExt; (N:N:N^2)'];
097     end
098     function [V_CH0,MAP_CH0] = GetBaseCH0(H_CH0)
099         global GL
100 
```

```
101         % allocate space
102         nk = size(GL.kPoints,1);
103         nE = size(H_CH0,1);           % # of electorns, total (per spin)
104         V_CH0    = zeros(nE,nE, 2);   % storage for column eigen-vectors
105         MAP_CH0 = zeros(nE, 6, 2);    % storage for [E,kPoint_index,band_index,  E-H index,kx,ky]
106         iBands = (1:16)';
107         % go through every k-point
108         jj = 1:16;
109         for ik = 1:nk
110             % k-point
111             k = GL.kPoints(ik,:);
112             % spin up/down
113             for spin = 1:2
114                 [V,E] = eig( H_CH0(jj,jj,spin) ); E = diag(E);
115                 V_CH0(jj,jj,spin)  = V;         % eigenvectors
116                 MAP_CH0(jj,1,spin) = E;         % energies
117                 MAP_CH0(jj,2,spin) = ik;        % kPoint index
118                 MAP_CH0(jj,3,spin) = iBands;    % band index
119                 MAP_CH0(jj,5,spin) = k(1);      % k_x
120                 MAP_CH0(jj,6,spin) = k(2);      % k_y
121             end
122             % iteration
123             jj = jj + 16;
124         end
125         % sort everything with increasing energy
126         for spin = 1:2
127             MAP_CH0(:,1,spin) = ReNormalize(MAP_CH0(:,1,spin));
128             [MAP_CH0(:,:,spin), ind] = sortrows(MAP_CH0(:,:,spin), 1);
129             V_CH0(:,:,spin) = V_CH0(:,ind,spin);
130         end
131         % set E-H index, used in RIXS table
132         MAP_CH0(:,4, 1) = 1:2:2*nE-1;
133         MAP_CH0(:,4, 2) = 2:2:2*nE;
134     end
135     function [Beta_occ, CoF, Beta_unc, Z, CH_iPoint, Eocc] =
136                     SetBetaMatrices(inv_V_CH0,MAP_CH0, file_CH, CH)
137         % load calculated core-hole Hamiltonian into CH1:
138         load( file_CH );
139         if CH1.CH ~= CH
140             disp('ERR: Core hole input data file mismatch.');
141         end
142         [V_up,E_up] = eig(CH1.H_eg(:,:,1));
143         [V_dn,E_dn] = eig(CH1.H_eg(:,:,2));
144         BetaFull_up = inv_V_CH0(:,:,1) * V_up;
145         BetaFull_dn = inv_V_CH0(:,:,2) * V_dn;
146
147         % allocate space
148         nE = size(MAP_CH0,1);
149         nF = nE / 8;
150         Beta_occ = zeros(   nF,nF,2);
151         CoF      = zeros(   nF,nF,2);
152         Beta_unc = zeros(nE-nF,nF,2);
153
154         % extract return values
155         Beta_occ(:,:,1) = BetaFull_up(1:nF,1:nF);
156         Beta_occ(:,:,2) = BetaFull_dn(1:nF,1:nF);
157
158         Z = [det(Beta_occ(:,:,1)), det(Beta_occ(:,:,2))];
159
160         CoF(:,:,1) = ( Z(1) .* inv(Beta_occ(:,:,1)) ).';
161         CoF(:,:,2) = ( Z(2) .* inv(Beta_occ(:,:,2)) ).';
162
163         Beta_unc(:,:,1) = BetaFull_up(nF+1:nE,1:nF);
164         Beta_unc(:,:,2) = BetaFull_dn(nF+1:nE,1:nF);
165
166         CH_iPoint = CH1.CH_site;
167
```

```
168         % get E_occ, the energy of occupied states for given C-H
169         E_up = diag(E_up);
170         E_dn = diag(E_dn);
171         Eocc = sum(sum( [E_up(1:nF), E_dn(1:nF)] ));
172     end
173     function SetGlobals(N)
174         % starting with blank GL and blank TMP:
175         global GL
176 
177         if mod(N,4)~=0 || N<4
178             error('ERR: N must be divisible by 4, and N >= 4.');
179         end
180 
181         GL.path = sprintf('_N%02i_data_',N);
182 
183         % load calculated base Hamiltonian into CH0:
184         load( sprintf('%s/_RIXS_/N%02i_CH0.mat', GL.path, N) );
185 
186         GL.N = N;
187         GL.C = CH0.C;
188 
189     % DELETE: redundant, left from older version:
190     %GL.U_eg = CH0.C.U;
191     %GL.Uch_eg = CH0.C.Uch;
192 
193     % DELETE:
194     %GL.figId = 30;
195         GL.dir_tables = [GL.path,'/_tables_'];
196         GL.kPoints = CH0.kPoints;
197     % DELETE:
198     %GL.figPref = sprintf('N=%i',N);
199 
200         % extended kPoints and indexes connecting with GL.kPoints
201         [kPoints_ext, ind_ext] = GetExtended_kPoints(GL.kPoints);
202         GL.kPointsExt = kPoints_ext;
203         GL.kIndexExt = ind_ext;
204 
205         % k-points for extended Brillouin zone
206         [GL.kPointsFull, GL.kPointsFullExt, GL.kIndexFullExt] = GetFull_kPoints(N);
207 
208         % return data from base Hamiltonian (CH0) ordered in increasing energy
209         [V_CH0,MAP_CH0] = GetBaseCH0(CH0.H_eg);
210         GL.MAP_CH0 = MAP_CH0;
211 
212         % create inverse once for re-occuring multiplication
213         inv_V_CH0 = zeros(size(V_CH0));
214         inv_V_CH0(:,:,1) = inv(V_CH0(:,:,1).').';
215         inv_V_CH0(:,:,2) = inv(V_CH0(:,:,2).').';
216 
217     %{
218     TFS NOTES:
219         TMP.Beta_occ is redundant since TMP.CoF is needed,
220         but keep for testing, for now!
221     %}
222 
223         % prepare beta matrices
224         nCH = 8;
225         nE = size(CH0.H_eg,1);
226         nF = nE / 8;                                % 8 -> electron filling
227         GL.Beta_occ = zeros(   nF, nF, 2, nCH);    % 2 -> spins
228         GL.CoF      = zeros(   nF, nF, 2, nCH);    % 2 -> spins
229         GL.Beta_unc = zeros(nE-nF, nF, 2, nCH);    % 2 -> spins
230         GL.Z = zeros(nCH,2);                        % 2 -> spins
231         GL.CH_iPoint = zeros(nCH, 2);               % 2 -> ix,iy
232         vEocc_CH = zeros(nCH,1);
233         for CH = 1:nCH
234             file_CH = sprintf('%s/_RIXS_/N%02i_CH%i.mat', GL.path,N,CH);
```

```
235             [Beta_occ, Cof, Beta_unc, Z, CH_iPoint, E_occ] =
236                             SetBetaMatrices(inv_V_CH0,MAP_CH0, file_CH, CH);
237             GL.Beta_occ(:,:,:, CH) = Beta_occ;
238             GL.CoF(:,:,:, CH) = Cof;
239             GL.Beta_unc(:,:,:, CH) = Beta_unc;
240             GL.Z(CH,:) = Z;
241             GL.CH_iPoint(CH,:) = CH_iPoint;
242             vEocc_CH(CH,1) = E_occ;
243         end
244
245         % calculating resonant term for each CH case
246         Eocc_CH0 = sum(sum( [GL.MAP_CH0(1:nF,1,1), GL.MAP_CH0(1:nF,1,2)] ));
247         omega_in = (vEocc_CH(2)-Eocc_CH0 + vEocc_CH(1)-Eocc_CH0) / 2;
248         g1 = GL.C.Gamma1;
249         g2 = GL.C.Gamma2;
250         vGamma = 1i * [g1,g2, g1,g2, g1,g2, g1,g2]';
251         GL.RES = 1.0 ./ (omega_in - (vEocc_CH - Eocc_CH0) + vGamma);
252
253         %{-
254         % adding distortions at Mn4+ sites:
255         ds = 0.01871;
256         dd = [  0,0; ...
257                  ds,-ds;...
258                 0,0; ...
259                 -ds, ds;...
260                 0,0; ...
261                  ds,-ds;...
262                 0,0; ...
263                 -ds, ds ];
264         GL.CH_iPoint = GL.CH_iPoint + dd;
265         %}
266     end
267
268     function SetRIXS(minmax_E)
269         global GL
270
271         nE = size(GL.MAP_CH0,1);
272         nF = nE / 8;
273         nk = size(GL.kPoints, 1);
274         nRows = 8*nk*nk * 14*2 * 2;        % same as: (nE-nF)*nF * 8 * 2
275         iRow = 1;
276         fprintf('    * Calculating RIXS table with %i rows...\n', nRows);
277
278         % RixsData Columns:
279         % 1-hole id, 2-electron id, 3-intensity, 4-energy
280         % 5:6-momentum, 7-spin, 8-indexes of k-points
281         RixsData = zeros(nRows,8);
282         DK = [0,0;  pi,0;  0,pi;  pi,pi;  -pi/2,-pi/2;  pi/2,-pi/2;  -pi/2,pi/2;  pi/2,pi/2];
283         mapOCC = GL.MAP_CH0(   1:nF,:, :);
284         mapUNC = GL.MAP_CH0(nF+1:nE,:, :);
285         rowUNC = zeros(8,nF, 2);
286         % amplitude calculation terms, for every {ke,le,kh,lh,  spin,K}:
287         PH = zeros(8,1);                            % phase
288         X1 = zeros(8,1);                            % one CH excitation
289         X0 = conj(GL.Z(:,1)) .* conj(GL.Z(:,2));    % no excitation
290         RES = GL.RES;                               % resonance denominator
291         for iUNC = 1:(nE-nF)
292             % extract rows for use with CoF
293             for CH = 1:8
294                 rowUNC(CH,:, 1) = GL.Beta_unc(iUNC,:, 1,CH);
295                 rowUNC(CH,:, 2) = GL.Beta_unc(iUNC,:, 2,CH);
296             end
297
298             % populate RIXS table
299             for iOCC = 1:nF
300                 for spin = 1:2
301                     % excitation contribution
```

```
302                 % example for spin up: Z_dn * DETERMINANT^[Beta(SwapedRow)_up]
303                 spin_neg = mod(spin,2)+1;
304                 for CH = 1:8
305                     X1(CH,1) = GL.Z(CH,spin_neg) .*
306                             (rowUNC(CH,:, spin) * (GL.CoF(iOCC,:, spin,CH)).');
307                 end
308
309 %{
310 % TEST DETERMINANT:
311     CH = 1;
312     r = GL.Beta_unc(iUNC,:, spin,CH);
313     B = GL.Beta_occ(:,:, spin,CH);
314     B(iOCC,:) = r;
315     d1 = det(B);
316     d2 = (rowUNC(CH,:, spin) * (GL.CoF(iOCC,:, spin,CH)).');
317     err = abs(d1 - d2);
318     if err > 1e-15
319         err
320     end
321 %}
322
323                 % k-indexes, band-indexes
324                 ik_h = mapOCC(iOCC,2, spin);    ik_e = mapUNC(iUNC,2, spin);
325 %               il_h = mapOCC(iOCC,3, spin);    il_e = mapUNC(iUNC,3, spin);
326                 iH   = mapOCC(iOCC,4, spin);    iE   = mapUNC(iUNC,4, spin);
327                 % momentum change in 1-st BZ
328                 dk = GL.kPoints(ik_e,:) - GL.kPoints(ik_h,:);
329                 % energy
330                 w = mapUNC(iUNC,1, spin) - mapOCC(iOCC,1, spin);
331
332                 for iDK = 1:8
333                     % momentum change in the extended BZ
334                     [q, iq] = CorrectQpt(-dk - DK(iDK,:));
335                     % phase
336                     PH = exp(-1i * (GL.CH_iPoint * q') );
337
338                     % amplitude for all CH
339                     %A = sum(PH .* X1 .* X0 .* RES,  1);
340                     A = sum(PH .* X1 .* X0,  1);
341 %A_tmp = PH .* X1 .* X0;
342 %A = A_tmp(3);
343
344                     % one data row for rixs table
345                     RixsRow = [
346                         iH, ...          % hole id
347                         iE, ...          % electron id
348                         A*conj(A), ...   % rixs intensity
349                         w, ...           % w energy
350                         q(1), ...        % q_x momentum
351                         q(2), ...        % q_y momentum
352                         spin, ...        % spin
353                         iq ...           % q-index
354                         ];
355                     RixsData(iRow,:) = RixsRow;
356                     iRow = iRow+1;
357                 end  % iDK
358             end  % spin
359         end  % iOCC
360     end  % iUNC
361     if iRow-1 ~= nRows
362         disp('ERR: RIXS Table - number of processed rows mismatched.');
363     end
364
365 %    RixsData = RixsData(1:iRow-1,:);
366
367     % reduce table to given energy bouds
368     RixsData = RixsData(RixsData(:,4) <= minmax_E(2), :);
```

```
369         RixsData = RixsData(RixsData(:,4) >= minmax_E(1), :);
370
371         % set new k-points for extended BZ
372         GL.kPoints = GL.kPointsFull;
373         GL.kPointsExt = GL.kPointsFullExt;
374         GL.kIndexExt = GL.kIndexFullExt;
375
376     %{-
377         % Averaging w.r.t. qx <-> -qx:
378         % create swap array for ik
379         N = GL.N;
380         nk = size(GL.kPoints,1);
381         ind_swap = (1:nk)';
382         for iOff = 0:N-1
383             for i = 1:N-1
384                 ind_swap(iOff*N + i) = iOff*N + N-i;
385             end
386         end
387         % process new table
388         RixsData_qxNeg = RixsData;
389         for i = 1:size(RixsData_qxNeg,1)
390             ik = ind_swap( RixsData_qxNeg(i,8) );
391             RixsData_qxNeg(i,8) = ik;
392             RixsData_qxNeg(i,5) = GL.kPoints(ik,1);
393         end
394         % merge with existing table, and averaging intensity
395         RixsData = [RixsData; RixsData_qxNeg];
396         RixsData(:,3) = RixsData(:,3) / 2;
397     %}
398
399         % sort by descending intensity and pass to global
400         GL.RIXS = sortrows(RixsData, -3);
401
402         % integrate all intensities, separately per spin
403         nk = size(GL.kPoints,1);    % must be recalculated, now for extended BZ
404         SumIrixs = zeros(nk,2);
405         for ik = 1:nk
406             SumIrixs(ik,1) = sum( RixsData(RixsData(:,8) == ik & RixsData(:,7) == 1, 3) );
407             SumIrixs(ik,2) = sum( RixsData(RixsData(:,8) == ik & RixsData(:,7) == 2, 3) );
408         end
409         if abs(sum(sum(SumIrixs)) - sum(RixsData(:,3))) > 1e-12
410             disp('ERR: Sum Irixs mismatch. See SetRIXS().');
411         end
412         GL.RIXS_SUM = SumIrixs;
413
414         % cleanup GL
415         GL = rmfield(GL, 'kPointsFull');
416         GL = rmfield(GL, 'kPointsFullExt');
417         GL = rmfield(GL, 'kIndexFullExt');
418         GL = rmfield(GL, 'Beta_occ');
419         GL = rmfield(GL, 'CoF');
420         GL = rmfield(GL, 'Beta_unc');
421         GL = rmfield(GL, 'Z');
422         GL = rmfield(GL, 'CH_iPoint');
423     end
424     %=========================================================
425     % This is  necessary to eliminate 14/15-th significant
426     % digit discrepancy in degenerate values
427     function EE = ReNormalize(E)
428         [EE, ind] = sortrows(E,1);
429         dig_eps = 1000*eps(EE(1));
430
431         igr = 1;
432         groups(igr,1) = 1;
433         val = EE(1);
434         for i = 2:size(EE,1)
435             % if values are not close
```

```
436             if abs(EE(i) - val) > dig_eps
437                 val = EE(i);
438                 groups(igr,2) = i-1;
439                 igr = igr+1;
440                 groups(igr,1) = i;
441             end
442         end
443         groups(igr,2) = i;
444 
445         % fixing values
446         for i = 1:size(groups,1)
447             a = groups(i,1);
448             b = groups(i,2);
449             avg = mean( EE(a:b,1) );
450             EE(a:b,1) = avg;
451         end
452 
453         EE = sortrows([EE, ind],2);
454         EE = EE(:,1);
455     end
456 
457     % map new q-value onto extanded BZ
458     function [q, iq] = CorrectQpt(q)
459         global GL
460 
461         Eps = 1e-10;
462         % kx values
463         if q(1) > pi
464             q(1) = q(1) - 2*pi;
465         elseif q(1) <= -pi + Eps
466             q(1) = q(1) + 2*pi;
467         end
468         % ky values
469         if q(2) > pi
470             q(2) = q(2) - 2*pi;
471         elseif q(2) <= -pi + Eps
472             q(2) = q(2) + 2*pi;
473         end
474         % indexes
475         kk = (GL.kPointsFull(:,1) - q(1)).^2 + (GL.kPointsFull(:,2) - q(2)).^2;
476         iq = find(kk < 1e-10);
477         q = GL.kPointsFull(iq,:);
478     end
479     %============================================================
480     % SAVING DATA:
481     function TableEnergy()
482         global GL
483 
484         file = sprintf('%s/N%02i__RIXS_Energies.txt',GL.dir_tables,GL.N);
485         fid = fopen(file, 'w');
486         fprintf(fid, '+-------------------------------------------+\r\n');
487         fprintf(fid, '| N = %2i: ELECTRON ENERGY SPECTRUM          |\r\n',GL.N);
488         fprintf(fid, '------+-----------+-----------------+----+----\r\n');
489         fprintf(fid, 'iE/iH |   Energy  |BZ:   kx      ky |band| sp \r\n');
490         fprintf(fid, '------+-----------+-----------------+----+----\r\n');
491 
492         nT = size(GL.MAP_CH0,1);
493         nF = nT/8;
494         cSp = {'u ',' d'};
495         for i = nT:-1:1
496             % spin down/up
497             for spin = [2,1]
498                 v = GL.MAP_CH0(i,:,spin);
499                 fprintf(fid, ' %4i | %9.4f |%s%s | %2d | %s\r\n', v(4), v(1), ...
500                     Num2Latex(v(5),0,[8,4]), Num2Latex(v(6),0,[8,4]), v(3), cSp{spin});
501             end
502             % fermi level separator
```

```
503             if i == nF+1
504                 fprintf(fid, '>---------------< FERMI LEVEL >--------------<\r\n');
505             end
506         end
507         fprintf(fid, '------+----------+----------------+----+----\r\n');
508         fclose(fid);
509 
510         fprintf('    * File [%s] have been generated.\n',file);
511     end
512     function TableIntensity()
513         global GL
514 
515         file = sprintf('%s/N%02i__RIXS_Intensity.txt',GL.dir_tables,GL.N);
516         fid = fopen(file, 'w');
517         fprintf(fid, '+-----------------------------------------------------------------+\r\n');
518         fprintf(fid, '| N = %2i: RIXS CALCULATION - PARTIAL TABLE                       |\r\n',
        GL.N);
519         fprintf(fid, '------+------+--------------------+---------+-----------------+---\r\n');
520         fprintf(fid, ' H_id | E_id |       I_RIXS       |  del_w  |    del_q(x,y)   | sp\r\n');
521         fprintf(fid, '------+------+--------------------+---------+-----------------+---\r\n');
522         nR = min(size(GL.RIXS,1), 170);     % limit to about 3 pages in PDF
523         cSp = {'u ',' d'};
524         for i = 1:nR
525             fprintf(fid, ' %4i | %4i | %.16f |%8.4f |%s%s | %s\r\n', GL.RIXS(i,1:4), ...
526                 Num2Latex(GL.RIXS(i,5),0,[8,4]), Num2Latex(GL.RIXS(i,6),0,[8,4]),
        cSp{GL.RIXS(i,7)});
527         end
528         fprintf(fid, '  ... |  ... |                ... |     ... |     ...     ... | ..\r\n');
529         fprintf(fid, '------+------+--------------------+---------+-----------------+---\r\n');
530         fclose(fid);
531 
532         fprintf('    * File [%s] have been generated.\n',file);
533     end
534     function TableSumIntensity()
535         global GL
536 
537         file = sprintf('%s/N%02i__RIXS_SumIntensity.txt',GL.dir_tables,GL.N);
538         fid = fopen(file, 'w');
539         fprintf(fid, '+-----------------------------------------------------------------+\r\n');
540         fprintf(fid, '| N = %2i: Integrated I_RIXS                                      |\r\n',
        GL.N);
541         fprintf(fid, '-----+--------------------+--------------------+----------------\r\n');
542         fprintf(fid, 'k_id | Sum I_RIXS_up      | Sum I_RIXS_dn      |      kx      ky\r\n');
543         fprintf(fid, '-----+--------------------+--------------------+----------------\r\n');
544         Nk = size(GL.kPoints,1);
545         for ik = 1:Nk
546             fprintf(fid, '  %2i | %.16f | %.16f |%s%s\r\n', ik, GL.RIXS_SUM(ik,:), ...
547                 Num2Latex(GL.kPoints(ik,1),0,[8,4]), Num2Latex(GL.kPoints(ik,2),0,[8,4]) );
548         end
549         fprintf(fid, '-----+--------------------+--------------------+----------------\r\n');
550         fclose(fid);
551 
552         fprintf('    * File [%s] have been generated.\n',file);
553     end
554     function Table_Matrix_kMap()
555         global GL
556 
557         sPref = sprintf('%s/N%02i__kMap',GL.dir_tables,GL.N);
558 
559         % export coordinate layout
560         kxy = GL.kPoints(1:GL.N,1);
561         file = sprintf('%s_kx-ky.txt',sPref);
562         fid = fopen(file, 'w');
563         fprintf(fid, 'kx values:\r\n');
564         fprintf(fid, '% .16f ',kxy);
565         fprintf(fid, '\r\n\r\nky values:\r\n');
566         fprintf(fid, '% .16f\r\n',flipud(kxy));
```

```
567         fclose(fid);
568 
569         % export k-map matrix values
570         nD = sum(GL.RIXS_SUM, 2);
571         nD2 = flipud(reshape(nD, GL.N, GL.N)');
572         file = sprintf('%s_matrix_rixs.txt',sPref);
573         fid = fopen(file, 'w');
574         for ir = 1:size(nD2,1)
575             fprintf(fid, ' % .16f',nD2(ir,:));
576             fprintf(fid, '\r\n');
577         end
578         fclose(fid);
579 
580         fprintf('    * Table file [%s] have been generated.\n',file);
581     end
582     %============================================================
583     % SAVING/LOADING:
584     function SaveCalcRixs()
585         % ACCESS to save
586         global GL
587 
588         save(sprintf('%s/_RIXS_/N%02i_CalcRixs.mat',GL.path,GL.N), 'GL');
589     end
590     %============================================================
```

REFERENCES

Ahn, K. H., Fedro, A. J. and van Veenendaal, M.: 2009, Dynamics and spectral weights of shake-up valence excitations in transition metal K-edge resonant inelastic x-ray scattering, *Physical Review B* **79**, 045103–045110.
http://link.aps.org/doi/10.1103/PhysRevB.79.045103

Ahn, K. H., Lookman, T. and Bishop, A. R.: 2004, Strain-induced metal-insulator phase coexistence in perovskite manganites, *Nature* **428**, 401–404.
http://www.nature.com/nature/journal/v428/n6981/full/nature02364.html

Ahn, K. H., Lookman, T., Saxena, A. and Bishop, A. R.: 2003, Atomic scale lattice distortions and domain wall profiles, *Physical Review B* **68**, 092101–092104.
http://link.aps.org/doi/10.1103/PhysRevB.68.092101

Ahn, K. H., Lookman, T., Saxena, A. and Bishop, A. R.: 2005, Electronic properties of structural twin and antiphase boundaries in materials with strong electron-lattice couplings, *Physical Review B* **71**, 212102–212105.
http://link.aps.org/doi/10.1103/PhysRevB.71.212102

Ahn, K. H. and Millis, A. J.: 2000, Effects of magnetic ordering on the anisotropy and temperature dependence of the optical conductivity in $LaMnO_3$: a tight-binding approach, *Physical Review B* **61**, 13545–13559.
http://link.aps.org/doi/10.1103/PhysRevB.61.13545

Ahn, K. H. and Millis, A. J.: 2001, Effects of uniaxial strain in $LaMnO_3$, *Physical Review B* **64**, 115103–115114.
http://link.aps.org/doi/10.1103/PhysRevB.64.115103

Alonso, J. A., Martínez-Lope, M. J., Casais, M. T. and Fernández-Díaz, M. T.: 2000, Evolution of the jahnteller distortion of MnO_6 octahedra in $RMnO_3$ perovskites ($R = Pr, Nd, Dy, Tb, Ho, Er, Y$): A neutron diffraction study, *Inorganic Chemistry* **39**, 917–923.
http://pubs.acs.org/doi/pdf/10.1021/ic990921e

Ament, L. J. P., van Veenendaal, M., Devereaux, T. P., Hill, J. P. and van den Brink, J.: 2011, Resonant inelastic x-ray scattering studies of elementary excitations, *Review of Modern Physics* **83**, 705–767.
http://link.aps.org/doi/10.1103/RevModPhys.83.705

Ashcroft, N. W. and Mermin, N. D.: 1976, *Solid State Physics*, first edn, Brooks Cole. Cengage Learning.

Bała, J. and Horsch, P.: 2005, Spin-orbital physics in the optical conductivity of quarter-filled manganites, *Physical Review B* **72**, 012404–012407.
http://link.aps.org/doi/10.1103/PhysRevB.72.012404

Balagurov, A. M., Bushmeleva, S. N., Pomjakushin, V. Y., Sheptyakov, D. V., Amelichev, V. A., Gorbenko, O. Y., Kaul, A. R., Gan'shina, E. A. and Perkins, N. B.: 2004, Magnetic structure of $NdMnO_3$ consistently doped with Sr and Ru, *Physical Review B* **70**, 014427–014434.
http://link.aps.org/doi/10.1103/PhysRevB.70.014427

Darling, T. W., Migliori, A., Moshopoulou, E. G., Trugman, S. A., Neumeier, J. J., Sarrao, J. L., Bishop, A. R. and Thompson, J. D.: 1998, Measurement of the elastic tensor of a single crystal of $La_{0.83}Sr_{0.17}MnO_3$ and its response to magnetic fields, *Physical Review B* **57**, 5093–5097.
http://link.aps.org/doi/10.1103/PhysRevB.57.5093

Davis, L. C. and Feldkamp, L. A.: 1979, Effect of electron correlations on photoemission from narrow-band metals, *Journal of Applied Physics* **50**, 1944–1949.
http://jap.aip.org/resource/1/japiau/v50/iB3/p1944_s1

Doh, H., Kim, Y. B. and Ahn, K. H.: 2007, Nematic domains and resistivity in an itinerant metamagnet coupled to a lattice, *Physical Review Letters* **98**, 126407–126411.
http://link.aps.org/doi/10.1103/PhysRevLett.98.126407

Dzero, M. O., Gorkov, L. P. and Kresin, V. Z.: 2000, Peculiarities in low temperature properties of doped manganites $A_{1-x}B_xMnO_3$, *The European Physical Journal B* **14**, 459–471.
http://www.springerlink.com/content/fulltext.pdf?id=doi:10.1007/s100510051054

Feldkamp, L. A. and Davis, L. C.: 1980, Asymptotic theory and core level x-ray photoemission spectra, *Physical Review B* **22**, 4994–4996.
http://link.aps.org/doi/10.1103/PhysRevB.22.4994

Fernandez-Baca, J. A., Dai, P., Hwang, H. Y., Kloc, C. and Cheong, S.-W.: 1998, Evolution of the low-frequency spin dynamics in ferromagnetic manganites, *Physical Review Letters* **80**, 4012–4015.
http://link.aps.org/doi/10.1103/PhysRevLett.80.4012

Fetter, A. L. and Walecka, J. D.: 2003, *Quantum Theory of Many-Particle Systems*, first edn, Dover Publications.

Grenier, S., Hill, J. P., Kiryukhin, V., Ku, W., Kim, Y.-J., Thomas, K. J., Cheong, S.-W., Tokura, Y., Tomioka, Y., Casa, D. and Gog, T.: 2005, $d - d$ excitations in manganites probed by resonant inelastic x-ray scattering, *Physical Review Letters* **94**, 047203–047206.
http://link.aps.org/doi/10.1103/PhysRevLett.94.047203

Herrero-Martín, J., Blasco, J., García, J., Subías, G. and Mazzoli, C.: 2011, Structural changes at the semiconductor-insulator phase transition in the single-layered

perovskite $La_{0.5}Sr_{1.5}MnO_4$, *Physical Review B* **83**, 184101–184113.
http://link.aps.org/doi/10.1103/PhysRevB.83.184101

Hüfner, S.: 2003, *Photoelectron Spectroscopy: Principles and Applications*, first edn, Springer-Verlag, Berlin.

Hwang, H. Y., Cheong, S.-W., Radaelli, P. G., Marezio, M. and Batlogg, B.: 1995, Lattice effects on the magnetoresistance in doped $LaMnO_3$, *Physical Review Letters* **75**, 914–917.
http://link.aps.org/doi/10.1103/PhysRevLett.75.914

Inami, T., Fukuda, T., Mizuki, J., Ishihara, S., Kondo, H., Nakao, H., Matsumura, T., Hirota, K., Murakami, Y., Maekawa, S. and Endoh, Y.: 2003, Orbital excitations in $LaMnO_3$ studied by resonant inelastic x-ray scattering, *Physical Review B* **67**, 045108–045113.
http://link.aps.org/doi/10.1103/PhysRevB.67.045108

Jin, S., Tiefel, T. H., McCormack, M., Fastnacht, R. A., Ramesh, R. and Chen, L. H.: 1994, Thousandfold change in resistivity in magnetoresistive La-Ca-Mn-O films, *Science* **264**(5157), 413–415.
http://www.sciencemag.org/content/264/5157/413.abstract

Keating, P. N.: 1966, Effect of invariance requirements on the elastic strain energy of crystals with application to the diamond structure, *Physical Review* **145**, 637–645.
http://link.aps.org/doi/10.1103/PhysRev.145.637

Kim, Y.-J., Hill, J. P., Wakimoto, S., Birgeneau, R. J., Chou, F. C., Motoyama, N., Kojima, K. M., Uchida, S., Casa, D. and Gog, T.: 2007, Observations on the resonant inelastic x-ray scattering cross section in copper oxide compounds, *Physical Review B* **76**, 155116–155122.
http://link.aps.org/doi/10.1103/PhysRevB.76.155116

Kimura, T., Goto, T., Shintani, H., Ishizaka, K., Arima, T. and Tokura, Y.: 2003, Magnetic control of ferroelectric polarization, *Nature* **426**, 55–58.
http://www.nature.com/nature/journal/v426/n6962/full/nature02018.html

Kimura, T., Ishihara, S., Shintani, H., Arima, T., Takahashi, K. T., Ishizaka, K. and Tokura, Y.: 2003, Distorted perovskite with e_g^1 configuration as a frustrated spin system, *Physical Review B* **68**, 060403–060406.
http://link.aps.org/doi/10.1103/PhysRevB.68.060403

Kiryukhin, V.: 2004, Nanoscale structural correlations in magnetoresistive manganites, *New Journal of Physics* **6**(1), 155.
http://stacks.iop.org/1367-2630/6/i=1/a=155

Kittel, C.: 2005, *Introduction to Solid State Physics*, eighth edn, John Wiley & Sons, Inc.

Kivelson, S. A., Bindloss, I. P., Fradkin, E., Oganesyan, V., Tranquada, J. M., Kapitulnik, A. and Howald, C.: 2003, How to detect fluctuating stripes in the high-temperature superconductors, *Review of Modern Physics* **75**, 1201–1241. http://link.aps.org/doi/10.1103/RevModPhys.75.1201

Kraus, R., Schrade, M., Schuster, R., Knupfer, M., Revcolevschi, A., Büchner, B. and Geck, J.: 2011, Signatures of electronic polarons in $La_{1-x}Sr_{1+x}MnO_4$ observed by electron energy-loss spectroscopy, *Physical Review B* **83**, 165130–165135. http://link.aps.org/doi/10.1103/PhysRevB.83.165130

Kumar, S. and Majumdar, P.: 2006, Insulator-metal phase diagram of the optimally doped manganites from the disordered holstein-double exchange model, *Physical Review Letters* **96**, 016602–016605. http://link.aps.org/doi/10.1103/PhysRevLett.96.016602

Lee, P. A., Nagaosa, N. and Wen, X.-G.: 2006, Doping a mott insulator: Physics of high-temperature superconductivity, *Review of Modern Physics* **78**, 17–85. http://link.aps.org/doi/10.1103/RevModPhys.78.17

Lee, Y. S., Arima, T., Onoda, S., Okimoto, Y., Tokunaga, Y., Mathieu, R., Yu, X. Z., He, J. P., Kaneko, Y., Matsui, Y., Nagaosa, N. and Tokura, Y.: 2007, Correlation of electronic structure and ordered charge and orbital patterns for single-layered manganites in a wide hole-doping range ($0 \leq x \leq 1$), *Physical Review B* **75**, 144407–144412. http://link.aps.org/doi/10.1103/PhysRevB.75.144407

Lee, Y. S., Onoda, S., Arima, T., Tokunaga, Y., He, J. P., Kaneko, Y., Nagaosa, N. and Tokura, Y.: 2006, In-plane anisotropy of the electronic structure for the charge- and orbital-ordered state in half-doped manganite with layered structure, *Physical Review Letters* **97**, 077203–077206. http://link.aps.org/doi/10.1103/PhysRevLett.97.077203

Littlewood, P. B.: 1986, Strain-induced ordering in silicon-germanium alloys, *Physical Review B* **34**, 1363–1366. http://link.aps.org/doi/10.1103/PhysRevB.34.1363

Liu, J. W., Zeng, Z., Zheng, Q. Q. and Lin, H. Q.: 1999, Effective transfer integrals for the jahn-teller distortion in $LaMnO_3$, *Physical Review B* **60**, 12968–12973. http://link.aps.org/doi/10.1103/PhysRevB.60.12968

Liu, K., Wu, X. W., Ahn, K. H., Sulchek, T., Chien, C. L. and Xiao, J. Q.: 1996, Charge ordering and magnetoresistance in $Nd_{1-x}Ca_xMnO_3$ due to reduced double exchange, *Physical Review B* **54**, 3007–3010. http://link.aps.org/doi/10.1103/PhysRevB.54.3007

Liu, X., Seman, T. F., Ahn, K. H., van Veenendaal, M., Casa, D., Prabhakaran, D., Boothroyd, A. T., Ding, H. and Hill, J. P.: 2012, Strongly momentum-dependent

screening dynamics in $La_{0.5}Sr_{1.5}MnO_4$ observed with resonant inelastic x-ray scattering. Submitted to Physical Review Letters.
http://arxiv.org/abs/1210.6634

Lookman, T., Shenoy, S. R., Rasmussen, K. Ø., Saxena, A. and Bishop, A. R.: 2003, Ferroelastic dynamics and strain compatibility, *Physical Review B* **67**, 024114–024140.
http://link.aps.org/doi/10.1103/PhysRevB.67.024114

Louca, D., Egami, T., Dmowski, W. and Mitchell, J. F.: 2001, Structural effect on colossal magnetoresistivity in manganites: Bond versus band, *Physical Review B* **64**, 180403–180406.
http://link.aps.org/doi/10.1103/PhysRevB.64.180403

Lynn, J. W., Erwin, R. W., Borchers, J. A., Huang, Q., Santoro, A., Peng, J.-L. and Li, Z. Y.: 1996, Unconventional ferromagnetic transition in $La_{1-x}Ca_xMnO_3$, *Physical Review Letters* **76**, 4046–4049.
http://link.aps.org/doi/10.1103/PhysRevLett.76.4046

Millis, A. J.: 1996, Cooperative jahn-teller effect and electron-phonon coupling in $La_{1-x}A_xMnO_3$, *Physical Review B* **53**, 8434–8441.
http://link.aps.org/doi/10.1103/PhysRevB.53.8434

Millis, A. J.: 1998, Lattice effects in magnetoresistive manganese perovskites, *Nature* **392**, 147–150.
http://www.nature.com/nature/journal/v392/n6672/full/392147a0.html

Millis, A. J., Littlewood, P. B. and Shraiman, B. I.: 1995, Double exchange alone does not explain the resistivity of $La_{1-x}Sr_xMnO_3$, *Physical Review Letters* **74**, 5144–5147.
http://link.aps.org/doi/10.1103/PhysRevLett.74.5144

Millis, A. J., Shraiman, B. I. and Mueller, R.: 1996, Dynamic jahn-teller effect and colossal magnetoresistance in $La_{1-x}Sr_xMnO_3$, *Physical Review Letters* **77**, 175–178.
http://link.aps.org/doi/10.1103/PhysRevLett.77.175

Mirgorodsky, A. P. and Smirnov, M. B.: 1993, Mechanical treatment of structural phase transitions and related phenomena in crystals: a lattice dynamical study of pressure-induced structural transformations in perovskite-like ReO_3, *Journal of Physics: Condensed Matter* **5**(20), 3313.
http://stacks.iop.org/0953-8984/5/i=20/a=004

Mochizuki, M. and Furukawa, N.: 2009, Microscopic model and phase diagrams of the multiferroic perovskite manganites, *Physical Review B* **80**, 134416–134437.
http://link.aps.org/doi/10.1103/PhysRevB.80.134416

Moon, J.: 2006, *Mode-based atomic-scale approach: Classical and quantum mechanical approach*, Senior thesis, Konkuk University, Seoul, South Korea.

Moreo, A., Yunoki, S. and Dagotto, E.: 1999, Phase separation scenario for manganese oxides and related materials, *Science* **283**(5410), 2034–2040.
http://www.sciencemag.org/content/283/5410/2034.abstract

Nozières, P. and de Dominicis, C. T.: 1969, Singularities in the x-ray absorption and emission of metals. iii. one-body theory exact solution, *Physical Review* **178**, 1097–1107.
http://link.aps.org/doi/10.1103/PhysRev.178.1097

Pines, D. and Nozières, P.: 1999, *The Theory Of Quantum Liquids*, first edn, Westview Press, Boulder.

Pradhan, K., Mukherjee, A. and Majumdar, P.: 2007, Distinct effects of homogeneous weak disorder and dilute strong scatterers on phase competition in manganites, *Physical Review Letters* **99**, 147206–147209.
http://link.aps.org/doi/10.1103/PhysRevLett.99.147206

Radaelli, P. G., Iannone, G., Marezio, M., Hwang, H. Y., Cheong, S.-W., Jorgensen, J. D. and Argyriou, D. N.: 1997, Structural effects on the magnetic and transport properties of perovskite $A_{1-x}A'_xMnO_3(x = 0.25, 0.30)$, *Physical Review B* **56**, 8265–8276.
http://link.aps.org/doi/10.1103/PhysRevB.56.8265

Röder, H., Zang, J. and Bishop, A. R.: 1996, Lattice effects in the colossal-magnetoresistance manganites, *Physical Review Letters* **76**, 1356–1359.
http://link.aps.org/doi/10.1103/PhysRevLett.76.1356

Rodríguez-Carvajal, J., Hennion, M., Moussa, F., Moudden, A. H., Pinsard, L. and Revcolevschi, A.: 1998, Neutron-diffraction study of the jahn-teller transition in stoichiometric $LaMnO_3$, *Physical Review B* **57**, R3189–R3192.
http://link.aps.org/doi/10.1103/PhysRevB.57.R3189

Salafranca, J. and Brey, L.: 2006, Phase diagram and incommensurate phases in undoped manganites, *Physical Review B* **73**, 024422–024430.
http://link.aps.org/doi/10.1103/PhysRevB.73.024422

Salamon, M. B. and Jaime, M.: 2001, The physics of manganites: Structure and transport, *Review of Modern Physics* **73**, 583–628.
http://link.aps.org/doi/10.1103/RevModPhys.73.583

Sánchez, D., Alonso, J. A. and Martínez-Lope, M. J.: 2002, Neutron-diffraction study of the jahnteller transition in $PrMnO_3$, *Journal of the Chemical Society, Dalton Transactions* **23**, 4422–4425.
http://pubs.rsc.org/en/content/articlelanding/2002/dt/b208660n

Seman, T. F., Ahn, K. H., Lookman, T., Saxena, A., Bishop, A. R. and Littlewood, P. B.: 2012, Effects of rare-earth ion size on the stability of the coherent jahn-teller distortions in undoped perovskite manganites, *Physical Review B* **86**, 184106–184115.
http://link.aps.org/doi/10.1103/PhysRevB.86.184106

Seman, T. F., Moon, J. and Ahn, K. H.: 2012, Symmetry-based atomic scale description of lattice dynamics and its applications for phonon mode analysis. Submitted.
http://arxiv.org/abs/0707.1921

Semba, T., Takahashi, M. and Igarashi, J.-i.: 2008, Theoretical analysis of resonant inelastic x-ray scattering spectra in $LaMnO_3$, *Physical Review B* **78**, 155111–155119.
http://link.aps.org/doi/10.1103/PhysRevB.78.155111

Sergienko, I. A., Şen, C. and Dagotto, E.: 2006, Ferroelectricity in the magnetic *e*-phase of orthorhombic perovskites, *Physical Review Letters* **97**, 227204–227207.
http://link.aps.org/doi/10.1103/PhysRevLett.97.227204

Shenoy, S. R., Lookman, T., Saxena, A. and Bishop, A. R.: 1999, Martensitic textures: Multiscale consequences of elastic compatibility, *Physical Review B* **60**(R12 537).

Sternlieb, B. J., Hill, J. P., Wildgruber, U. C., Luke, G. M., Nachumi, B., Moritomo, Y. and Tokura, Y.: 1996, Charge and magnetic order in $La_{0.5}Sr_{1.5}MnO_4$, *Physical Review Letters* **76**, 2169–2172.
http://link.aps.org/doi/10.1103/PhysRevLett.76.2169

Tranquada, J. M., Sternlieb, B. J., Axe, J. D., Nakamura, Y. and Uchida, S.: 1995, Evidence for stripe correlations of spins and holes in copper oxide superconductors, *Nature* **375**, 561–563.
http://www.nature.com/nature/journal/v375/n6532/pdf/375561a0.pdf

van den Brink, J. and van Veenendaal, M.: 2006, Correlation functions measured by indirect resonant inelastic x-ray scattering, *Europhysics Letters* **73**(1), 121.
http://stacks.iop.org/0295-5075/73/i=1/a=121

van der Laan, G., Westra, C., Haas, C. and Sawatzky, G. A.: 1981, Satellite structure in photoelectron and auger spectra of copper dihalides, *Physical Review B* **23**, 4369–4380.
http://link.aps.org/doi/10.1103/PhysRevB.23.4369

van Veenendaal, M. A. and Sawatzky, G. A.: 1993, Nonlocal screening effects in 2p x-ray photoemission spectroscopy core-level line shapes of transition metal compounds, *Physical Review Letters* **70**, 2459–2462.
http://link.aps.org/doi/10.1103/PhysRevLett.70.2459

Vergés, J. A., Martín-Mayor, V. and Brey, L.: 2002, Lattice-spin mechanism in colossal magnetoresistive manganites, *Physical Review Letters* **88**, 136401–136404. http://link.aps.org/doi/10.1103/PhysRevLett.88.136401

von Helmolt, R., Wecker, J., Holzapfel, B., Schultz, L. and Samwer, K.: 1993, Giant negative magnetoresistance in perovskitelike $La_{2/3}Ba_{1/3}MnO_x$ ferromagnetic films, *Physical Review Letters* **71**, 2331–2333. http://link.aps.org/doi/10.1103/PhysRevLett.71.2331

Weber, F., Rosenkranz, S., Castellan, J.-P., Osborn, R., Mitchell, J. F., Zheng, H., Casa, D., Kim, J. H. and Gog, T.: 2010, *d*-*d* excitations in bilayer manganites probed by resonant inelastic x-ray scattering, *Physical Review B* **82**, 085105–085111. http://link.aps.org/doi/10.1103/PhysRevB.82.085105

Yamauchi, K., Freimuth, F., Blügel, S. and Picozzi, S.: 2008, Magnetically induced ferroelectricity in orthorhombic manganites: Microscopic origin and chemical trends, *Physical Review B* **78**, 014403–014412. http://link.aps.org/doi/10.1103/PhysRevB.78.014403

Zeng, L. J., Ma, C., Yang, H. X., Xiao, R. J., Li, J. Q. and Jansen, J.: 2008, Structural modulation and electronic structural features in the charge ordered state of $La_{0.5}Sr_{1.5}MnO_4$, *Physical Review B* **77**, 024107–024112. http://link.aps.org/doi/10.1103/PhysRevB.77.024107

Zhang, J., Dai, P., Fernandez-Baca, J. A., Plummer, E. W., Tomioka, Y. and Tokura, Y.: 2001, Jahn-teller phonon anomaly and dynamic phase fluctuations in $La_{0.7}Ca_{0.3}MnO_3$, *Physical Review Letters* **86**, 3823–3826. http://link.aps.org/doi/10.1103/PhysRevLett.86.3823

Zhu, J.-X., Ahn, K. H., Nussinov, Z., Lookman, T., Balatsky, A. V. and Bishop, A. R.: 2003, Elasticity-driven nanoscale electronic structure in superconductors, *Physical Review Letters* **91**, 057004–057008. http://link.aps.org/doi/10.1103/PhysRevLett.91.057004